UHH Universität Hamburg
DER FORSCHUNG | DER LEHRE | DER BILDUNG

Search for long lived particles in the CMS muon system

Dissertation
zur Erlangung des Doktorgrades
an der Fakultät für Mathematik, Informatik und Naturwissenschaften
Fachbereich Physik
der Universität Hamburg

vorgelegt von
Jörg Christoph Schindler

Hamburg
2023

Eidesstattliche Versicherung / Declaration on oath

Hiermit versichere ich an Eides statt, die vorliegende Dissertationsschrift selbst verfasst und keine anderen als die angegebenen Hilfsmittel und Quellen benutzt zu haben.

Hamburg, den 15-09-2023

Schindle

Unterschrift der Doktorandin / des Doktoranden

Gutachter/innen der Dissertation: Prof. Dr. Gregor Kasieczka
Prof. Dr. Peter Schleper

Zusammensetzung der Prüfungskommission: Dr. Sarah Heim
Prof. Dr. Gregor Kasieczka
Dr. Isabell Melzer-Pellmann
Prof. Dr. Peter Schleper
Prof. Dr. Günter H. W. Sigl

Vorsitzende/r der Prüfungskommission: Prof. Dr. Günter H. W. Sigl

Datum der Disputation: 05.12.2023

Vorsitzender Fach-Promotionsausschusses PHYSIK: Prof. Dr. Markus Drescher

Leiter des Fachbereichs PHYSIK: Prof. Dr. Wolfgang J. Parak

Dekan der Fakultät MIN: Prof. Dr.-Ing. Norbert Ritter

Abstract

This thesis presents two searches for long-lived particles (LLP) with long lifetimes, leading to flight distances in the order of meters. The searches are performed with data from proton-proton collisions at a center-of-mass energy of 13 TeV from the Large Hadron Collider (LHC) corresponding to an integrated luminosity of $\mathcal{L} = 137\,\mathrm{fb}^{-1}$ recorded with the Compact Muon Solenoid (CMS) detector.

Both searches target long-lived particles decaying hadronically inside the CMS muon system, which is uniquely suited for such a search. The Drift Tubes (DT) and Cathode Strip Chambers (CSC) are placed within the iron return yoke, which allows the usage of the muon system as a sampling calorimeter for hadronic showers. These Muon Detector Showers (MDS) are reconstructed with a density based clustering algorithm (DBSCAN), clustering the detector level hits together. This newly created object was developed for the analyses presented in this thesis.

The first analysis considers a Twin Higgs benchmark model, with long-lived particle masses between 7 and 55 GeV and lifetimes between 0.1 and 100 m, with decays into a pair of b quarks, d quarks or τ leptons being considered. The LLPs will create an isolated hadronic shower in the muon system, a large amount of missing transverse momentum pointing in the same direction and an initial state radiation jet on the other side of the detector. The main background consists of Standard Model particles from pileup with large displacements and is estimated using a data-driven ABCD method. The analysis finds no evidence for long-lived particles, but improves the current best upper limits at 95 % confidence level on the possible branching ratio of the long-lived particle by a factor between 2 to 6, depending on the mass and lifetime of the LLP.

The second analysis targets long-lived heavy neutral leptons (HNL), with HNL masses between 1 and 3.5 GeV and lifetimes between 1 mm and 10 m. The HNL can either be Majorana or Dirac type, each of which decays into a lepton and a hadronically decaying W boson, forming a shower in the muon system. The signal signature consists of an isolated hadronic shower being aligned with the $p_{\mathrm{T}}^{\mathrm{miss}}$ and a prompt lepton on the other side of the detector. The background consists of pileup and $\mathrm{Z} \rightarrow \mu\mu$ events, where one muon emits bremsstrahlung, and is estimated using a data driven ABCD method. No evidence for HNLs is found but an upper limit at 95 % confidence level on the mixing angle is set for the different HNL masses and flavors. The current best limit is improved for HNL masses between 1.9 and 3.3 GeV depending on the flavor of the HNL.

Zusammenfassung

Diese Doktorarbeit präsentiert zwei Suchen nach Teilchen mit langen Lebenszeiten, welche zu einer Verschiebung ihrer Zerfallsorte in der größe einiger Meter führt. Die Analysen wurden mit Daten von Proton-Proton-Kollisionen mit einer Schwerpunktsenergie von 13 TeV, welche am Large Hadron Collider (LHC) stattfanden, durchgeführt. Der Compact Muon Solenoid Detektor nahm die Daten auf, welche einer integrierte Luminosität von $\mathcal{L} = 137\,\mathrm{fb}^{-1}$ entsprechen.

Beide Analysen befassen sich mit langlebigen Teilchen, welche innerhalb der CMS Muondetektoren hadronisch zerfallen. Der CMS Detektor ist für derartige Zerfälle besonders gut geeignet, da die Drift Tubes (DT) und Cathode Strip Chambers (CSC) Detektoren in das Eisenrücklaufjoch eingebettet sind. Zusammen fungieren diese Komponenten dann als ein Samplingkalorimeter für hadronische Zerfälle. Für die Analyse solcher Zerfälle wurde das neue Objekt der Muonen Detektor Schauer (MDS) definiert, welches mithilfe eines dichte basierten geometrischen Clusteralgorithmus (DBSCAN) rekonstruiert wird.

Die erste Analyse sucht nach langlebigen Teilchen mit Massen zwischen 7 und 55 GeV und Lebenszeiten zwischen 0.1 und 100 m, welche vom einem Twin Higgs Modell vorhergesagt werden. Zerfälle der langlebigen Teilchen in ein Paar von b oder d Quarks, sowie der Zerfall in ein paar Tau Leptonen, werden berücksichtigt. Diese Zerfälle erzeugen einen isolierten hadronischen Teilchenschauer in den Muondetektoren, welcher gleichzeitig mit einer großen Menge von fehlendem Transversalimpuls und einem Teilchen-Jet auf der gegenüberliegenden des Detektors einhergeht. Der Großteil der Untergrundprozesse besteht aus stabilen Standardmodellteilchen, welche durch weitere, gleichzeitig mit dem eigentlichen Kollisionsereignis stattfindenden Kollisionen (pileup), erzeugt werden können und mithilfe einer datengetriebenen ABCD-Methode abgeschätzt werden. Die vorgestellte Analyse findet keine Hinweise für langlebige Teilchen dieser Art, setzt aber obere Ausschlussgrenzen mit 95 % CL auf die möglichen Zerfallsbreiten. Die bisherigen besten Ausschlussgrenzen werden um einen Faktor von 2 bis 6 verbessert, je nach Masse und Lebenszeit des spezifischen langlebigen Teilchens.

Die zweite Analyse ist eine Suche nach langlebigen schweren neutralen Leptonen (HNL), welche eine Masse zwischen 1 und 3.5 GeV und Lebenszeiten zwischen 1 mm und 10 m haben. Diese HNLs können sowohl Dirac- als auch Majorana-Teilchen sein, wobei sie in beiden Fällen in ein Lepton und ein hadronisch zerfallendes W-Boson zerfallen. Hierbei entsteht ein hadronischer Teilchenschauer in den Muondetektoren, wobei dies wiederum mit einem fehlenden Transversalimpuls in der selben Richtung im Detektor einhergeht. Zusätzlich wird ein isoliertes Lepton auf der gegenüberliegenden Seite des Detektors erwartet. Die Untergrundprozesse sind hierbei wieder pileup, aber auch der $Z \rightarrow \mu\mu$ Prozess, falls eines der beiden Muonen Bremsstrahlung abgibt. Beide Prozesse werden mithilfe einer datengetriebenen ABCD-Methode abgeschätzt. Die Analyse findet keinen Hinweise für HNLs, kann aber eine obere Ausschlussgrenze mit 95 % CL für Mischungswinkel setzen. Die bisherigen besten Ausschlussgrenzen werden für HNL Massen zwischen 1.9 und 3.3 GeV, je nach Lepton-Flavor, übertroffen.

Contents

1 Introduction

“What is the world made of?”. This is one of the most fundamental questions humankind has asked itself. Particle physics tries to answer this question by studying the smallest known building blocks, that make up all matter in the universe. The field has come a long way, from greek philosophers arguing, whether there is even a smallest building block, to the current century, where the the Higgs boson was experimentally discovered at the Large Hadron Collider. The Higgs boson was predicted by the Standard Model (SM) of particle physics, which is a quantum field theory aiming to describe all elementary particles and their interactions. It describes the interactions of three of the four known fundamental forces, with only gravity not covered yet. Countless experimental results have validated the predictions of the SM and precision measurements have measured the free parameters. With the last missing particle of the SM being found, naively one could ask if that is the end of the road for particle physics. However, experimental evidence points towards physics beyond the SM. From existence of dark matter and dark energy, to the masses of neutrinos, to the inclusion of gravity within the SM, it is clear that the work for particle physicists is not done yet. In addition, theoretical problems, like the hierarchy problem of the Higgs boson mass, are also pointing towards new physics beyond the SM.

In order to explain the experimental observations and answer open questions, several theoretical models have been developed, extending the SM. A subset of such theories, designed to solve the hierarchy problem of the Higgs boson mass, are the so-called Twin Higgs models. These models introduce a new sector of twin particles, with the SM Higgs being the only particle able to interact with its twin particle, thereby acting as a portal between the SM and the new sector. The decay of this twin partner of the Higgs boson can result in two long-lived particles, which are able to travel a large distance inside a detector. Another set of models extends the SM by introducing right-handed partners to the neutrinos, the heavy neutral leptons. This addition aims to introduce neutrino masses into the SM, while also providing a dark matter candidate.

These theories are the basis for the two searches presented in this thesis. Both searches target long-lived particles with a long enough lifetime to decay inside the

CMS muon system. Such decays lead to hadronic showers inside the muon detector chambers, which are detected as a so-called Muon Detector Shower (MDS). This provides a signature for the decay of long-lived particles, that is relatively background free, but requires the development of new analysis techniques for the reconstruction of the MDS.

The thesis is structured as follows: In Ch. 2 a general overview about particle physics is given, with a special focus on Twin Higgs and HNL theories. Next, Ch. 3 introduces the experimental setup of the LHC and the CMS detector is discussed. Afterwards, in Ch. 4 the reconstructed analysis objects, including the newly developed MDS, are introduced. The next two chapters, Ch. 5 and Ch. 6, then present the two previously mentioned searches for long-lived particles. At the end of the thesis a summary and outlook on the future for these type of searches is given in Ch. 7.

2 Theory

In the following chapter the theoretical foundation of particle physics, the so called Standard Model, is discussed. For a more in-depth review, see Ref. [1] and Ref. [2]. If not specified otherwise, natural units are used for this thesis, as in the speed of light c and Planck's constant $\hbar$ are equal to one.

2.1 The Standard Model of Particle Physics

The Standard Model (SM) of particle physics describes the elementary particles and their interactions. Three out of the four fundamental forces are included in the SM, with gravity not being able to be integrated into the SM so far. In the scope of elementary particle physics, it is assumed that gravity is simply too weak of a force to significantly impact the results or predictions. The SM is formulated in terms of a quantum field theory (QFT), in which particles are described as quantized excitations of fields and forces are mediated via interactions between particles. The fundamental interactions are related to gauge symmetries, with the symmetry group characterizing the SM being given by

$$SU(3) \times SU(2) \times U(1), \tag{2.1}$$

with the strong interaction $SU(3)$, weak interaction $SU(2)$ and the electromagnetic interaction $U(1)$.

Within the SM there are two fundamental types of particles: Fermions, which carry half-integer spin and follow Fermi-Dirac statistics [3, 4] and bosons, which carry an integer spin and follow the Bose-Einstein statistics [5]. Table 2.1 summarizes all fermions with their masses, electric charges and isospins. Fermions consist of six quarks and six leptons, where for each of the fermions an anti-particle exists, that has the same mass but opposite charge. Leptons are grouped into three generations, with one charged lepton (e, μ, τ), each having the same electric charge e, and one neutrino of the same flavor $(\nu_e, \nu_\mu, \nu_\tau)$ being placed in each generation. So far only left-handed neutrinos have been experimentally observed, since the detection of neutrinos is done through the weak interaction, which only couples to left-handed particles. At

Table 2.1: Standard model fermions with their electric charge, Isospin T_3 and their masses. For some mass values the corresponding uncertainties were too small to reasonable display here. From [2]

Fermion	Electric Charge in e	T_3	Mass
electron neutrino ν_e	0	1/2	$< 0.8\,\mathrm{eV}$
electron e	−1	−1/2	$0.51\,\mathrm{MeV}$
muon neutrino ν_μ	0	1/2	$< 0.19\ \mathrm{MeV}$
muon μ	−1	−1/2	$105.66\,\mathrm{MeV}$
tau neutrino ν_τ	0	1/2	$< 18.2\ \mathrm{MeV}$
tau τ	−1	−1/2	$1776.86 \pm 0.12\,\mathrm{MeV}$
up quark u	2/3	+/2	$2.16^{+0.49}_{-0.26}\,\mathrm{MeV}$
down quark d	−1/3	−1/2	$4.67^{+0.48}_{-0.17}\,\mathrm{MeV}$
charm quark c	2/3	1/2	$1.27 \pm 0.02\,\mathrm{GeV}$
strange quark s	−1/3	−1/2	$93.4^{+8.6}_{-3.4}\,\mathrm{MeV}$
top quark t	2/3	1/2	$172.69 \pm 0.3\,\mathrm{GeV}$
bottom quark b	−1/3	−1/2	$4.18^{+0.03}_{-0.02}\,\mathrm{GeV}$

first neutrinos were assumed to be massless, but experimental evidence of neutrino oscillation points towards neutrinos having a very small mass [6–8]. For neutrino oscillation to be possible, the weak eigenstates ν_e, ν_μ, ν_τ have to be made up of a superposition of the mass eigenstates ν_1, ν_2, ν_3. Currently the mass of the neutrinos is unknown, but upper limits have been set [2, 9–11]. Quarks are also grouped into three generations, each with an up- and down-type quark, where the up-type quarks carry a $\frac{2}{3}$e charge, while down-type quarks carry a $-\frac{1}{3}$e charge. The quarks of the first generations are the up and down quarks, the second generation consists of the charm and strange quarks and the third generation consists of the top and bottom quarks. In addition to their electric charge, the quarks also carry a color charge allowing them to interact via the strong interaction.

Interactions within the SM, i.e. the electromagnetic, weak and strong interactions, are mediated by so-called gauge bosons, with spin 1. Table 2.2 gives an overview of all gauge bosons with their masses, charges and isospins. In the next sections an overview of these interactions is given, followed by a discussion of the Higgs mechanism. The description follows the series of overview articles in Ref. [2].

2.1.1 Electroweak Interaction

The electroweak interaction (EWK) [12–16] is based on the SU(2) × U(1) gauge group, resulting in four massless bosons W^i_μ (with $i = 1, 2, 3$) and B_μ. Quarks and leptons are arranged as left-handed SU(2) doublets:

$$\text{Leptons} : \Psi_i = \begin{pmatrix} \nu_i \\ l_i^- \end{pmatrix}, \text{Quarks} : \Psi_i = \begin{pmatrix} u_i \\ d_i^{\prime} \end{pmatrix}, \tag{2.2}$$

Table 2.2: Standard model gauge bosons with their charge, Isospin T_3 and their masses. From [2]

Bosons	Interaction	Electric Charge in e	T_3	Mass
Photon γ	electroweak	0	0	0
$W^{\pm}$ bosons	electroweak	± 1	± 1	$80.379 \pm 0.012\,\mathrm{GeV}$
Z boson	electroweak	0	0	$91.1876 \pm 0.0021\,\mathrm{GeV}$
8 gluons	QCD	0	0	0

with up-type quarks u_i, leptons l_i^- and neutrinos ν_i. Here $d^{'}_i = \sum_j V_{ij} d_j$, with the Cabibbo-Kobayashi-Maskawa mixing matrix V_{ij} [17, 18], making $d^{'}_i$ a superposition of the mass eigenstates for down-type quarks d_j. The right handed states transform as singlets under the SU(2) transformation. With the Weinberg angle the the physical bosons can be written as:

$$\begin{pmatrix} A \\ Z \end{pmatrix} = \begin{pmatrix} \cos\theta_W & \sin\theta_W \\ -\sin\theta_W & \cos\theta_W \end{pmatrix} \begin{pmatrix} B^0 \\ W^0 \end{pmatrix}, \tag{2.3}$$

$$W^{\pm} = \frac{1}{\sqrt{2}}(\mathrm{W}_1 \mp i\mathrm{W}_2), \tag{2.4}$$

The Z and W boson get their masses via the Higgs mechanism, which will be discussed in Ch. 2.1.3. With the addition of the Higgs mechanism for spontaneous symmetry breaking, the Lagrangian for the fermion fields ψ_i is:

$$\begin{aligned} \mathcal{L}_F = & \sum_i \bar{\psi}_i \left(i\partial\!\!\!/ - m_i - \frac{m_i H}{v} \right) \psi_i - \frac{g}{2\sqrt{2}} \sum_i \bar{\Psi}_i \gamma^{\mu}(1-\gamma^5)(T^+ W^+_{\mu} + T^- W^-_{\mu})\Psi_i \\ & - e \sum_i Q_i \bar{\psi}_i \gamma^{\mu} \psi_i A_{\mu} - \frac{g}{2\cos\theta_W} \sum_i \bar{\psi}_i \gamma^{\mu}(g^i_V - g^i_A \gamma^5)\psi_i Z_{\mu}. \end{aligned}$$

Here m_i is the mass, Q_i the electric charge of the fermion field, $T^{\pm}$ denotes the weak isospin operators and θ_W is the so called Weinberg angle. The first term describes the kinematic term, mass term and the Yukawa coupling of the Higgs boson to fermions. The second term describes the charged current weak interaction, which is the coupling of $W^{\pm}$ bosons to fermions. The third term describes electromagnetic interactions, meaning the coupling of photons to electrically charged fermions, and the last term describes the weak neutral-current interactions, which is the coupling of the Z boson and fermions.

2.1.2 Quantum Chromodynamics

The strong interaction of particles carrying color charge, i.e. quarks and gluons, is described by Quantum Chromodynamics (QCD) [19–21], which is a gauge field theory with a SU(3) symmetry group. The QCD Lagrangian is given by

$$\mathcal{L} = \sum_q \bar{\psi}_{q,a}(i\gamma^{\mu}\partial_{\mu}\delta_{ab} - g_s \gamma^{\mu} t^C_{ab} A^C_{\mu} - m_q \delta_{ab})\psi_{q,b} - \frac{1}{4} F^A_{\mu\nu} F^{A\,\mu\nu}, \tag{2.5}$$

with $\psi_{q,a}$ being the quark-field spinor for a quark of flavor q with mass m_q and color a, with the color index going from a=1 to a=3, indicating three different possible colors. The eight gluons are represented by the vector field A^C_μ with C going from C=1 to C=8. The parameter g_S is the QCD coupling constant (which can also be written as $\alpha_s = \frac{g_s^2}{4\pi}$) and t^C_{ab} corresponds to the eight generators of the SU(3) group, which enable rotations in the color space. The variable $F^A_{\mu\nu}$ is the so called field strength tensor. Besides the masses of the quarks, which are not a result of QCD but rather of electroweak origin via the Higgs mechanism, the QCD coupling constant is the fundamental parameter of QCD. The first term of the Lagrangian describes the kinematics and interaction of quarks and gluons and also includes the mass term for quarks. The second term consists of the kinetic term of the gluons and the interactions of gluons with each other.

Two key properties of QCD are confinement and asymptotic freedom. The term confinement describes the behavior of the QCD coupling constant at large distances or low energies, leading to large couplings. Because of this, quarks and gluons can not exist as free particles, but they rather have to form color-neutral bound states, which are called hadrons. Asymptotic freedom means, that for small distances or high energies the QCD coupling constant decreases, resulting to the fact, that the quarks or gluons will not interact strongly but rather only interact weakly.

2.1.3 The Higgs Boson

In the above discussion of the SM the masses of the Z and W boson are assumed to be zero, which conflicts with the observation that the Z and W bosons are both massive. Additionally, the fermions are also considered massless, again clashing with experimental results. To give the particles their masses, the Higgs mechanism [22–24] is introduced, which adds the so-called electro weak symmetry breaking to the SM. The Higgs mechanism introduces an additional $\mathrm{SU(2)_L}$ doublet field with four degrees of freedom:

$$\Phi = \frac{1}{\sqrt{2}} \begin{pmatrix} \sqrt{2}\phi^+ \\ \phi^0 + ia^0 \end{pmatrix}, \tag{2.6}$$

with the CP even component ϕ_0 and the CP odd neutral component a^0. A scalar potential then is defined as

$$V(\Phi) = m^2\Phi^\dagger\Phi + \lambda(\Phi^\dagger\Phi)^2. \tag{2.7}$$

For $\lambda > 0$ and $m^2 < 0$ the neutral component of the scalar doublet acquires a non-zero vacuum expectation value (VEV) v. The ground state of the Higgs doublet then is

$$\langle\Phi\rangle = \frac{1}{\sqrt{2}} \begin{pmatrix} 0 \\ v \end{pmatrix}. \tag{2.8}$$

With this in mind, the neutral component ϕ^0 can be written as $\phi^0 = H + \langle\phi^0\rangle = H + v$. The Higgs Lagrangian then is:

$$\mathcal{L}_{\mathrm{Higgs}} = (D_\mu\Phi)^\dagger(D^\mu\Phi) - V(\Phi), \tag{2.9}$$

with the covariant derivative $D_\mu\Phi$:

$$D_\mu\Phi = (\partial_\mu + ig\sigma^a W^a_\mu/2 + ig'YB_\mu/2)\Phi, \tag{2.10}$$

where W^a and B are the fields of the electroweak gauge group, g and g' are their respective couplings and σ^a are the Pauli matrices. Three of the four degrees of freedom of the Higgs doublet are absorbed to give the physical Z and $W^{\pm}$ bosons their masses, which are:

$$m_W^2 = \frac{g^2 v^2}{4}, \; m_Z^2 = \frac{(g'^2 + g^2) v^2}{4}. \tag{2.11}$$

The last remaining degree of freedom then is the physical Higgs boson H, a new scalar particle. The new boson is a CP-even scalar of spin 0 with a mass of $m_H = \sqrt{2\lambda} v$, with the self coupling constant λ which is a free parameter in the SM and has to be measured. The VEV v is given by

$$v = (\sqrt{2} G_F)^{-\frac{1}{2}} \approx 246 \, \text{Gev}. \tag{2.12}$$

Experimentally the Higgs boson mass is measured to be $m_H = 125.25 \pm 0.17 \, \text{Gev}$ [2].

The fermions in the SM get their masses through Yukawa interactions, coupling the fermion fields to the Higgs doublet. The masses of the fermion then are

$$m_f = \frac{y_f v}{\sqrt{2}}, \tag{2.13}$$

with the Yukawa coupling constant y_f and the VEV v. Each of the fermions has their own Yukawa coupling constant, which are free parameters.

2.2 Physics Beyond the Standard Model of Physics

Even though the SM is able to predict most of the experimental results in particle physics, experimental evidence and theoretical problems point towards physics beyond the SM.

One fundamental problem is, that currently gravity can not be described by a QFT and the SM does therefore not contain it. There is also an open question regarding the so-called Higgs mass hierarchy problem. With the discovery of the Higgs boson and the measurement of its mass of $m_H = 125.25 \pm 0.17 \, \text{Gev}$ [2] the last missing particle of the SM was found. Since the mass of the Higgs boson is one of 20 free parameters in the SM, it can not be predicted by the SM but rather has to be measured. Nevertheless the possible Higgs boson mass was constrained before its discovery, either due to earlier measurements of other SM particles or due to theoretical considerations. Compared to the experimentally measured mass of the Higgs boson, a larger mass was preferred based on the experimental and theoretical constraints to keep the SM valid up to the Planck scale, where gravitational effects can no longer be neglected. The corrections to the Higgs boson mass are dependent on interactions with other massive particles and to keep the SM valid up to the Planck scale, the correction would be orders of magnitude larger than the Higgs boson mass, which is the so called hierarchy problem. This large amount of fine-tuning is considered unnatural from a theoretical point of view.

In addition to the theoretical problems within the SM, there are also experimental results that are not explainable within the SM, e.g. measurements of the rotation speed of galaxies and measurements of the cosmic microwave background show deviations from the predicted behavior based on the visible matter. One possibility to fix these deviations is to introduce a new type of matter, the so-called dark matter, that only interacts via gravity and is otherwise not visible. Many of the extensions to the SM try to introduce a new particle, that acts as a dark matter candidate. In addition to dark matter, in recent years cosmic measurements have also pointed towards an unknown type of energy, dark energy, that accelerates the expansion of the universe [25, 26]. The baryon asymmetry, which is the observed imbalance of matter and antimatter in the universe, can also not be explained within the SM.

Outside of cosmological results, there have also been results in high energy physics experiments pointing towards physics beyond the SM: In the SM the neutrinos are massless, but to explain the observed neutrino oscillations [6–8], neutrinos have to be massive. It is also possible that neutrinos are so called Majorana particles, meaning the neutrinos and antineutrinos are the same particle, which generate a Majorana mass term after EW symmetry breaking. Otherwise neutrinos would be Dirac particles, generating their mass term like the other fermions. In both cases, a right handed partner needs to be introduced, e.g. heavy neutral leptons (See Ch. 2.2.2).

Additionally, in recent years there have been multiple experimental observations that are incompatible with the SM, e.g. the 2022 measurement of the W boson mass by the CDF experiment [27], which found significant difference in the W boson mass compared to other published results, or the first results from the Muon g-2 experiment [28], which are at the time of this thesis still being discussed and have to be verified by additional experiments and research.

In the following section, two specific extensions of the SM are explained in more detail, which form the basis for the later presented analyses.

2.2.1 Twin Higgs Models

The experimental evidence of the existence of dark matter poses the question whether this dark matter is part of a larger hidden or so-called dark sector [29], in which there are multiple new types of particles. If one assumes, that the new particles are interacting only via gravity, the direct detection of this dark sector becomes nearly impossible. The dark sector might become accessible via portal interactions, where some SM effective field theories are coupled with the dark sector fields and allow a potential detection at the LHC.

One of such model is the so called Twin Higgs models [29–31], which is also providing a solution to the hierarchy problem in the SM. In the Twin Higgs models, a mirror (or twin) partner for each of the SM particles is introduced and these twin particles only interact with the SM particles via the SM Higgs boson and its twin partner. Such a model is also called a hidden valley type model [32, 33]. From a theoretical point of view this is achieved by introducing a new SU(4) gauge group, where the SM-like Higgs boson is realized as a pseudo Goldstone boson of this new gauge group. In this case the gauge and Yukawa couplings explicitly break the global symmetry to a discrete $\mathcal{Z}_2$ symmetry. This symmetry protects the Higgs boson mass from the large corrections of the top quark, since the top quark and its new twin partner cancel each other out.

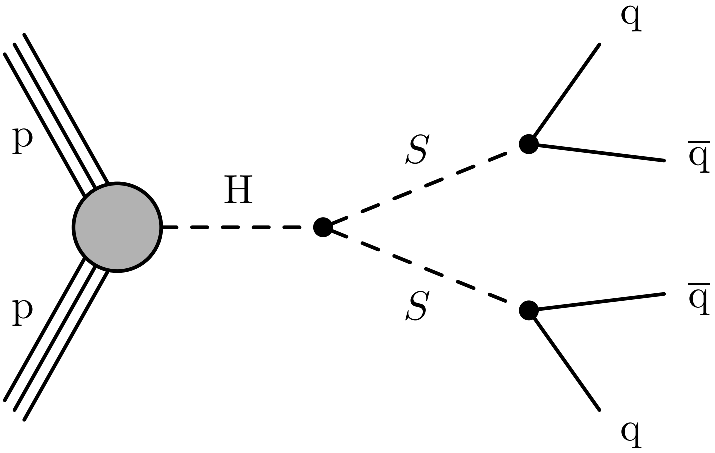

Figure 2.1: Feynman diagram for the Higgs decay into two long-lived scalars S.

An extension to this model is the so called Fraternal Twin Higgs model [34], where only the twins of the third generation of fermions exist (top quark, bottom quark, tau lepton and tau neutrino). These twin particles, due to the absence of the light mirror particles, then decay into the twin gluons, which then hadronize and form a so called glueball. This glueball is relatively stable and can travel a macroscopic distance. Only the lightest twin glueball can mix and interact with the SM Higgs boson, decaying back to a detectable SM particle via an off-shell Higgs boson.

In this thesis a simplified version of a Twin Higgs model is considered (See Ref. [35]), where the Higgs boson decays into a pair of long-lived scalars S. These long-lived scalars then decay into a pair of SM fermions or photons. In the search presented in this thesis, masses of these long-lived scalars between 0.4 and 55 GeV are considered. The dominant decay channel is the decay into a $b\overline{b}$ pair, but other decay modes are also considered. The considered production channels are the standard Higgs production channels, with the gluon fusion channel being the most dominant one. A Feynman diagram of the process is shown in Fig. 2.1.

2.2.2 Heavy Neutral Leptons

The observation of neutrino oscillations shows, that neutrinos have a non-zero mass. Their mass is currently not known, but an upper limit on the mass can be given either through cosmological evidence or direct measurements. The current upper limits point towards neutrino masses that are much smaller compared to the other SM fermions. One possible explanation for this much lower mass is the existence of heavy neutral leptons (HNLs), which are right-handed partners to the SM neutrinos, giving rise to the mass of the SM neutrinos through a type-I seesaw mechanism. In this seesaw mechanism, the HNL has a Majorana mass M_{ν_R} and interacts with a single generation of SM leptons through a Yukawa coupling y_ν. After mass mixing the light neutrino mass eigenvalue m_ν is given by

$$m_\nu = y_\nu^2 v^2 / M_{\nu_R}, \tag{2.14}$$

with the Yukawa coupling y_v^2 and the Higgs vacuum expectation value v. Examining this equation shows why this is called a "seesaw" mechanism: If one assumes $y_\nu \simeq 1$,

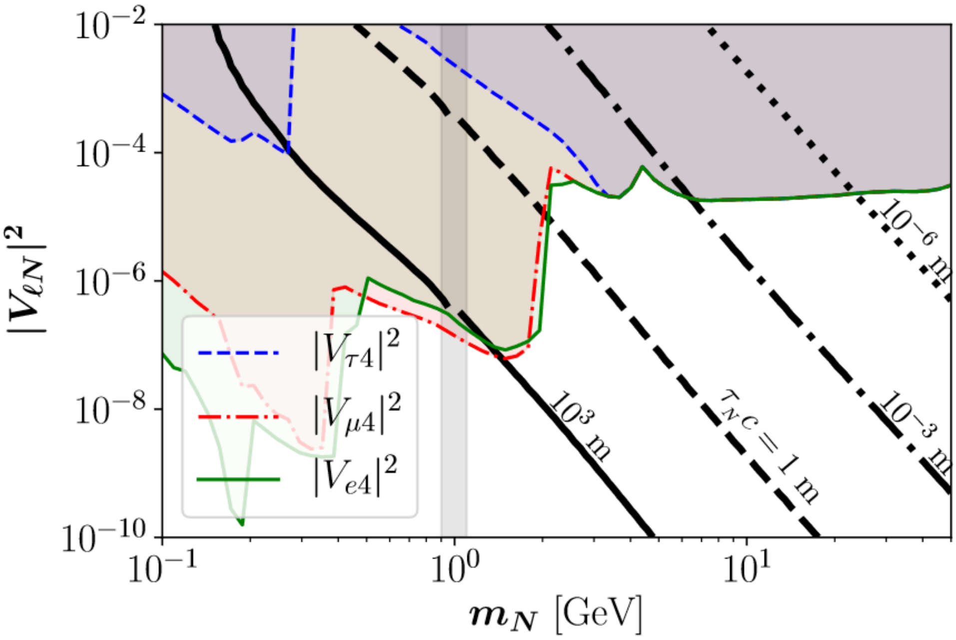

Figure 2.2: Contour lines and exclusion limits for the HNL decay length $\tau_{\mathrm{N}} c$ for different HNL flavors. Shaded areas are excluded by different experiments. Taken from Ref. [36].

then a light neutrino mass eigenvalue m_ν in the order of eV can be achieved by M_{ν_R} of the order $10^{14} - 10^{15}$ GeV [37]. The lower the light neutrino mass eigenvalue m_ν, the higher M_{ν_R} has to be. Of course y_ν can be fine tuned to allow for much lower values of M_{ν_R}.

This idea is included in the so called Neutrino Minimal Standard Model (νMSM) [38], which is designed as an extension to the SM trying to include the phenomenology of the experimental observations not yet in the SM. The νMSM does not only introduce neutrino masses to the SM, but also offers solutions to other open questions of the SM, as it also provides a dark matter candidate [39, 40] and may also explain the baryon asymmetry of the universe [41]. This model adds three HNLs (N_1, N_2 and N_3) to the SM. The lightest HNL N_1 is usually selected as the dark matter candidate due to its low mass. Additionally, the νMSM is able to explain the anomalous muon magnetic moment g-2 [42, 43].

As described before, HNLs can only be produced via mixing with the SM leptons. Therefore the coupling strength between the SM and sterile neutrinos is a limiting factor for the discovery potential. HNLs couple to the SM fields the same way as active neutrinos, except that the coupling is strongly suppressed by the small mixing angles [44]. The mixing angle is denoted by V_{Nl}, where l denotes the SM neutrino flavor.

Special focus in this thesis is set on the parameter space of long-lived HNLs. The semi-leptonic HNL decays can be characterized depending on the HNL mass [44]. For this thesis HNL masses m_{N} larger then 1 GeV, but smaller than the W boson mass are considered. In this case the HNL decay is best described by a three-body decay into a pair of quarks, coming from a W boson, and a lepton: $N \rightarrow q\bar{q}l_2$. The

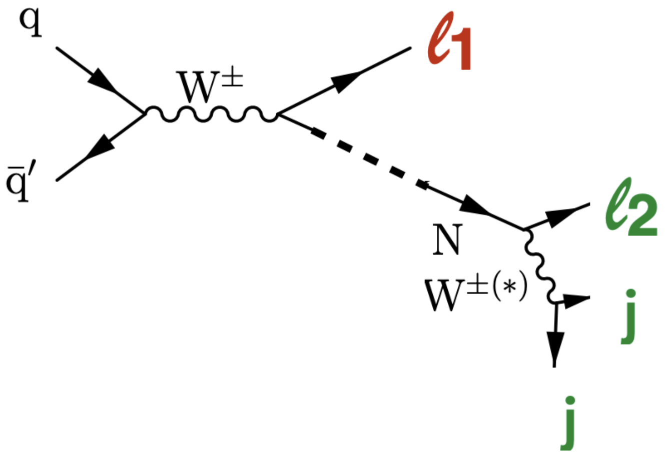

Figure 2.3: Feynman diagram for the charged-current production of a HNL (N) via mixing with a SM neutrino.

lifetime of the HNL can be expressed as

$$\tau_\mathrm{N} \propto M_\mathrm{N}^{-5} |V_{Nl}|^{-2}. \tag{2.15}$$

Fig. 2.2 shows the HNL decay length for the case that all couplings to the neutrino generations are equal.

The total decay width Γ_N is approximately

$$\Gamma_\mathrm{N} \propto \mathrm{G}_\mathrm{F}^2 m_\mathrm{N}^5 \sum_{l=e,\mu,\tau} |V_l|^2, \tag{2.16}$$

if the HNL couples to all three generations simultaneously. The total decay width is related to the particle lifetime τ via $\tau = \frac{1}{\Gamma_\mathrm{N}}$ and therefore has a significant impact on the displacement for long-lived HNL scenarios.

The analysis presented in this thesis focuses on the production of HNLs via the charged-current interaction:

$$q\bar{q}' \to \mathrm{W}^\pm \to l_1^\pm N, \tag{2.17}$$

using the resulting prompt lepton l_1 to select the events with dedicated single electron or muon triggers.

A Feynman diagram for this process is shown in Fig. 2.3. The off-shell W boson decays hadronically via a three body decay:

$$N \to l_2 jj. \tag{2.18}$$

It is important to note, that l_1 and l_2 are of the same flavor if the HNL couples to one SM neutrino generation only, and are of a different flavor if at least two of V_e,V_μ or V_τ are non-zero. Additionally, for Dirac-type HNLs, l_1 and l_2 will be of opposite sign charge, since Dirac-type HNLs are lepton number conserving (LNC), while Majorana-type HNLs allow both opposite and same-sign charge final states, making them lepton number violating (LNF). This leads to the Dirac-type decay width being exactly half of that of a Majorana-type HNL with the same mass and mixing parameters.

2.3 Hadron Collider Physics

The analyses presented in this thesis are based on proton-proton (pp) collision data, therefore in the following the central concepts of particle collisions, and explicitly pp collisions, are introduced.

The rate of a scattering process is given by

$$\frac{\mathrm{dN}}{\mathrm{dt}} = \sigma L, \tag{2.19}$$

with the cross section σ, which denotes the probability for a scattering process, and the instantaneous luminosity L, which can be viewed as the number of potential collisions per cross section and time. The cross section can be calculated via Fermi's golden rule with

$$\sigma = 2\pi |\mathcal{M}_{i\to f}|^2 \cdot \rho, \tag{2.20}$$

where i denotes the initial and f denotes the final states, ρ is the final-state phase space and $|\mathcal{M}|^2$ denotes the squared matrix element (ME) of the process. The matrix element can be calculated via perturbation theory and is usually visualized using Feynman diagrams. The cross section is usually calculated up to next-to-leading or in some cases even next-to-next-to-leading order. One complication arises due to the fact that protons are not elementary particles, but rather a composite of quarks and gluons, the so called partons. This in turn means, that for pp collisions the partons are interacting, rather then the full protons, making it necessary to know the momentum fraction of the interacting partons. The probability to find a parton i with momentum fraction x_i at a given energy scale Q^2 is given by the so called parton density functions (PDFs). PDFs are not calculated, but rather constructed from measurements of different scattering experiments at different energy scales. The NNPDF Collaboration provides PDFs most commonly used within the CMS collaboration, which use the measurements from HERA and the LHC [45, 46]. Fig. 2.4 shows PDFs provided by the NNPDF collaboration at different energy scales, showing that at high momentum fractions the u and d quark have the highest probability. It can also be seen that at larger energy scales the probability to find quarks at low momentum fractions increases.

The cross section for pp collisions at the LHC with these PDFs, here denoted with $f(x, \mu_F^2)$, is given by

$$\sigma(\mathrm{p}_1, \mathrm{p}_2 \to \tilde{f}) = \sum_{i,j} \int_0^1 \mathrm{d}x_i \int_0^1 \mathrm{d}x_j f_i(x_i, \mu_F^2) f_j(x_j, \mu_F^2) \sigma(\hat{\mathrm{p}}_i, \hat{\mathrm{p}}_j \to \tilde{f}), \tag{2.21}$$

where p_1 and p_2 are the momenta of the initial protons, x_i and x_j are the momentum fractions of the interacting partons i and j and $\sigma(\hat{\mathrm{p}}_i, \hat{\mathrm{p}}_j \to \tilde{f})$ is the cross section of the given process at the parton level. Lastly μ_F is the factorization scale which defines the energy at which the interaction is factorized into a soft energy region described by the PDFs and a high energy part described by the partonic cross section.

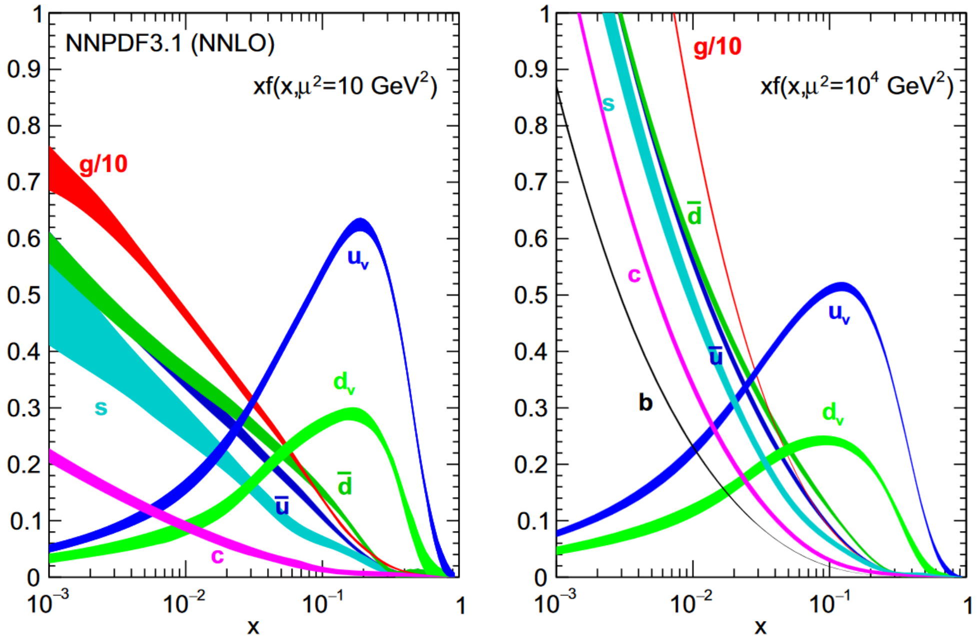

Figure 2.4: Parton distribution functions (PDFs) at different energy scales μ^2 of 10 GeV (left) and 10^4 GeV (right). Taken from the NNPDF Collaboration from Ref. [46].

2.4 Simulation of Particle Collisions

To evaluate the recorded data at collider experiments, simulated data based on theory predictions is often necessary. In the case of the searches for new physics, distributions of the recorded data are compared to theoretical predictions, allowing the detection of differences between the two. To generate simulated collision events, Monte-Carlo (MC) event generators are used that randomly sample from theoretical probability distribution functions. For this, many different steps in the simulation chain are needed, going from simulating the interactions during the hard and soft scattering, simulating the hadronization, to simulating the interaction and readout with the detector. A short overview of these methods is given in the following section.

The initial hard pp scattering is generated based on the PDFs and the matrix element of the process. The matrix element is available in different orders, usually leading or next-to-leading order.

Afterwards, the showering process, which is the radiation of additional gluons and the splitting of gluons into quark-antiquark pairs, is simulated. The shower can be modeled up to the point where the scale of the process is so low that non-pertubative effects play a major role. Since the resulting particles can not exist as free particles, they hadronize, which is simulated in the next step. For this purpose, phenomenological methods are used like the cluster hadronization model [47] or the Lund String model [48]. In addition to the main parton interaction, the additional parton interactions within the same pp interaction, which are called the underlying event, are taken into account and are usually measured in data and the simulation is then later corrected. The same thing is done for pileup interactions, which are additional interactions due to multiple protons interacting, since the collisions at the LHC are done by colliding proton bunches, instead of single protons.

After this chain of different simulation tools the simulated event consist of the final state particles one would expect in an actual event from the experiment. Lastly the detector and readout response is simulated. For the CMS detector the simulation is usually performed using the `GEANT` software package [49]. In addition to the exact detector geometry and material budget, the electronic readout is also simulated, which in the end yields a simulated event, which should be as similar as possible to a recorded event and therefore can be analyzed and processed in the same way.

3 Experimental Setup

The data used for the statistical analysis in this thesis was produced by pp collisions at the Large Hadron Collider (LHC) [50, 51] and recorded with the Compact Muon Solenoid (CMS)[52, 53] during the years 2016 to 2018. In the following chapter the LHC and each of the subdetectors of the CMS detector is described in more detail. A special focus is placed on the dedicated muon detectors, which play a central role in the analysis.

3.1 The Large Hadron Collider

Located close to Geneva at the European Organization for Nuclear Research (CERN), the LHC is the largest and most powerful circular particle accelerator and collider in the world with a circumference of 26.7 km. The collider is designed to collide either heavy ions or protons, where the latter had a center-of-mass energy of $\sqrt{\text{s}} = 13\,\text{TeV}$ for the 2016 to 2018 data taking period (Run2). The center-of-mass energy was upgraded with regards to the first data taking period from 2011 to 2012, during which the LHC was operated at a center-of-mass energy of $\sqrt{\text{s}} = 7\,\text{TeV}$ for pp collisions. During the Run2 data taking period a total of about $145\,\text{fb}^{-1}$ integrated luminosity was collected. The LHC is currently already in its third data taking period (Run3), with a center-of-mass energy of $\sqrt{\text{s}} = 14\,\text{TeV}$. After the current data taking period there is a significant upgrade planned for both the accelerators and the detectors to start the so called High-Luminosity LHC phase [55].

The full accelerator complex of the LHC is shown in Fig. 3.1. To reach the target center-of-mass energy of the LHC, the particles go through different pre-accelerators. A duoplasmatron is used to ionize hydrogen atoms, breaking them down into electrons and protons. The protons are then accelerated up to 750 keV through Radio Frequency Quadrupoles (QRF). This 750 keV proton beam is then injected into the linear accelerator (LINAC2), which accelerates the protons up to 5 MeV. Subsequently the particles are accelerated to 1.4 GeV, then 25 GeV and finally 450 GeV by the Proton Synchrotron (PS) Booster, the Proton Synchrotron and the Super Proton Synchrotron (SPS). This 450 GeV beam is then injected into the LHC, where the beam is split into two separate beams, one traveling clockwise and the other anti-clockwise. In

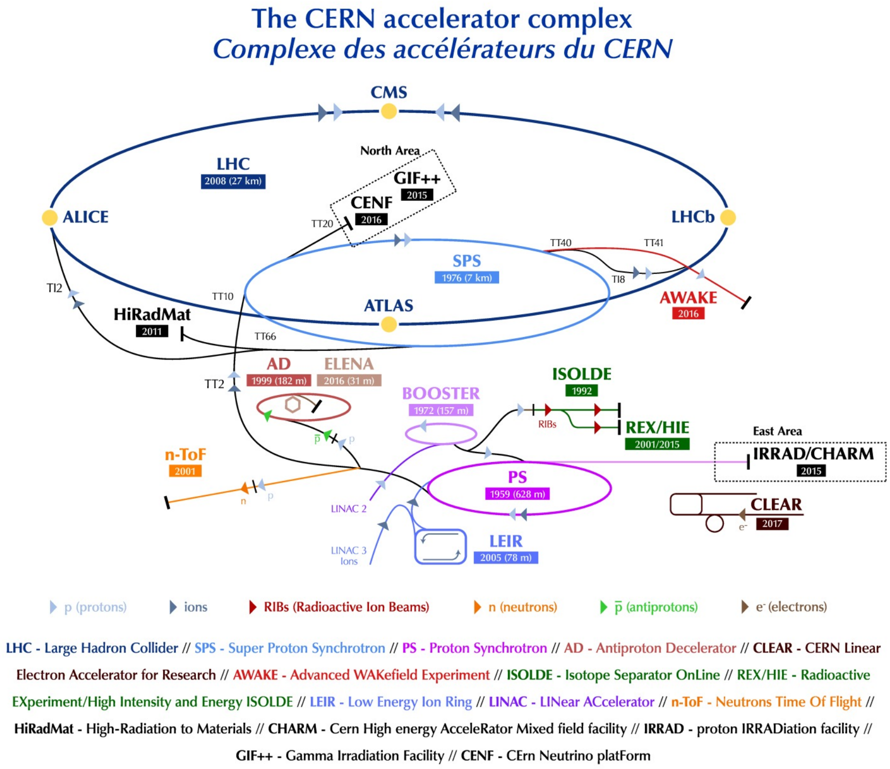

Figure 3.1: The LHC accelerator complex at CERN in 2018. Figure taken from Ref. [54].

the LHC the protons are then accelerated to their final energy of 6.5 TeV, yielding a center-of-mass energy of $\sqrt{s} = 13\,\text{TeV}$.

The LHC uses high-frequency cavities, which generate oscillating electric fields to accelerate the particles. Conveniently, this method of accelerating particles groups the particles together in so-called bunches, which are spaced apart along the beam line. Due to the 40 MHz frequency of the cavities used in the LHC, the nominal bunch crossing frequency is 25 ns. To keep the particles in a circular orbit, 1232 superconducting dipole magnets are placed along the beam line. Additionally the LHC deploys 474 superconducting quadrupole magnets to focus the beam.

The LHC is designed with 8 different interaction points, where particles can be brought to collision and experiments can be situated. Four of these interaction points are used by experiments: The A Toroidal LHC Apparatus (ATLAS) [56] and CMS experiment are multipurpose detectors, which were used to detect the Higgs Boson in 2012 and are currently studying the Standard Model of physics to the highest precision and are also trying to find new physics beyond the Standard Model. The A Large Ion Collider Experiment (ALICE) [57] is a specialized detector designed to study heavy ion collisions and the Large Hadron Collider beauty (LHCb) [58] experiment is designed to study B Hadrons.

The particle flux at the interaction points is characterized by the instantaneous luminosity $\mathcal{L}$:

$$\mathcal{L} = N_b f_r \frac{n_1 n_2}{4\pi\sigma_x\sigma_y} \tag{3.1}$$

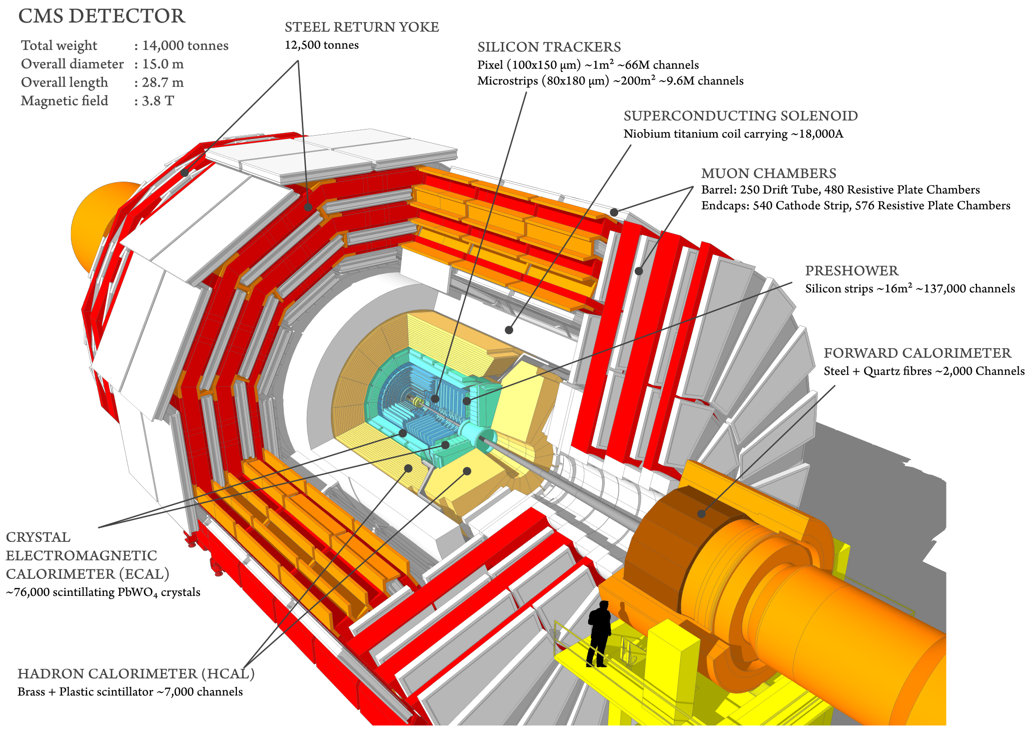

Figure 3.2: 3D cutaway of the CMS experiment, figure taken from Ref. [60].

where N_b is the number of proton bunches, f_r is the collision frequency of 40MHz, n_1 and n_2 are the number of particles in the colliding proton bunches and σ_x and σ_y characterize the transverse beam sizes in x- and y-direction.

Particles are brought to collision within bunches and the instantaneous luminosities of up to $1.5 \times 10^34\,\mathrm{cm}^{-2}s^{-1}$ [59] are large enough for multiple pp interactions to occur within the same bunch crossing. Usually there is one initial high momentum pp scattering of interest in the event, and the additional collisions are not of interest. These additional collisions are called pileup and will produce concurrent, additional particles in the detector, that will impact the measurement of the desired variables. Some pileup mitigation techniques deployed at the CMS experiment will be discussed in Ch. 4 and in more detail in Ref. [59].

3.2 The Compact Muon Solenoid Detector

The Compact Muon Solenoid detector is a multi-purpose detector used for Standard Model measurements and Beyond Standard Model searches. The detector gets its name from being more compact compared to other collider experiments, placing the calorimeter inside its solenoid magnet and focusing on the detection of muons.

The detector has a cylindrical shape and is build around the particle interaction point. The closest sub detector to the interaction point is the tracker, which is used to measure charged particles and their trajectories. The calorimeter system is placed afterwards, which is divided in an electromagnetic (ECAL) and hadronic calorimeter (HCAL), which are used to measure the energy of electromagnetic and strongly interacting particles. Up until now all subdetectors are placed inside a super conduction solenoid magnet, providing a strong magnetic field of 3.8 T, leading to curved charged particle tracks inside the tracker and muon system. Lastly the muon detectors are embedded inside an iron flux return yoke, which is used to guide the magnetic field outside of the solenoid. A 3D model of the CMS detector is shown in Fig. 3.2.

In the following chapter each of the subdetectors will be discussed in more detail, with a special focus on the muon chambers. Additionally some general conventions will be explained.

3.2.1 Coordinate System

For the CMS experiment it is useful to define two coordinate systems: A Cartesian coordinate system and motivated by the form of the detector, a cylindrical coordinate system. For the Cartesian coordinates the x-axis points radially towards the center of the LHC ring, the y-axis points towards the surface and the z-axis points along the beam direction. For the cylindrical coordinates the azimuth angle ϕ is defined in line with the x and y plane, where $\phi = 0$ points towards the positive z direction, while the polar angle θ is defined from the z-axis to the x-y plane. Lastly the radial distance in the x-y plane is defined as the radius r.

At high energy particle physics experiments the transverse momentum is usually one of the most important and studied observables, due to it being invariant under a Lorentz boost alongside the z-axis. Additionally, due to the initial transverse momentum of the colliding particles being zero, the sum of all transverse momenta has to be zero as well. The magnitude of the transverse momentum is defined as:

$$p_\mathrm{T} = \sqrt{p_x^2 + p_y^2}. \tag{3.2}$$

It is useful to define the so-called rapidity y

$$y = \frac{1}{2}\ln\left(\frac{E + p_z}{E - p_z}\right), \tag{3.3}$$

and the more commonly used pseudorapidity η:

$$\eta = -\ln\left[\tan\left(\frac{\theta}{2}\right)\right], \tag{3.4}$$

Each interval in the pseudorapidity has approximately an equal amount of the particle flux. Finally, the Lorentz-invariant angular distance between two objects is usually defined as:

$$\Delta R = \sqrt{(\Delta\eta)^2 + (\Delta\phi)^2}, \tag{3.5}$$

where $\Delta\eta = \eta_1 - \eta_2$ and $\Delta\phi = \phi_1 - \phi_2$.

3.2.2 Trigger

As already mentioned, the LHC is operating with a collision frequency of 40 MHz, which means each experiment would be recording 40 million collisions and their resulting particles. Saving every event at this collision frequency is technically impossible, both due to bandwidth limitations of the data streams and the limited computing resources for reconstructing the events. Fortunately it is not necessary to store every event, since most collisions lead only to QCD multijet interactions, which have been studied in detail at previous particle accelerators. Experiments at the LHC are mostly focused on rare processes, that can be studied due to the higher center-of-mass energy. To select these rarer events and reduce the overall data rate at the CMS experiment a trigger system is used [61, 62].

The CMS trigger is split into two different tiers: The Level-1 trigger (L1) is implemented with a dedicated set of programmable electronics placed close to the detector which reduces the data rate to around 100 kHz. The total processing time of the L1 trigger system is $3\,\mu$s, during which the data is stored in the front end electronics. Due to this time requirement, the L1 system can only access calorimeter and muon detector hits and has to either keep or reject the events based on this limited information. Afterwards the high-level trigger (HLT) is able to access more detailed information from all subdetectors of the event and is able to apply a more high level event selection based on the properties of physics objects. The processing time at the HLT is around 1 s and is therefore still around two orders of magnitude less compared to the later offline reconstruction time. Due to this limited processing time the objects reconstructed at the HLT level are not using the information of the events to its fullest potential and are not using the full reconstruction algorithms. Therefore the objects at the HLT stage are only an approximation of the later offline reconstructed objects. The HLT outputs a rate of around 1 kHz, which is then sent to the offline computing centers, where the events are fully reconstructed and distributed for further analysis. The HLT deploys so called HLT paths, each targeting a different physics objects, whose quality selections can be fine tuned for specific use cases. In general the rate of each path is defined by the thresholds applied to the objects used in the trigger, e.g. a so called single muon trigger uses a muon object to form the trigger decision and has to place a p_{T} cut on the object. If the p_{T} cut is set too high, much of the targeted physics process might be missed. If the p_{T} cut is set too low, the overall trigger rate of the path goes up and might push the overall HLT rate outside of the technical rate limit. If lower thresholds on the trigger objects are needed and the rate of the HLT path would be deemed to large, it is possible to prescale the HLT path. A prescaled HLT path uses looser thresholds for the objects but does not select every event that fulfills the requirements, but rather every second, third or so forth event.

3.2.3 Inner Detector Systems

In the following section the inner part of the detector will be discussed. Inner part in this case is defined as all detector systems contained inside the solenoid magnet of CMS, namely the tracker and calorimeters.

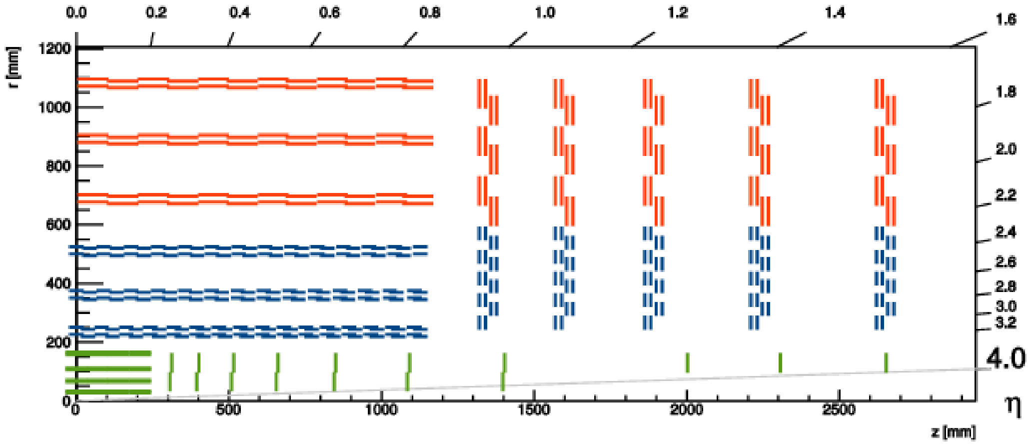

Figure 3.3: 2D sketch of one quarter of the tracker layout. Pixel detectors are shown in green, while the silicon strip modules are shown in blue and red. Figure taken from Ref. [63].

Tracker

The tracker is the innermost detector and closest to the interaction point. Its main purpose is to measure the trajectories of charged particles, which are bent due to the strong magnetic field from the solenoid magnet. The tracker allows the measurement of the sign of the charge and the transverse momentum of the particles. In addition the reconstruction of tracks also allows the reconstruction of the primary and potential secondary vertices, allowing the detection of displaced objects, like jets originating from b quarks or even potential new physics in form of long-lived particles.

The tracker has a length of 5.6 m and a diameter of 2.6 m, consisting of two different silicon based detector modules: The pixel detector modules are closest to the interaction point while the strip detector modules are used in the rest of the tracker. The pixel modules offer a higher resolution compared to the strip detector of around 10 μm, which is needed for a high efficiency in the vertex reconstruction. The pixels have a size of 100 μm by 150 μm and are readout individually. The pixel detector was upgraded after the 2016 data taking period, from 66 million to 124 million pixels. The upgrade also replaced the old pixel modules, due to the accumulation of radiation damage and additional pixel layers were added in the barrel and endcap. The silicon strip detectors consist of 15148 detector modules, leading to 9.6 million read-out channels. In the barrel the strips provide a measurement in the $r-\phi$ plane, while in the endcap they provide a measurement in the $z-\phi$ plane. A 2D sketch of the CMS tracker is presented in Fig. 3.3, showing the positions of the strip and pixel modules.

Calorimeters

Directly outside of the tracker the calorimeters of the CMS experiment are located, with their main purpose to measure the energy of the particles. CMS uses two different detector technologies to detect particles that are mainly interacting electromagnetically or are interacting strongly.

The innermost calorimeter is the so called electromagnetic calorimeter [64], which is used to measure the energy of electrons and photons. The ECAL consists of 75848

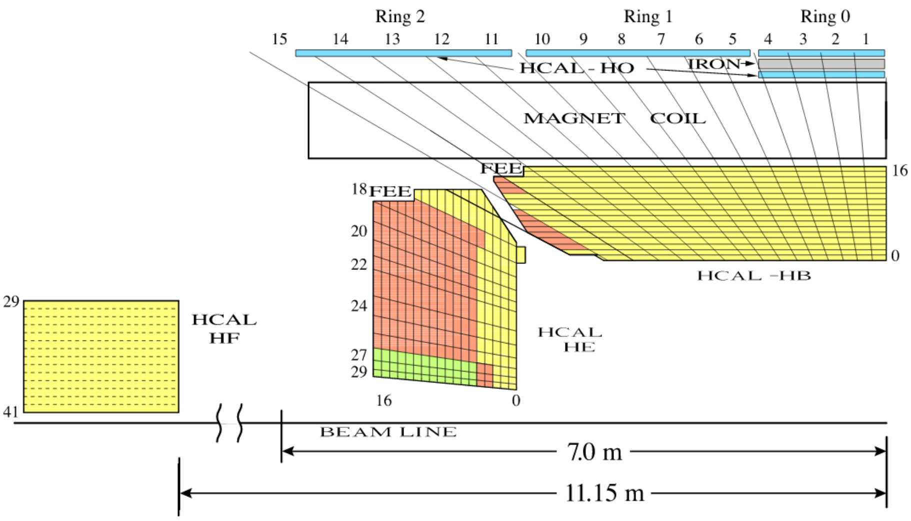

Figure 3.4: Quarter slice of the CMS HCAL detector, Figure taken from Ref.[66].

lead tungstate ($PbWO_4$) scintillating crystals and is a homogeneous calorimeter, where the absorber and scintillator are the same material. $PbWO_4$ is used due to its high radiation tolerance, small radiation length ($X_0 = 0.89$cm) and Molière radius ($r_M = 2.19$cm) and fast response time ($< 100\,$ns). In the barrel region,the crystals have a length of around 24 X_0 (22 cm), while in the endcap region the crystals have a length of 25 X_0 (23 cm). Due to the low light yield of $PbWO_4$, external photodetectors with internal amplification are required to readout the signal. The performance of the ECAL has been measured with an electron test beam [65], where the resolution has been measured as

$$\frac{\sigma_E}{E} = \frac{2.8\%}{\sqrt{E[\text{GeV}]}} \bigoplus \frac{12\%}{E[\text{GeV}]} \bigoplus 0.3\%, \tag{3.6}$$

where the first term describes stochastic fluctuations, the second describes the impact of noise and the third describes constant effects like calibration errors.

The main part of a hadronic shower is then captured in the hadron calorimeter (HCAL) [66] that is placed right after the ECAL. The HCAL consists of four different subs subsystems: The barrel (HB), endcap (HE), outer (HO) and forward (HF) calorimeters. A schematic overview of the HCAL is given in Fig. 3.4, showing the four different sub systems The barrel and endcap calorimeters are placed inside the solenoid magnet and are sampling calorimeters consisting of brass absorbers and plastic scintillators. Since the space inside the solenoid is highly limited, the HB thickness at $\eta = 0$ is only 5.8 hadronic interaction lengths, increasing to 10 interaction lengths at $|\eta| = 1.2$. To increase the reconstruction efficiency at $\eta = 0$ additional scintillators are placed outside the solenoid magnet, this is the so-called outer calorimeter. The forward calorimeter is constructed with a steel absorber and quartz fiber sensors, covering a range up to $|\eta| < 5.2$.

3.2.4 Muon System

While the calorimeters are able to contain hadron decays and the decays of photons and electrons, muons are able to travel through the detector materials with relatively

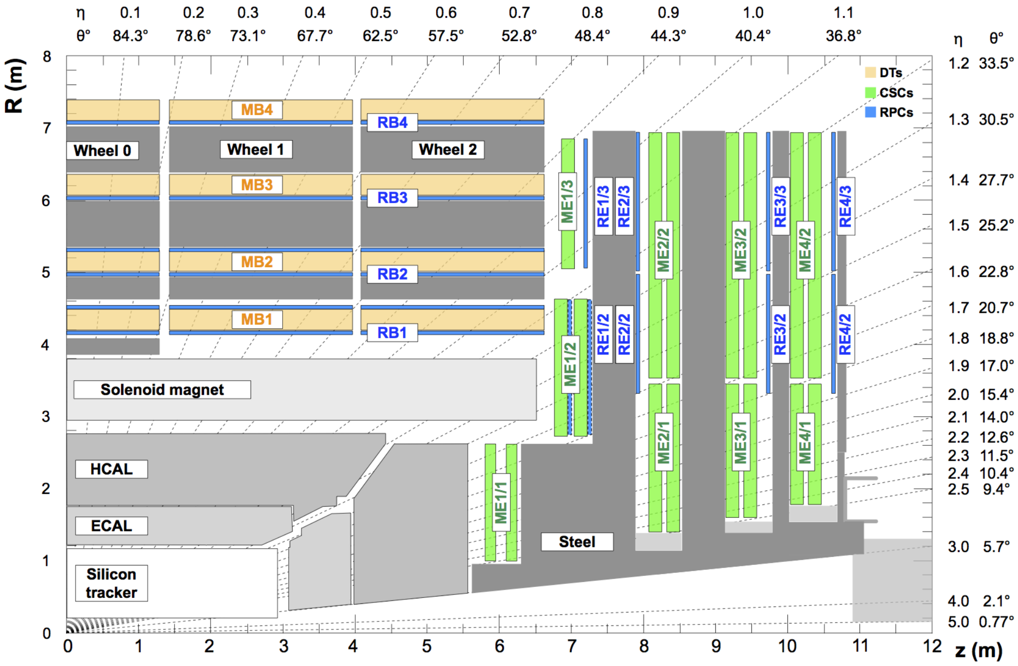

Figure 3.5: Quarter slice of the CMS Muon System, figure taken from Ref. [67]

low energy losses, since the muon is a minimum ionizing particle. Therefore outside the solenoid, specialized muon detectors are placed, with the so called drift tubes (DT) being placed in the barrel region and the cathode strip chambers (CSC) being placed in the forward region. Additionally, resistive plate chambers (RPC) are placed in both regions to provide additional measurements of the timing and improved trigger capabilities. A charged particle traversing the detectors ionizes the gas inside the chambers and eventually the signal is read out by the electronics. The description of the hit reconstruction in the following sections follows Ref. [67]. The full muon system deployed in Run2 is shown in Fig. 3.5.

Drift Tubes

In the barrel region of the CMS detector drift tubes (DTs) are used, since the residual magnetic field and the particle flux is low enough to allow the use of this technology to measure the tracks of outgoing and even incoming muons.

A DT is a wire chamber composed of a anode wire and cathode strips inside a tube filled with a gas mixture, that detects charged particles and photons and measures their trajectories. In Fig. 3.6 a single DT cell and a complete DT chamber are shown. A DT cell is a rectangular drift tube with a size of 4.2 cm x 1.3 cm, with its length varying between 2 and 4 m, depending on the position of the cell. The cells are filled with an argon and CO_2 (85/15) gas mixture. The spatial resolution of a DT cell is around 200 μm, the resulting radial resolution after the reconstruction is 100 μm. The cells are arranged in parallel to form a layer. Groups of four layers are then grouped together to form a super layer. One single DT chamber consists of 3 superlayers, which are arranged so that two are measuring the ϕ position, while one super layer measures the z position.

The DT chambers are arranged in 5 different so-called wheels in the z direction, where wheel 0 is in the center of the barrel. Each wheel then is made out of 12

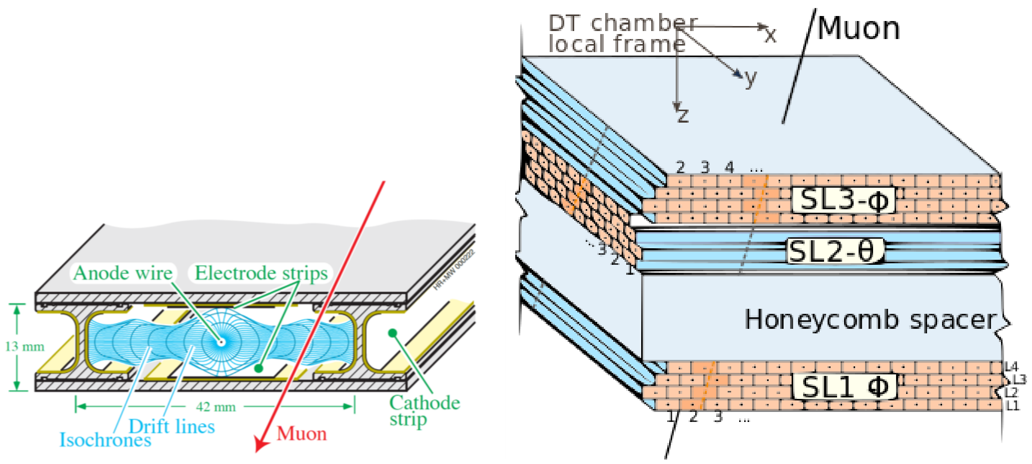

Figure 3.6: Overview of the CMS DT system: A single DT cell (left) and a complete DT chamber (right) is shown, figure taken from Ref. [69]

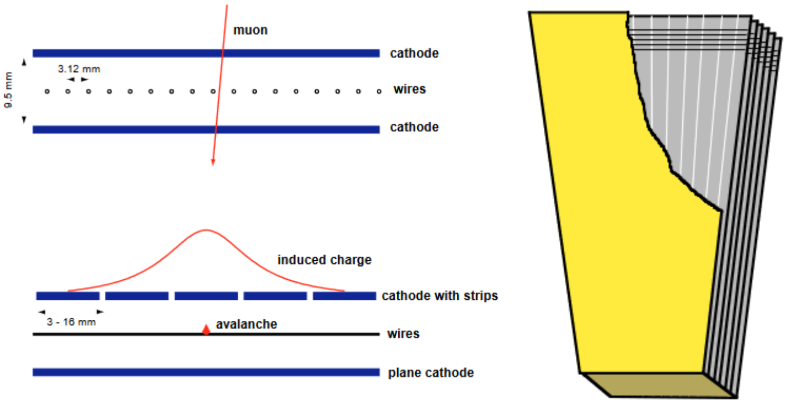

Figure 3.7: CSC operation principle (left) and schematic view of a CMS CSC chamber with 6 layers (right), figure taken from Ref. [68]

azimuthal slices, named sectors. Each sector is organized in 4 rings of chambers, the stations are named MB1/2/3/4 going from inward to outward. There are a total of 250 DT chambers in the CMS muon system [68].

A charged particle traversing a DT cell ionizes the gas, which is collected at the anode wire. The arrival time is recorded and with the electron drift velocity, the hit position can be reconstructed. The arrival time is corrected by a time pedestal, which accounts for the time between the bunch crossing until the trigger decision arrives at the chamber electronics. The drift time is assumed to be constant for particles traversing the cell perpendicular to the plane of the wires. The hits are then used in a track reconstruction algorithm, which yields so called DT segment (See Ch. 4.1). Only after the segment reconstruction timing information for the DT tracks is obtained, with a resolution of around 2 ns. This means that at the level of individual DT RecHits, no timing information is readily available.

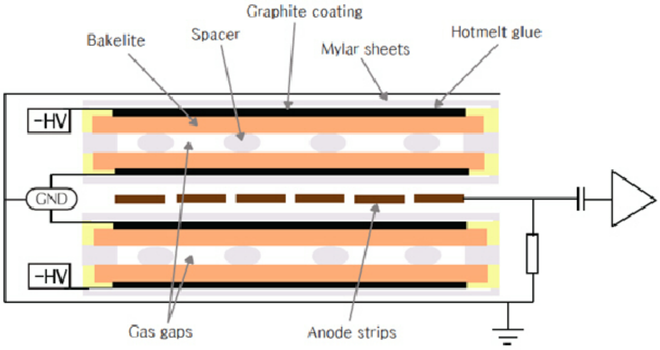

Figure 3.8: Schematic view of a double gap RPC used in CMS, Figure taken from Ref. [70]

Cathode Strip Chambers

In the forward region, cathode strip chambers (CSC) are used due to the large particle flux and the larger residual magnetic field, compared to the barrel region.

A CSC is a gaseous ionization detector, composed of an anode wire plane and finely segmented cathode strips. The chambers are filled with an $Ar/CO_2/CF_4$ (30/50/20) gas mixture and the spatial resolution is between 45 μm and 145 μm depending on the specific chamber, where the innermost chambers have a better resolution.

Fig. 3.7 shows the layout of the CSC. The chambers are arranged in rings which are mounted on eight disks, four in each endcap. The chambers are named with ME $\pm$ S/R, where 'ME' stands for Muon Endcap, the $\pm$ notes in which of the two endcaps the chamber is located ($+$ in forward direction, $-$ in backward direction), S indicates the station, which corresponds to the disks and R is the ring number.

To reconstruct a hit in the CSC the information of the cathode strips and anode wires is combined. The strips are providing the ϕ angle, while the anode wires provide the radial direction measurement. The hit is reconstructed at the intersection points of the strips and wires. For a CSC RecHit a timing measurement is provided, which will be used in the later analysis (See Ch. 4.6 for the reconstruction of the muon detector showers).

Resistive Plate Chambers

Resistive plate chambers (RPC) are gaseous parallel-plate detectors which are used in both the barrel and endcap to provide additional trigger capabilities due to their good spatial resolution and time resolution.

RPCs consist of four parallel phenolic resin (bakelite) plates separated by two small gas gaps (See Fig. 3.8). One side of the bakelite plate is coated with graphite to form electrodes. In the center of the chamber aluminum anode strips are placed to collect the signals. The chambers are operated in the so-called avalanche mode to be able to handle the high rates present at the LHC. The spatial resolution of the RPCs is in the order of a few cm, while muons from the collision events can be triggered within a few ns.

The RPC is used as a dedicated muon trigger, being able to identify the bunch crossing (BX) for the muon track, even under high rates and backgrounds. The RPC layout in the barrel follows the DT segmentation, while placing two RPC chambers per DT chamber for the two innermost DT chambers, one on each side of the DT chamber, and one RPC chamber per DT chamber for the two outermost DT chambers. In the forward region four RPC layers are placed, following the CSC segmentation (see also Fig. 3.5 for the exact positions of the RPCs).

3.2.5 Data Processing

Since the analyses presented in this thesis use an unusual data format, a short overview of the CMS data processing is given. The description is based on Ref. [71] and Ref. [72].

As described before, the CMS detector saves events based on the L1 and HLT trigger decisions. But not every event recorded with the CMS detector has to be used in an analysis and trying to do so would be impossible due to the sheer size of the resulting dataset. Therefore the dataset is skimmed, reducing the size and also increasing the usability. This is done by both reducing the number of events, but also by removing no longer needed information from the events. For example, after the track reconstruction (see Ch. 4.1) is performed, hits in the tracker that are not part of a reconstructed track are removed. Likewise, it is useful to skim the event by preapplying a selection on an object, for example the analysis presented in Ch. 5 is performed on a skimmed dataset, where a $p_{\mathrm{T}}^{\mathrm{miss}}$ cut of $p_{\mathrm{T}}^{\mathrm{miss}} > 200\,\mathrm{GeV}$ is already applied.

At CMS the data has the following formats, going from the least processed data format to the most processed:

- RAW: This data format is essentially just the detector-level information, with the least amount of reconstruction performed, usually only the quantities reconstructed during the HLT processing are stored. The L1 trigger result and the HLT selections, so called HLT trigger bits, are also saved.
- RECO: RAW is then reconstructed into the RECO data format. This step is one of the most computationally expensive steps in the reconstruction chain. The detector-level information is processed and reconstructed objects (tracks, vertices, jets, muons, etc.) are saved.
- Analysis Object Data (AOD): Going to AOD, the number of objects is reduced. Only a limited amount of detector level information is kept at this point, for example not all hits in the tracker or CMS muon system are saved, but rather only the hits that have been used to reconstruct the reconstructed tracks. During Run1 this was a widely used data format, but in recent years most analyses have switched to more processed data formats.
- MiniAOD: Further reduction of the number of objects. AOD-level objects are passed through more selections and standard algorithms (like JEC). Almost all detector level information is removed at this point.
- NanoAOD: The final data format, only storing "high-level" objects with additional information. NanoAOD is expected to have enough information for about 50 % of CMS analyses. [72]

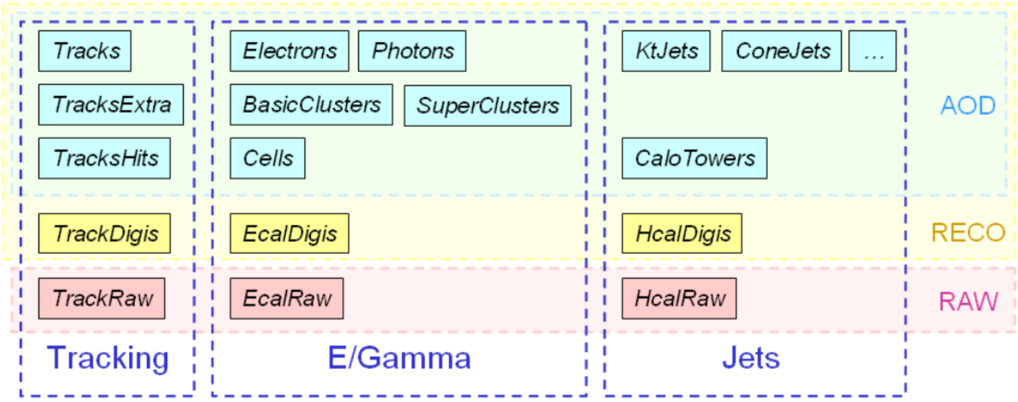

Figure 3.9: Schematic overview of tracking, ECAL and HCAL based objects and their additional information available in the different data tiers (up to AOD). From [72]

Fig. 3.9 shows the different information that is available in the lower data tier formats for tracker, ECAL and HCAL based objects.

While CMS still keeps a record of all the recorded data in the RAW format, which mostly will be stored on a tape based storage solution, analyzers are mostly working with datasets that are available on the CMS computing clusters. Since the goal of the processed data formats is to save disk space and also to reduce computation times while working on the datasets, RAW and RECO data formats are at some point deleted from the computing clusters. Raw data is stored on tape disks that is normally not accessible to users. For the Muon Detector Showers (See Ch. 4.6) the access to all the RecHits in the DT and CSC systems are required, which necessitates the use of the RECO format. As already mentioned, this data format is mostly not readily available and it requires to create copies in local, user-accessible disks.

4 Object Reconstruction

The particles created in the proton-proton collisions inside the CMS detector interact with the detector material, or in the case of non-stable particles their decay products do. These interactions are then recorded as electronic signals within each of the sub detectors. Usually the analysis of the physics processes use reconstructed particles to study the underlying physics, therefore requiring the reconstruction and identification of all the objects, like jets and leptons. This chapter introduces the particle reconstruction methods used in the later analyses and also describes the corrections applied on these objects.

Each particle leaves a unique signature across all the different sub detectors, that can be used for its identification. First the tracker will use the hits from charged particles to reconstruct a so called track, which is used for p_{T} measurements due to the curvature of the track in the magnetic field. Additionally the sign of the charge can also be determined. Next the electromagnetic and hadronic calorimeters measure the energy of electrons, photons and charged hadrons by reconstructing the decay cascade as a so called particle jet. Muons will pass through the calorimeters while only depositing small amounts of energy. The muons will produce hits inside the muon detectors and hits are combined with the tracks from the tracker to reconstruct a global muon candidate. CMS deploys the so-called particle flow algorithm [73], which combines the information of all sub-systems and outputs candidates for hadrons and leptons.

This chapter aims to introduce the reconstruction methods used at CMS focusing on the objects used in the analyses. In particular the Muon Detector Shower (MDS) object will be introduced, which is a new object with its own unique reconstruction, that was designed and first implemented for the analyses presented in this thesis.

4.1 Tracks and Vertices

Good track reconstruction and resolution are an essential requirement for nearly all physics analyses, since they allow to determine the nature of the particles and their energies with great precision. Additionally, a good resolution allows the reconstruction of the primary and secondary interaction points, also called vertices. Usually the primary vertex is the origin of the physics process that is being analyzed, while the secondary vertices are from pileup interactions, which mostly are not relevant to the main interaction. Lastly, identifying displaced signatures, such as jets originating from b quarks or potential long-lived particles, that decay inside the tracker, require precise tracking as well. One core problem of the track reconstruction is the computational challenge associated with the reconstruction. With on average 32 pp interactions [59] per bunch crossing, the resulting event has thousands of charged particles that pass through the tracker material, which increases the combinatorics. The following sections will describe the track reconstruction at CMS, for a more detailed overview see Ref. [74].

4.1.1 Track Reconstruction

The first step of track reconstruction consists of reconstructing the hits inside the pixel and strip detectors. A charged particle traveling through the silicon detector material induces a cascade of electrons in the silicon. In order to reduce the contribution of electronic noise, the induced signal needs to be above a threshold before the reconstruction starts.

For pixel sensors two algorithms are used to determine the position of the pixel cluster. The first-pass hit algorithm is a fast algorithm used during the so called track seeding and pattern recognition. Here the algorithm either takes the center of a pixel or two pixels at the end of a cluster as the position for the hit, correcting the position for the Lorentz drift. Later on for the final track fit a more precise algorithm is deployed, called template-based hit reconstruction. In this reconstruction step, simulated clusters are used, which allows to compensate for radiated sensors. For strip sensors the position of the hit is determined from the charge-weighted average of its strip positions, correcting for the Lorentz drift. The hits are then used to form trajectories (also called tracks) by applying the iterative combinatorial track finder which is based on the Kalman Filtering [75]. In this iterative tracking approach the tracks are reconstructed in four stages.

First the track candidates are seeded based on the hits and their position in the tracker. Next the initial seeded track is extrapolated to search for additional hits originating from the same particle. With each new hit found the track is updated and the search continues in the next tracker layer. In the third step the track is refitted taking into account additional parameters like hit uncertainties, multiple scattering or energy losses. In the fourth step, tracks that do not fulfill some quality requirements are discarded, such as the goodness of the fit or the number of associated hits.

For hits in the muon system, the reconstruction is different for each of the three subdetectors (DT,CSC and RPC). For DTs the hit position is reconstructed by using the position of the wire that registered the signal and the drift time for electrons in the gas mixture. For hits in the CSC the position is calculated from the position of the wires and strips inside the chamber. In the RPC the hit is reconstructed by taking the mean strip of all strips that got hit. The reconstruction then takes all the hits from the sub detectors and builds so called muon segments, which are then later used to build the standalone muon candidates.

4.1.2 Primary and Secondary Vertices

The position of the interaction vertices can be determined with the reconstructed tracks. In a collision event there is usually one "hard interaction" vertex, also called the primary vertex (PV), which is the vertex with most of the energy involved and multiple vertices from pileup collisions, also called secondary vertices (SV). To determine the PV only tracks passing multiple track quality requirements are selected: The tracks require the value of significance of the transverse impact parameter to be <5 relative to the beam spot, at least 2 hits in the pixel layer and at least 5 hits in the pixel and strip layer and that the normalized χ^2 from the fit is less then 20. For this reconstruction there is no requirement on the p_{T} of the tracks. The tracks are then clustered based on the z position of the point of closest approach to the center of the beam spot. The clustering algorithm used is a deterministic annealing algorithm [76]. Lastly the parameters of the vertices are determined using an adaptive vertex fitter [77].

4.2 Particle Flow

The particle flow (PF) algorithm aims to combine and correlate each of the reconstructed objects (tracks and energy clusters) within each of the sub detectors (tracker, ECAL, HCAL, Muon system) to identify each final-state particle. This concept was first used in $\mathrm{e}^+\mathrm{e}^-$ collider experiments, namely ALEPH [78], and the concept is also planned to be deployed at future $\mathrm{e}^+\mathrm{e}^-$ collider experiments. For hadron collider experiments, CMS was the first experiment to deploy the PF approach. Before the start of the LHC it was believed that the number of particles in the event would reduce the advantages of the PF algorithm. A fine spatial granularity is needed in the detector for the PF algorithm to work, otherwise multiple different particles, which may be from different pp interactions, merge into a shared signal, reducing the reconstruction efficiency. In the following, the PF algorithm reconstruction will be introduced for each of the different particles. For a more detailed overview see Ref. [73].

After the PF elements in each sub detector are reconstructed, a link algorithm is deployed, that links the different elements together to form a PF block. For example track candidates from the tracker are extrapolated to the calorimeters and matched to the energy clusters. For the linking, the distance between two elements is a major parameter, where a smaller distance results in a better quality of the link. After such a block is found, the reconstruction order is as follows: First the muon candidates are reconstructed inside the block by searching for a link between tracks in the tracker and tracks inside the muon system. The momentum of the muon is mainly measured with the information from the tracks, since the deposits inside the calorimeters are minimal. If a candidate is found, the corresponding PF elements are removed from the block for the following reconstructions. Afterwards the electron and photon reconstruction is performed, with the main challenge being collecting all bremsstrahlung photons associated to the electron candidate. The photon signature requires a calorimeter cluster with no track being linked and that the energy in the HCAL clusters does not exceed 10 % of the total energy. Additionally the photons can convert into e^+e^- pairs, which usually happens in the tracker material. The electron reconstruction requires a ECAL cluster with a linked track, where the same 10 % requirement on the calorimeter clusters is applied. For the electron candidates additional quality criteria on the track are applied. After the isolated photon and electron candidates are removed, the remaining elements have to be either non-isolated photons, neutral hadrons or charged hadrons. The remaining ECAL cluster that have no track linked are then identified as non-isolated photons, while the remaining HCAL clusters with no linked tracks are identified as neutral hadrons. Lastly, HCAL clusters with a linked track are then identified as charged hadrons. For all of these candidates the energies are calculated combining the track momenta and cluster energies.

4.3 Lepton Reconstruction and Identification

While the PF algorithm reconstructs all the leptons in the event, most analyses require additional quality requirements for each of the objects, to only select leptons from the physics process that is being analyzed and to minimize the selection of objects being misidentified as electrons or muons. In the following the additional requirements on electrons and muons will be discussed, both of which are used in the later analyses. For a more detailed overview see Ref. [79] and Ref. [67].

4.3.1 Electrons

The electrons used in the later analyses are required to be a PF electron candidate. So called IDs for electrons are applied, that add additional requirements on the electron objects. The analyses presented in this thesis use the loose and tight ID requirement, which will be summarized in the following, but more details can be found in Ref. [79]:

First the electrons are split into two groups, depending on their η position, where electrons with $|\eta| <= 1.479$ are in the barrel region and electrons with $|\eta| > 1.479$ are in the end cap region. The ID then consists of the following selections: A selection on the angular separation between the track and the ECAL cluster ($\Delta\eta$,$\Delta\phi$), a cut on the lateral extension of the shower along the η direction $\sigma_{\eta\eta}$, a cut on the difference between the calorimeter cluster energy and the track momentum $1/E_\mathrm{e}$- $1/p$, a cut on the ratio of hadronic to electromagnetic energy H/E and a cut on the number of allowed missing hits in tracker for the corresponding track. Additionally a veto is added, that rejects electrons produced by the conversion of photons within the tracker material. This veto is derived by exploiting the pattern of track hits that a photon conversion leaves in the tracker. Next selections on the impact parameters d_0 and d_z are applied, so that the selected electron originates from the primary vertex of the event. Lastly an isolation requirement is added, so that the electron has no surrounding hadronic activity. The so called PF isolation is defined as

$$\mathrm{Iso}_\mathrm{PF} = \sum p_\mathrm{T}^\mathrm{charged} + \max\left[0, \sum p_\mathrm{T}^\mathrm{neutral\ had} + \sum p_\mathrm{T}^{\gamma} - p_\mathrm{T}^\mathrm{PU}\right], \tag{4.1}$$

where all charged PF candidates, neutral hadrons and photons are chosen within a ΔR cone around the electron, for the later analyses a cone of ΔR <0.3 is chosen. Additionally a correction related to the event pileup p_T^PU is added as well. For the isolation cut the relative isolation variable $\mathrm{Iso}_\mathrm{PF,rel}$ is defined as the ratio of Iso_PF

Table 4.1: Cut values on the specific vetos for the 2016 cut-based electron ID

	Barrel		End cap	
	Loose ID	Tight ID	Loose ID	Tight ID
$\Delta\eta <$	0.00477	0.00308	0.00868	0.00605
$\Delta\phi <$	0.222	0.0816	0.213	0.0394
$\sigma_{\eta\eta} <$	0.011	0.00998	0.0314	0.0292
$1/E_\mathrm{e}$- $1/p <$	0.241	0.0129	0.14	0.0129
$H/E <$	0.298	0.0414	0.101	0.0641
missing hits <=	1	1	1	1
$d_0 <$	0.05	0.05	0.1	0.1
$d_z <$	0.1	0.1	0.2	0.2
$\mathrm{Iso}_{\mathrm{PF,rel}} <$	0.0994	0.0588	0.107	0.0571

Table 4.2: Cut values on the specific vetos for the 2017 cut-based electron ID

	Barrel		End cap	
	Loose ID	Tight ID	Loose ID	Tight ID
$\Delta\eta <$	0.00377	0.00255	0.00674	0.00501
$\Delta\phi <$	0.0884	0.022	0.169	0.0236
$\sigma_{\eta\eta} <$	0.0112	0.0104	0.0425	0.0353
$1/E_\mathrm{e}$- $1/p <$	0.193	0.159	0.111	0.0197
$H/E <$	$0.05+\frac{1.16}{E_\mathrm{e}}+\frac{0.0324\rho}{E_\mathrm{e}}$	$0.026+\frac{1.15}{E_\mathrm{e}}+\frac{0.0324\rho}{E_\mathrm{e}}$	$0.0441+\frac{2.54}{E_\mathrm{e}}+\frac{0.183*\rho}{E_\mathrm{e}}$	$0.0188+\frac{2.06}{E_\mathrm{e}}+\frac{0.183*\rho}{E_\mathrm{e}}$
missing hits <=	1	1	1	1
$d_0 <$	0.05	0.05	0.10	0.10
$d_z <$	0.10	0.10	0.20	0.20
$\mathrm{Iso}_{\mathrm{PF,rel}} <$	$0.112+\frac{0.506}{p_\mathrm{T}}$	$0.0287+\frac{0.506}{p_\mathrm{T}}$	$0.108+\frac{0.963}{p_\mathrm{T}}$	$0.0445+\frac{0.963}{p_\mathrm{T}}$

divided by the electron p_T. The specific cuts differ for the barrel and end cap region, as well as for the tight and loose ID requirement. A summary of the specific values is given in Tab. 4.1 for the 2016 data taking period and Tab. 4.2 for the 2017 and 2018 data taking period. For 2017 the H/E and $\mathrm{Iso}_{\mathrm{PF,rel}}$ cuts are modified, and are dependent on the p_T, energy of the electron and the effective area ρ, therefore creating a dynamic cut.

4.3.2 Muons

The muons used in the analysis are required to be a PF muon candidate. Similar to the electron reconstruction a muon ID as well as a isolation requirement is applied. For a more detailed overview see Ref. [67]. The isolation requirement is defined as

$$\mathrm{Iso}_\mu = \sum p_\mathrm{T}^{\mathrm{charged}} + \max\left[0, \sum p_\mathrm{T}^{\mathrm{neutral\ had}} + \sum p_\mathrm{T}^{\gamma} - \frac{1}{2}\sum p_\mathrm{T}^{\mathrm{PU}}\right], \qquad (4.2)$$

all charged PF candidates, neutral hadrons and photons are chosen within a $\Delta R < 0.4$ cone around the muon. In this isolation definition the sum of p_{T} from pileup is scaled by a factor of 0.5, which is estimated from simulations as the ratio of neutral particles to charged particles in inelastic proton-proton collisions. Similar to the electron isolation described before, the muon isolation is applied as a relative isolation $\mathrm{Iso}_{\mu,\mathrm{rel}}$, which is the ratio of Iso_{μ} divided by the muon p_{T}. In the analyses both loose and tight ID requirements are used, which are summarized in the following.

The loose ID only requires a PF muon candidate and that the muon is either a global muon, which is a muon candidate being reconstructed from both tracker and muon tracks, or a tracker muon. This last requirement removes so called Standalone Muons, which are muons that are reconstructed using only muon detector tracks.

For the tight ID a PF muon candidate is required, that is reconstructed as a global muon. Additionally cuts on global muon track are added which are: The χ^2/ndf of the global-muon track fit needs to be <10, suppressing hadronic punch-through and muons from decays in flight, at least one hit in the global-muon track fit needs to be located in a muon chamber, the muon segments need to be in at least two muon stations, the number of pixel hits needs to be larger than 0, the number if tracker layers with hits needs to be larger than 5, a selection on the the transverse impact parameter of $d_{xy} < 2\,\mathrm{mm}$ and a selection on the longitudinal distance of the tracker track $d_z < 5\,\mathrm{mm}$.

4.4 Jets

Quarks and gluons can not be observed as free particles due to confinement, but rather as a cascade of strongly interacting particles, which form a so called jet. A jet consists of charged and neutral hadrons, as well as leptons and photons, each leaving deposits in the ECAL and HCAL. Reconstructing each single particle in the jet is close to impossible due to the large number of particles potentially very close to each other. Therefore the particles are combined in a jet object with its own properties, which in turn allows the properties from the initial particle that initiated the jet to be determined. This approach necessitates the use of a clustering algorithm, which selects the particles belonging to the jets and rejects particles from other origins. The reconstructed jet object is shaped like a cone. The following section will describe the jet clustering algorithm deployed at CMS and also introduce the algorithm used to tag jets originating from the decay of b quarks.

4.4.1 Jet Clustering Algorithms

In general the jet clustering algorithm used needs to be infrared and collinear safe. This just means that the algorithm should not change the resulting jet if a soft or collinear parton splitting occurs. Nowadays the anti-k_T algorithm [80] is used within CMS, while in earlier data taking periods, the so-called Cambridge-Aachen [81] clustering also used. For the anti-k_T algorithm two distance variables are used, which are defined as:

$$d_{ij} = \min\left(k_{ti}^{-2}, k_{tj}^{-2}\right) \frac{\Delta R_{ij}^2}{R^2}, \tag{4.3}$$

$$d_{iB} = k_{ti}^{-2}, \tag{4.4}$$

where d_{ij} defines the distance between PF candidate i and j by using their transverse momenta k_{ti}, the radius parameter R for the jet, which is a selectable parameter and ΔR is the angular distance between the candidates. d_{iB} defines the distance between the PF candidate and the beam pipe. The order of the particles that are clustered is important; for the anti-k_T algorithm the particles with the largest p_T are clustered first, compared to other algorithms like Cambridge-Aachen that cluster particles with the smallest p_T first. The anti-k_T algorithm calculates the distances d_{ij} and d_{iB} for each PF candidate. If the minimal distance is d_{ij}, then the corresponding PF candidates are i and j are combined and this combination is added back into the clustering algorithm. If d_{iB} is the smallest distance, then i is called a jet and is removed from the clustering. The algorithm terminates once there is no particle left in the input. The jets used in the analyses presented in this thesis have been clustered using a distance parameter R of 0.4, with the jets then being called AK4-jets. Additionally the charged-hadron subtraction (CHS) method is used to mitigate the impact of pileup on the jet, by removing charged hadrons from the input collection that originate from pileup interactions. To identify such charged hadrons, their associated tracks are matched to pileup vertices.

4.4.2 b-tagging

Due to the lifetime of b quarks, jets originating from the day of b quarks are displaced from the primary vertex by a few millimeters. They can be tagged by identifying secondary vertices close by the primary vertex. Additionally the radial energy profile and the inclusion of leptons in the final state also are indicators for a b-jet. A similar approach can be adopted to identify c quarks, since their lifetime is similar to that of a b quark, therefore allowing c-tagging jets as well.

CMS deploys a multitude of different b-tagging algorithms, nowadays mostly neural network based taggers like DeepCSV [82] are used. For the HNL analysis presented later the CSVv2 [83] tagger is used. CSVv2 is a neural network based tagger that uses secondary vertex and track-based lifetime information to classify jets between b-jets, c-jets and other jets. Different working points for the b-tagger are provided and in the later analysis a medium working point is used, which corresponds to a discriminator value cutoff of 0.8838.

4.5 Missing Transverse Momentum

The total transverse momentum of all particles in a hard scattering interaction is zero. A challenge arises if some part of the decay products is not detected, for example due to them leaving no significant trace in the detector, like neutrinos, or due to mismeasurements of the p_T of the detected particles. In this case, the sum of all measured momenta in the event is non-zero. This phenomenon can be quantified by introducing the so called missing transverse momentum (also called MET or $p_\mathrm{T}^\mathrm{miss}$), which is defined as

$$\vec{p}_\mathrm{T}^\mathrm{miss} = -\sum_i \vec{p}_{\mathrm{T},i}. \tag{4.5}$$

Note that due to the transverse nature of $p_\mathrm{T}^\mathrm{miss}$ only a ϕ direction can be assigned to this variable. Jet corrections and PU both have an impact on the MET and are therefore accounted in the calculation, by introducing a correction which is propagated through the $p_{\mathrm{T}}^{\mathrm{miss}}$ calculation. One interesting feature of $p_{\mathrm{T}}^{\mathrm{miss}}$ is that long-lived signatures, that have a large displacement, like the signals presented in this analysis, also produce a significant amount of $p_{\mathrm{T}}^{\mathrm{miss}}$ which is also aligned in ϕ-direction with the signal object, like the clusters in the muon system. This is due to the fact that the clusters in the muon system are not considered in the $p_{\mathrm{T}}^{\mathrm{miss}}$ calculation, since these are not PF objects.

4.6 Muon Detector Shower

The main signal object for the analyses presented in this thesis are the newly developed objects called Muon Detector Showers (MDS). A LLP with a large enough displacement from the PV can decay within or just prior to the CMS muon system. The muon system consists of detector chambers and the iron return yoke, acting as a sampling calorimeter. Due to the hadronic decay of the LLP considered in this analysis, a hadronic shower will be induced in the iron return yoke and the shower will create a geometrically localized and also isolated cluster of hits in the DT or CSC system. Usually the DT and CSC systems record the signal pulses on their respective anode or cathode wires, which are then reconstructed to form a two-dimensional point in each chamber layer, which is called a RecHit. Due to the location of the chamber being known in the detector, a third dimension can be added to the hit, but this position has then only discrete values. In the usual muon track reconstruction the RecHits are used to form straight-line segments in the chamber.

Initially segments were studied to be used for the analysis, since segments are available in the AOD data format (for a description of the different data formats see Ch. 3.2.5), which makes the data processing easier and less time consuming, since this data format is readily available. During these studies it was found, that the segment reconstruction does saturate at some point, meaning that the number of reconstructed segments at some point does not increase with more hits in the same area. Therefore only a limited number of segments is reconstructed in a shower. Additionally changes to the 2017 and 2018 segment reconstruction further suppressed the efficiency for this signal. Because of this, the choice was made to go to the RECO data format and use the CSC and DT RecHits directly. Additional studies were performed to validate the agreement between simulated and reconstructed RecHits. Fig. 4.1 shows the number of segments and number of RecHits for a signal event simulated according to 2016 data taking conditions, showing that the RecHits provide a better cluster signature compared to the segments.

The RecHits are clustered using their η and ϕ position by deploying the density-based spatial clustering of applications with noise (DBSCAN) [84] algorithm. The algorithm requires two choosable parameters, the minimum distance for two points to be grouped together ΔR, which in literature is usually called ϵ, and the minimum number of points n required for a cluster. The algorithm starts by selecting an arbitrary starting point and calculates the distance to its neighboring points. If the algorithm finds at least more points as n with a distance smaller then ΔR, a new cluster is started. All neighboring points satisfying the distance requirement are also added to this cluster and for each point the same check of the distance for neighboring points is performed. If not enough points are found within the distance the point is considered noise, if it does not already belong to a cluster. Once all points in the created cluster have been checked, a different new point outside of the cluster is chosen and the same algorithm is performed. The algorithm terminates once all points have been checked and either been labeled as part of a cluster or as noise.

For the analyses the minimum number of RecHits to form a cluster is required to be 50 and the distance parameter is required to be $\Delta R = 0.2$. Additionally if two clusters are within $\Delta R < 0.6$ then the clusters are merged into one. This is done until all clusters within the event are isolated. This procedure is introduced to eliminate double counting of one LLP decay as two clusters.

The minimum number of RecHit requirement was chosen large enough to reject clusters originating from a muon, which would leave 24 RecHits in the CSC and 46 RecHits in the DT. This parameter has little impact on the final signal efficiency, since the signal region will add a more stringent cut on the number of RecHits. A study was performed where the minimum number of RecHits was reduced to 30, which resulted in a 5 % increased inclusive cluster efficiency. But this increase was mostly adding clusters with a small number of RecHits associated to them, which fall outside of the signal region. No increase in the signal efficiency was observed for this study.

The distance parameter ΔR is motivated by the ΔR spread of all clusters. The ΔR spread is defined as:

$$\sqrt{\frac{\sum(\eta_i-\bar{\eta})^2+(\phi_i-\bar{\phi})^2}{N}}, \tag{4.6}$$

where η_i and ϕ_i are position of the i-th RecHit, $\bar{\eta}$ and $\bar{\phi}$ are the center of the cluster, and N is the number of RecHits in the cluster. The distribution of the ΔR spread for different ΔR selections for simulated signal is shown in Fig. 4.2. The plot on the left shows that 90 % of the clusters have a ΔR spread of less then 0.2, motivating the 0.2 distance parameter. The right plot shows that changing the ΔR parameter does not change the shape of the number of RecHit distribution significantly, therefore no

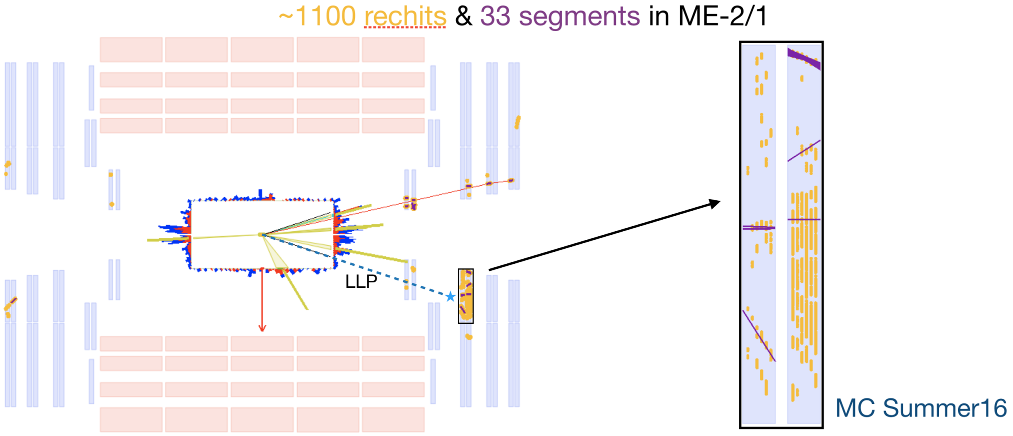

Figure 4.1: An event display of a simulated signal event, showing 1100 reconstructed RecHits (yellow dots) and only 33 reconstructed segments (purple line segments).

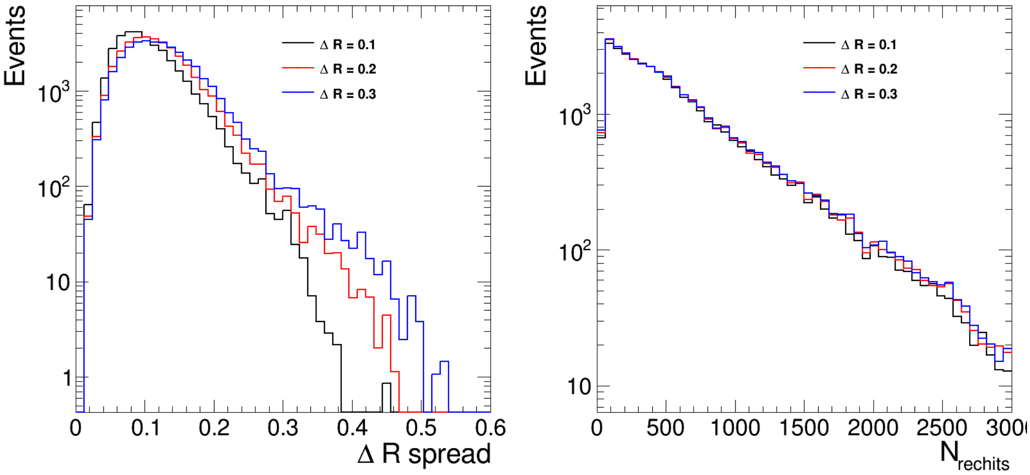

Figure 4.2: The ΔR spread (Left) and $N_{rechits}$ (Right) distributions scanning the ΔR parameters of the clustering algorithm.

large change in the sensitivity is expected. Additionally changing the cut from 0.2 to 0.3 only increases the inclusive clustering efficiency by 1 %.

The MDS main variables then are its position in the detector and the timing information from the RecHits. The position of the MDS is defined by taking the mean of all η and ϕ positions of the RecHits belonging to the MDS. Additionally, it is useful to define the average station number as a proxy for the z-position in case of CSC clusters and as a proxy for the r position in case of DT clusters. This variable is calculated by taking the average of the RecHits station number (if the station contains at least 10 RecHits). The station number ranges from 1 (closest to the interaction point) to 4. Additionally the variable $N_{Station}$ is defined by the number of stations in the cluster with at least 10 RecHits. This variables gives a handle on the size of the MDS. The 10 RecHit cut for both variables is applied to suppress counting stations with single muon tracks, since a single muon track would only leave 6 RecHits per station in the CSCs and 9 RecHits per station the DTs.

For MDS in the CSC the cluster time is defined as the average time of all RecHits making up the cluster. The time for each RecHit is calculated similarly to the CSC segment time definition [85] by taking the average of the wire and strip time, applying a positive tail pruning to the wire time. Fig. 4.3 shows the CSC cluster time for a twin Higgs signal model and data. For both signal and data clusters the jet and muon veto (described in the later analysis chapters Ch. 5.4.1 and Ch. 6.4) have been applied. It can be seen that the signal is centered in the in-time region, while the background clusters show a periodic peak at 20 ns, which is the collision rate of the LHC. The in-time region therefore is defined between -5 and 12.5 ns, with a larger positive tail due to delays from slow moving LLPs.

For MDS in the DTs the cluster time has to be defined via the timing information of a nearby RPC hit, since the DT RecHits do not have the required timing information available. Therefore each MDS in the DTs has to match at least one RPC hit, which has to be in the same DT wheel as the MDS and be within $\Delta\phi < 0.5$. It is possible to match multiple RPC hits to the same MDS. The RPC hits have timing information available in the form of the bunch crossing (BX) information. This variable is an

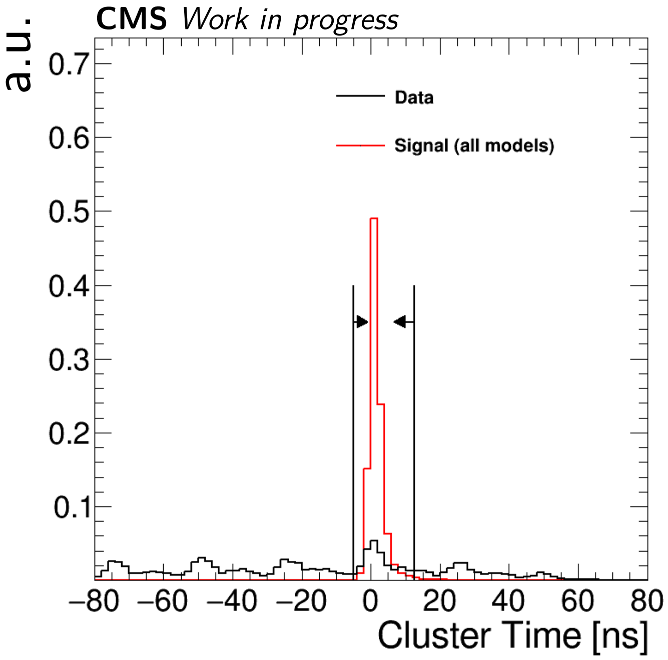

Figure 4.3: The signal and background distribution for the CSC cluster time is shown. Both signal and background clusters are required to pass the jet and muon veto.

integer which is zero if the hit can be attributed to the current bunch crossing time wise. The DT cluster time is then defined by the statistical mode of all RPC hits matched to the cluster. The in-time region then is defined for clusters with a cluster time of zero.

4.7 Corrections to Simulated Data

Even though the simulated data tries to match the data taking conditions of the CMS detector, some effects may not be known at the time or have changed over time. Some effects are also difficult to model in simulation, which necessitates some corrections derived from actual detector data. In the following some corrections to the simulated data will be introduced.

4.7.1 Jet Corrections

After jets are clustered with their respective jet clustering algorithm and the pileup contributions are suppressed with algorithms like CHS, the jet energy still needs to be corrected. The jet energy correction (JEC) [86] corrects the energies for non-linear responses of the detector. This correction is applied to both data and the simulation, but data has some additional steps applied. First the JEC removes additional pileup contributions using simulated events. Next corrections are derived for the non-linear detector responses, like the p_{T} dependence of the calorimeter response or the tracking efficiency. The next steps are only applied to recorded data: The first step corrects jets with large η, since these are in a region which is less well calibrated. The second step corrects p_{T} dependent effects using $\gamma+$ jet or Z+jet events. The last step is then again applied to both simulation and recorded data, which is a correction to the jet flavor.

Afterwards differences between the recorded and simulated jets can be observed in the jet energy resolution (JER) [86]. Usually the resolution in recorded data is worse compared to simulation, which is corrected by smearing the JER in simulation to better match the recorded data.

4.7.2 Pileup Reweighting

The amount of pileup interaction during a pp interaction depends on the cross section and the instantaneous luminosity, therefore it is heavily dependent on the data taking conditions. The generated samples usually are simulated using some initial assumption about the pileup, which are then afterwards corrected with the recorded distribution of the number of pileup events.

4.7.3 Lepton Corrections

The reconstruction and identification efficiencies for electrons and muons in simulated and recorded data are observed to be different. This is due to the fact that the recorded data is biased, e.g. due to detector misalignment. To account for these differences so called lepton scale factors are derived and applied to the simulated data [87–91]. Since both the electron and muon objects use an identification requirement and isolation requirement, scale factors are derived for both variables. The scale factor is measured with a tag and probe method in either a $\mathrm{Z} \rightarrow \mu\mu$ sample for the muon scale factors or a $\mathrm{Z} \rightarrow \mathrm{ee}$ sample for the electron scale factors. The efficiency of the variable is measured in bins of p_T and η and the difference in recorded and simulated data is taken as a scale factor, used to reweight the simulated events. For muons specifically an additional scale factor is derived for the track efficiency.

For reconstructed muons the measured momentum is different in simulated and recorded data, due to small uncertainties in the magnetic field, which affect the momentum measurement which is based on the curvature of the tracks. These differences are corrected by adding the so-called Rochester corrections [87], that affect the muon momentum scale and resolution.

4.7.4 Trigger Scale Factors

The efficiency for the triggers used in the analyses can also differ between simulated and recorded data. This difference can again be reduced by introducing trigger scale factors. This scale factor usually is measured in a control region of the analysis, which is orthogonal to the analysis phase space and therefore has close to no signal contamination. In this control region then the trigger efficiency is measured as a function of the variable deployed to perform the trigger decision. E.g. for a $p_\mathrm{T}^\mathrm{miss}$ trigger the control region is defined by events passing a single muon trigger and the trigger efficiency is then measured as a function of $p_\mathrm{T}^\mathrm{miss}$. A single muon trigger is used, since it is orthogonal to the $p_\mathrm{T}^\mathrm{miss}$ trigger and also has a good trigger efficiency, allowing for a large enough dataset to perform this study. The difference in this distribution is then taken as a scale factor correction. This specific trigger scale measurement is performed in Ch. 5.1.2.

5 Search for Long-Lived Particles Decaying in the CMS Endcap Muon System

In the following a search for neutral long-lived particles (LLPs) decaying in the CMS end cap muon system using LHC Run 2 data at a center-of-mass energy of $\sqrt{s} = 13\,\text{TeV}$ is presented. This is the first-of-its-kind analysis within the CMS experiment using the Muon Detector Shower (MDS) cluster objects developed specifically for this analysis. This analysis uses the Cathode Strip Chambers (CSC) in the forward CMS muon system and the iron material of the return yoke as a sampling calorimeter to detect the MDS clusters. The analysis has been published and can be found in Ref. [92, 93]. The search targets a Higgs boson mediated production of two long-lived scalars S with masses between 7 GeV and 55 GeV, using the simplified twin Higgs model described in Ch. 2.2.1. The proper lifetime $c\tau$ is a free parameter of the model and the analysis targets lifetimes between 1 cm and 100 m.

Previous searches targeting this benchmark model include the displaced jet search performed by the CMS collaboration [94], yielding good sensitivity for proper lifetimes below 0.2 m, and the muon spectrometer search performed by the ATLAS collaboration [95, 96], providing good sensitivity for proper lifetimes above 1 m. The analysis presented in this chapter achieves its best sensitivity between 1 m and 5 m. While the analysis presented in this chapter focuses on single LLP clusters in the CSC system, an extension to the analysis has been made to include decays in the DT and to include two LLP decays in the muon system. This extension will be briefly discussed at the end, while more details can be found in the published results in Ref. [97].

The chapter is structured as follows: First an overview of the general analysis strategy is given including a discussion of the trigger strategy of the analysis. Next the simulated and recorded datasets used in the analysis are discussed, with a focus on the signal process simulation. Following this, the objects used in the analysis are discussed, introducing additional analysis specific selections on the objects described

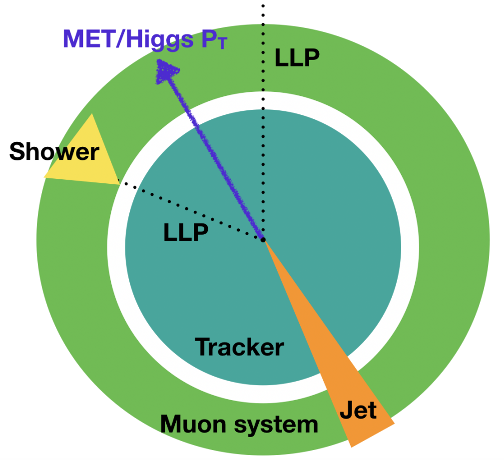

Figure 5.1: An illustration of the Twin Higgs Model signature showing the MDS with the aligned MET and the ISR jet on the other side of the detector.

in Ch. 4. Afterwards, the event selections are discussed, specifically the selections placed on the cluster properties to enhance the S/B ratio for the signal. Subsequently the data-driven background estimation method and the systematic uncertainties of the analysis are discussed, specifically validating the simulation of the signal clusters. Lastly the results for the search are presented and the extension of the analysis to include the DT chambers and a two cluster category is discussed.

5.1 Analysis Strategy

Due to the large lifetime and therefore large displacement of the LLPs their decay occurs beyond the CMS calorimeters inside the muon system. This leads to a significant amount of $p_\mathrm{T}^\mathrm{miss}$ in a signal event, since the $p_\mathrm{T}^\mathrm{miss}$ calculation is based on the calorimeter deposits in the event, which do not include the energy of the LLP, if it decays in the muon system. For the twin Higgs benchmark model a large amount of $p_\mathrm{T}^\mathrm{miss}$ is present, if the Higgs is produced with significant recoil from initial state radiation (ISR), which also leads to the $p_\mathrm{T}^\mathrm{miss}$ being aligned with the MDS cluster. Figure 5.1 illustrates a typical signal event for the Twin Higgs benchmark model. To target events with the therefore expected large amounts of $p_\mathrm{T}^\mathrm{miss}$, the analysis is performed with events that pass $p_\mathrm{T}^\mathrm{miss}$ based HLT trigger paths, as detailed in Section 5.1.1. The LLP decay has multiple possible decay channels, with the analysis being most sensitive in channels where the LLP in the muon system decays into quarks ($\mathrm{b}\bar{\mathrm{b}}$ and $\mathrm{d}\bar{\mathrm{d}}$), with decays into τ are also considered.

5.1.1 Trigger Strategy

Due to the expected high $p_\mathrm{T}^\mathrm{miss}$ of signal events, the trigger decision is based on HLT paths requiring a large amount of $p_\mathrm{T}^\mathrm{miss}$. The main path in all three data taking years requires a $p_\mathrm{T}^\mathrm{miss}$ of at least 120 GeV and additionally that there are zero muons present in the event. The muon requirement is applied in order to be able to measure the trigger efficiency with orthogonal single muon trigger paths. Since the analysis is selecting events with zero muons, this additional requirement on the HLT trigger path does not impact the signal efficiency significantly. For the 2017 data taking period it was observed that the p_T^{miss} path suffered from a high noise contribution to the trigger rate. The noise is mitigated by switching to a HLT path with an additional requirement on the scalar sum of the transverse momentum of all PF jets (H_T) of $H_T > 60\,\mathrm{GeV}$. This path is added for the 2017 and 2018 data taking periods. Lastly in 2017 and 2018 a p_T^{miss} path with $p_T^{\mathrm{miss}} > 140$ GeV is added. These last two paths act as a protection against the prescaling of the main path in case the LHC beam conditions are such, that the delivered luminosity is high and the total HLT rate has to be reduced by introducing prescales to HLT paths with high rates.

5.1.2 Trigger Efficiency Scale Factor

To account for potential mismodeling of the trigger efficiency in simulation compared to recorded data, a trigger efficiency scale factor is used. As mentioned before, the trigger efficiency is measured in an orthogonal dataset compared to the dataset used in the analysis. In recorded data, events are required to pass the single muon HLT path `HLT_IsoMu27`, which requires one isolated muon with $p_T > 27\,\mathrm{GeV}$. The scale factor in simulated events is measured using a $\mathrm{W} \rightarrow l\nu$ sample and the events are required to pass the same HLT paths as the recorded events. Additionally the events are required to have exactly one reconstructed muon with a p_T between 30 and 100 GeV with tight identification and isolation requirements applied (as discussed in Ch. 4.3.2) The upper cut on the p_T is used since high momentum muons have a higher chance to have their p_T mismeasured, which would impact the p_T^{miss} calculation. Lastly the events need to pass the METfilters, described in Ch. 5.3.5. The trigger efficiency is then measured as a function of p_T^{miss}, with the muon p_T being ignored in the p_T^{miss} calculation. The measurement is performed for each year of data taking separately and the results are shown in Fig. 5.2.

The data-to-simulation ratio of the trigger efficiency is applied to the simulated signal samples as a p_T^{miss} dependent event weight, which decreases the signal yield by 5 % in all signal models.

5.2 Dataset

The analysis uses data from proton-proton collision at a center of mass energy of $\sqrt{\mathrm{s}} = 13\,\mathrm{TeV}$ taken in 2016, 2017 and 2018. To reconstruct the MDS clusters, access to the CSC RecHits and therefore the RECO data tier (See Ch. 3.2.5) is needed. This is difficult and time consuming, which was one of the main challenges in this analysis. Additionally the RECO data sample had a p_T^{miss} selection of >200 GeV already applied, therefore the analysis later will also be required to use the same selection.

In the following sections the simulated samples used in the analysis are discussed.

5.2.1 Signal Simulation

Simulated $\mathrm{H} \rightarrow \mathrm{SS}$ signal samples are generated using the Monte Carlo (MC) event generator `POWHEG` 2.0 [98–100] at next-to-leading order (NLO) accuracy. The parton shower, hadronization and underlying event are simulated using `PYTHIA` 8.205 for the

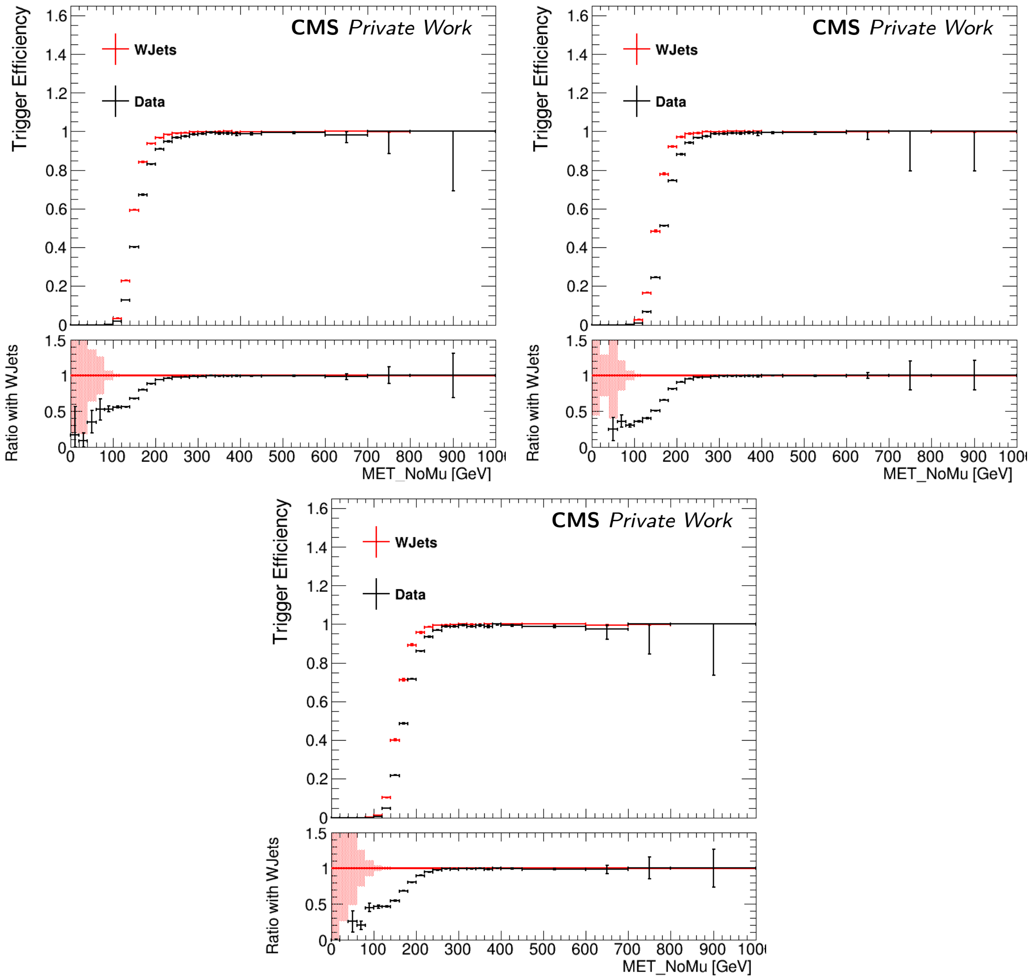

Figure 5.2: The trigger efficiency as a function of $p_{\mathrm{T}}^{\mathrm{miss}}$, for data and simulation in 2016 (Left), 2017 (Middle), and 2018 (Right) data-taking conditions.

2016 data taking period and 8.230 [101] for the 2017 and 2018 data taking period. The underlying event for the simulated signal sample is corrected with a so-called tune, which is derived from data and adjusts the simulation to describe the data better. For the 2016 data taking period the CUETP8M1 [102] tune is used and for the 2017 and 2018 data taking periods the CP5 [103] tune is used. The signal simulation considers gluon fusion, vector boson fusion, WH, ZH and $\mathrm{t\bar{t}H}$ production modes with the Higgs mass being set to 125 GeV, while the mass of the long-lived scalar S (m_S) is set to 7, 15, 40 or 55 GeV with a proper lifetime $c\tau$ of 0.001, 0.01, 0.1, 1,20 and 100 m. Three different decay modes for S are considered: The decay into four b quarks (4b), into four d quarks (4d) and into four τ leptons (4τ). The NNPDF 3.0 [45] and 3.1 [46] parton distribution functions are used. Lastly, the detector response of the CMS detector is simulated with `GEANT4` [49]. To account for additional pp interactions within the same bunch crossing (pileup), minimum bias events are added to the simulation to match the observed pileup distribution in data.

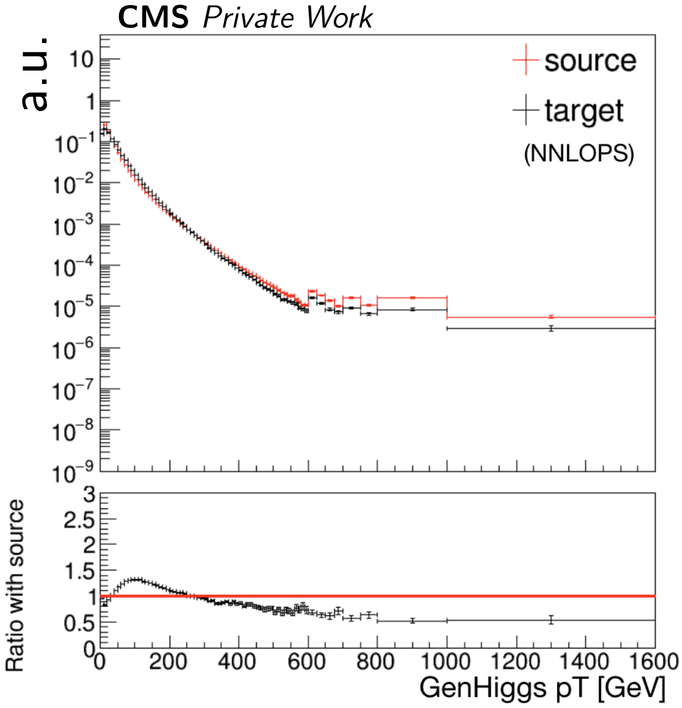

Figure 5.3: The generator level Higgs p_T of the generated signal sample and an alternative theory prediction (NNLOPS) are shown. The bottom subplot shows the ratio of the NNLOPS prediction and the generator prediction. This ratio is used as an event weight.

Table 5.1: Signal yield increase in the signal region after applying the Higgs p_T correction. There are no events selected in the signal region for the 55 GeV and $c\tau = 0.1\,\mathrm{m}$ signal sample.

	$c\tau = 0.1\mathrm{m}$	$c\tau = 1\mathrm{m}$	$c\tau = 10\mathrm{m}$	$c\tau = 100\mathrm{m}$
15 GeV	5.11%	1.48%	2.47%	0.65 %
40 GeV	7.28%	0.84%	2.18%	4.28 %
55 GeV	\	4.22%	2.9%	3.13 %

Higgs p_T spectrum correction

The p_T of the simulated Higgs boson for the ggH production mode is reweighted to a NNLOPS [104] prediction. The distributions of the Higgs boson p_T from the generated sample and the NNLOPS theoretical prediction are shown in Fig. 5.3. The Higgs p_T correction increases the signal yield depending on the mass and lifetime of the sample, as shown in Tab. 5.1. The signal yield in the signal region increases between 0.65% and 7.28 %, depending on the mass and lifetime.

LLP Lifetime Reweighting

The generated samples only contain LLPs with a small number of discrete lifetimes, as discussed in Ch. 5.2. Intermediate lifetimes can be accessed by reweighting the generated events to a different lifetime. In the H → SS signal model both scalars

S can be long-lived and the decay length of each one is independent of the other. The scalars decay with an exponential probability, therefore the event distribution is given by the product of the two decay probabilities:

$$p(t_1, t_2|\tau) = \frac{1}{\tau^2} \exp^{-t_1/\tau} \exp^{-t_2/\tau}, \tag{5.1}$$

where τ is the lifetime of the LLP, t is the lifetime of the LLP in its rest frame given by $t = \frac{s}{\gamma \cdot \beta}$, with the travel distance in the lab frame s, γ is the Lorentz factor and β is the velocity of the LLP. A sample with a new lifetime then can be obtained by assigning a weight to a simulated events, where the weight is:

$$w = (\frac{\tau_{\text{old}}}{\tau_{\text{new}}})^2 \exp[(t_1 + t_2) \times (\frac{1}{\tau_{old}} - \frac{1}{\tau_{new}})]. \tag{5.2}$$

For this analysis each intermediate lifetime is reweighted using two generated simulated samples, whose lifetimes are closest to the intermediate lifetime. For events where the sum of the two LLP proper lifetimes is greater than half of the longer lifetime, the weights from the longer lifetime are used, otherwise weights from the shorter lifetime are used. Therefore, for example a sample with a lifetime of 3 m is obtained by using the generated samples with lifetimes of 1 m and 10 m. If the lifetimes of the two LLPs are larger than 5 m, weights from the 10 m sample are used, otherwise the 1 m sample is used. This procedure results in smaller weights compared to those obtained if only one sample is used. Additionally the procedure reduces the statistical uncertainty of the reweighted sample.

5.2.2 Background Simulation

The background contributions in this analysis are estimated using data driven methods, therefore no simulated samples for the background processes are used for the background estimation. Simulated samples of the background processes are however still used to study general features, to optimize the event selections and to measure simulation to data correction factors.

A $W \rightarrow l\nu$ sample is used to perform signal selection optimization, specifically deriving the cluster identification variable (See Ch. 5.4.2).

5.3 Object Reconstruction and Identification

In the following sections the reconstructed objects used in the analysis are described. Standard objects described in Ch. 4 are used, if not specified otherwise.

5.3.1 Cluster Reconstruction and Efficiency

MDS clusters are reconstructed from individual RecHits with the DBSCAN algorithm, with $\Delta R < 0.2$ and a minimum RecHit threshold of 50 (See Ch. 4.6). The cluster efficiency is defined as the efficiency for a LLP decaying within the acceptance of the CSC detector volume to result in a reconstructed MDS cluster. The denominator is the number of generator level LLPs that decay within the geometric acceptance of the CSC detector system. The numerator is the number of LLPs within the CSC detector system that are matched to a MDS cluster within $\Delta R < 0.4$. The cluster efficiency as a function of the LLP decay position in R and Z is shown in Fig. 5.4. The efficiency is nearly flat throughout the CSC, except when the LLP decays near the outer edges of the CSC (in both r and z), where there is limited space for the detector to register all the RecHits from the shower. It is also observed, that the efficiency increases, if the LLP decays in the steel right before the CSC. Fig. 5.5 shows the 2D cluster efficiency as a function of the decay position of the LLP in the r-z plane, overlaying the detector geometry.

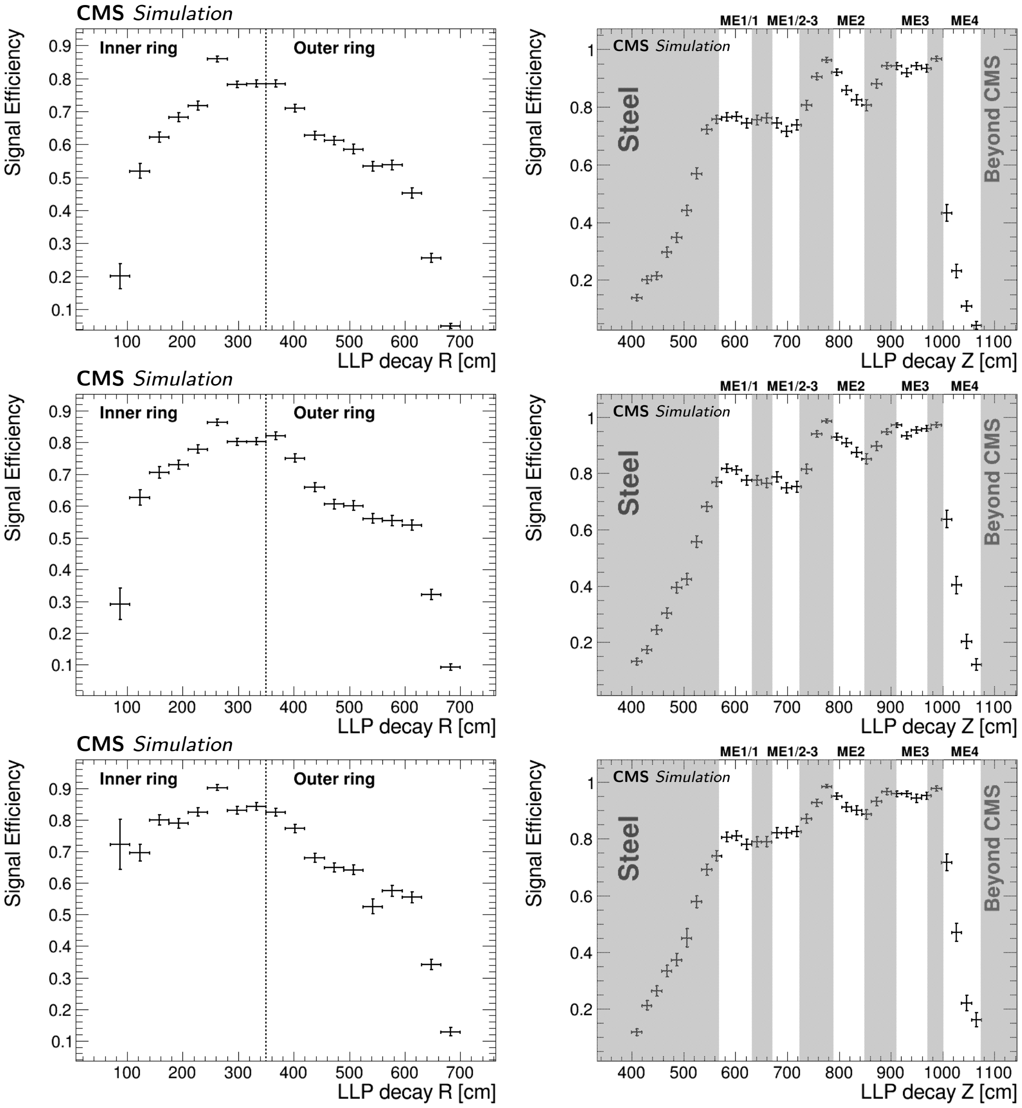

Figure 5.4: The clustering efficiency as a function of the radial direction (left) and Z direction (right) is shown for LLP decays into 2b with LLP masses of 15 (top), 40 (middle), and 55 GeV (bottom). The clustering efficiency is defined as the fraction of LLPs decaying inside the CSC acceptance and produce a successfully reconstructed MDS.

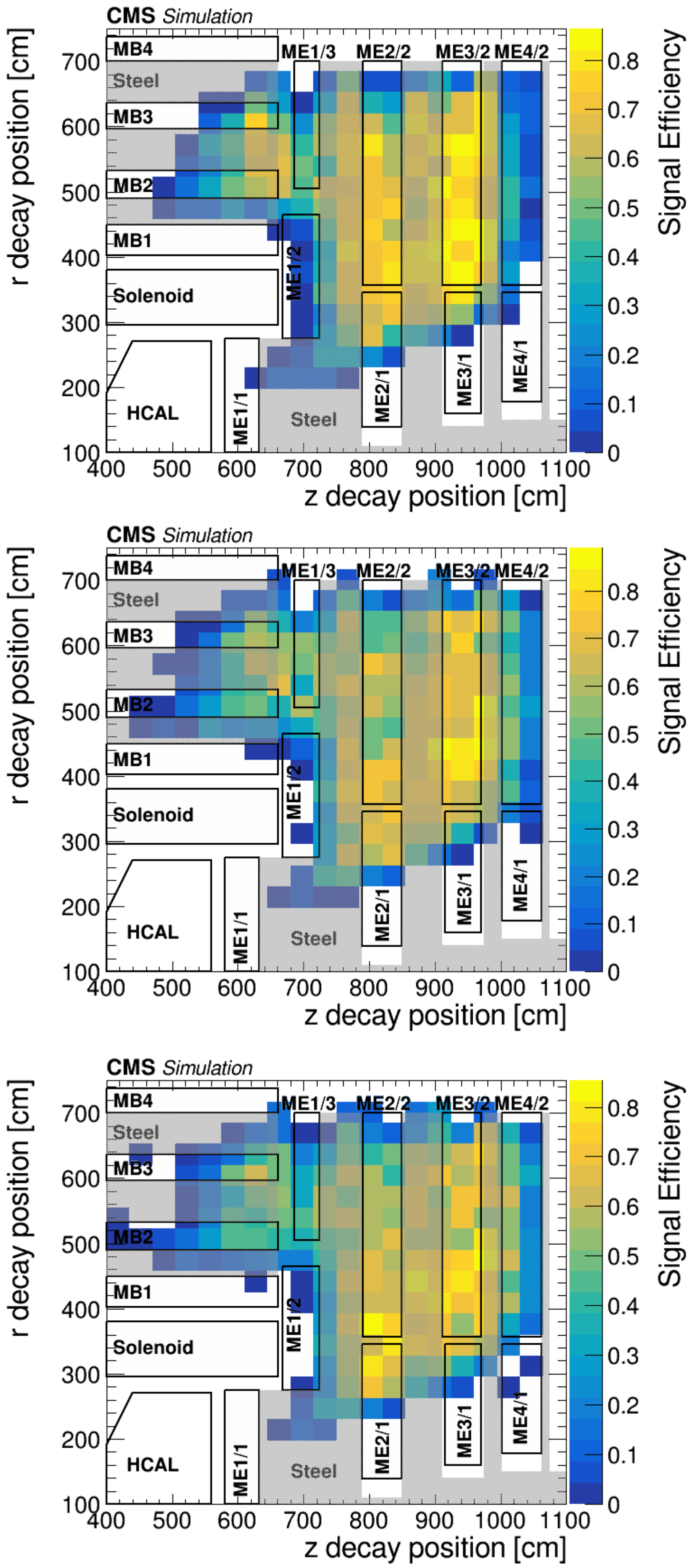

Figure 5.5: The signal efficiency with respect to the LLP decay position in the radial direction and the Z direction is shown. Signal samples where the LLP decays into 2b with LLP masses of 15(top), 40 (middle), and 55 GeV (bottom) are shown.

5.3.2 Jets

The jets used are reconstructed with the anti-k_T algorithm (described in Ch. 4.4) with a distance parameter of 0.4, forming so-called AK4 jet. Additionally, to reduce pileup, the Charge Hadron Substracted (CHS) algorithm is used to remove charged particles not originating from the primary vertex during the jet clustering [105]. Jets are used to veto clusters in the CSC, if their centroid is within $\Delta\mathrm{R} < 0.4$ of a jet with $p_\mathrm{T} > 10\,\mathrm{GeV}$ and $|\eta| < 2.4$. This veto is used to reduce background clusters from punch-through jets, which are jets that are energetic enough to not be fully contained in the calorimeters and therefore can produce hits in the muon detector chambers.

Events are also required to have at least one jet with $p_\mathrm{T} > 50\,\mathrm{GeV}$, passing a lepton veto ID and to fulfill $\Delta\mathrm{R} > 0.4$ to the MDS cluster. This is due to the high $p_\mathrm{T}^\mathrm{miss}$ requirement implying that a high p_T ISR jet is present in the event that is recoiling against the Higgs boson.

5.3.3 Muons

Muon objects are used to veto clusters originating from bremsstrahlung. Muon objects with $p_\mathrm{T} > 20\,\mathrm{GeV}$ and $|\eta| < 2.4$ are used to veto MDS clusters that are within a $\Delta\mathrm{R} < 0.4$ cone of the muon. No ID requirements are applied to these muon objects and therefore the muon does not have to be a global reconstructed muon (formed with both tracker and muon chamber tracks), but can be based on tracker or muon chamber tracks only.

Additionally events with isolated muons with $p_\mathrm{T} > 20\,\mathrm{GeV}$, $|\eta| < 2.4$, a loose muon ID criteria, a relative isolation of less than 0.25 and a 3D impact parameter significance of less than 4 are vetoed to suppress the $\mathrm{W} \to l\nu$ background.

5.3.4 Electrons

Electrons are reconstructed with the Gaussian Sum Filter algorithm [106] and events containing isolated electrons with $p_\mathrm{T} > 35\,\mathrm{GeV}$, $|\eta| < 2.4$ and passing the loose electron ID criteria are vetoed to suppress the $\mathrm{W} \to l\nu$ background.

5.3.5 Missing Transverse Momentum

The $p_\mathrm{T}^\mathrm{miss}$ used in this analysis is corrected to reduce known simulation biases. It is observed that the $p_\mathrm{T}^\mathrm{miss}$ distribution is dependent on ϕ, even though due to the rotational symmetry around the beam axis, $p_\mathrm{T}^\mathrm{miss}$ should be independent of ϕ. Possible reasons for this ϕ dependence are the displacement of the beamspot, detector misalignment, inactive calorimeter cells or anisotropic detector responses [107]. To correct this effect, the origin of the coordinate system in the transverse momentum plane is shifted, which changes the signal and background yield by a small amount (1 %). For the 2017 data taking period the $p_\mathrm{T}^\mathrm{miss}$ is affected by an issue with noisy towers in the EE calorimter. To resolve this issue, jets with $2.65 < |\eta| < 3.139$ and $p_\mathrm{T} < 50$ GeV are ignored in the $p_\mathrm{T}^\mathrm{miss}$ calculation for the 2017 data taking period in data and also in the simulated samples. Lastly, the so called MET filters, which are designed to identify “fake” $p_\mathrm{T}^\mathrm{miss}$ from detector noise, cosmic rays or beam-halo particles, are applied to both the simulated and recorded data samples. The signal efficiency for these filter is above 98 % for all signal models

5.4 Event Selection

This section details the event and cluster selections applied to separate the signal process from the background processes. A summary of the signal efficiencies of all event and cluster selection is given at the end of the section, in Tab. 5.3. An overview over all selections applied is given in Tab. 5.2. As described before, the sample used for the recorded data already requires $p_{\mathrm{T}}^{\mathrm{miss}}$ >200 GeV, which therefore is also required for the analysis. Ideally, since the thresholds of the trigger paths are much lower, reducing this cut could have improved the sensitivity of the analysis. The analysis chooses to veto any events with electrons and muons, as described in Ch. 5.3.4 and Ch. 5.3.3. The signal efficiency for this lepton veto is above 99 % for all signal models. The p_{T} and $|\eta|$ thresholds of the lepton cuts is chosen to ensure that this analysis is orthogonal with an anticipated later analysis that uses leptonic final states.

The large amount of $p_{\mathrm{T}}^{\mathrm{miss}}$ expected in the signal process requires a high p_{T} ISR jet recoiling against the Higgs boson, therefore at least one jet with $p_{\mathrm{T}} > 50\,\mathrm{GeV}$ and $|\eta| < 2.4$ is required. The signal efficiency for this jet requirement is between $94 - 98\,\%$, depending on the mass and lifetime of the signal model.

5.4.1 Cluster Selections

To veto background processes with signal-like clusters, the considered clusters are further selected. The background processes consist of jets that punch-through the shielding or muons undergoing bremsstrahlung. A possible process for both cases, that also fulfills the $p_{\mathrm{T}}^{\mathrm{miss}}$ requirement, is the decay of a highly boosted W boson, with either a leptonic decay of the W boson for the muon bremsstrahlung or a hadronic decay for the jet punch-through. Due to this process so closely resembling the signal process, aggressive vetoes are needed for the background estimation method (See Ch. 5.5) to work correctly. These selections will be discussed in the following. The

Table 5.2: Summary of event selection described in Ch. 5.4 .

Object	Selection
Jet	p_{T} >50 GeV
$p_{\mathrm{T}}^{\mathrm{miss}}$	$p_{\mathrm{T}}^{\mathrm{miss}} > 200$ GeV & $p_{\mathrm{T}}^{\mathrm{miss}}$ filters
Lepton	$N_{\mathrm{Lepton}} = 0$
CSC cluster	$N_{\mathrm{CSC+DT\ rings}} \leq 10$
CSC cluster	$N_{\mathrm{cluster}} \geq 1$ & $N_{\mathrm{RecHits}} > 50$
CSC cluster	No muons with p_{T} >20 GeV,$|\eta| < 2.4$ within $\Delta R(\mathrm{cls}, \mu) < 0.4$
CSC cluster	No jets with p_{T} >10 GeV,$|\eta| < 2.4$ within $\Delta R(\mathrm{cls}, \mathrm{jet}) < 0.4$
CSC cluster	$-5\,\mathrm{ns} < t_{\mathrm{cluster}} < 12.5\,\mathrm{ns}$
CSC cluster	No ME-1/1 or ME-1/2 hits matched within $\Delta R < 0.4$
CSC cluster	No RE1/2 RecHits matched within $\Delta R < 0.4$
CSC cluster	No MB1 segments or RB1 RecHits matched within $\Delta R < 0.4$
CSC cluster	$|\eta| < 2.0$
CSC cluster	$t_{\mathrm{spread}} < 20\,\mathrm{ns}$
CSC cluster	Cut-based ID

Table 5.3: Signal Efficiency (in %) of each selection for LLP mass 15 GeV with different lifetimes, decaying to 2 b quarks. The cumulative efficiency is calculated with respect to the acceptance, $p_{\mathrm{T}}^{\mathrm{miss}}$ and trigger selections.

	$c\tau = 0.1$m		$c\tau = 1$m		$c\tau = 10$m		$c\tau = 100$m	
Selection	cut eff	cumulative eff	cut eff	cumulative eff	cut eff	cumulative eff	cut eff	cumulative eff
Acceptance	2.68	2.68	27.54	27.54	9.00	9.00	1.08	1.08
Trigger and MET cut	2.54	0.07	0.84	0.23	0.92	0.08	1.00	0.01
MET filters	97.13	97.13	98.28	98.28	99.31	99.31	99.26	99.26
$N_{\mathrm{lepton}} = 0$	99.45	96.59	99.54	97.82	99.69	99.00	99.91	99.16
$N_{\mathrm{jet}} \geq 1$	96.37	93.09	94.84	92.77	95.02	94.07	94.31	93.52
$N_{\mathrm{CSC+DT\ rings}} \leq 10$	100.00	93.09	100.00	92.77	100.00	94.07	100.00	93.52
$N_{\mathrm{cluster}} \geq 1$	81.83	76.17	63.04	58.48	52.56	49.44	51.69	48.34
muon veto	92.66	70.58	93.56	54.71	94.22	46.58	95.52	46.17
jet veto	85.88	60.62	87.41	47.82	86.58	40.33	88.03	40.65
Time cut	99.79	60.49	99.76	47.71	97.78	39.44	95.85	38.96
ME1/1 veto	75.36	45.58	86.03	41.04	88.55	34.92	88.41	34.44
ME1/2 veto	62.91	28.68	72.18	29.63	73.41	25.64	72.29	24.90
RE1/2 veto	98.06	28.12	97.80	28.98	97.66	25.04	98.84	24.61
MB1 veto	95.36	26.81	95.67	27.72	96.61	24.19	98.37	24.21
RB1 veto	97.55	26.16	97.31	26.98	96.68	23.38	96.93	23.47
η cut	76.36	19.97	87.87	23.70	90.28	21.11	87.28	20.48
time spread cut	98.98	19.77	98.81	23.42	99.02	20.90	98.68	20.21
cut-based ID	84.46	16.70	91.87	21.52	89.94	18.80	91.86	18.57
$\Delta\phi$(cluster,$p_{\mathrm{T}}^{\mathrm{miss}}$)	100.00	16.70	88.59	19.06	68.70	12.92	68.54	12.72
N_{rechit} cut	93.06	15.54	81.99	15.63	79.46	10.26	71.09	9.05

signal efficiencies of these cuts for a 15 GeV signal sample is shown in Tab. 5.3, while for masses of 40 and 55 GeV the tables can be found in the appendix (Tab. A.1 and Tab. A.2).

To suppress clusters from out of time pileup, the clusters are required to be in time by applying a cut in the cluster time t_{cluster}, described in Ch. 4.6. The signal region is defined to be the region of t_{cluster} between -5 and 12.5 ns. Additionally the time spread of all RecHits is defined as

$$t_{\mathrm{spread}} = \sqrt{\frac{\sum (t_i - \bar{t})^2}{N}}, \tag{5.3}$$

where t_i is the time of the i-th RecHit, $\bar{t}$ is the mean time of all RecHits in the cluster and N is the number of RecHits in the cluster. This time spread is required to be less then 20 ns to further veto out-of-time pileup.

In addition clusters that are geometrically matched to jets or muons are vetoed. A cluster is vetoed, if it is matched within $\Delta R < 0.4$ to any jet with $p_{\mathrm{T}} > 10$ GeV and $|\eta| < 2.4$. Similarly a cluster is vetoed if it is matched within $\Delta R < 0.4$ to any muon with $p_{\mathrm{T}} > 20$ GeV and $|\eta| < 2.4$. No muon ID requirement is applied for this veto, therefore the muon does not have to be a globally reconstructed muon, meaning that a tracker or muon system only track that results in a muon candidate is also considered for this veto. The specific veto thresholds are derived by studying background clusters in a $\mathrm{W} \rightarrow l\nu$ simulated sample and signal clusters in a simulated signal sample. For this study the clusters are required to pass the event-level selections and to be in-time. Additionally the signal clusters are required to be matched to a LLP decaying inside the CSC detector volume. The p_{T} distribution for matched jets and muons in these samples is shown in Fig. 5.6. The background shape of the jet p_{T} plot has a peak at

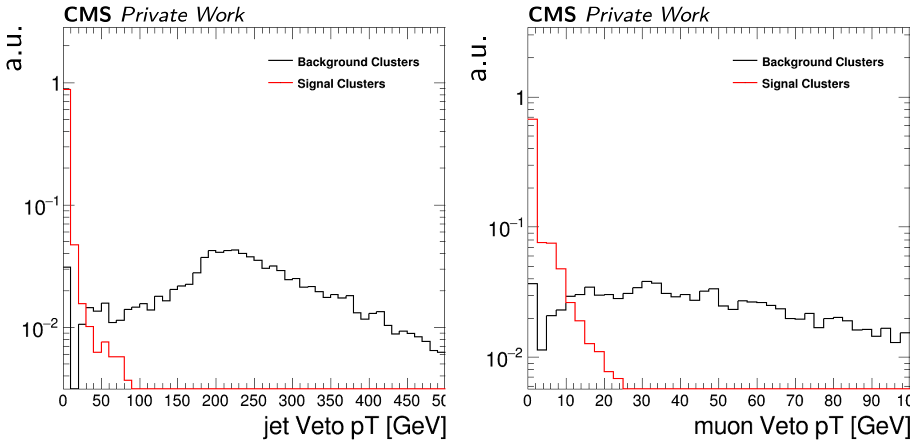

Figure 5.6: The distribution of p_T of jets (left) and muons (right) matched to signal and background clusters. Signal consists of signal models of all available mass/$c\tau$ points and background are clusters from $\mathrm{W} \rightarrow l\nu$.

around 200 GeV because the background clusters are produced by punch-through of the jets recoiling against the W boson that has p_{T} of around 200 GeV due to the $p_{\mathrm{T}}^{\mathrm{miss}} > 200\,\mathrm{GeV}$ requirement. Both cuts are chosen so that the signal efficiency is at 90 %, resulting in the 10 and 20 GeV selections for jets and muons respectively.

To further reduce the jet punch-through and muon bremsstrahlung, additional chamber specific vetoes are derived. The vetoed chambers are the CSC and DT stations closest to the interaction point, since these have the least amount of shielding in front of them. The CMS muon system is shown in Fig. 5.7, with the vetoed chambers being crossed-out in the plot to better visualize the vetoes discussed in the following. The vetoes are derived and optimized in two background-enriched control regions: An in-time region, where $N_{\mathrm{rechit}} < 80$ is applied to be far enough away from the signal region of $N_{\mathrm{rechit}} > 130$, and an early out of time region with $t_{\mathrm{cluster}} < -12.5\,\mathrm{ns}$.

Clusters that have any RecHit in the CSC station ME1/1 or ME1/2 are vetoed, since these stations have the least amount of shielding, being situated closest to the interaction point. The distribution of the number of RecHits in ME1/1 and ME1/2 is shown in Fig. 5.8. For this test the jet and muon vetoes are already applied. It can be seen, that the distributions from both background enriched control regions agree well and show a clear difference compared to the signal processes. Vetoing all clusters with hits in these chambers leads to a signal efficiency of about 60 % and a background efficiency of 5%, leading to an improved signal-to-background ratio. In addition, any cluster that matches hits within $\Delta R < 0.4$ in the RPC in RE1/2, which is the RPC station right behind ME1/2, are also vetoed. Clusters are also vetoed, if they match a DT segment within $\Delta R < 0.4$ in the MB1 station or if the clusters match any RPC hit within $\Delta R < 0.4$ in the RB1. These vetos suppress muon bremsstrahlung backgrounds going through the DT system first before showering in the CSC system. The distribution of hits matched to a cluster in RE1/2, RB1 and the number of matched DT segments in MB1 is shown in Fig. 5.9. For these plots the previously mentioned ME1/1 and ME1/2 vetoes are already applied in addition to the jet and muon veto.

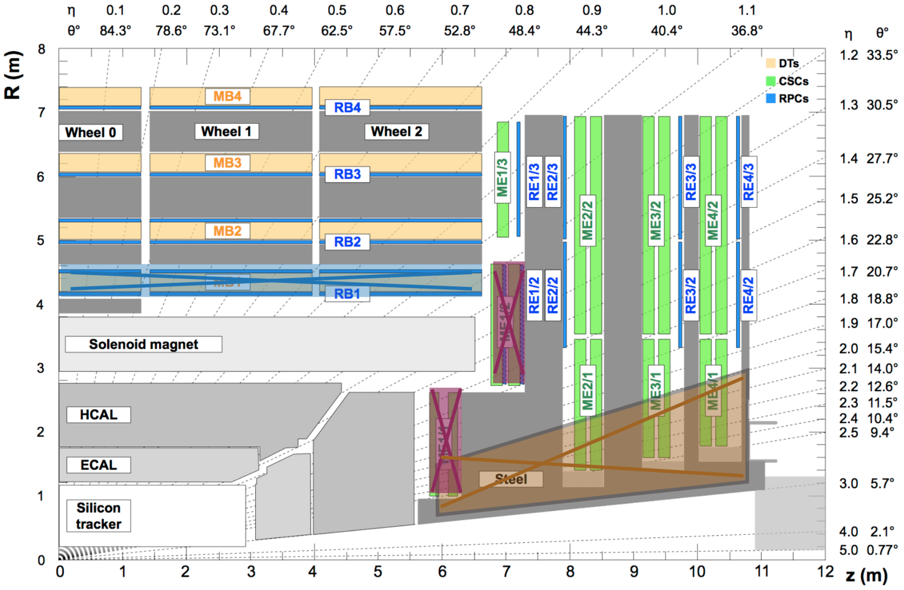

Figure 5.7: The detector geometry of the CMS muon system is shown. Clusters that are matched to RecHits in the regions marked with red (ME11 and ME12 veto) and blue (MB1 veto) are being vetoed, while clusters that fall in the orange region ($\eta < 2.0$) are also vetoed. Figure is based on Ref. [67].

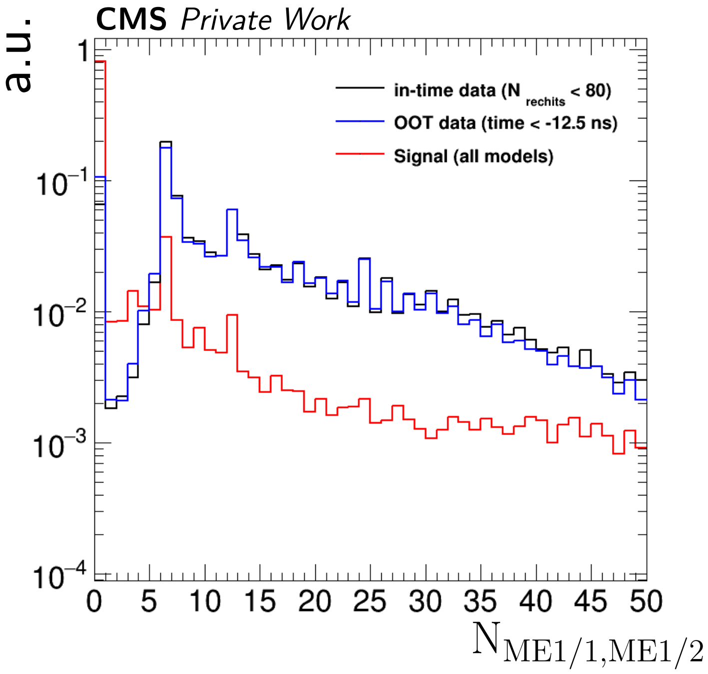

Figure 5.8: Signal and background distribution for the number of hits in the ME1/1 and ME1/2 chamber. All events have to pass the jet and muon veto. The signal is simulated, while the two background distributions are measured in the OOT and in-time control regions.

To further suppress muon bremsstrahlung, clusters at high eta ($|\eta| > 2$) are vetoed since it is found that high p_T muons in this region have a worse reconstruction

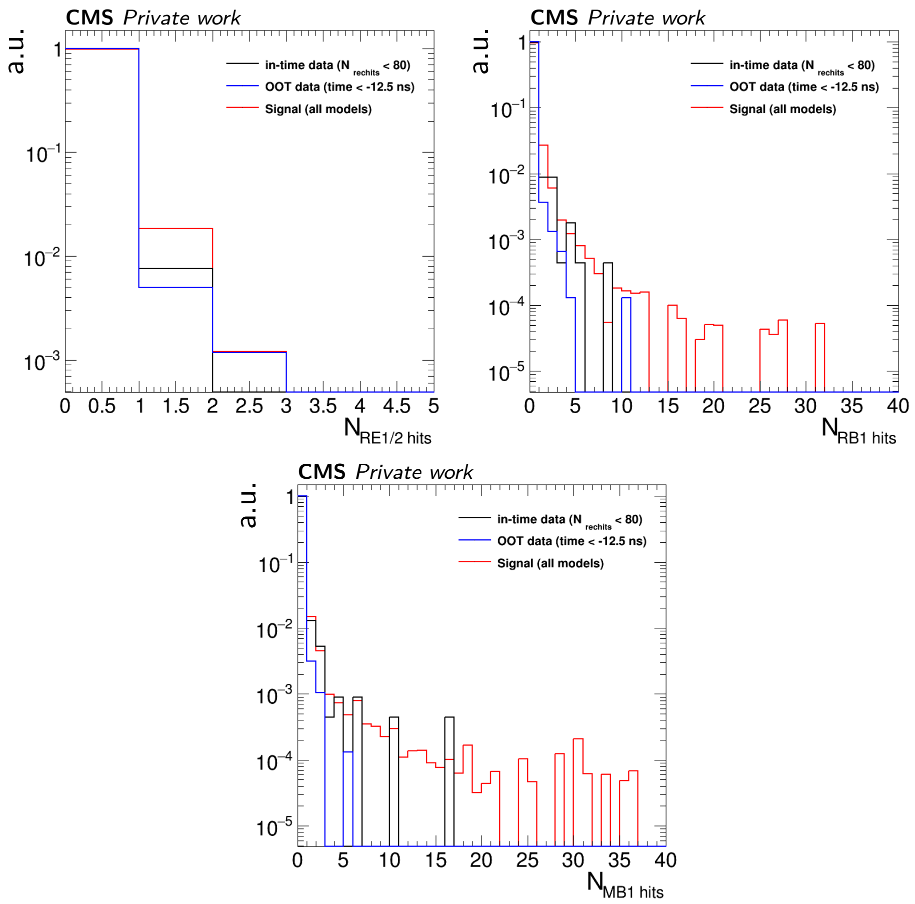

Figure 5.9: The signal and background distributions of the number of hits in RE1/2 (top left), the number of hits in RB1 (top right), and the number of segments in MB1 (bottom) are shown. Clusters are required to pass the jet and muon veto and the ME1/1 and ME1/2 vetos.

efficiencies and therefore the muon veto would fail for these background clusters. The distribution of the cluster $|\eta|$ position is shown in Fig. 5.10, illustrating the motivation for the $|\eta|$ cut.

5.4.2 Cluster ID

To further enhance the sensitivity of the analysis, a cluster identification, called cluster ID, is derived. As described in Ch. 4.6, the main variables describing the cluster are its size, the time signature and the position in the detector. The cut-based cluster ID is based on the shape and location to differentiate signal clusters from the remaining background, which mostly is in-time pileup. It is found that pileup clusters occur more often at larger values of $|\eta|$, are closer to the primary interaction point and tend to be contained in less stations compared to a signal cluster. The cluster ID consists of cuts on the cluster $|\eta|$ position, the average station number and the N_{Station} variable (see Ch. 4.6). To derive and optimize the ID cuts the early out-of-time validation clusters are used as background clusters, since these also are a result of pileup and have the same geometric features as the in-time pileup. Signal clusters are required to be matched to a LLP that decays inside the CSC system. The

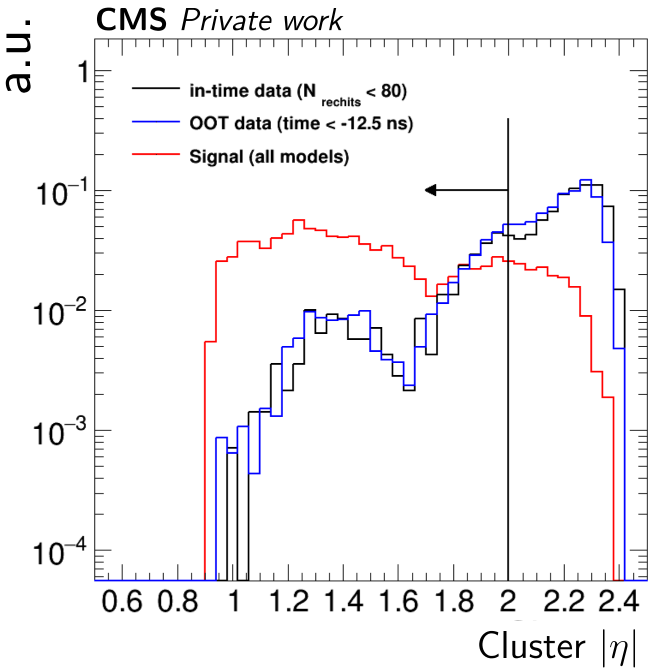

Figure 5.10: Distribution of the cluster $|\eta|$. Data in-time region is unblinded up to $N_{\text{rechit}} = 80$.

event level and cluster selections introduced before are applied. The distributions for the cluster η position, the average station number and the $N_{Station}$ variable are shown in Fig. 5.11, where additionally the in-time validation region is added to confirm the OOT cluster features. The ID is then derived by a rough optimization, where the signal efficiency within each average station is maximized, while keeping the background to a negligible level. The result is a series of progressively tighter cuts on $|\eta|$ as the number of stations and the average station decreases. The specific cuts are summarized in Tab. 5.4 and resulting in a signal efficiency of 82 %, while the number of background events is reduced by a factor of 3. Additionally a BDT-based cluster ID was studied, but no large increase in the performance could be observed compared to the cut based cluster ID, therefore the BDT-based ID is not used in this analysis.

Table 5.4: Summary of the cut-based cluster ID selection. The implicit cut for the case with NStation = 1 and Avg Station = 1 is due to the ME1/1 and ME1/2 RecHit veto.

NStation and Avg Station	$\|\eta\|$ requirement
NStation > 1	$\|\eta\| < 1.9$
NStation $= 1$ and Avg Station $= 4$	$\|\eta\| < 1.8$
NStation $= 1$ and Avg Station $= 3$	$\|\eta\| < 1.6$
NStation $= 1$ and Avg Station $= 2$	$\|\eta\| < 1.6$
NStation $= 1$ and Avg Station $= 1$	implicit $\|\eta\| < 1.1$

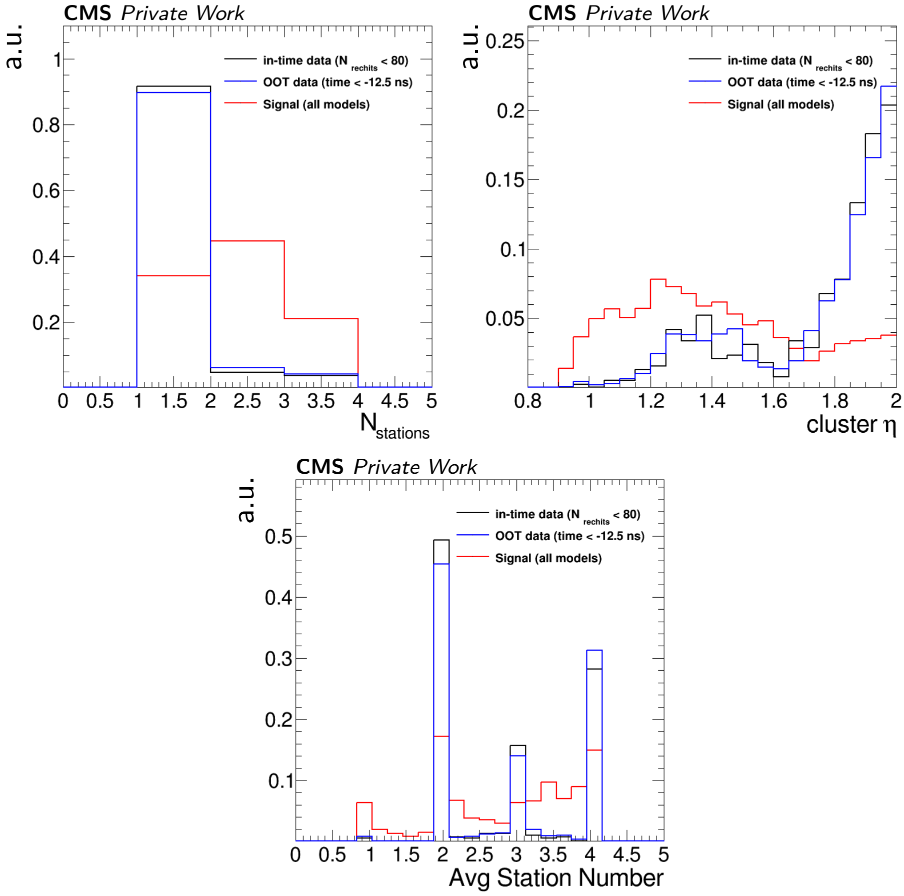

Figure 5.11: Signal and background distributions for the variables used to construct the cut-based ID. Data from the in-time and OOT regions follow a similar distribution due to both being the result of pileup background clusters.

5.4.3 Cosmic Muon Shower

Another type of background for the analysis consists of cosmic muon showers reaching the detector and creating large clusters in the CMS muon system. Fig. 5.12 shows an event display of such a shower: It can be observed, that over 10000 CSC RecHits are present in such an event distributed across the whole CMS detector volume. To veto this type of event a new variable called CSC and DT ring is introduced: Because of the circular symmetry in the detector, each CSC/DT station ($\mathrm{ME}\pm1/1$, $\mathrm{ME}\pm1/2$ and so on) is actually a ring in the r-ϕ-plane. These rings then can be used to construct a new veto by counting the number of rings with at least 50 RecHits. Comparing the signal events to an early OOT cluster sample, where additionally more than 2000 early ($< -25\,\mathrm{ns}$) CSC RecHits are required, it can be seen that the signal is concentrated in a few rings while a cosmic muon shower shows a large number of DT and CSC rings, as shown in Fig. 5.13. Therefore events with more then 10 CSC or DT rings with more then 50 RecHits are vetoed. This requirement has close to 100 % signal efficiency. The signal efficiency is validated in data in a muon bremsstrahlung control region, confirming the efficiency of the veto is close to 100 %.

Lastly it should be noted that cosmic muons can also undergo a rare bremsstrahlung process that produces a cluster passing the signal cluster selections. An event with such a cluster could pass the event selection, if there is enough $p_{\mathrm{T}}^{\mathrm{miss}}$ in the event to pass the $p_{\mathrm{T}}^{\mathrm{miss}}$ cut of 200 GeV, which either requires the cosmic muon to be close to parallel to the beamline in order to traverse the calorimeter in addition to the CSC detector or that the cosmic muon undergoes an additional bremsstrahlung process to produce sufficient energy deposits in the calorimeter. Both cases are incredibly rare, and therefore a cosmic muon producing a cluster would most likely be uncorrelated to the $p_{\mathrm{T}}^{\mathrm{miss}}$ from the collision process.

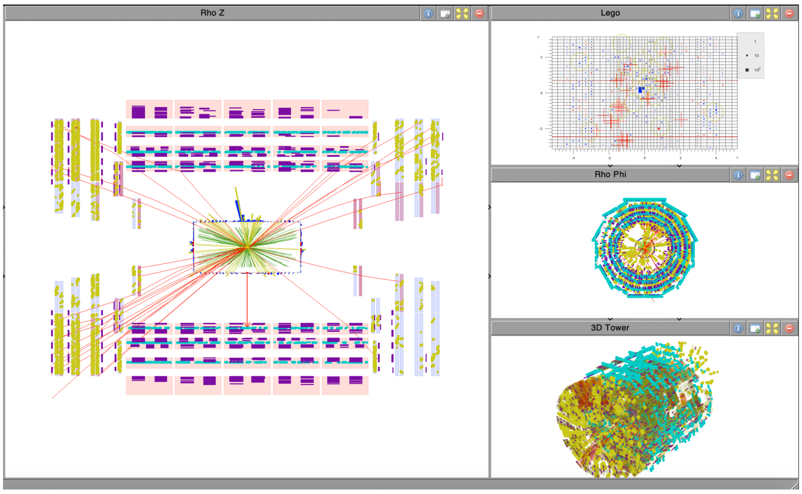

Figure 5.12: Event display of a cosmic muon shower event that creates showers with a large number of CSC, DT, and RPC RecHits. The red lines in the left figure are reconstructed muons. The yellow dots are CSC RecHits; purple lines are RPC RecHits; Cyan lines are DT RecHits.

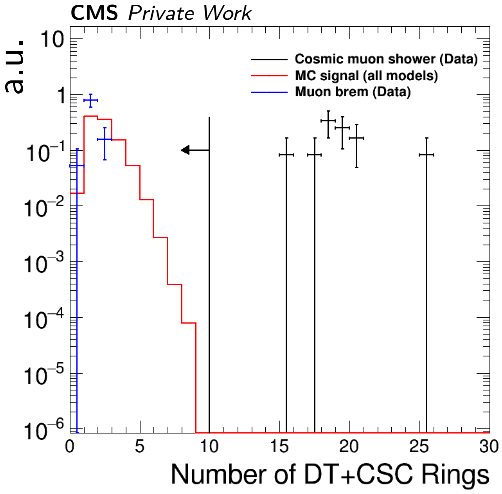

Figure 5.13: The number of DT and CSC rings with at least 50 RecHits is shown for a cosmic muon shower control sample, the signal simulation sample, and a muon bremsstrahlung control sample.

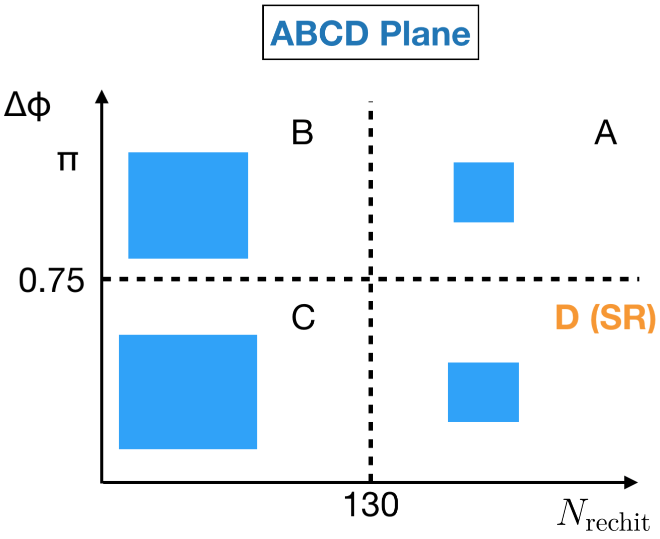

Figure 5.14: The diagram of the ABCD plane is shown.

5.5 Background Estimation

This section describes the data-driven background estimation used in this analysis. After applying the cluster and event level selections the dominant background are clusters produced by in-time pileup. Pileup can produce a signal-like signature via SM particles like K_L or neutrons. The background is estimated using the data driven ABCD method, with the cluster size N_{rechit} as one, and the distance in ϕ between the $p_{\text{T}}^{\text{miss}}$ and the cluster, $\Delta\phi(\text{cluster},p_{\text{T}}^{\text{miss}})$, as the other independent variable required for this method. The background estimation targets pileup clusters, but the ABCD method is not limited to estimating pileup clusters, but rather any event, where both ABCD variables are uncorrelated, r.g. a cosmic muon resulting in a cluster.

The ABCD plane is spanned by the two variables and is shown in Fig. 6.15. It is divided in four bins A,B,C and D where bin D is the bin with the most signal. Since the two variables are uncorrelated, the estimation of the number of events in each bin is expressed as follows:

$$\begin{aligned}
N_A &= B_A + \mu \cdot S_A \\
N_B &= B_B + \mu \cdot S_B \\
N_C &= B_C + \mu \cdot S_C \\
N_D &= B_A \cdot B_C / B_B + \mu \cdot S_D,
\end{aligned}$$

where:

- B_A, B_B, B_C, B_D are number of background events in each bin;
- S_A, S_B, S_C, S_D are number of signal events in each bin, taken from simulation;
- μ is the signal strength (i.e. the parameter of interest).

The four unknown variables (B_A,B_B,B_C,μ) are extracted from a maximum likelihood fit with the following likelihood expression:

$$L = \prod_{i}^{\text{ABCD}} \text{Pois}(\text{obs}_i | N_i) \times \prod_{i}^{\text{nuisances}} \text{Constraints}(\sigma_j | \hat{\sigma}_j), \tag{5.4}$$

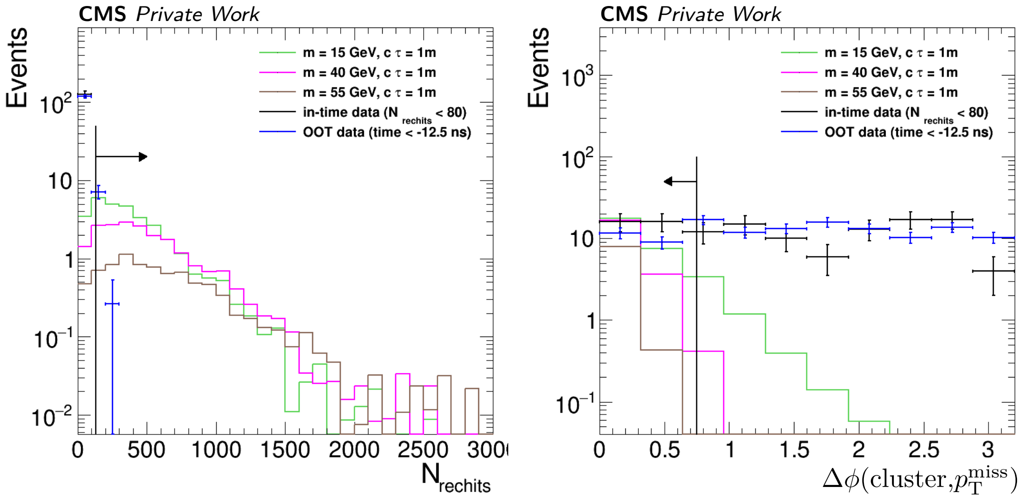

Figure 5.15: The distribution of N_{rechit} (left) and $\Delta\phi(\text{cluster},p_{\mathrm{T}}^{\text{miss}})$ (right) for signal and background estimated with the ABCD method in the two control regions (See Ch. 5.5.2). The branching ratio for signal is set to 1% and the data in-time control region is unblinded up to $N_{rechits} = 80$. The data OOT region has the same event and cluster selection as the in-time region, while the overall normalization in the OOT-region is scaled to the number of events in the in-time region.

where obs_i is the number of observed events in each bin and σ_j are nuisance parameters. All the nuisance parameters are implemented with a log-normal distribution, such that the logarithm of the distribution is a Gaussian constraint. The number of background events in bin ABC(B_A,B_B,B_C) are treated as unconstrained nuisance parameters in the fit.

Exclusion limits on the production cross section are evaluated using the modified frequentist approach [108–110], with the binned profile likelihood ratio as the test statistic. The exclusion limits are calculated with the asymptotic limit method implemented in the HiggsCombine tool [110] and are evaluated with the asymptotic formulae [111].

The distribution of $\Delta\phi(\text{cluster},p_{\mathrm{T}}^{\text{miss}})$ is expected to peak at zero for the signal process, since the cluster and the $p_{\mathrm{T}}^{\text{miss}}$ are aligned, due to the cluster being produced by the decay of the LLP in the CSC and the $p_{\mathrm{T}}^{\text{miss}}$ is a result of the LLP being undetected in the tracker and calorimeter and therefore is not considered in the $p_{\mathrm{T}}^{\text{miss}}$ calculation. For background this variable is expected to be uniformly distributed, since the cluster is resulting from pileup, which is uncorrelated to the $p_{\mathrm{T}}^{\text{miss}}$ from the primary interaction. The N_{rechit} variable is the main discriminant of the analysis and signal clusters are expected to have larger values of N_{rechit}.

The distributions for N_{rechit} and $\Delta\phi(\text{cluster},p_{\mathrm{T}}^{\text{miss}})$ for signal simulation and background derived from data is shown in Fig. 5.15.

5.5.1 Signal Region Optimization

The ABCD threshold for $\Delta\phi(\text{cluster},p_{\mathrm{T}}^{\text{miss}})$ is chosen to have 90 % signal efficiency, which leads to a cut of $\Delta\phi(\text{cluster},p_{\mathrm{T}}^{\text{miss}}) < 0.75$, while the bin boundary for N_{rechit}

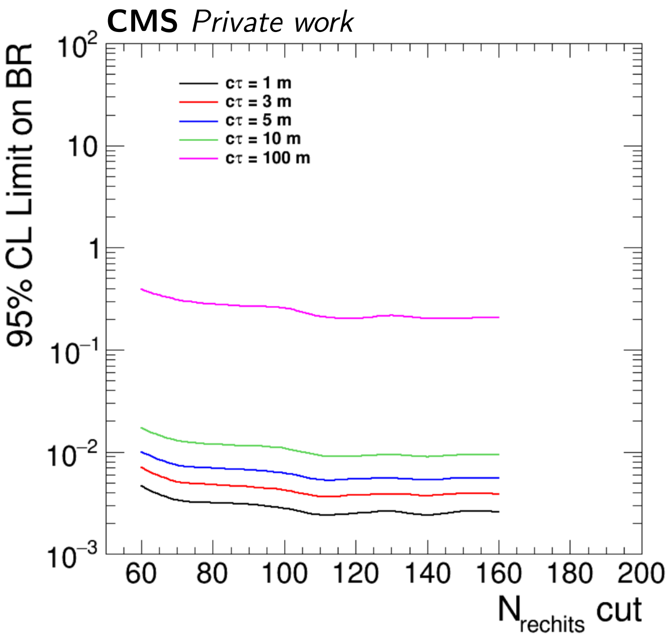

Figure 5.16: The expected limit at different N_{rechit} cuts for signal with different LLP lifetimes.

is optimized to maximize the expected limit. The number of background events in the signal-region (D) are estimated by extrapolating the background prediction from the out-of-time validation region to the signal region. This extrapolation is done in order to remain fully blinded in the signal region and to reduce the statistical uncertainty of the background yield predictions, since the signal region ABCD is expected to have large statistical fluctuations due to the limited sample size for the in-time control region. The extrapolation is done with the following equation:

$$N_{\text{intimepass}} = \frac{N_{\text{OOTpass}} \times N_{\text{intimefail}}}{N_{\text{OOTfail}}}, \tag{5.5}$$

where $N_{\text{intimepass}}$ is the number of background events estimated for the signal region, $N_{\text{intimefail}}$ is the number of background events in the in-time region failing the cluster ID, N_{OOTpass} and N_{OOTfail} are the number of background events in the OOT region passing and failing the cluster ID, respectively. The expected limit is then calculated for different N_{rechit} thresholds and the results are shown in Fig. 5.16 for different LLP lifetimes. The expected limit improves as the N_{rechit} cut increases up to around 130, beyond the limit does not improve significantly. Therefore the N_{rechit} cut for the ABCD plane is chosen at 130.

5.5.2 Closure Tests

The background estimation is validated in two separate validation regions, the in-time validation region and the early out-of-time (OOT) region.

The in-time validation region is defined by inverting the cluster ID in the event selection, thereby suppressing the signal and forming a background-only validation region. The background composition is expected to be similar to the signal region, being mostly pileup clusters but also a small amount of muon bremsstrahlung.

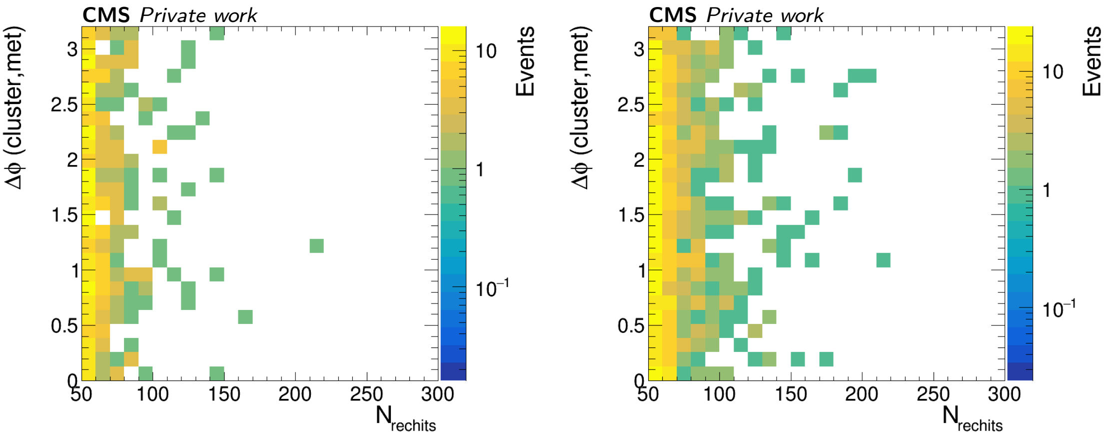

Figure 5.17: The distribution of $\Delta\phi(\text{cluster},p_{\mathrm{T}}^{\text{miss}})$ and N_{rechit} for clusters that pass (left) and fail (right) cluster ID in the early OOT validation region.

The OOT validation region selects clusters purely from out-of-time pileup interactions and is defined by selecting cluster with $t_{\text{cluster}} < -12.5\,\text{ns}$. This region allows a validation of the background estimation for pileup clusters that pass the cluster ID.

OOT Validation Region

The early OOT validation region is defined by applying the signal selections, expect for the cut-based ID and by modifying the t_{cluster} cut to select OOT clusters. The cluster ID is not applied in this region to allow a validation of the OOT region independently for clusters that pass and fail the cluster ID. The positive time windows is excluded, since slow LLPs could create delayed shower with a large positive time signature.

To confirm that the two ABCD variables are uncorrelated, the Pearson correlation coefficient between N_{rechit} and $\Delta\phi(\text{cluster},p_{\mathrm{T}}^{\text{miss}})$ is calculated in this region and is found to be 0.02, indicating that the two variables are indeed uncorrelated in this region. As described before, the OOT validation region is split in two regions, depending on whether the cluster passes or fails the cluster ID. The distributions of $\Delta\phi(\text{cluster},p_{\mathrm{T}}^{\text{miss}})$ and N_{rechit} are shown in Fig. 5.17 for clusters that pass and fail the cluster ID. Table 5.5 shows the ABCD prediction and observation in this validation region. Good closure is observed, showing agreement within the statistical uncertainty. In Tables 5.5 to 5.9 scans for different N_{rechit} and $\Delta\phi(\text{cluster},p_{\mathrm{T}}^{\text{miss}})$ thresholds are shown. The observed yields in bin D and the prediction agree in most cases and show no significant trends as the N_{rechit} and $\Delta\phi(\text{cluster},p_{\mathrm{T}}^{\text{miss}})$ thresholds are varied. For the chosen thresholds of N_{rechit} and $\Delta\phi(\text{cluster},p_{\mathrm{T}}^{\text{miss}})$ the observed and predicted yields agree well.

Table 5.5: Validation of the ABCD method in the OOT validation region at the nominal cut values of $N_{\text{rechit}} > 130$ and $\Delta\phi(\text{cluster},p_{\text{T}}^{\text{miss}}) < 0.75$. The uncertainty of the prediction is the statistical uncertainty propagated from bin A, B, and C.

Cluster ID	A	B	C	D	Prediction ($\frac{A\times C}{B}$)
Pass Cluster ID	5	373	97	2	1.30 ± 0.60
Fail Cluster ID	26	732	222	6	7.89 ± 1.66

Table 5.6: Validation of the ABCD method in the early OOT, pass ID validation region, for different N_{rechit} cuts with $\Delta\phi(\text{cluster},p_{\text{T}}^{\text{miss}}) < 0.75$. The uncertainty of the prediction is the statistical uncertainty propagated from bin A, B, and C.

N_{rechit}	A	B	C	D	Prediction ($\frac{A\times C}{B}$)
100	25	353	96	3	6.80 ± 1.57
110	14	364	96	3	3.69 ± 1.07
120	10	368	96	3	2.61 ± 0.88
130	5	373	97	2	1.30 ± 0.60
140	4	374	97	2	1.04 ± 0.53
150	1	377	98	1	0.26 ± 0.26
160	1	377	98	1	0.26 ± 0.26

Table 5.7: Validation of the ABCD method in the early OOT, fail ID validation region, for different N_{rechit} cuts with $\Delta\phi(\text{cluster},p_{\text{T}}^{\text{miss}}) < 0.75$. The uncertainty of the prediction is the statistical uncertainty propagated from bin A, B, and C.

N_{rechit}	A	B	C	D	Prediction ($\frac{A\times C}{B}$)
100	72	686	208	20	21.83 ± 3.10
110	46	712	215	13	13.89 ± 2.32
120	36	722	218	10	10.87 ± 2.00
130	26	732	222	6	7.89 ± 1.66
140	19	739	226	2	5.81 ± 1.40
150	14	744	226	2	4.25 ± 1.18
160	12	746	227	1	3.65 ± 1.09

Table 5.8: Validation of the ABCD method in the OOT, pass ID validation region, for different $\Delta\phi(\text{cluster},p_{\mathrm{T}}^{\mathrm{miss}})$ cuts with $N_{\mathrm{rechit}} > 130$. The uncertainty of the prediction is the statistical uncertainty propagated from bin A, B, and C.

$\Delta\phi(\text{cluster},p_{\mathrm{T}}^{\mathrm{miss}})$	A	B	C	D	Prediction ($\frac{A\times C}{B}$)
0.60	5	397	73	2	0.92 ± 0.43
0.65	5	392	78	2	0.99 ± 0.46
0.70	5	379	91	2	1.2 ± 0.55
0.75	5	373	97	2	1.3 ± 0.6
0.80	5	365	105	2	1.44± 0.66
0.85	5	354	116	2	1.64± 0.75
0.90	5	343	127	2	1.85 ±0.85

Table 5.9: Validation of the ABCD method in early OOT, fail ID validation region, for different $\Delta\phi(\text{cluster},p_{\mathrm{T}}^{\mathrm{miss}})$ cuts with $N_{\mathrm{rechit}} > 130$. The uncertainty of the prediction is the statistical uncertainty propagated from bin A, B, and C.

$\Delta\phi(\text{cluster},p_{\mathrm{T}}^{\mathrm{miss}})$	A	B	C	D	Prediction ($\frac{A\times C}{B}$)
0.60	26	783	171	6	5.68 ± 1.21
0.65	26	768	186	6	6.3 ±1.34
0.70	26	752	202	6	6.98 ± 1.48
0.75	26	732	222	6	7.89 ± 1.66
0.80	25	715	239	7	8.36 ± 1.78
0.85	25	696	258	7	9.27 ± 1.97
0.90	25	685	269	7	9.82 ± 2.09

In-time Validation Region

The in-time validation region is defined by applying the signal selections, expect for inverting the cut-based ID. The background composition in this validation region resembles the signal region more closely compared to the OOT region, since this region is not only targeting pileup. The Pearson coefficient between $\Delta\phi(\text{cluster},p_{\text{T}}^{\text{miss}})$ and N_{rechit} is 0.04, again indicating that the two variables are independent. The distribution of $\Delta\phi(\text{cluster},p_{\text{T}}^{\text{miss}})$ and N_{rechit} are shown in Fig. 5.18, while Tab. 5.10 compares the observed and predicted yields in bin D, showing a good agreement.

Similar to the OOT region, the $\Delta\phi(\text{cluster},p_{\text{T}}^{\text{miss}})$ and N_{rechit} thresholds are scanned and the results are shown in Tab. 5.11 to 5.12 showing good agreement in most cases and no overall trend can be observed.

5.5.3 Summary of Background Estimation

A background only fit is performed, yielding the post fit yields in the bins A, B and C shown in Tab. 5.13. The table also shows the then predicted yield in bin D, based on the yields of A, B and C.

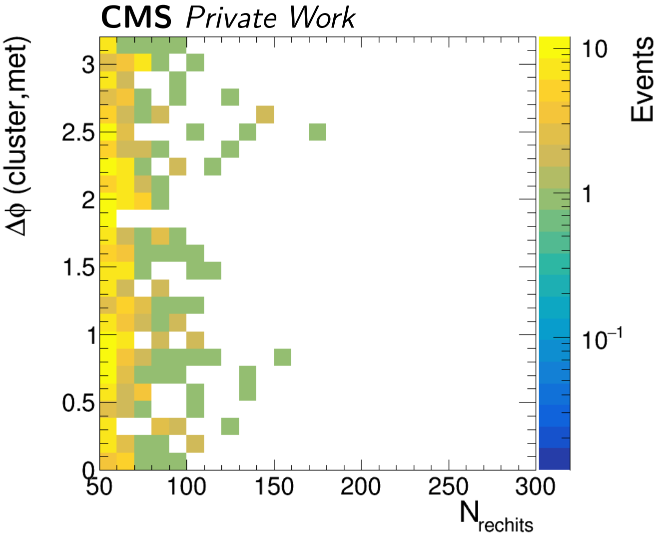

Figure 5.18: The distribution of $\Delta\phi(\text{cluster},p_{\text{T}}^{\text{miss}})$ and N_{rechit} in the in-time validation region.

Table 5.10: Validation of the ABCD method in the in-time validation region at the nominal cut values of $N_{\text{rechit}} > 130$ and $\Delta\phi(\text{cluster},p_{\text{T}}^{\text{miss}}) < 0.75$. The uncertainty of the prediction is the statistical uncertainty propagated from bin A, B, and C.

Cluster ID	A	B	C	D	Prediction $(\frac{A\times C}{B})$
Fail Cluster ID	5	269	74	2	1.38 ±0.64

Table 5.11: Validation of the ABCD method in the in-time validation region, for different N_{rechit} cuts with $\Delta\phi(\text{cluster},p_{\text{T}}^{\text{miss}}) < 0.75$. The uncertainty of the prediction is the statistical uncertainty propagated from bin A, B, and C.

N_{rechit}	A	B	C	D	Prediction ($\frac{A\times C}{B}$)
100	18	256	69	7	4.85± 1.32
110	10	264	73	3	2.77± 0.95
120	7	267	73	3	1.91 ±0.77
130	5	269	74	2	1.38 ±0.64
140	4	270	76	0	1.13 ±0.58
150	2	272	76	0	0.56 ±0.4
160	1	273	76	0	0.28 ±0.28

Table 5.12: Validation of the ABCD method in the in-time validation region, for different $\Delta\phi(\text{cluster},p_{\text{T}}^{\text{miss}})$ cuts with $N_{\text{rechit}} > 130$. The uncertainty of the prediction is the statistical uncertainty propagated from bin A, B, and C.

$\Delta\phi(\text{cluster},p_{\text{T}}^{\text{miss}})$	A	B	C	D	Prediction ($\frac{A\times C}{B}$)
0.60	6	287	56	1	1.17 ± 0.51
0.65	6	282	61	1	1.3 ± 0.56
0.70	5	275	68	2	1.24 ± 0.58
0.75	5	269	74	2	1.38 ± 0.64
0.80	5	262	81	2	1.55 ± 0.72
0.85	4	262	81	3	1.24 ± 0.64
0.90	4	244	99	3	1.62 ± 0.83

Table 5.13: Resulting background only post fit values of the yields in bin A, B and C. Additionally, the predicted yield in bin D, based on the values of bin A, B and C, is shown.

Bkg-only post fit values			Prediction
A	B	C	$D = (\frac{A\times C}{B})$
4.0 ± 1.9	95.0 ± 9.9	48.0 ± 6.6	2.0 ± 1.0

5.6 Validation of the Signal Cluster Simulation

This chapter details the studies performed to validate the accuracy of the simulation of the detector response, cluster reconstruction and cluster identification. The MDS signature is a very rare process in the SM and therefore muon bremsstrahlung MDS clusters are used as a proxy to study the signal clusters. This allows the use of a dedicated $\mathrm{Z} \to \mu\mu$ sample, where one muon emits bremsstrahlung while the second muon is used as the trigger object. This dedicated sample is also large enough to allow a dedicated study that is not limited by the rarity of this process. A tag-and-probe approach is used to select a pure sample of muons from the Z boson decay. Clusters matched to isolated muons are then compared in simulation and recorded data, studying the features of the clusters.

5.6.1 Tag-and-Probe Method

The study was performed with data recorded in the year 2017, which were the only accessible data samples with CSC RecHits available. The recorded data sample uses events, that have to pass a single muon trigger, while the simulated samples uses a $\mathrm{Z} \to \mu\mu$ sample, where the trigger requirement is also applied. Additionally the simulated $\mathrm{Z} \to \mu\mu$ sample is split into different invariant mass bins (50-120, 120-200, 200-400 and 400-800 GeV). Then a tag-and-probe method is used to select $\mathrm{Z} \to \mu\mu$ events:

Events are selected with two muons with opposite charges with $p_{\mathrm{T}} > 50$ GeV, $|\eta| < 2.4$ and an invariant mass $> 120\,\mathrm{GeV}$, where one muon passes tight ID and isolation requirements, the so-called tag muon, and the other muon passing loose ID and isolation requirements, the so-called probe muon. The probe muon then has to be matched with a cluster in this study. For simulated events the muons are required to match two generator level muons.

The simulated samples are normalized to the corresponding cross section and then a k-factor is derived for each mass bin individually, such that the yields in the simulated sample are normalized to the yields in the recorded sample. After applying these k-factors to the simulated sample the dimuon mass distribution between recorded and simulated data is compared in Fig. 5.19 , showing an overall good agreement.

5.6.2 Cluster Efficiency

Since the clusters in this sample originate from muon bremsstrahlung, the cluster efficiency probes the product of the muon bremsstrahlung probability and the cluster reconstruction efficiency. The cluster efficiency is defined as the number of events where a cluster can be matched to the probe muon divided by the number of events passing the tag-and-probe selections. Any differences that are observed between the recorded and simulated data are either due to mismodeling of the muon bremsstrahlung rate or the mismodeling of the cluster reconstruction efficiency. Since the signal clusters are not a result of muon bremsstrahlung, only the mismodeling in the cluster reconstruction efficiency is of interest. Although the mismodeling of the bremsstrahlung rate is more likely due to the need for accurate modeling of material budgets and the tuning of simulation parameters, the full difference of the cluster

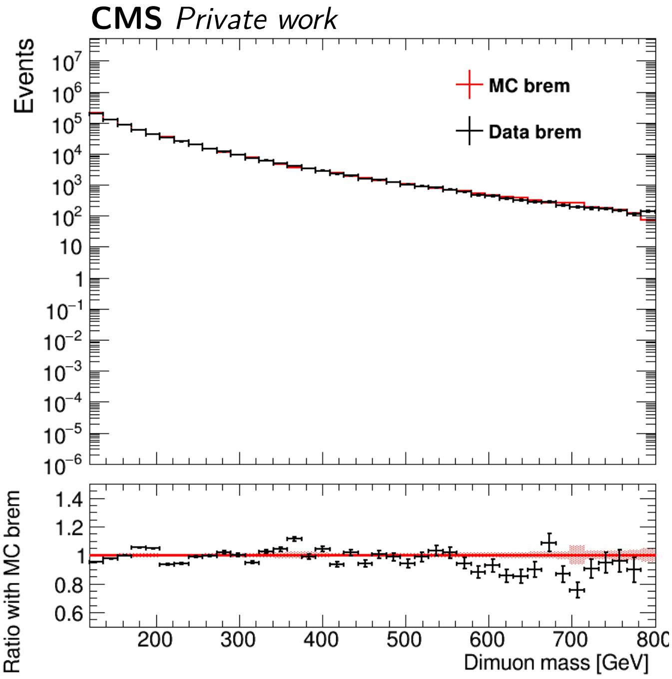

Figure 5.19: The dimuon mass distributions of recorded and simulated data for muon bremsstrahlung events that pass the tag-and-probe selections.

efficiency is propagated as a systematic uncertainty on the cluster efficiency to have a very conservative estimate of the signal prediction.

To test the cluster efficiency, the hit multiplicity response of the detector is studied. Fig. 5.20 shows the N_{rechit} distribution of the cluster matched to the probe muon for the simulated and recorded data with the tag-and-probe selections applied. The distributions show a reasonably good agreement, therefore indicating that the simulation is reasonably accurate in predicting the hit multiplicity. It is found that $0.58\% \pm 0.04\%$ of probe muons in simulation and $0.51\% \pm 0.01\%$ of probe muons in recorded data produce a cluster with $N_{\text{rechit}} > 130$. For simulation to match the same fraction (0.51%) of muons producing a cluster, a 5% reduction to the hit-multiplicity response in simulation yields is applied. This results in a reduction in the yield in the signal region by a few percent, depending on the mass and lifetime of the specific model. The maximum difference between the original and corrected signal yields is taken as a conservative systematic uncertainty, which is found to be 3.5 %.

5.6.3 Cluster ID Efficiency

The modeling of the efficiency of the cluster ID (See Ch. 5.4.2) in simulation is studied. The cluster ID is essentially just a selection based on the $|\eta|$ of the cluster, depending on the number of stations the cluster is located in and the average station number. Potential mismodeling of the cluster ID might be a result of mismodeling of the N_{station} and average station number distributions. The η distribution is only dependent on the production mechanism and not on the detector response, therefore no mismatch in simulation and recorded data is found.

The distribution of N_{station} and the average station number are studied in simulated and recorded $Z \to \mu\mu$ events selected with the tag-and-probe method. The comparison

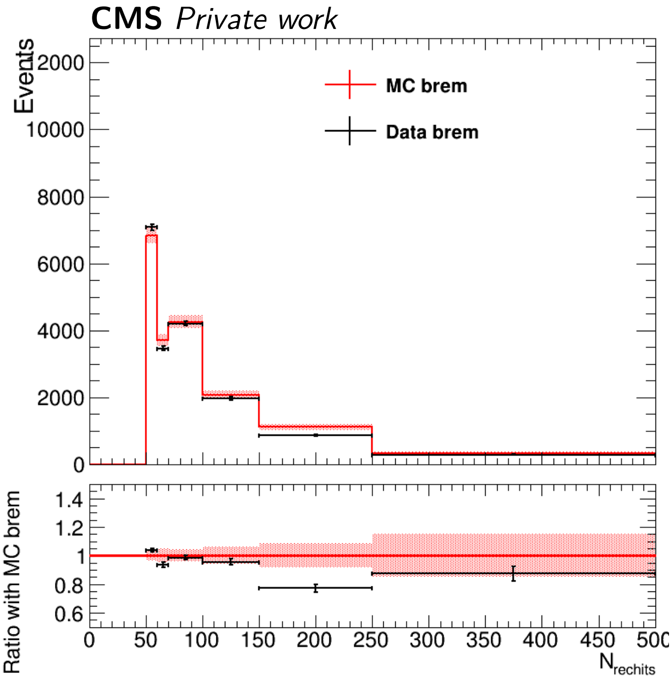

Figure 5.20: The N_{rechit} distributions of recorded and simulated data for muon bremsstrahlung events that pass the tag-and-probe selections.

is shown in Fig. 5.21. Since the cluster ID only has two discrete values for N_{station} ($N_{\mathrm{station}} = 1$ or $N_{\mathrm{station}} > 1$), only two bins are shown in the plot. For the average station an additional requirement of $N_{\mathrm{station}} = 1$ is applied, for clusters with N_{station} >1 no additional requirement on the average station is placed in the cluster ID.

The difference between the simulated and recorded data sample are taken as a correction factor, which are then applied to the simulated samples resulting in a 1-5 % correction of the signal yield in the signal region, depending on the mass and lifetime. Therefore the largest correction of 5 % is taken as a systematic uncertainty.

5.6.4 Jet Veto Efficiency

The jet veto, as discussed in Ch. 5.4, is designed to suppress clusters originating from punch-through jets by vetoing clusters that are matched to jets. The efficiency for signal clusters therefore is caused by the accidental matching of signal clusters to either pileup jets or from jets that are a result of the second LLP in the event decaying closer to the interaction point. Since this veto efficiency depends on the decay of this second LLP, it therefore also depends on the mass and lifetime of the signal model, which determines the probability of this LLP decaying close to the interaction point. It is found that the the accidental LLP decay only dominates for signal models with $c\tau = 100\,\mathrm{mm}$, for the other signal models the inefficiency is dominated by the accidental matching to pileup jets. The jet veto efficiency is measured in the tag-and-probe Z $\rightarrow \mu\mu$ control region. The accidental matching of clusters to pileup jets is checked with the following procedure: First a random (η, ϕ) position from the η and ϕ distributions of clusters passing all selections except the jet veto is selected. It is then checked if a jet with $p_{\mathrm{T}} > 10$ GeV is within a cone of $\Delta R < 0.4$. The measures probability that a randomly selected position is

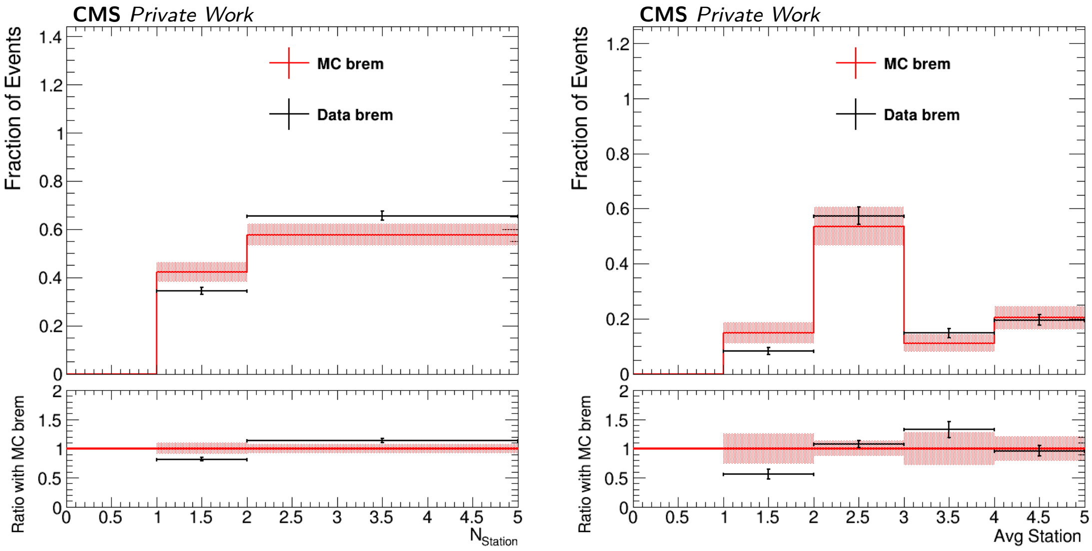

Figure 5.21: The N_{station} (left) and average station number (light) distributions for clusters passing a N_{rechit} cut of 130.

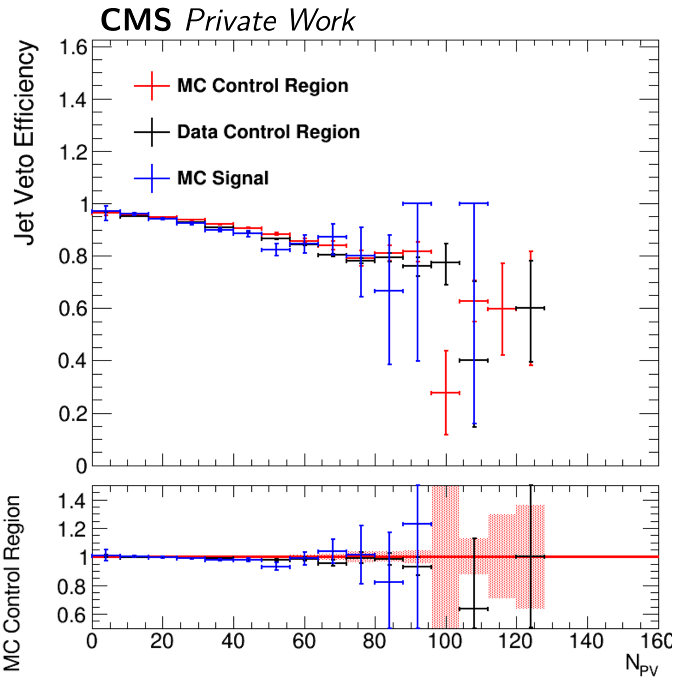

Figure 5.22: The jet veto efficiency measured in simulation and data in the Z → $\mu\mu$ control region and signal simulation in the signal region.

not matched to a jet is defined as the jet veto efficiency. The measured jet veto efficiency is $91.98\% \pm 0.02\%$ in simulated and $93.42\% \pm 0.06\%$ for recorded data. The measured difference of 1.54% is applied as a correction to the signal simulation and the statistical uncertainty (0.07%) is propagated as a systematic uncertainty. The jet veto efficiency with respect to the number of primary vertices is shown in Fig. 5.22. A decrease in the jet veto efficiency as N_{PV} increases is observed, as it gets more likely that a random match occurs with increasing amount of pileup.

5.6.5 Muon Veto Efficiency

The efficiency for the muon veto, as described in Ch. 5.4, in the signal simulation is 10% and made up of two different effects: 3 % is a result of random matching of the cluster to pileup muons, while 7 % is due to tracks produced by the decay products of the signal LLP which then are reconstructed as a standalone muon.

For the inefficiency due to the random matching the same procedure as for the jets is applied. The inefficiency is measured in the $Z \to \mu\mu$ control region, where the events are required to pass the tag-and-probe selections. The accidental matching is again determined by randomly selecting a (η, ϕ) position from the signal cluster distributions passing all the cluster selections for the signal region, expect for the muon veto. Additionally, the cluster is required to be far away from the two muons from the Z boson decay, ensured by requiring the distance between the two muons and the cluster to be $\Delta R > 0.4$. Now it is checked whether a muon with $p_{\mathrm{T}} > 20$ GeV can be geometrically matched within $\Delta R < 0.4$. The measured probability that the randomly selection position is not matched to a muon is the muon veto efficiency. In simulated data the muon veto efficiency is $96.83\% \pm 0.01\%$ for simulated and $96.86\% \pm 0.04\%$ for recorded data. The difference between the simulated and recorded data is small compared to the other signal systematic uncertainties and therefore no correction is applied. The muon veto efficiency as a function of the number of primary vertices is shown in Fig. 5.23.

The inefficiency due to track segments from the LLP decay being reconstructed as a standalone muon is measured in a QCD-dominated control region. For this the clusters are required to be matched to trackless jets, requiring a high neutral energy fraction (NEF) (>0.95) and therefore a small amount of charged energy fraction to remove calorimeter noise in addition to the signal region selections. It is found that clusters in the signal region tend to have smaller η values than clusters in this QCD control region. Because of this the muon veto efficiency is measured as a function of the cluster η position in the QCD control region. Then scale factors in bins of the cluster η are derived, where due to the limited statistics in the first two η bins, the neutral energy fraction selection is loosened to 0.8, while for all other bins the 0.95 selection is applied, since trackless jets with a higher NEF are more similar to the LLP signal. The SF measurement is shown in Fig. 5.24 and the inclusive muon veto efficiency is 82.4% for simulated and 75.4% for recorded data. This is a rather large difference in the signal inefficiency and therefore a 7% correction to the signal simulation is applied while also propagating the statistical uncertainty of 4.5 % as a signal systematic.

5.6.6 RecHit and Segment Veto Efficiency

As described in Ch. 5.4, clusters that are matched to hits in specific chambers (ME1/1, ME1/2, RE1/2 and RB1) or to DT segments in MB1 are vetoed to further suppress the jet punch-through and muon bremsstrahlung backgrounds. The veto efficiency for these five vetos is measured together in the $Z \to \mu\mu$ control region, where the events are required to pass the tag-and-probe selections. The same method as the for the jet and muon efficiencies is used: A random (η, ϕ) position from the signal cluster distributions passing all the cluster selections for the signal region, expect the RecHits and segment vetoes, is selected. Additionally the cluster is required

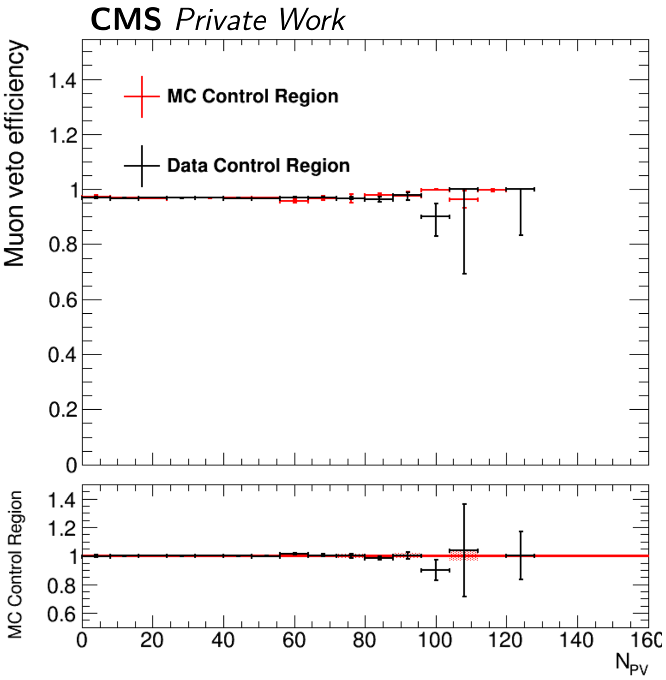

Figure 5.23: The muon veto efficiency measured using the random direction method is shown as a function of the number of primary vertices for simulation and data in the $Z \to \mu\mu$ control region.

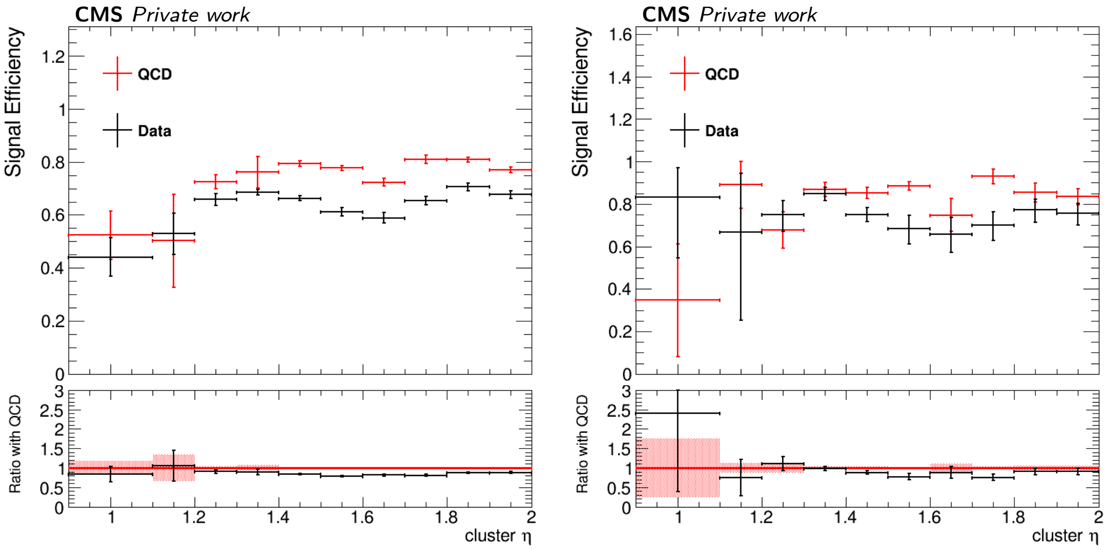

Figure 5.24: The muon veto efficiency as a function of cluster η for trackless jets requiring $0.8 < \mathrm{NEF} < 0.99$ (left) and $0.95 < \mathrm{NEF} < 0.99$ (right) for both data and MC are shown.

to be far away from the two muons from the Z decay by requiring the cluster to be $\Delta R > 0.4$ away from the muons. The random position is now used to check if there is a RecHit or segment nearby, that would be vetoed. The probability that the randomly selected position is not matched to a RecHit/Segment is the veto efficiency. The measured inclusive efficiency is $80.97\% \pm 0.03\%$ for recorded and $83.74\% \pm 0.08\%$ for simulated data. Therefore a 3.3% correction is applied to the signal simulation and the statistical uncertainty of 0.1% is assigned as a systematic uncertainty to the signal process. The veto efficiency as a function of the number of primary vertices is shown in Fig. 5.25. Similarly to the jet veto efficiency a decrease in the veto efficiency for increasing N_{PV} can be observed.

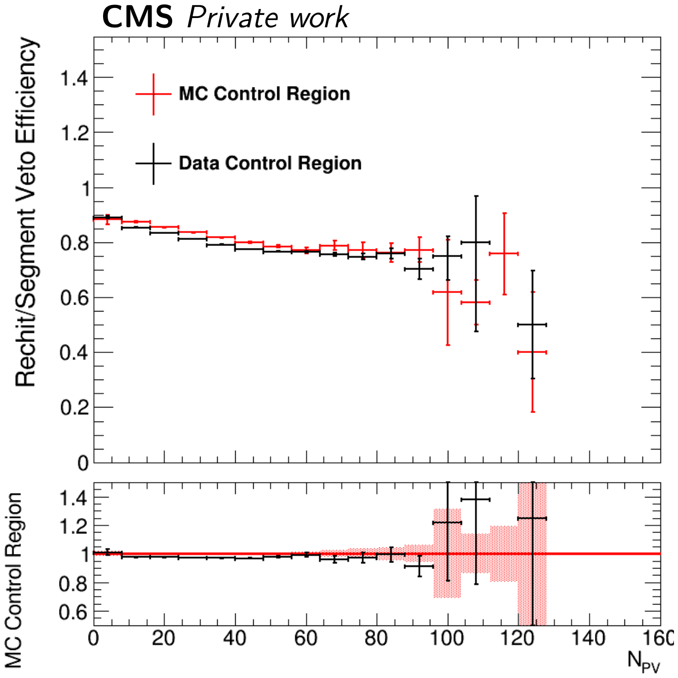

Figure 5.25: The Rechit/Segment veto efficiency measured as a function of the number of primary vertices for simulation and data in the Z → $\mu\mu$ control region.

5.6.7 Cluster Time Efficiency

As explained in Ch. 5.4, signal clusters are required to have a t_{cluster} of $-5\,\mathrm{ns} < t_{\mathrm{cluster}} < 12.5\,\mathrm{ns}$ and that t_{spread} is <20. To validate that the t_{cluster} and t_{spread} are well modeled, events are selected that pass the tag-and-probe selections and additionally have a cluster matched to the probe muon. The signal selections except for the t_{cluster} and t_{spread} are applied.

The cluster time t_{cluster} and time spread t_{spread} for both simulated and recorded data is shown in Fig. 5.26. The distributions show that most clusters for the Z → $\mu\mu$ control region are sharply centered around 0, with a relatively small values of t_{spread}. The efficiency of the in-time cut is $98.94\% \pm 0.31\%$ for recorded and $99.84\% \pm 0.11\%$ for simulated data. The difference is propagated as a uncertainty of 0.9 %. The efficiency for the t_{spread} cut is $93.05\% \pm 0.65\%$ for recorded and $95.74\% \pm 1.3\%$ for simulated data. An uncertainty of 2.8% is assigned as the time spread cut uncertainty.

5.6.8 Data Year Comparison

As mentioned before, the simulated samples are only available for the 2017 data taking conditions. Therefore it has to be checked whether the measured veto efficiency are different for the different data taking years. No large difference in any of the measured vetos across the different years is observed. As an example Fig. 5.27 shows

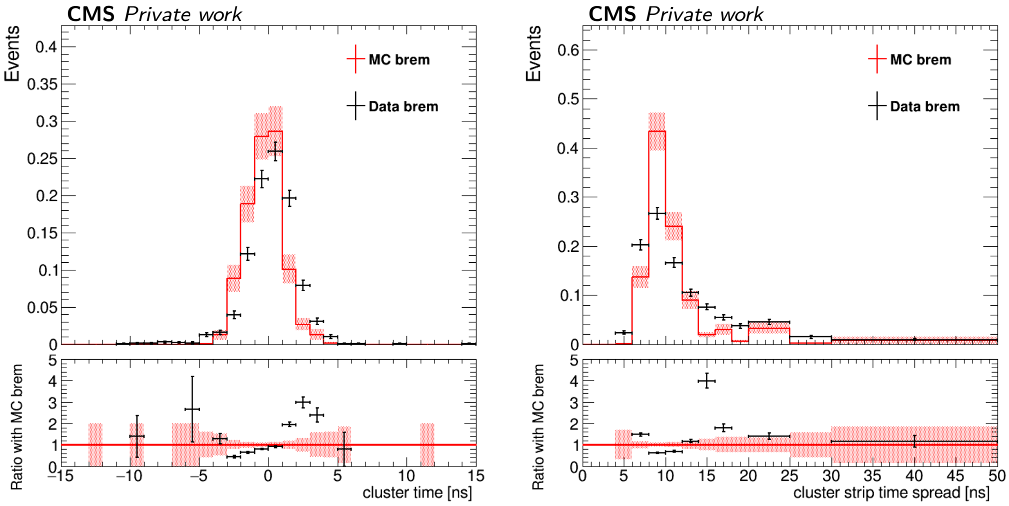

Figure 5.26: The cluster time (left) and time spread (right) distributions for simulation and data in the Z → $\mu\mu$ control region.

the cluster η, average station number, N_{station} and N_{rechit} distributions for all three years. Overall a good agreement between distributions in the recorded data for the different years is observed. A larger difference is observed in the N_{station} plot, which could be pileup-related, due to the changing data taking conditions.

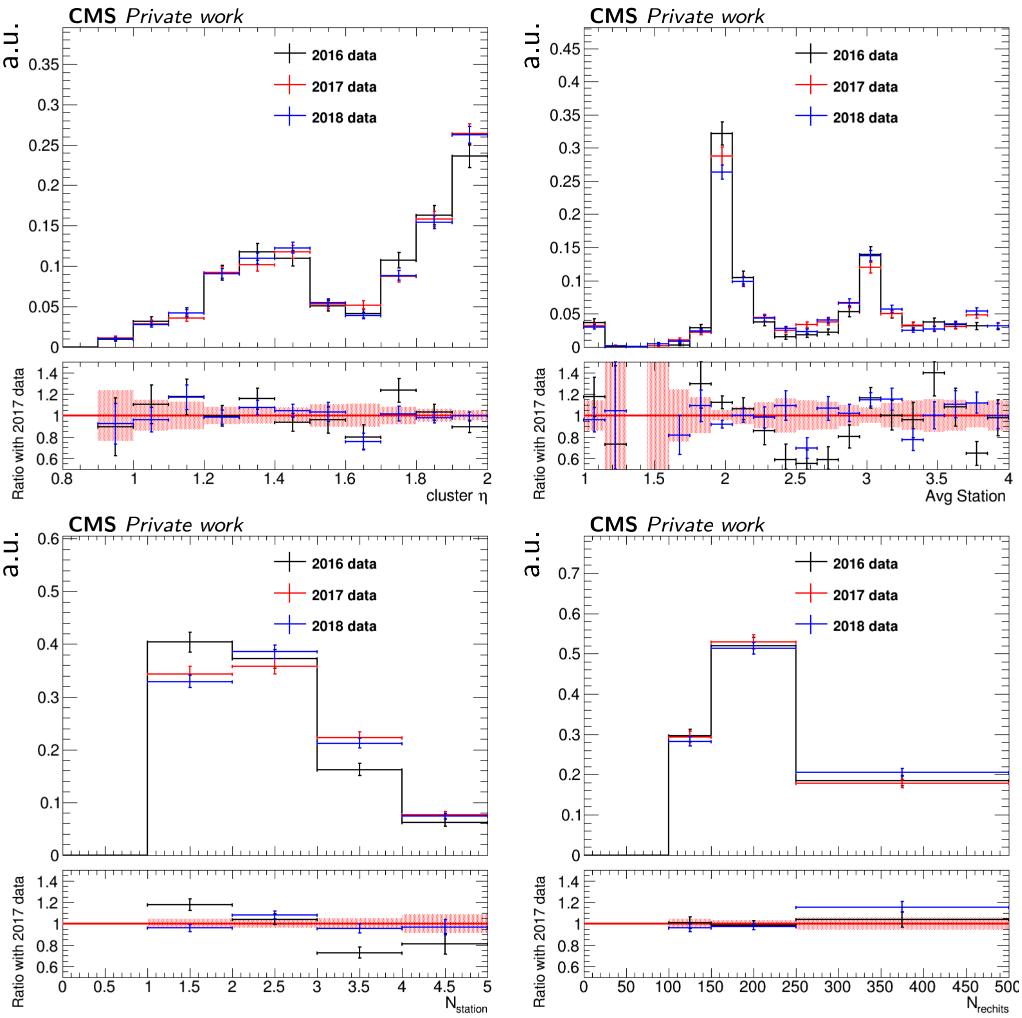

Figure 5.27: The cluster η (top left), average station number (top right), $N_{stations}$ (bottom left), and $N_{rechits}$ (bottom right) distributions in data from all 3 years. The difference in the $N_{stations}$ distribution for different years could be pileup-related, due to the changing number of pileup interactions in the different years.

5.7 Systematic Uncertainties

5.7.1 Background Uncertainty

The closure tests described in Ch. 5.5 show a good agreement between the predicted and observed yields in both validation regions. Therefore no systematic background uncertainty is assigned and the background prediction will be dominated by the statistical uncertainty in the background dominated bins A, B and C.

5.7.2 Signal Uncertainties

The systematic uncertainties considered for the signal prediction in the ggH production channel are summarized in Tab. 5.14 and will be discussed in more detail in the next sections. The signal uncertainties are dominated by the theoretical uncertainties, specifically the Higgs p_{T} shape uncertainty, discussed in Ch. 5.2.1.

Cluster Modeling

This uncertainty consist of the measured uncertainties of the cluster efficiency, cut-based ID efficiency, jet veto efficiency, muon veto efficiency, RecHit/segment veto efficiency, cluster time and time spread described in Ch. 5.6. The largest uncertainties are due to the cluster ID and the muon veto, with uncertainties of 5.1 % and 4.5 % respectively.

Table 5.14: Signal systematic uncertainty in each bin of ABCD plane.

Uncertainty	A	B	C	D
Cluster eff	3.5%	3.5%	3.5%	3.5%
Cluster ID	5%	5%	5%	5%
Muon veto	4.5%	4.5%	4.5%	4.5%
Jet veto	0.07%	0.07%	0.07%	0.07%
Rechit veto	0.1%	0.1%	0.1%	0.1%
cluster time	0.9%	0.9%	0.9%	0.9%
cluster time spread	2.8%	2.8%	2.8%	2.8%
CSC readout	1%	1%	1%	1%
JES	8.4%	8.3%	4.2%	4.1%
Pileup	0.8%	1.1%	1.1%	1.1%
xsec(ggH)	$^{+4.6\%}_{-6.7\%}$	$^{+4.6\%}_{-6.7\%}$	$^{+4.6\%}_{-6.7\%}$	$^{+4.6\%}_{-6.7\%}$
PDF+α_s(ggH)	3.2%	3.2%	3.2%	3.2%
Higgs p_{T} (ggH)	$^{+13.3\%}_{-20.5\%}$	$^{+13.3\%}_{-20.5\%}$	$^{+13.3\%}_{-20.5\%}$	$^{+13.3\%}_{-20.5\%}$
Luminosity	1.8%	1.8%	1.8%	1.8%
Simulation sample size	7-15%	10-25%	5%	3%

CSC Readout

The readout of a CSC station is triggered by a special pre-trigger that must coincide with the L1 trigger decision. This pre-trigger is formed, if there are at least two hits at different CSC layers matching a pre-defined pattern of hits. This pre-trigger is not present in the signal simulation and therefore could affect the signal yield prediction, e.g. the clustering could include hits in chambers that are not readout in recorded data. This effect is estimated in simulation by only counting RecHits if the chamber contains > 5 hits, which ensures that the pre-trigger forms and the chamber is readout. The effect on the signal efficiency is found to be small ($< 0.1\%$).

Additionally the CSC readout might also affect the ME1/1 and ME1/2 vetos. To study this effect the ME1/1 and ME1/2 veto is loosened, so that signal clusters are allowed to be matched to ME1/1 or ME1/2 hits, but these hits are only allowed to occupy either 1, 2 or 3 layers in the chamber. The signal gain is 0.7 %, 1.3 % and 2.5 % respectively and therefore a 1% systematic uncertainty is assigned.

Jet Energy Scale

The size of the Jet Energy Scale [86] uncertainty is between 5-8% for all signal models and also affects the efficiency of the trigger, since the JES affects the $p_{\mathrm{T}}^{\mathrm{miss}}$ calculation. The impact of the JES uncertainty is estimated by varying the p_{T} of all jets considered for the jet veto up and down by 1 σ and propagating the change to the $p_{\mathrm{T}}^{\mathrm{miss}}$ as well.

Pileup Reweighting

As described in Ch. 4.7.2, the simulated distribution of the number of pileup interactions is reweighted to describe the recorded data better. The weights are derived from minimum bias samples during the data taking periods. The uncertainty due to this reweighting is estimated by varying the pp inelastic cross section up and down one standard deviation and measuring the variation in the signal yield, resulting in a 1% uncertainty for all signal models [59].

Signal Cross Section

The uncertainty on the theory cross section used for the normalization for each signal production mode is taken from Ref.[112] The uncertainties for ggH, VBF, WH, qqZH, ggZH, and ttH are shown in Tab. 5.15.

PDF and Strong Coupling Constant

The uncertainty stemming from the uncertainty of the PDF and strong coupling constant (α_{S}) is taken from Ref.[112] and the uncertainties for ggH, VBF, WH, qqZH, ggZH, and ttH are shown in Tab. 5.15.

Higgs boson p_{T} Correction Uncertainty for Gluon Fusion

For gluon fusion the Higgs boson p_{T} correction uncertainty is calculated by adjusting the renomalization and factorization scale by a factor of 0.5 and 2 and re-evaluating the signal yield. Figure 5.28 shows the Higgs boson p_{T} distribution with different

Table 5.15: Cross section, PDF and strong coupling constant uncertainties depending on the production channel.

	ggH		VBF		WH		qqZH		ggZH		ttH	
	Up	Down	Up	Down	Up	Down	Up	Down	Up	Down	Up	Down
Cross section	4.6%	6.7%	0.4%	0.3%	0.5%	0.7%	0.5%	0.6%	8.9%	25.1%	5.8%	9.2%
PDF & α_S	3.2 %		2.1 %		1.9 %		1.9 %		2.4 %		3.6 %	

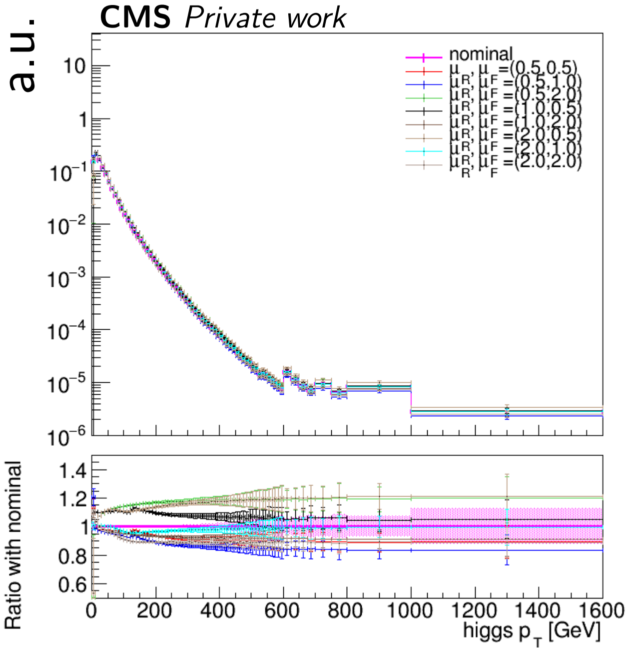

Figure 5.28: The Higgs p_T shape calculated from different renormalization and factorization scale.

renomalization and factorization scales. The total uncertainty is calculated by summing the variations in quadrature, which results in a 20.5 % downward uncertainty (from the three variations with down variations in the scales) and a 13.3 % upward uncertainty (from the three variations with up variations in the scales). The size of this uncertainty is independent of the signal models.

Higgs p_T Correction Uncertainty for VBF, VH and ttH

For the subdominant production channels VBF, VH and ttH, the Higgs p_T uncertainty is also calculated by adjusting the renomalization and factorization scales by a factor of 0.5 and 2 and re-evaluating the signal yield. The uncertainties for each different production channel are listed in Tab. 5.16.

Luminosity

The recorded data used in this analysis amounts to an integrated luminosity of 137 fb^{-1} combined for all three years of data taking and the simulated samples are normalized to this number. The measurement of the luminosity during the data

Table 5.16: Higgs p_T uncertainty in each bin of ABCD plane.

	VBF		WH		qqZH		ggZH		ttH	
	Up	Down	Up	Down	Up	Down	Up	Down	Up	Down
A	2.2%	4.6%	2.6%	7.1%	3.3%	12.5%	12.0%	19.4%	0.7%	1.2%
B	3.2%	15.9%	2.4%	4.0%	1.8%	5.7%	12.3%	19.8%	6.6%	14.8%
C	1.2%	0.7%	0.4%	0.3%	0.6%	1.0%	13.4%	20.8%	1.6%	5.1%
D	1.0%	0.6%	1.8%	5.4%	0.6%	1.7%	13.3%	20.8%	1.0%	2.8%

taking is subject to systematic and statistical uncertainties, which are propagated as a total uncertainty of 1.8%[113–115].

Simulation Sample Size

The number of events in the simulated samples is finite and therefore an uncertainty due to the size of the simulated sample is assigned. The size of this uncertainty depends on the specific signal model and is less than 5 % in bins C and D, increasing to about 10% for signal models with small acceptance. The uncertainty in bins A and B is about 7-25 %.

5.8 Results

Table 5.17 shows the signal yield of different mass and lifetimes in each of the different production channels for an assumed branching ratio of BR(H→SS) = 1%. It can be seen that the ggH production channel is the most sensitive, expecting up to 21 events in the signal region depending on the mass and lifetime. But the subdominant production modes also contribute around 35 % of the signal yields. The yields are corrected by 10.5 % due to the measured differences in the jet, muon and RecHit/Segment vetoes.

Table 5.18 shows the signal contamination in the background enriched bins A, B and C, again assuming a branching ratio of BR(H→SS) = 1%. Comparing these yields to the background prediction in Tab. 5.13 shows that the signal contamination is small. The largest signal contamination can be seen for the 15 GeV and 1 m sample, yielding an overall number of events of 14.1 in bins A, B and C combined. Compared to the prediction from the background-only fit in Tab. 5.13, which yields an overall number of events of 147. The resulting maximum signal contamination therefore is 9.5 %, while other mass and lifetimes have a way smaller signal contamination.

The number of events observed in data is shown in Tab. 5.19. In the signal bin D 2.2 ± 1 events are predicted as the background yield while 3 events are observed in the data. Therefore no statistical significant excess is observed in this analysis. The N_{rechit} and $\Delta\phi(\mathrm{cluster}, p_{\mathrm{T}}^{\mathrm{miss}})$ distributions of the observed data are shown in Fig. 5.29, where additionally 3 different signal models are overlayed. Fig. 5.30 shows the 2D distribution of N_{rechit} and $\Delta\phi(\mathrm{cluster}, p_{\mathrm{T}}^{\mathrm{miss}})$. Lastly, event displays for the 3 observed events are shown in Figures 5.31 to 5.33. It can be seen that the event shown in Fig. 5.33 has a 12 GeV muon matched to the cluster, which is below the applied muon veto of 20 GeV. Fig. 5.32 also has a muon near to the cluster, which might be a possible candidate for this cluster. Lastly, Fig. 5.32 shows the most signal like event, with no obvious candidate pointing towards the cluster.

Table 5.17: Predicted signal yield in the signal region in bin D for different production modes, assuming BR(H→ss) = 1% .

ggH

LLP mass $c\tau$	0.1 m	1 m	10 m	100 m
15 GeV	6.3	21.4	5.1	0.6
40 GeV	0.2	17.4	14.9	1.8
55 GeV	0.0	7.1	18.6	2.8

VBF

LLP mass $c\tau$	0.1 m	1 m	10 m	100 m
15 GeV	1.9	6.3	1.5	0.1
40 GeV	0.0	5.3	4.4	0.7
55 GeV	0.0	2.2	5.9	0.9

WH

LLP mass $c\tau$	0.1 m	1 m	10 m	100 m
15 GeV	0.6	2.2	0.5	0.1
40 GeV	0.0	1.7	1.2	0.2
55 GeV	0.0	0.8	1.8	0.2

qqZH

LLP mass $c\tau$	0.1 m	1 m	10 m	100 m
15 GeV	0.3	1.1	0.2	0.0
40 GeV	0.0	1.1	0.8	0.1
55 GeV	0.0	0.5	1.0	0.2

ggZH

LLP mass $c\tau$	0.1 m	1 m	10 m	100 m
15 GeV	0.1	0.4	0.1	0.0
40 GeV	0.0	0.4	0.3	0.1
55 GeV	0.0	0.1	0.4	0.1

ttH

LLP mass $c\tau$	0.1 m	1 m	10 m	100 m
15 GeV	0.4	1.5	0.3	0.0
40 GeV	0.0	1.1	0.9	0.1
55 GeV	0.0	0.5	1.2	0.2

Table 5.18: Signal contamination in the signal region in bin A, bin B and bin C, assuming BR(H→ss) = 1% .

Bin A

LLP mass $c\tau$	0.1 m	1 m	10 m	100 m
15 GeV	0.0	4.3	3.1	0.4
40 GeV	0.0	0.3	1.3	0.2
55 GeV	0.0	0.0	0.2	0.0

Bin B

LLP mass $c\tau$	0.1 m	1 m	10 m	100 m
15 GeV	0.0	1.8	1.9	0.4
40 GeV	0.0	0.1	0.4	0.1
55 GeV	0.0	0.0	0.1	0.0

Bin C

LLP mass $c\tau$	0.1 m	1 m	10 m	100 m
15 GeV	1.0	8.0	2.3	0.4
40 GeV	0.0	4.4	6.2	0.8
55 GeV	0.0	1.3	7.2	1.3

Table 5.19: Number of observed events in the signal region and the number of predicted events by the background-only fit using the ABCD method.

	A	B	C	D
Bkg-only fit prediction	4.0 ± 1.9	95.0 ± 9.9	48.0 ± 6.6	2.0 ± 1.0
Observed	3	96	47	3

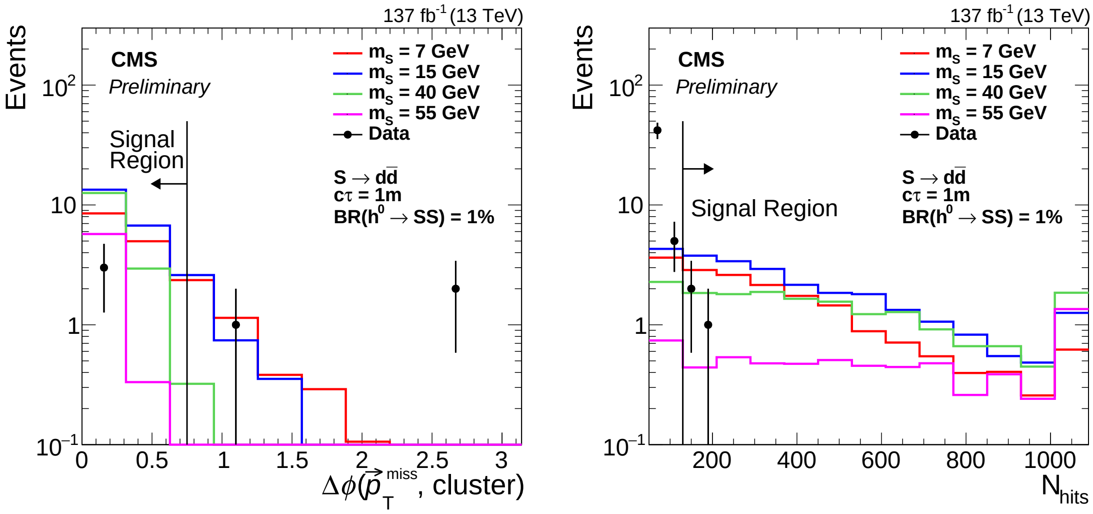

Figure 5.29: The 1D distributions of $\Delta\phi$(cluster,p_T^{miss}) (left) and N_{rechit} (right) are shown. Three different simulated signal samples with decays into 2d with masses of 15, 20 and 55 GeV with a $c\tau = 1$ m are also shown. The assumed BR for these samples is BR(H→ss) = 1%. The black lines show the ABCD thresholds. The N_{rechit} plot includes bins C and D, while the $\Delta\phi$(cluster,p_T^{miss}) plot includes bins A and D.

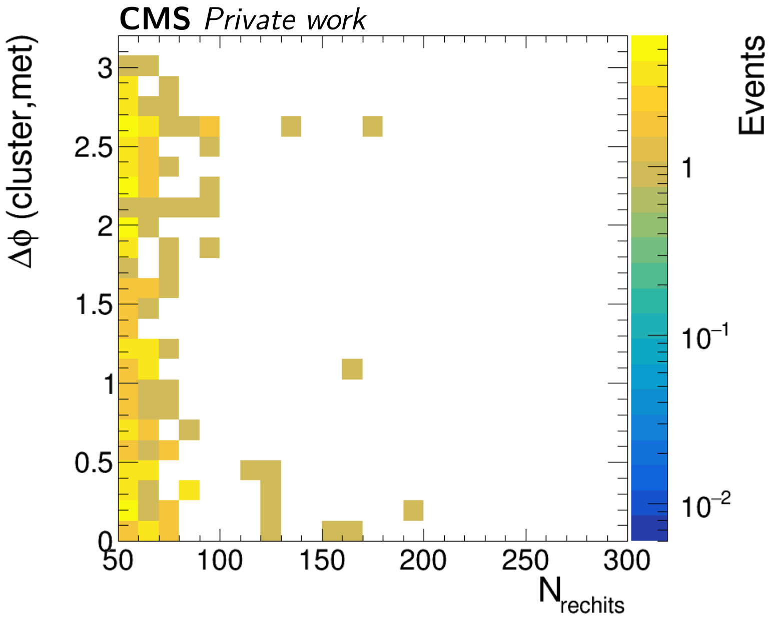

Figure 5.30: The 2D distribution of $\Delta\phi(\text{cluster},p_{\mathrm{T}}^{\text{miss}})$ and N_{rechit} in the signal region for recorded data. The ABCD thresholds are at N_{rechit} >130 and $\Delta\phi(\text{cluster},p_{\mathrm{T}}^{\text{miss}}) < 0.75$.

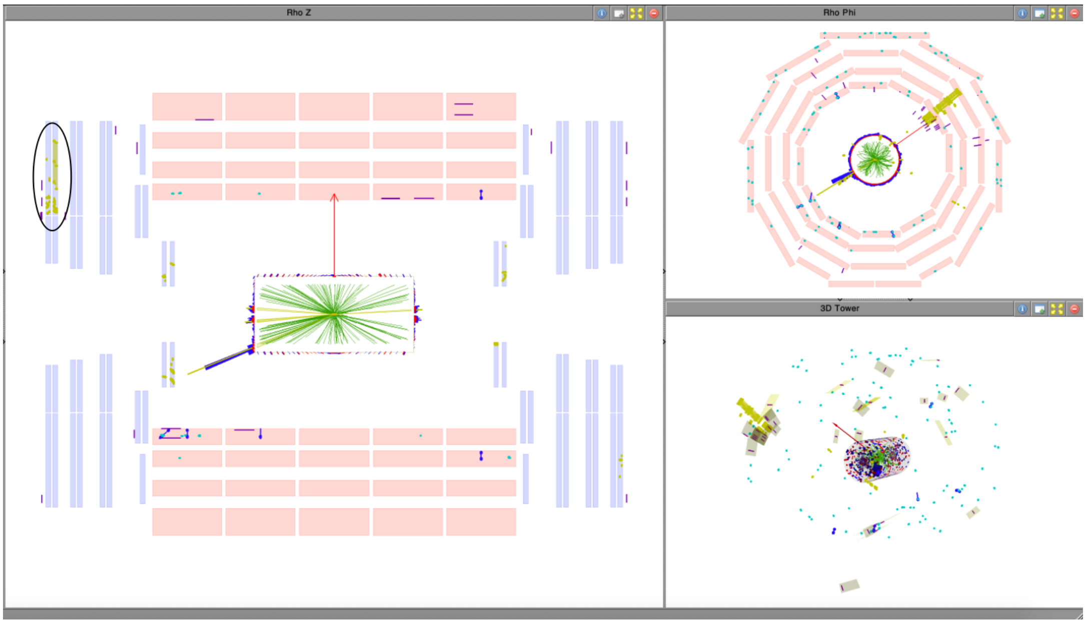

Figure 5.31: The event display of an observed event in bin D, with run number 317627, lumi section 214, and event number 292396821. The N_{rechit} is 156 and $\Delta\phi(\text{cluster},p_{\mathrm{T}}^{\text{miss}})$ is 0.01.

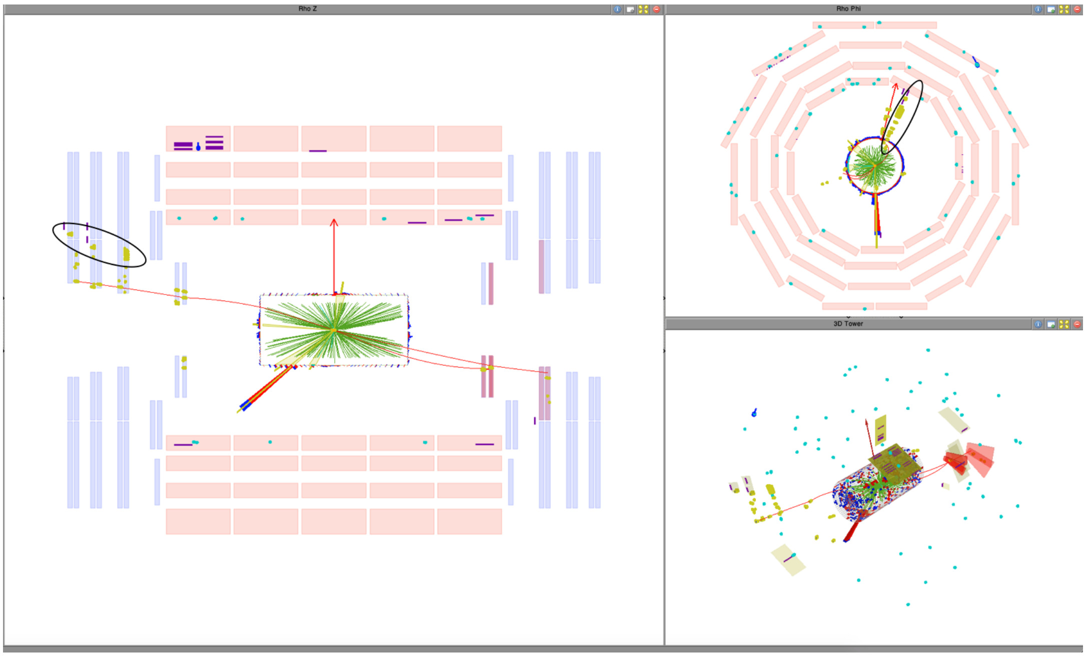

Figure 5.32: The event display of an observed event in bin D, with run number 324293, lumi section 656, and event number 1224149306. The N_{rechit} is 192 and $\Delta\phi(\text{cluster},p_{\text{T}}^{\text{miss}})$ is 0.21.

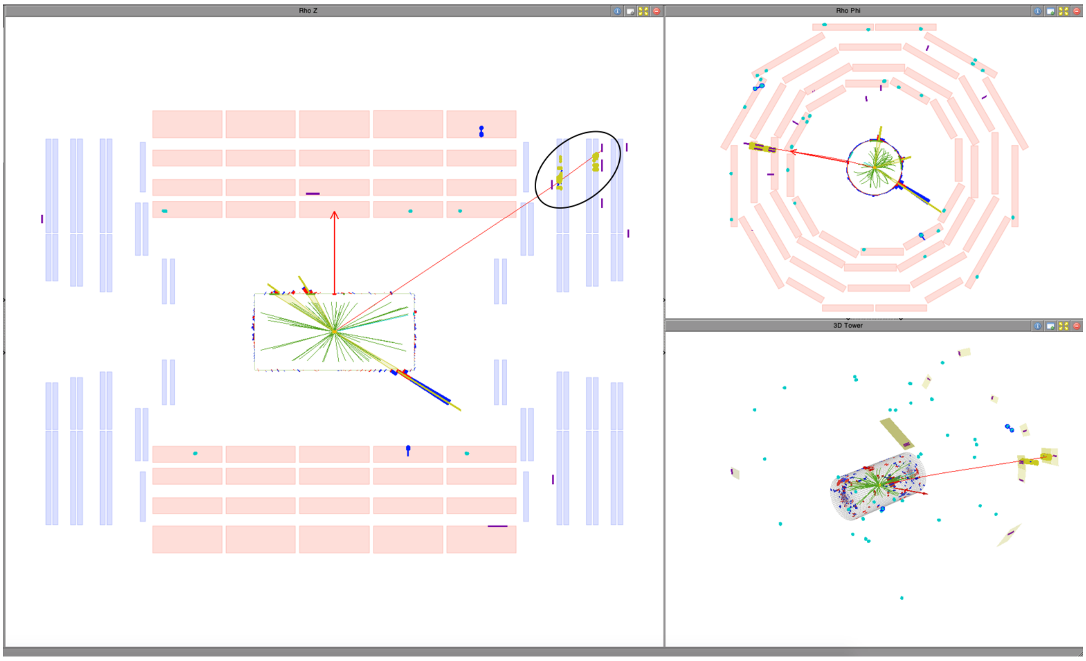

Figure 5.33: The event display of an observed event in bin D, with run number 275376, lumi section 1901, and event number 2835605820. The N_{rechit} is 169 and $\Delta\phi(\text{cluster},p_{\text{T}}^{\text{miss}})$ is 0.01.

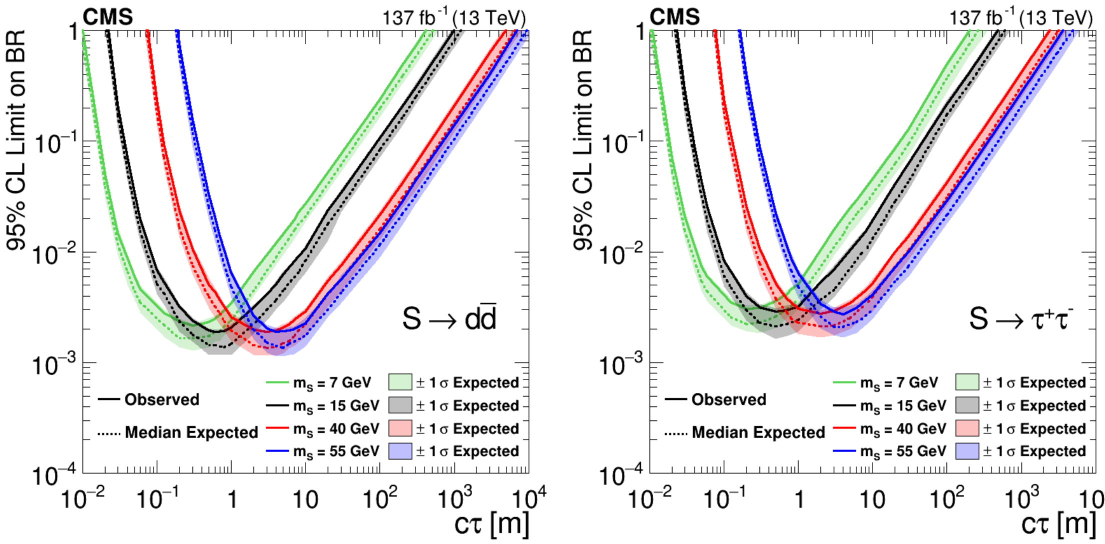

Figure 5.34: The observed and expected limits at the 95 % confidence level for signal predictions with all production modes for 2d (left), 2τ (right) decay modes are shown.

5.8.1 Expected and Observed Limits

Since no significant excess is observed, a limit on the branching fraction of Higgs bosons decaying into long-lived scalars is set. The expected and observed limits at the 95 % confidence level are set using the background estimation method described in Ch. 5.5. Figure 5.34 shows the observed and expected limits for the 2d and 2τ decay channels. The limits for the 2b decay channel is within 3 % of the exclusion limits for the 2d decay channel for $m_S > 2m_b$ and are therefore not shown. For the limit calculation all production modes are considered. It can be seen that the sensitivity across the different decay modes is similar, only the mass and lifetime affects the sensitivity. The sensitivity also stay consistent for the different mass points, leading to the conclusion that this type of search is sensitive to the low mass LLPs. The lowest mass considered in this search is 7 GeV, but a new analysis was published recently, including lower mass points (See next section).

The limits presented here did set the most stringent limits at the time of publishing (being superseded by the analysis presented in Ch. 5.9), improving the previously best limits from the ATLAS collaboration [95, 96] for lifetimes of $c\tau > 6, 20, 40\,\mathrm{m}$, and LLP masses of 7, 15 and 40 GeV, respectively. For $c\tau > 100\,\mathrm{m}$ this search improves the limits by a factor of 6 and 2 for LLP masses of 7 and $\geq 15\,\mathrm{GeV}$, respectively.

5.9 Run2 Combination Analysis

The analysis presented so far is only considering LLP decays inside the CSC system of the CMS detector. Naturally this analysis can be extended to also include the DT system, increasing the sensitivity further. The choice to first start and complete an analysis with only the CSC system was motivated by technically easier access of the RecHits and specifically the timing information of CSC RecHits.

An updated analysis has been published in Ref. [97]. This new updated analysis adds the DT system, which extends the coverage of the analysis further to decay positions with a smaller η position. Due to the difference in geometric acceptance, the addition of DT clusters improves the sensitivity at longer proper decay lengths, compared to CSC clusters which have a better sensitivity at lower proper decay lengths. The DT category is split into three separate regions, depending on the DT station that contains most of the hits in the cluster (MB2, MB3 or MB4). The muon veto for the DT category is tightened compared to the CSC region, lowering the p_{T} veto threshold from 20 GeV to 10 GeV. The background estimation is again performed with a data driven ABCD method, with the same variables as the CSC cluster region. The cuts are tuned independently for DT clusters, and are $\Delta\phi(\text{cluster},p_{\mathrm{T}}^{\mathrm{miss}}) < 1$ and $N_{\mathrm{rechit}} > 100$. The background due to punch-through jets is not accounted for in the ABCD method, and therefore is estimated using a punch-through enriched control region. The transfer from this control region to the signal region also introduces the only source of a systematic uncertainty in the background prediction.

Additionally, the analysis adds a double-cluster category, where both LLPs decay in the CMS muon system. This double-cluster category is the most sensitive category of the combined analysis, improving the previous result by a factor of 2. The double-cluster category is further split into three different regions: One where both clusters are in the CSC system (CSC-CSC), one where both clusters are in the DT system (DT-DT) and one where one cluster is in the DT and the other cluster is in the CSC system (CSC-DT). The background is estimated using a data-driven ABCD background estimation, using the number of DT and CSC hits as the two variables. For the CSC-CSC and DT-DT regions the two variables are symmetric, and therefore two of the bins in the ABCD estimation are combined.

The three different categories (single CSC cluster, single DT cluster and double cluster) are combined for the final result. All the ABCD planes are mutually exclusive and for the combination each ABCD plane is fit simultaneously. Overlapping events are assigned to one category with the following priority: double cluster, single CSC cluster and single DT cluster. For the calculation of the limits, all theoretical uncertainties and all experimental uncertainties not related to the clusters are fully correlated between the three categories. Experimental uncertainties associated with the cluster selections are considered as fully uncorrelated.

In addition since, it is found that the cluster efficiency does not depend on the mass of the LLP, even lower mass regimes were tested, reaching as far as 0.4 GeV. Furthermore, different signal models are considered in this search, extending the scope of this analysis.

The expected and observed limits at the 95 % confidence level are shown in Fig. 5.35 for the Twin Higgs model, with decays into 2d, $2\pi_0$ and 2τ being considered. The limits for 2d and 2τ decays show a clear improvement compared to the single CSC clusters shown in Fig. 5.34, improving the results by a factor of 2 of lifetimes $c\tau$ above 0.2, 0.5, 2 and 18 m for LLP masses of 7, 16, 40 and 55 GeV respectively.

5.10 Summary

A search for long-lived particles in the CMS CSC system has been presented, using proton-proton collision data recorded with the CMS detector at a center-of-mass energy $\sqrt{s} = 13$ TeV, corresponding to an integrated luminosity of 137 fb^{-1} . The

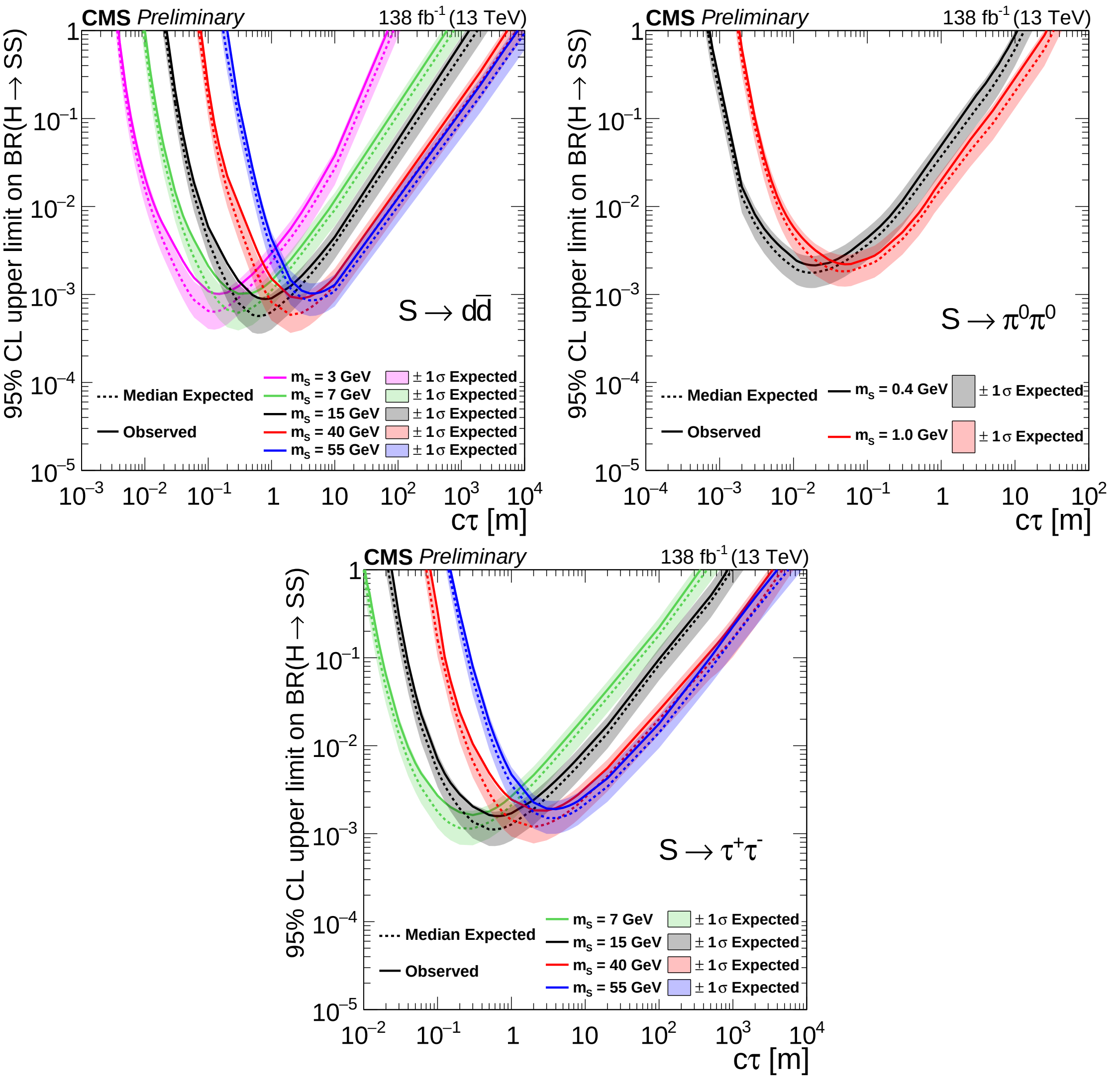

Figure 5.35: The observed and expected limits at the 95 % confidence level for signal predictions with all production modes for 2d (top left), $2\pi_0$ (top right), τ (bottom) decay modes are shown.

Twin Higgs model with large enough scalar masses leads to largely displaced LLPs, which can decay in the CSC system, causing a hadronic shower, also called muon detector shower (MDS). The MDS is a unique signature that is very rare in SM processes, allowing strong background suppression. The signal signature in this model consists of a large amount of $p_{\mathrm{T}}^{\mathrm{miss}}$, which coincides with the cluster, while on the other side of the detector a jet is present,that recoils to the decaying Higgs boson. The search finds no significance excess above the SM background prediction, which then is interpreted as a 95 % confidence level limit in the branching ratio of the LLP decay, setting strong limits between $c\tau$ values of 0.1 and 100 m for LLP masses between 7 and 55 GeV.

6 Search for Long-Lived Heavy Neutral Leptons

In the following a search for heavy neutral leptons decaying in the CMS Muon System using LHC Run 2 data at a center of mass energy of $\sqrt{s} = 13\,\mathrm{TeV}$ is presented. The analysis has recently been published in Ref. [116] and is described in more detail in this thesis. This analysis uses high multiplicity clusters in the muon system to search for largely displaced long-lived HNLs. In contrast to the previous search targeting twin Higgs models, the HNL signature consists of a prompt lepton, which allows the use of single electron and muon triggers, which improve the signal efficiency. Additionally, no ISR/FSR jet is needed for the recoil of the large amount of $p_{\mathrm{T}}^{\mathrm{miss}}$ for the required trigger path. Nevertheless, new challenges arise due to the required presence of a lepton leading to a different background composition.

Past searches for HNLs at CMS targeted both prompt and long-lived HNL decays [117, 118]. The analysis presented here targets a mass region between $1\,\mathrm{GeV}$ and $4\,\mathrm{GeV}$, using the long-lived signature of a high multiplicity cluster, yielding a signal signature which is unique and relative background free. Additionally, it can be shown (See Ch. 6.3.1) that the cluster efficiency is not dependent on the flavor of the HNL, meaning the analysis is sensitive to all different flavors and also to a multitude of different flavor and mixing scenarios.

The chapter is structured as follows: First an overview of the general analysis strategy is given, including an overview of the trigger strategy of the analysis. Next the simulated and recorded datasets used in the analysis are discussed, placing a focus on the signal process simulation. Afterwards, the objects used in the analysis are introduced, adding analysis specific selections on the objects described in Ch. 4. Following this, the event selections are discussed, specifically the selections placed on the cluster properties to enhance the S/B ratio for the signal. Next the data-driven background estimation method is introduced and afterwards the systematic uncertainties of the analysis are discussed. Lastly the results for the search are presented.

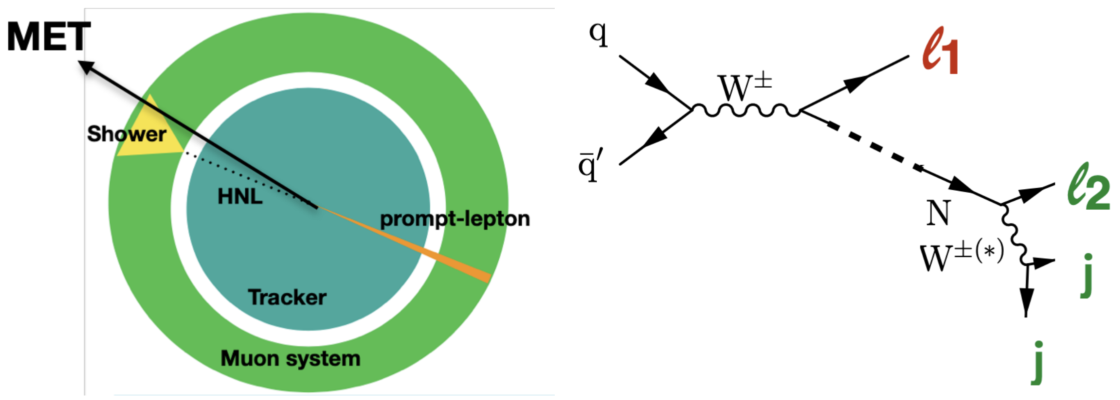

Figure 6.1: On the left: An illustration of the HNL signature showing the MDS with the aligned MET and the prompt lepton on the other side of the detector. On the right: The Feynman diagram of the signal process for the charged current production.

6.1 Analysis Strategy

Since this analysis is focused on the charged-current production (See Ch. 2.2.2) the signal process is naturally very similar to the leptonic decay of a W boson in the SM. The lepton, either an electron or a muon, from the production W decay is used for the trigger decision. With this in mind, it is natural to separate the analysis into two different channels: One where an electron and one where a muon is used as a trigger lepton. Going forward these two channels are called the electron or muon channel. The trigger efficiency of single tau triggers is not high enough to justify a dedicated tau channel with a dedicated tau trigger path. Instead the muon and electron channel can be combined and reinterpreted as a tau-HNL signature, using the muon or electron of the leptonic tau decay of the prompt tau decay for the trigger decision. Instead of a SM neutrino, the signal process has an HNL, which is long-lived and travels to the muon system. It leaves no tracks in the tracker and no energy deposits in the calorimeters, decaying through an off-shell W/Z boson. This HNL decay will also be reconstructed as $p_{\mathrm{T}}^{\mathrm{miss}}$, since the decay products are largely displaced from the interaction point and do not deposit their energy in the calorimeter. The hadronic decay of the off-shell W/Z boson is then causing a hadronic shower in the muon system, due to the interactions with the steel between the chambers. This shower is detected as a large amount of hits in the CSC and/or DT chambers. The signal process signature is illustrated in Fig. 6.1 (left) and the Feynman diagram from Ch. 2.2.2 (right) is also shown.

6.1.1 Trigger Strategy

As described before, single electron and muon triggers are used in the analysis. Since many other processes also include the presence of a single lepton, further offline selections are applied in the analysis in addition to the single lepton triggers. Due to the hadronic decay and resulting difficult reconstruction of tau leptons and the large background due to other similar hadronic decay signatures from QCD processes, single tau triggers usually have higher p_{T} thresholds to not exceed the total allowed trigger rate. This leads to a low trigger efficiency for the HNL events involving tau leptons and therefore dedicated tau trigger paths are not used in this analysis. Leptonically decaying tau leptons can still be accessed by combining the already existing electron and muon channel and reinterpreting the result as a tau-HNL signature. Here the single electron and muon triggers are used to detect the leptonic decay products from the prompt tau decay. The HLT path menu is still being changed during data taking periods and therefor the specific thresholds of the triggers can change in between the data taking periods each year. None of the paths used in this analysis have been prescaled.

Events recorded in 2016 targeting the electron channel need to be accepted by one of three single electron trigger paths: The first trigger path requires an identified and isolated electron with a $p_T > 27\,\text{GeV}$. The other two trigger paths require either a non-isolated high p_T electron with $p_T > 115\,\text{GeV}$ or a photon with $p_T > 175\,\text{GeV}$. The photon path is used since a electron can be miss-identified at the HLT as a photon. Non-isolated electron paths are still include, even though the isolated electrons are selected in a later analysis step, due to possible differences in the objects at the HLT level and the offline level. In 2017 additional trigger paths were added to the HLT menu, increasing the overall HLT rate and pushing the overall rate over the technical limit. To keep the overall HLT rate below the limit, the thresholds of various HLT paths were raised to reduce the rates of these paths. This included the isolated single electron trigger, which saw a threshold increase from $p_T > 27\,\text{GeV}$ to $p_T > 35\,\text{GeV}$. For the 2018 data taking period the p_T threshold for the isolated single electron path was decreased to $p_T > 32\,\text{GeV}$.

Events targeting the muon channel need to be accepted by one of four single muon triggers: For intermediate p_T muons the HLT requires one isolated muon with $p_T > 24\,\text{GeV}$ for the 2016 data taking period. To recover additional efficiency at high p_T the HLT requires one non-isolated muon with $p_T > 50\,\text{GeV}$ for the 2016 data taking period. For the 2017 data taking period the thresholds of these triggers have also been raised, from $p_T > 24\,\text{GeV}$ to $p_T > 27\,\text{GeV}$ and from $p_T > 50\,\text{GeV}$ to $p_T > 100\,\text{GeV}$ for the isolated and non-isolated paths respectively. For the 2018 data taking period the thresholds have been lowered again to the 2016 threshold values.

6.2 Dataset

The analysis uses data from proton-proton collision at a center of mass energy of $\sqrt{s} = 13\,\text{TeV}$ taken in 2016, 2017 and 2018. The analysis, similar to the datasets described in Ch. 5.2, uses the RECO data format to access the CSC, DT and RPC RecHits. This comes with the same drawbacks as described before, mainly the larger needed disk spaces and longer computing times.

In the following sections the simulated samples used in the analysis are discussed.

6.2.1 Signal Simulation

The simulated HNL signal samples used in the analysis are generated using the Monte Carlo (MC) event generator `MADGRAPH5_aMC@NLO` [119–122] at leading order (LO) accuracy. The parton shower, underlying event and hadronization are simulated

Table 6.1: Mass and lifetime points of the generated electron and muon type HNL signal samples.

HNL Type	HNL mass [GeV]	HNL $c\tau$ [mm]
Electron & Muon Type	1.0	4, 10, 100, 1000, 10000
Electron & Muon Type	2.0	10, 100, 1000, 10000
Electron & Muon Type	2.5	10, 100, 1000
Electron & Muon Type	3.0	10, 100, 1000
Electron & Muon Type	3.5	10, 100, 1000
Electron & Muon Type	4.0	10, 100, 1000
Electron & Muon Type	4.5	1000, 5000
Electron & Muon Type	7.0	100, 1000, 10000
Electron & Muon Type	10.0	100, 1000, 10000

using `PYTHIA 8.226` [101]. The signal sample simulation only considers the W production channel, which is produced at leading order with up to two additional partons being considered in the matrix element (ME) calculations. In addition, the next-to-next-to-leading order (NLLO) W boson production cross section is used to account for higher order effects, by normalizing the signal sample cross section to this NNLO cross section. The simulated samples are Majorana-type HNLs, but they can also be interpreted as a Dirac-type HNLs by taking the Majorana-type HNL signal yields as Dirac-type HNLs with twice the lifetime. The underlying event for the simulated sample is corrected with the so-called "tunes", which are derived from data and adjust the simulation to describe the data better. For the 2016 data taking period the CUETP8M1 [102] tune is used and for 2017 and 2018 the CP5 tune [103]. To account for additional pp interactions within the same bunch crossing (pileup), minimum-bias events are added to the simulation. The events are then reweighted so that the number of collisions per bunch crossing in simulation agree with data. The average number of pileup interaction per bunch crossing is 23 for the 2016 data taking period and 32 for the 2017-2018 data taking period [114, 115, 123]. Finally, the CMS detector geometry and response is simulated with `GEANT4` [49].

The simulated samples are generated with different mass and lifetime combinations, where the HNL is displaced enough to decay inside the CMS muon system. For each different HNL flavor (electron-, muon- and tau-type HNLs) individual samples are simulated. Tab. 6.1 and Tab. 6.2 summarize all mass and lifetime points, where the number of events depends on the specific mass and lifetime. For the electron and muon samples the lowest generated $c\tau$ point for a specific mass usually has the highest number of generated events of around 5-6 million events, while the other lifetimes have between 500 and 600 thousand events. For the tau sample 900 thousand events were generated. In addition to the generated Majoranna-type HNL samples, a Dirac-type sample was generated with a HNL mass of 4 GeV and a HNL lifetime of $c\tau = 1\,\mathrm{m}$. This sample is used to verify that Majoranna-type HNL samples can be reinterpreted as Dirac-type HNL samples. In the following sections corrections to the signal samples are discussed.

Table 6.2: Mass and lifetime points of the generated tau type HNL signal samples

HNL Type	HNL mass [GeV]	HNL $c\tau$ [mm]
Tau Type	1.0	100, 1000
Tau Type	2.0	100, 1000
Tau Type	4.0	100, 1000

W p_{T} Spectrum Correction

The W p_{T} spectrum of the simulated signal samples are reweighted to the NNLO DYTURBO [124] spectrum, which allows a more accurate description of the boost of the HNL signal. A W $\rightarrow l\nu$ simulation is used for cross checks and signal selection optimizations and is also reweighted the same way. The impact of this reweighting on the signal acceptance in the signal region is around 1.6 % (See Ch. 6.7.1)

HNL Lifetime Reweighting

As shown in Tab. 6.1 and Tab. 6.2 only a specific set of discrete HNL lifetimes are simulated. For later analysis of these samples it is beneficial to also have access to the intermediate lifetimes. This can be achieved by reweighting the available samples:

Due to the exponential probability of the HNL decay in the rest frame, the events follow the distribution:

$$p(t|\tau) = \frac{1}{\tau}e^{-\frac{t}{\tau}}, \tag{6.1}$$

where τ is the lifetime of the HNL in the t is the lifetime of the HNL in the rest frame given by $t = \frac{s}{\gamma \cdot \beta}$, where s is the travel distance in the lab frame, γ is the Lorentz factor and β is the velocity of the HNL. To reweight a simulated sample with lifetime τ_1 to a sample with a new lifetime τ_2 a weight w is calculated:

$$w = \frac{\tau_1}{\tau_2} exp\left[t \times (\frac{1}{\tau_1} - \frac{1}{\tau_2})\right]. \tag{6.2}$$

The left of Fig. 6.2 shows the decay length distribution of a signal sample with a 4 GeV mass and two different lifetimes, 10 cm and 100 cm. On the right both of these samples are reweighted to a lifetime of 2 cm showing a good agreement between the two.

HNL mass reweighting

To interpolate the HNL masses between the generated sample points, it is assumed that the cluster properties and event level properties are not dependent on the HNL mass, only the relativistic boost factor and the cross section changes. The boost factor affects the acceptance of the HNL in the fiducial detector region and the signal yield changes proportional to the changed cross section.

As described in Ch. 2.2.2, the branching ratio is proportional to m^{-5}, Fig. 6.3 shows the cross section times branching fraction for different HNL masses at a decay length of $c\tau = 1\,\mathrm{m}$. In this double logarithmic plot a linear fit with a slope of -5 describes the points very well, therefore confirming the mass dependence.

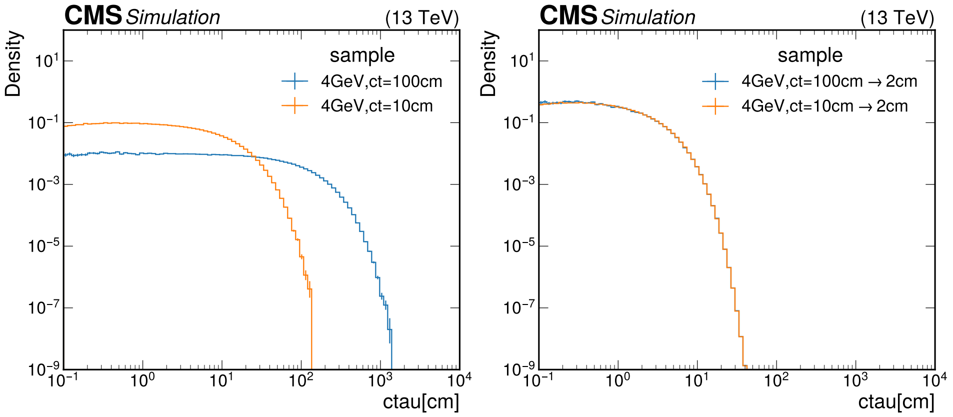

Figure 6.2: The distribution of the decay length for a HNL signal sample with a 4 GeV mass and two different lifetimes of 10 cm and 100 cm is shown on the left. On the right both samples have been reweighted to a lifetime of 2 cm, showing a good agreement between the two samples.

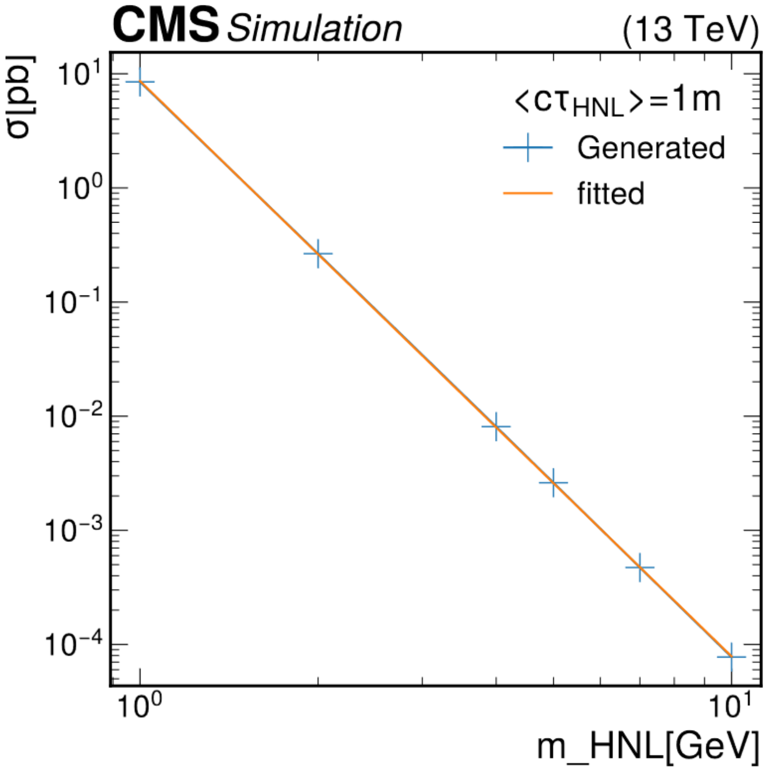

Figure 6.3: Cross sections of generated HNL samples for different HNL masses at a constant decay length of $c\tau = 1\,\mathrm{m}$. The fit shows the m^{-5} dependency of the cross section.

It is assumed that the acceptance is proportional to the decay length of the HNL in the lab frame

$$\beta\gamma c\tau = p \cdot c\tau/m, \tag{6.3}$$

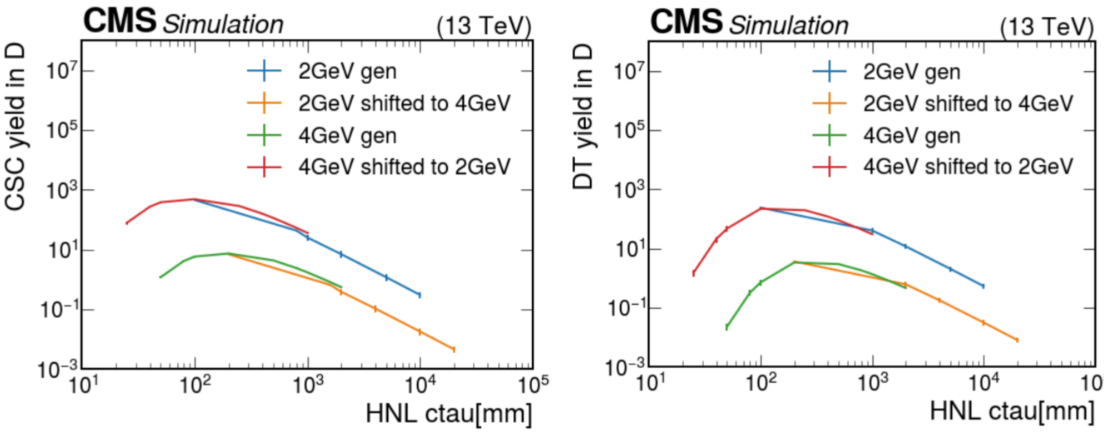

Figure 6.4: Shown are the yields for signal samples simulated with HNL masses of 2 and 4 GeV as well as signal samples reweighted to those values.The reweighted and generated yields agree well.

where p is the magnitude of the HNL's momentum and τ is the mean proper decay length. As long as $c\tau/m$ stays constant, the acceptance will stay the same, therefore the acceptance for a HNL with twice the $c\tau$ is the same as with half the mass, thereby compensating for the smaller Lorentz boost.

Fig. 6.4 verifies this relation showing expected yields in the CSCs and DTs for signals that were either simulated at 2 or 4 GeV masses or reweighted into the respective other mass. The resulting reweighted data points show good agreements with the generated ones, allowing the interpolation between generated mass points.

Dirac HNL signal samples

As described in Ch. 2.2.2, the decay width of the Dirac-type HNL is exactly half of a Majorana-type HNL with the same mass and mixing parameter. Therefore the Dirac yields are predicted by using the simulated Majorana-type HNLs. The hadronic shower in the muon system is indistinguishable between the Majorana and Dirac-type HNLs. Fig. 6.5 (6.6) shows the cluster properties for a CSC (DT) cluster, comparing a generated Majorana sample and a generated Dirac sample at a HNL mass of 4 GeV and $c\tau = 1\,\mathrm{m}$. The cluster properties show no significant difference between a Dirac and a Majorana-type HNL.

Mixed Coupling scenarios

The analysis is also sensitive to mixed flavor HNL scenarios. For this the relative ratios between the couplings are introduced:

$$|V_e| : |V_\mu| : |V_\tau| \equiv f_e : f_\mu : f_\tau. \tag{6.4}$$

The relative couplings are varied in steps of 0.02, while the constraint of $f_e + f_\mu + f_\tau = 1$ has to be satisfied. This results in a total of 1324 equidistant barycentric coupling points that are tested. To reweight the samples to each of the different mixing scenarios the following relation is used:

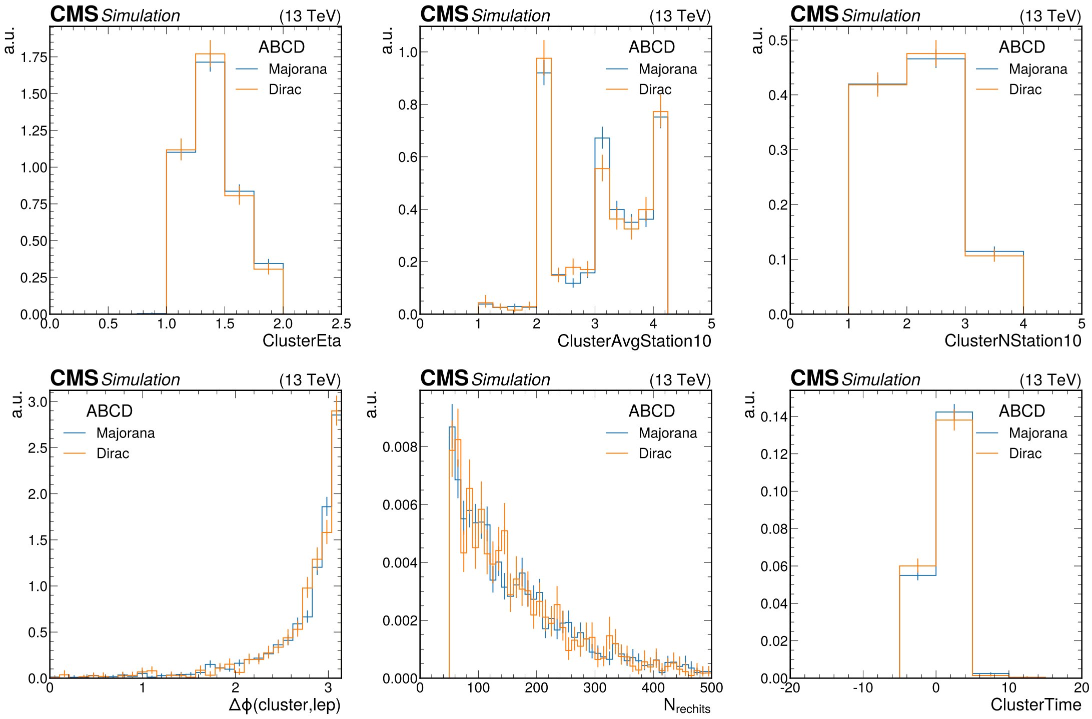

Figure 6.5: Comparison of CSC cluster properties for Dirac and Majorana HNL at 4 GeV, $c\tau = 1\,\mathrm{m}$.

$$N_{f_e,f_\mu,f_\tau} = N_e \cdot f_e + N_\mu \cdot f_\mu + N_\tau \cdot f_\tau, \tag{6.5}$$

where N_{f_e,f_μ,f_τ} denotes the number of events for the chosen coupling scenario, f_X is the relative coupling strength and N_X denotes the number of events for a single flavor sample.

This method is validated by comparing the reweighted samples to generated mixed samples, where two of the three flavors had the same coupling strength and the last coupling is set to 0. The ABCD method, which will be discussed in Ch. 6.5.1, is used for the following studies. Tab. 6.3 to 6.5 compare the yields for these generated and reweighted samples and show only a small disagreement for coupling scenarios where the coupling with the same flavor as the prompt lepton is non-zero. There is a significant difference for mixings where the coupling with the same flavor as the prompt lepton is zero. In this case the prompt lepton used for the trigger decision is produced by the leptonic decay of a tau lepton, which results in a reduced efficiency in the trigger compared to prompt electrons or muons. Additionally, the event yields in these channels contribute less then 10 % to the overall yield. This difference and the overall difference in the yields is accounted for by introducing a 10 % uncertainty for the reweigted mixed samples.

Acceptance

The geometric acceptance is calculated by requiring the HNL decay to occur inside the DT or CSC detector volume. The acceptance then is defined as the ratio of HNL

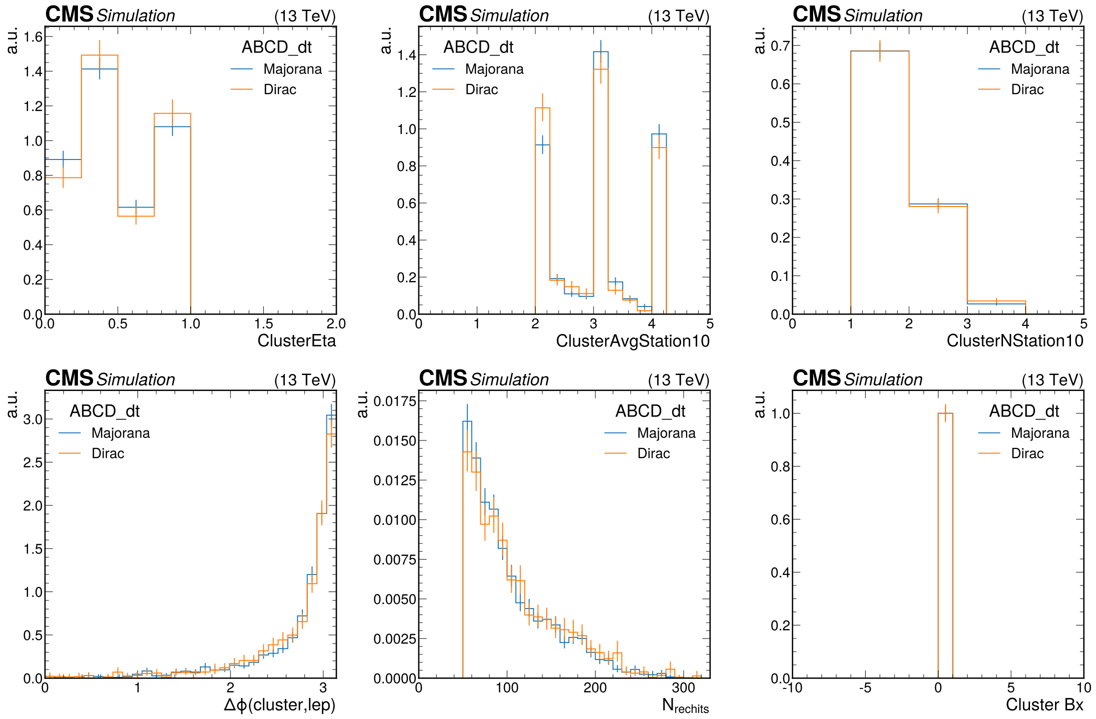

Figure 6.6: Comparison of DT cluster properties for Dirac and Majorana HNL at 4 GeV, $c\tau = 1\,\mathrm{m}$.

Table 6.3: Number of events in the ABCD plane for a generated mixed coupling sample with relative coupling of $(f_e, f_\mu, f_\tau) = (0.5, 0.5, 0)$ and reweighted yields from pure coupling samples. The samples are generated with a HNL mass of 4 GeV and a $c\tau$ of 1 m

Channel	Region	Reweighted yields	Simulated yields (0.5,0.5,0)
Electron	DT	1.334 ± 0.0045	1.284 ± 0.0066
Electron	CSC	0.999 ± 0.0033	0.942 ± 0.0048
Muon	DT	2.733 ± 0.009	3.208 ± 0.016
Muon	CSC	2.421 ± 0.008	2.336 ± 0.010

Table 6.4: Number of events in the ABCD plane for a generated mixed coupling sample with relative coupling of $(f_e, f_\mu, f_\tau) = (0, 0.5, 0.5)$ and reweighted yields from pure coupling samples. The samples are generated with a HNL mass of 4 GeV and a $c\tau$ of 1 m

Channel	Region	Reweighted yields	Simulated yields (0,0.5,0.5)
Electron	DT	1.42 ± 0.01	0.18 ± 0.002
Electron	CSC	0.21 ±0.001	0.02 ± 0.0002
Muon	DT	3.80 ± 0.013	3.97 ± 0.03
Muon	CSC	3.14 ± 0.011	3.30 ± 0.02

Table 6.5: Number of events in the ABCD plane for a generated mixed coupling sample with relative coupling of $(f_e, f_\mu, f_\tau) = (0.5, 0, 0.5)$ and reweighted yields from pure coupling samples. The samples are generated with a HNL mass of 4 GeV and a $c\tau$ of 1 m

Channel	Region	Reweighted yields	Simulated yields (0.5,0,0.5)
Electron	DT	1.54 ± 0.005	1.71 ± 0.006
Electron	CSC	1.21 ± 0.002	1.31 ± 0.005
Muon	DT	0.01 ± 0.005	0.01 ± 3e-07
Muon	CSC	0.72 ± 0.004	0.12 ± 0.0004

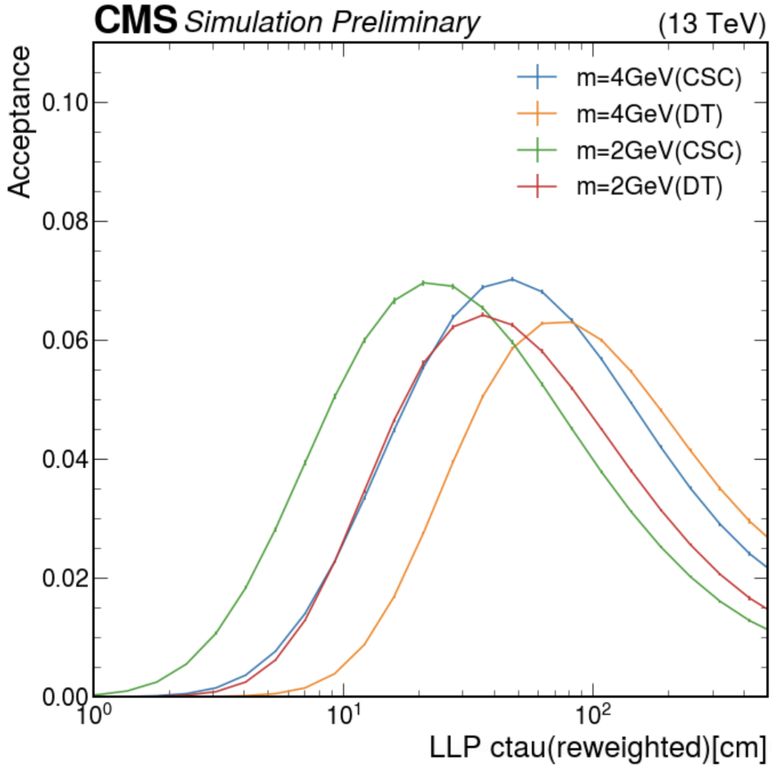

Figure 6.7: Geometric acceptance for the HNL decay as a function of the HNL proper lifetime.

decays inside the detector volume divided by the total number of HNL decays of the specific sample. This can then be parametrized as a function of $c\tau$, shown in Fig. 6.7, where a peak geometric acceptance for masses between 1 and 4 GeV, for a lifetime of 1 m, can be observed. Additionally, the DT and CSC acceptances slightly differ, due to the geometry of the two detectors, therefore increasing the sensitivity range for the analysis.

6.2.2 Background Simulation

The background contributions n this analysis are estimated using data driven methods. Simulated samples of background processes are however still used to study general features, to optimize the event selections and to measure simulation to data correction factors.

For the measurement of the $\mathrm{Z} \rightarrow \mu\mu$ background contribution in the muon channel (See Ch. 6.5.4), a $\mathrm{Z} \rightarrow \mu\mu$ simulated sample is used to derive the data to simulation transfer factor.

Additionally, a $\mathrm{W} \rightarrow l\nu$ sample was used to perform signal selection optimization, acting as a pseudo background in full simulation based studies. Lastly, a minimum bias sample was used to derive the pileup corrections (See Ch. 4.7)

6.3 Object Reconstruction and Identification

In the following sections the reconstructed objects used in the analysis are described. Standard objects described in Ch. 4 are used if not specified otherwise.

6.3.1 Cluster Reconstruction and Efficiency

Clusters are reconstructed with the DBSCAN algorithm, with $\Delta R < 0.2$ and a minimum hit threshold of 50 (See Ch. 4.6). The cluster efficiency is defined as the efficiency for a HNL decaying within the acceptance of the DT and CSC detectors to produce a cluster object. For this efficiency the denominator is the number of generator HNLs that decay within the geometric acceptance of the DT or CSC detectors. The numerator is the number of HNLs that additionally can be matched to a cluster object within a ΔR of 0.4. The cluster efficiency as a function of the HNL energy is shown in Fig. 6.8 for both CSC and DT clusters in both the electron and muon channel. Fig. 6.9 and 6.10 show the cluster efficiency as a function of the HNL decay position in r- and z-direction respectively for both CSC and DT clusters in the muon channel.

It can be seen that the cluster efficiency is highest inside the return yoke material and declines inside the DT/CSC chambers. This is due to the fact that an HNL decay within the DT/CSC chambers does not generate a large enough shower and therefore not enough hits to reach the 50 hit lower limit applied in the cluster reconstruction. This shower is also not energetic enough to fully penetrate the steel to reach the next detector chamber. Therefore the shower needs to originate inside the steel, so that it is large enough to produce at least 50 hits.

In the 2016 data taking period, specific run numbers contain DT clusters with a large amount of hits, entirely localized in a specific wheel/sector (Wheel 1, Sector 2) region of the DT. These clusters are a result of noisy wires in the DTs during the data taking. Clusters found in these specific data taking runs (specifically late runs in the 2016 B and early runs ins 2016 C dataset) and in this specific detector area are vetoed for the analysis. Fig. 6.11 shows the cluster location during the problematic data taking period in the out of time control region (See later Ch. 6.5.3). A sharp spike at DT Wheel 1/Sector 2 can be seen.

6.3.2 Jets

Jets are reconstructed with the anti-k_T algorithm (Described in Ch. 4.4), with a distance parameter of 0.4, forming a so-called AK4 jet. Additionally, to reduce pileup, the Charge Hadron Substracted (CHS) algorithm is used to remove charged particles not originating from the primary vertex during the jet clustering [105]. These jets are used to veto clusters in the CSC(DT), if their centroid is within $\Delta \mathrm{R} < 0.4$ of a jet with $p_{\mathrm{T}} > 10(20)\,\mathrm{GeV}$ and $|\eta| < 3.0$. This veto is used to reduce background clusters from punch-through jets, which are jets that are energetic enough to not be fully contained in the calorimeters and therefore can produce hits in the muon detector chambers.

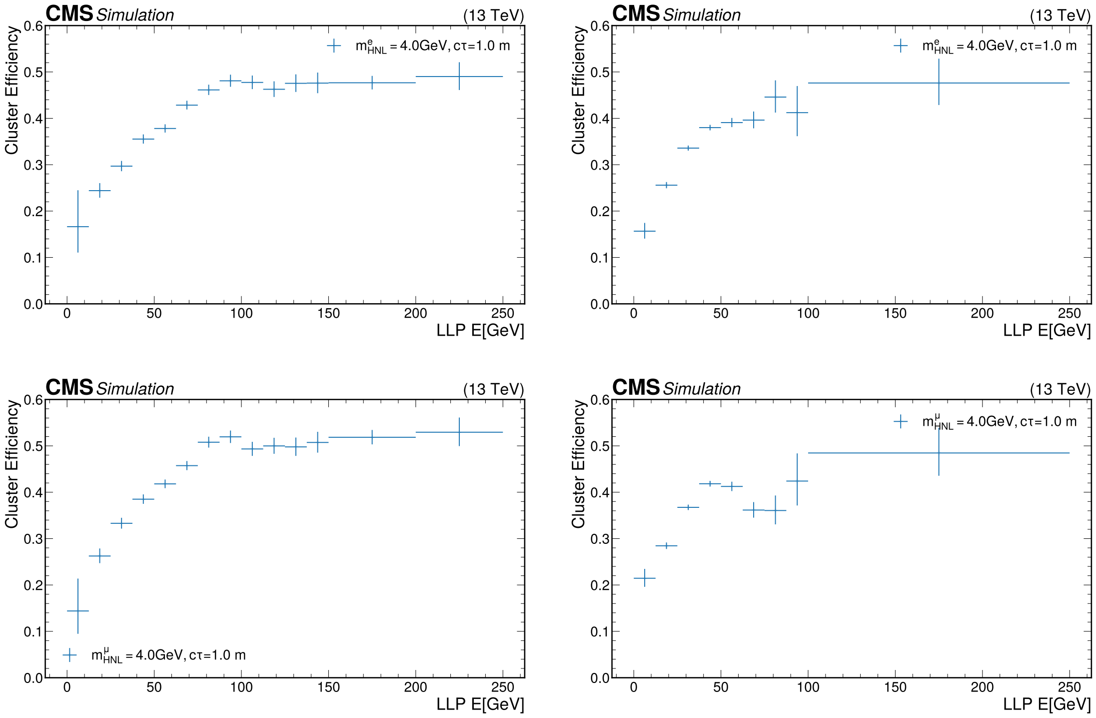

Figure 6.8: Cluster efficiency as a function of the HNL/LLP energy for CSC(DT) cluster on the left(right) for the electron channel (top) and muon channel (bottom)

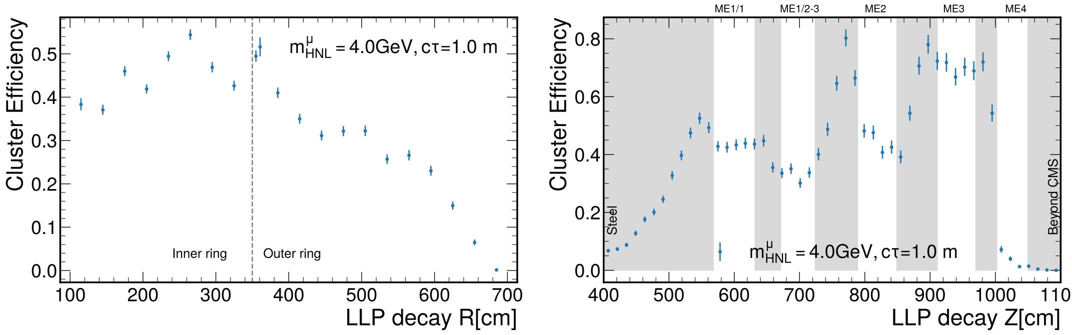

Figure 6.9: Cluster efficiency as a function of the HNL/LLP decay position in radial direction (left) and z direction (right) for CSC clusters in the muon channel. The white area indicates the muon detectors and the grey area indicates the regions without detectors. The signal sample has a mass of 4.0 GeV and $c\tau = 1.0$ m.

6.3.3 Muons

Two different muon objects are used in this analysis. The first object is used to select the prompt muon that is used to trigger on the event. For this muon, the standard CMS muon reconstruction is used (described in Ch. 4.3.2) to obtain global muon candidates. Muons with $p_{\mathrm{T}} > 25$ GeV and $|\eta| < 2.4$ are considered for the 2016

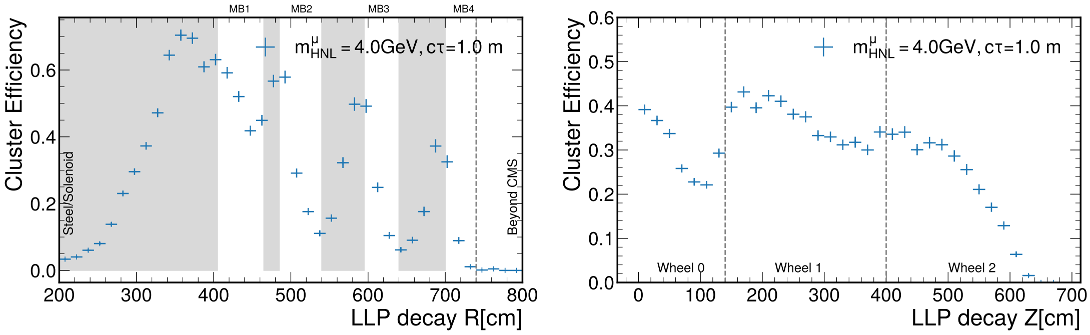

Figure 6.10: Cluster efficiency as a function of the HNL/LLP decay position in radial direction (left) and z direction (right) for DT clusters in the muon channel. The white area indicates the muon detectors and the grey area indicates the regions without detectors. The signal sample has a mass of 4.0 GeV and $c\tau = 1.0$ m.

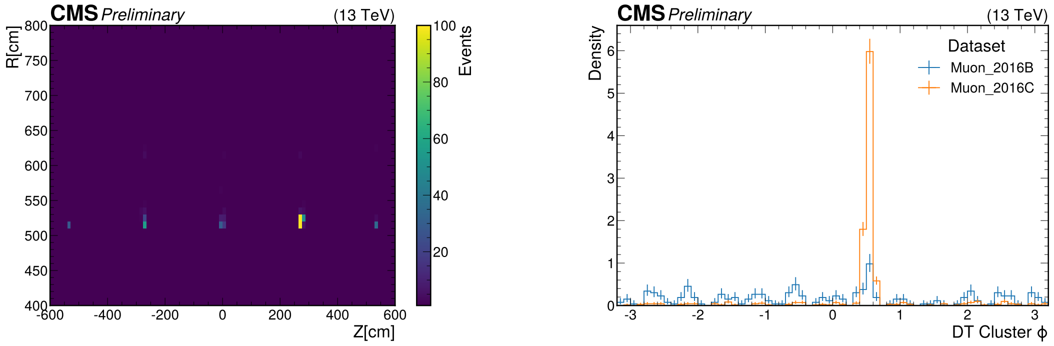

Figure 6.11: The cluster position in the R-Z plane (left) and as a function of ϕ in the OOT control region in the 2016 B and C data taking periods. A clear spike in the DT Wheel 1/Sector 2 can be observed.

and 2018 data taking periods. With the increase in the trigger threshold in 2017, the p_T threshold of the muon also has to be increased accordingly to $p_T > 28$ GeV. Additionally, the muons are required to pass the tight ID criteria and to pass the tight isolation requirement described in Ch. 4.3.2. The prompt muon is also required to match the HLT muon object within $\Delta R < 0.1$.

The second muon object is used to veto clusters in the muon system produced by muon bremsstrahlung. The requirement for these muon objects are lower than for the prompt trigger muons, only requiring $p_T > 20(10)$ GeV and $|\eta| < 2.4$ for CSC(DT) clusters. No additional requirements on the muons are posed. If the centroid of a cluster is within $\Delta R < 0.8$ of this muon, the cluster is vetoed due to the assumption that the cluster is caused by bremsstrahlung from the muon. This veto is tighter compared to the muon veto presented in the previous analysis. Fig. 6.12 illustrates the choice of this selection: Here the distribution of the ΔR between the selected prompt muon and the cluster is shown in a background enhanced region by inverting the ME11/12 and MB1 vetos. A sharp peak from 0.4 to 0.7 can be

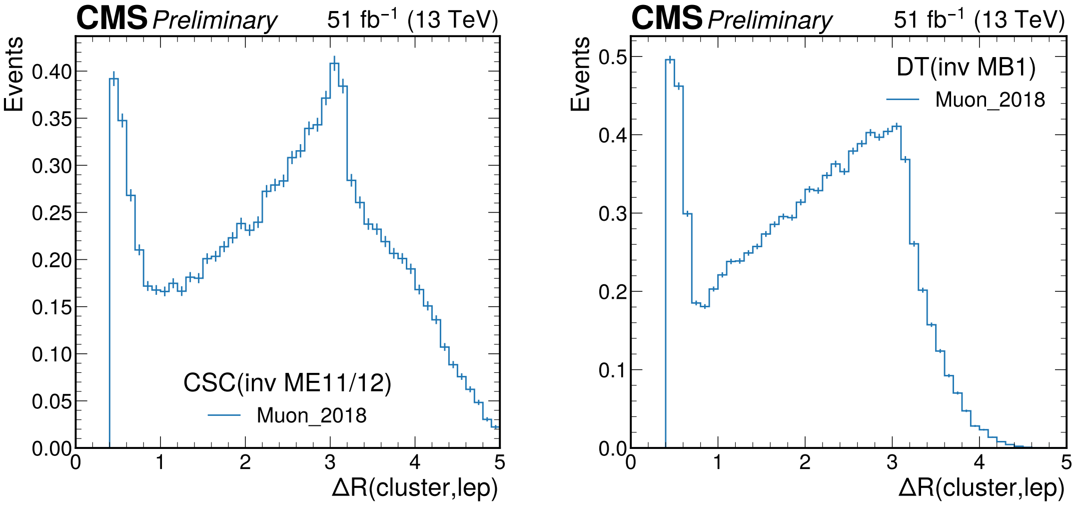

Figure 6.12: ΔR distribution between the selected prompt muon and a selected signal cluster in the CSC (left) or DT (right) in the 2018 single muon dataset for a background enhanced region.

observed, motivating the tighter muon veto. The resulting loss in signal efficiency due to the tighter cut is around 1 %.

6.3.4 Electrons

Electrons are reconstructed with the Gaussian Sum Filter algorithm [125] and are required to have $p_{\mathrm{T}} > 30(35)$ GeV and $|\eta| < 2.5$ for the year 2016 (2017,2018), according to the changes in the electron trigger path. Electron candidates additionally are required to pass tight electron ID criteria and a PF-based isolation. The electron candidates also need to match the HLT electron object within ΔR < 0.1.

6.3.5 Missing Transverse Momentum

The $p_{\mathrm{T}}^{\mathrm{miss}}$ used in this analysis is corrected to reduce known simulation biases with the same corrections described in Ch. 5.3.5.

6.4 Event Selection

As mentioned before, the analysis targets the W production mode where the prompt lepton is used to trigger on the events. An electron or muon is selected based on the requirements listed in Ch. 6.3.3 and Ch. 6.3.4. With this selection, QCD multijet background is already largely rejected. Signals events are expected to contain a significant amount of $p_{\mathrm{T}}^{\mathrm{miss}}$ since the MDS are not considered in the $p_{\mathrm{T}}^{\mathrm{miss}}$ calculation. Therefore further background rejection is achieved by additionally requiring $p_{\mathrm{T}}^{\mathrm{miss}} > 30\,\mathrm{GeV}$. After these cuts the dominant background consists of W $\rightarrow l\nu$. Next a CSC or DT cluster with at least 50 hits is required, to which cluster selections, described in Ch. 6.4.1, are added to further suppress the background from muon bremsstrahlung, punch-through jets and pileup clusters.

After the cluster selections, the main sources of background are low momentum hadrons, which come from pileup interactions, and for the muon channel there is a significant contribution from the $Z \to \mu\mu$ process. To estimate this $Z \to \mu\mu$ contribution a data driven transfer factor is derived, as described in detail in Ch. 6.5.4.

6.4.1 Cluster Selections

A major part of the background contribution is a result from out-of-time (OOT) pileup, where the cluster is a remnant from an earlier collision. These clusters can be identified by using the cluster time defined in Ch. 4.6.

For the signal region, CSC clusters are required to have a time signature of $-5\,\text{ns} < t_{\text{cluster}} < 12.5\,\text{ns}$. The signal has a small positive tail due to slow moving HNLs, therefore the upper bound on the time signature is larger, compared to the lower bound. Additionally, the time spread (introduced in Eq. 5.3) is required to be $t_{\text{spread}} < 20\,\text{ns}$. The timing requirement additionally allows the definition of a out-of-time control region by requiring $t_{\text{cluster}} < -12.5\,\text{ns}$. The OOT region uses only the negative timing to allow for later reinterpretations of the results for different signal models, with even slower moving or even delayed HNL signals.

As explained in Ch. 4.6 the cluster time for MDS in the DT only has the bunch crossing (BX) information available and due to the use of the statistical mode to average the different timing information the resulting time will be an integer where zero stands for the current bunch crossing. The analysis requires that the DT time signature for the signal process is $\text{BX}_{\text{cluster}} = 0$. The negative OOT control region is then defined as $\text{BX}_{\text{cluster}} < 0$, again only selecting negative time signatures to leave room for later reinterpretations.

The CSC and DT cluster timing distributions for signal and a $W \to l\nu$ sample are shown in Fig. 6.13. The distributions clearly shows that the signal process is mostly confined in the in-time region, while the $W \to l\nu$ sample is mostly flat in this distribution, due to the fact that the clusters in the $W \to l\nu$ sample are coming from pileup interactions.

To suppress clusters produced by jets that are not fully contained in the calorimeters and are therefore punching through to the CSC and DT systems, CSC(DT) clusters which are within $\Delta R < 0.4$ to an AK4 jet with $|\eta| < 3.0$ and $p_{\text{T}} > 20(10)\,\text{GeV}$ are vetoed. The innermost chambers of both the DT and CSC are most prone to noise from punch-through, due to the least amount of shielding in front of the chambers. Therefore CSC clusters which are matched within $\Delta\text{R} < 0.4$ to hits in the innermost chambers ME11 and ME12 and DT clusters which are matched within $\Delta\text{R} < 0.4$ to more then 1 hit in the MB1 chamber are also vetoed. CSC clusters are also vetoed if they match within $\Delta\text{R} < 0.4$ to a hit in the RPC chamber RE1/2 or if the cluster match to a MB1 segment or RB1 hit within $\Delta\text{R} < 0.4$.

To suppress cluster originating from muons undergoing bremsstrahlung, any cluster matching within $\Delta\text{R} < 0.4$ to a global muon candidate with $p_{\text{T}} > 10(20)\,\text{GeV}$ for DT(CSC) are vetoed. In the DT system there are two regions (chimneys) at $\eta = 0.3, \phi = 1.7$ and $\eta = -0.3, \phi = 1.15$ being occupied by cables, cooling and other service. This in turn means that there are no DT chambers in this specific region, which in turn reduces the muon reconstruction efficiency. For this analysis

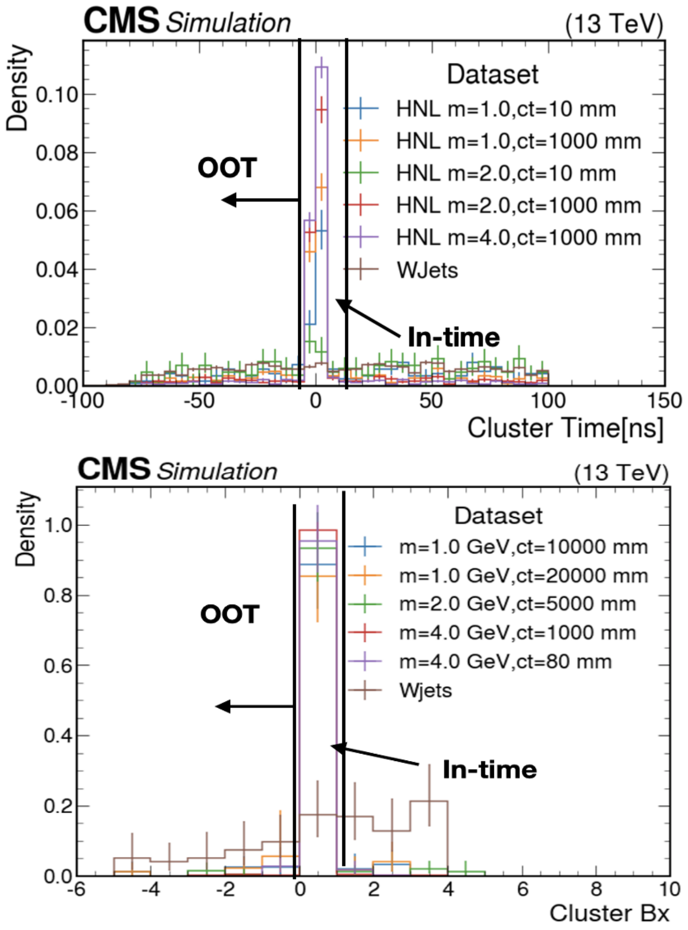

Figure 6.13: Cluster timing distributions of CSC (top) and DT (bottom) clusters for W → $l\nu$ and various signal processes.

specifically the chamber specific vetos, like the MB1 veto, completely fail, since there is no MB1 chamber in this region. Therefore clusters who are within $\Delta R < 0.3$ of the two chimneys are vetoed.

For CSC clusters the cut-based ID described in Ch. 5.4.2 is applied.

Lastly, if the the cluster occupies both the CSC and DT regions, the cluster in the DT region is prioritized due to a lower background level. The fraction of signal events in simulation where this overlap exists is less then 1 %.

An overview of all event selections is given in Tab. 6.6. Table 6.7 shows the efficiencies for the different selection steps for CSC clusters in the muon channel and Tab. 6.8 shows the same for DT clusters in the muon channel (for the electron channel see Ch. B). By comparing the efficiencies of the selections applied to a simulated signal sample and to the recorded data, the performance of the selections can be evaluated. The selection enhancing the signal region the most is the ME11/12 veto, removing clusters originating from muon bremsstrahlung. Without hits in ME11/12 the muon reconstruction is highly likely to fail, this also explains the small impact of the later muon veto. The second best performing cut in terms of S/B improvement is the

Table 6.6: Summary of event selection described in Ch. 6.4.1 .

Object	Muon Channel	Electron Channel
Lepton	$p_{\mathrm{T}} > 25(28)\,\mathrm{GeV}, \lvert\eta\rvert < 2.4$	$p_{\mathrm{T}} > 30(35)\,\mathrm{GeV}, \lvert\eta\rvert < 2.4$
Lepton	TightID, $I_{\mathrm{rel}} < 0.15$	TightID
Lepton	$N_{\mathrm{lepton}} = 1$	
MET	$p_{\mathrm{T}}^{\mathrm{miss}} > 30$ GeV	
CSC cluster	$N_{\mathrm{RecHits}} > 50$	
CSC cluster	No ME-11/ME-12 hits matched within $\Delta R < 0.4$	
CSC cluster	No muons with $p_{\mathrm{T}} > 20\,\mathrm{GeV}, \lvert\eta\rvert < 2.4$ within $\Delta R(\mathrm{cls}, \mu) < 0.8$	
CSC cluster	No jets with $p_{\mathrm{T}} > 10\,\mathrm{GeV}, \lvert\eta\rvert < 3.0$ within $\Delta R(\mathrm{cls}, \mathrm{jet}) < 0.4$	
CSC cluster	No RE1/2 RecHits matched within $\Delta R < 0.4$	
CSC cluster	No MB1 segments or RB1 RecHits matched within $\Delta R < 0.4$	
CSC cluster	$-5\,\mathrm{ns} < t_{\mathrm{cluster}} < 12.5\,\mathrm{ns}$	
CSC cluster	$t_{\mathrm{spread}} < 20\,\mathrm{ns}$	
CSC cluster	Cut-based ID	
DT cluster	$N_{\mathrm{RecHits}} > 50$	
DT cluster	No more than 1 MB1 hits within $\Delta R < 0.5$	
DT cluster	No jets with $p_{\mathrm{T}} > 20\,\mathrm{GeV}, \lvert\eta\rvert < 3.0$ within $\Delta R(\mathrm{cls}, \mathrm{jet}) < 0.4$	
DT cluster	No muons with $p_{\mathrm{T}} > 10\,\mathrm{GeV}, \lvert\eta\rvert < 2.4$ within $\Delta R(\mathrm{cls}, \mu) < 0.8$	
DT cluster	Matched to >= 1 RPC hit(s) in the same wheel within $\Delta\phi < 0.5$	
DT cluster	Not more than 8 MB1 hits in the adjacent wheel within $\Delta\phi < \pi/4$	
DT cluster	Mode of the BX of RPC hits=0, RPC matched within $\Delta\phi < 0.5$	
DT cluster	Veto cluster near DT chimneys within $\Delta R < 0.3$ around $((\eta, \phi) = (0.3, 1.7)$ or $(-0.3, 1.15))$	

in-time requirement of the clusters, effectively removing most clusters originating from pileup interactions. Lastly the Cluster ID enhances the signal region further.

Table 6.7: Efficiencies for CSC cluster selections in the muon channel. The Efficiencies for data is compared with a μ-HNL signal with a mass of 4 GeV and $c\tau$ of 1 m. The signal yield corresponds to a luminosity of 120 fb^{-1} within the CSC fiducial acceptance. For each selection, the cumulative efficiency and the individual selection efficiency are computed. The last column corresponds to the ratio of individual selection efficiency between signal and data.

	Data - Muon Channel			Signal μ-HNL (4 GeV,1m)			
Selection	No. of Events	cum.	eff.	Yield	cul.	eff.	eff. S/B
	3.09e+08	-	-	54.8	-	-	-
Trigger	2.50e+08	8.09e-01	0.809	26.7	4.98e-01	0.498	0.62
MET	1.57e+08	5.08e-01	0.628	18.7	3.48e-01	0.700	1.11
METfilters	1.57e+08	5.08e-01	1.000	18.7	3.48e-01	1.000	1.00
Good lepton	1.02e+08	3.30e-01	0.650	17.1	3.20e-01	0.919	1.41
$n_{\text{cls}} >= 1$	6.12e+07	1.98e-01	0.600	8.74	1.63e-01	0.508	0.85
$\Delta R(\text{l}, \text{cls}) > 0.8$	1.77e+07	5.73e-02	0.289	8.26	1.54e-01	0.947	3.28
ME11/ME12 veto	1.19e+06	3.85e-03	0.067	5.63	1.06e-01	0.686	10.24
Jet Veto	1.07e+06	3.46e-03	0.899	5.15	9.69e-02	0.918	1.02
Muon Veto	1.06e+06	3.43e-03	0.991	4.94	9.29e-02	0.958	0.97
MB1 segment veto	1.06e+06	3.43e-03	1.000	4.88	9.19e-02	0.988	0.99
RB1 veto	1.05e+06	3.40e-03	0.991	4.79	9.01e-02	0.981	0.99
RE12 veto	1.04e+06	3.37e-03	0.990	4.72	8.89e-02	0.986	1.00
In-time Cut	1.88e+05	6.08e-04	0.181	4.67	8.79e-02	0.989	5.46
TimeSpread Cut	1.23e+05	3.98e-04	0.654	4.6	8.64e-02	0.983	1.50
ClusterID	8.97e+04	2.90e-05	0.073	2.75	5.17e-02	0.598	8.19

Table 6.8: Efficiencies for DT cluster selections in the muon channel. The efficiencies for data is compared with a μ-HNL signal with a mass of 4 GeV and $c\tau$ of 1 m. The signal yield corresponds to a luminosity of $120 fb^{-1}$ within the DT fiducial acceptance. For each selection, the cumulative efficiency and the individual selection efficiency are computed. The last column corresponds to the ratio of individual selection efficiency between signal and data.

	Data - Muon Channel			Signal μ-HNL (4 GeV,1m)			
Selection	No. of Events	cum.	eff.	Yield	cul.	eff.	eff. S/B
	3.09e+08	-	-	58.2	-	-	-
Trigger	2.50e+08	8.09e-01	0.809	36.1	6.20e-01	0.620	0.77
MET	1.57e+08	5.08e-01	0.628	24.9	4.28e-01	0.690	1.10
METfilters	1.57e+08	5.08e-01	1.000	24.9	4.28e-01	1.000	1.00
Good lepton	1.02e+08	3.30e-01	0.650	22.9	3.93e-01	0.920	1.42
$n_{\text{cls}} >= 1$	4.24e+07	1.37e-01	0.416	9.75	1.68e-01	0.426	1.02
$\Delta R(\text{l}, \text{cls}) > 0.8$	3.53e+06	1.14e-02	0.083	9.0	1.55e-01	0.923	11.12
MB1 Veto	1.18e+05	3.82e-04	0.033	4.81	8.26e-02	0.534	16.18
Jet Veto	8.63e+04	2.79e-04	0.731	4.68	8.04e-02	0.973	1.33
Muon Veto	8.52e+04	2.76e-04	0.987	3.07	5.27e-02	0.656	0.67
RPC>1	4.95e+04	1.60e-04	0.581	3.02	5.19e-02	0.984	1.71
MB1 adj. wheel	4.54e+04	1.47e-04	0.917	2.94	5.05e-02	0.974	1.06
Time cut(BX=0)	1.11e+04	3.59e-05	0.244	2.9	4.98e-02	0.986	4.09
DT chimney veto	9.69e+03	3.14e-05	0.873	2.62	4.50e-02	0.903	1.04

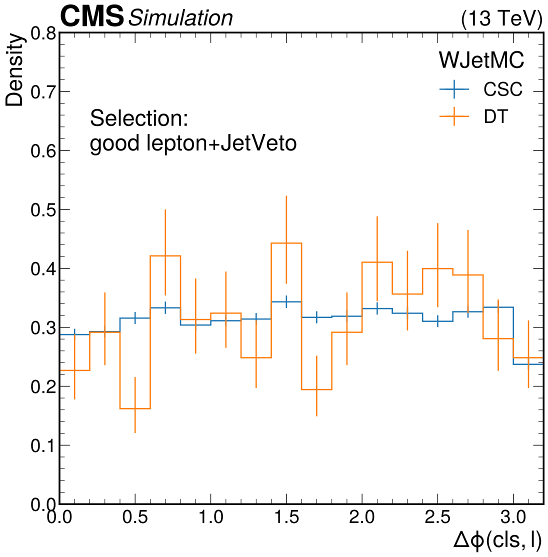

Figure 6.14: $\Delta\phi_{\mathrm{lep}}$ distribution between CSC and DT clusters of simulated $\mathrm{W} \to l\nu$ events with lepton selections and jet vetos applied.

6.5 Background Estimation

After applying all event and cluster selections described in Ch. 6.4 the dominant background is $\mathrm{W} \to l\nu$. The cluster in this case is the result of a low momentum hadron from pileup, recoil or the underlying event. For pileup, this was confirmed by studying simulated $\mathrm{W} \to l\nu$ samples with and without pileup, where it was observed that the only generator level particles that are geometrically matched to the cluster are pions, kaons, protons and neutrons with a p_{T} below 2 GeV. To estimate the background contribution an ABCD data-driven method used, where the size of the cluster acts as the main discriminant and the $\Delta\phi(\mathrm{cluster}, \mathrm{lep})$ variable is the second variable. Background clusters in general have less hits compared to the signal process, which motivates the number of hits in a cluster as a variable. For the pileup background the $\Delta\phi(\mathrm{cluster}, \mathrm{lep})$ distribution is flat, since the cluster and the lepton are independent from each other. In the muon channel there is additionally a large contribution of the $\mathrm{Z} \to \mu\mu$ process, where one muon is not reconstructed properly and additionally undergoes bremsstrahlung, producing a cluster in the muon system. This background is predicted in a control region and the background yields in the signal region are then predicted via a transfer factor.

6.5.1 ABCD Method

The background is estimated with the data driven ABCD method. This method requires two uncorrelated variables, meaning that introducing a cut on one does not change the shape of the distribution of the other variable. As already mentioned before, $\Delta\phi(\mathrm{cluster}, \mathrm{lep})$ is a flat distribution for background and peaks close to π for signal, since the lepton and cluster are expected to be back to back, as can be seen in Fig. 6.14.

Here the clusters are mostly from pileup, which makes the clusters uncorrelated to the lepton in the event. The main discriminant is the size of the cluster, N_{rechit}, since

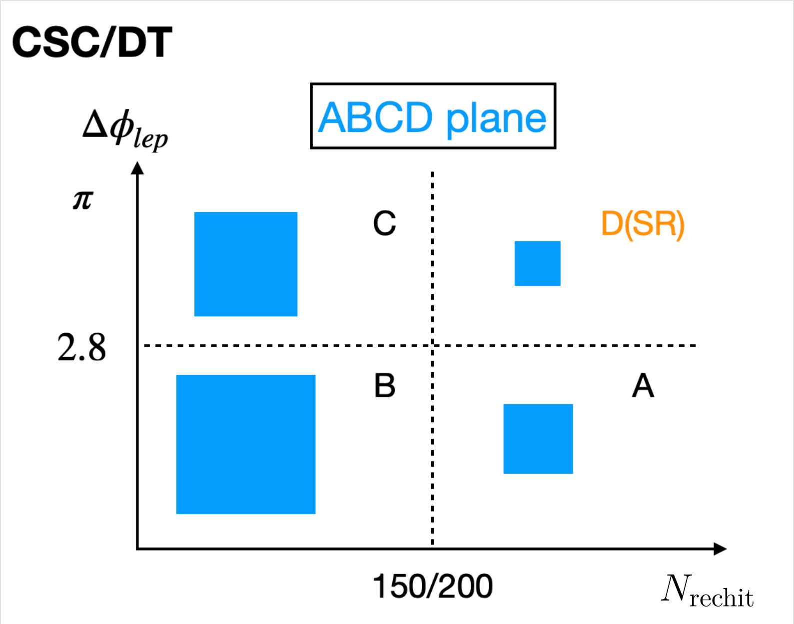

Figure 6.15: Definition of the ABCD plane. The N_rechit cut for DT(CSC) of 150(200) and the $\Delta\phi_\text{lep}$ cut of 2.8 are shown. The size of the blue squares indicates the size of the background contributions in each bin.

signal clusters tend to produce hadronic showers with a larger hit multiplicity. The background estimation targets pileup clusters, but the ABCD method is not limited to estimating pileup clusters, but rather any event, where both ABCD variables are uncorrelated, e.g. a cosmic muon resulting in a cluster.

The ABCD plane is spanned by the two variables and is shown in Fig. 6.15. It is divided in four bins A,B,C and D where bin D is the bin with the most signal. The estimation of the number of events in each bin follows the description given in Ch. 5.5, where the four unknown variables (B_A,B_B,B_C,μ) are also extracted from a maximum likelihood fit, with the same treatment of the nuisance parameters. The exclusion limits are also evaluated with the same frequentist approach [108–110].

6.5.2 Signal Region Optimization

For the ABCD method a cut on each of the two variables has to be introduced, splitting the ABCD plane in four separate regions. These cuts impact the sensitivity of the search significantly, therefore the cuts are optimized based on the expected limit on the cross section of a HNL model with a mass of 4 GeV and $c\tau = 1\,\text{m}$. Instead of using recorded data, the background used for the optimization is estimated using a OOT control region and applying a transfer factor to transfer the OOT prediction to the in-time region.

The OOT control region is defined by requiring the cluster time to be $t_\text{cluster} < -12.5\,\text{ns}$ for CSC clusters and $\text{BX}_\text{cluster} < 0$ for DT clusters. Measuring the OOT to in-time transfer factor requires the definition of an in-time control region. For this, a cut on the $\Delta\phi(\text{cluster},p_\text{T}^\text{miss})$ is introduced of $\Delta\phi(\text{cluster},p_\text{T}^\text{miss}) > 0.7$. For signal the p_T^miss and the cluster will be aligned, as the p_T^miss is a result of the cluster in the PF algorithm. This cut is indirectly applied to the signal region, since $\Delta\phi(\text{cluster},p_\text{T}^\text{miss})$ and $\Delta\phi(\text{cluster},\text{lep})$ are strongly correlated for the signal.

To make both control regions comparable, the $\Delta\phi(\text{cluster},p_{\mathrm{T}}^{\text{miss}})$ cut is also introduced to the OOT control region for the transfer factor measurement. The transfer factor $\mathrm{TF}_{\text{OOT-InTime}}$ then is defined as:

$$\mathrm{TF}_{\text{OOT-InTime}} = \frac{\mathrm{InTime}(\Delta\phi(\text{cluster}, p_{\mathrm{T}}^{\text{miss}}) > 0.7)}{\mathrm{OOT}(\Delta\phi(\text{cluster}, p_{\mathrm{T}}^{\text{miss}}) > 0.7)}. \tag{6.6}$$

The transfer factor is measured to be 0.9 for DT and 0.25 for CSC clusters in both the muon and electron channel. To estimate the background contribution in the signal region the following relation is used:

$$\mathrm{OOT}(N_{\text{rechit}} > X, \Delta\phi_{\text{lep}} > Y) \times \mathrm{TF}_{\text{OOT-InTime}} \times R_{\text{lumi}}, \tag{6.7}$$

where X and Y are the thresholds and R_{lumi} is the ratio of full Run-2 luminosity to the processed Run-2 luminosity, since at the point of this study the full Run-2 data set was not yet fully processed. The thresholds for $\Delta\phi(\text{cluster}, \text{lep})$ are scanned between 1.0 and π and N_{rechit} is varied between 100 and 340 for CSC clusters and 100 to 200 for DT clusters, which corresponds to the tail end of the N_{rechit} distribution. At each tested point the background is evaluated by applying the transfer factor to the OOT control region to obtain the background prediction, while the signal yields are obtained from simulation. All systematic uncertainties are considered during the limit calculation (See Ch. 6.7).

Figure 6.16 shows the expected limit as projections on $\Delta\phi(\text{cluster}, \text{lep})$ and N_{rechit}, showing the optimal thresholds. Figure 6.17 shows the background yields in bin D as a function of N_{rechit}.

The scans from the OOT extrapolation show a best performance at thresholds of $N_{\text{rechit}} > 170(130)$ for CSC(DT) clusters, but the $\mathrm{Z} \to \mu\mu$ background has a significant impact and uncertainty, while mostly being present at lower N_{rechit} thresholds (See Ch. 6.5.4 for the detailed $\mathrm{Z} \to \mu\mu$ background estimation method). Therefore slightly tighter N_{rechit} cuts close to the optimal point, are chosen to reduce this background yield while still maintaining a sensitivity close to the optimum. Thresholds of N_{rechit} $> 200(150)$ for CSC(DT) clusters and$\Delta\phi(\text{cluster}, \text{lep}) > 2.8$ are chosen.

Tab. 6.9 summarizes the signal and background yields at the chosen thresholds.

The $\mathrm{Z} \to \mu\mu$ background is a major contribution to the analysis (See later Ch. 6.5.4) in the muon channel. It is found that the $\mathrm{Z} \to \mu\mu$ background is mostly present in DT clusters that have most of their hits in the MB2 station. A possible explanation for this is the thin shielding between MB1 and MB2, compared to the shielding between MB2 and MB3. Splitting the DT region into two different regions, a MB2 region and a MB3/4 region, therefore improves the sensitivity of the analysis. Events in the muon channel with clusters in the DT are split on where most of the hits of the clusters are located, so if most of the cluster is located in the MB2 chamber, the cluster is assigned to the MB2 region.

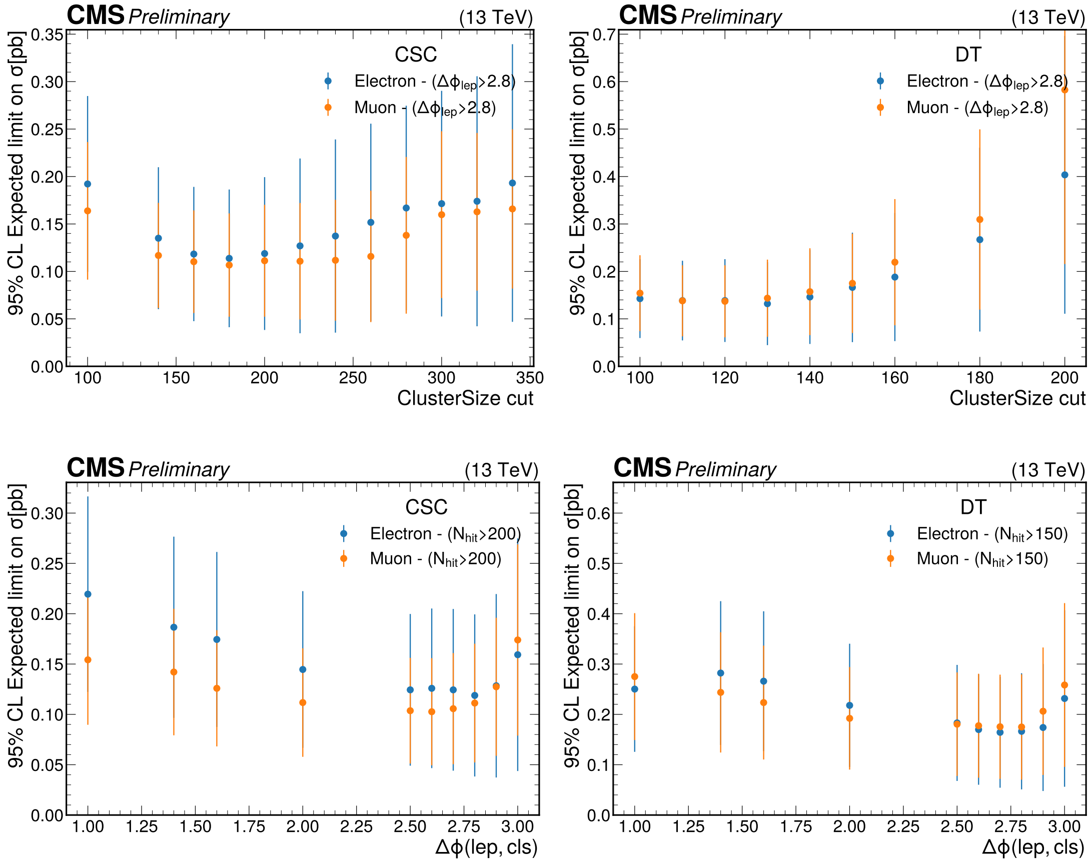

Figure 6.16: Expected limits as a function of cuts on N_{rechit} (top) and $\Delta\phi(\text{cluster}, \text{lep})$ (bottom) for CSC clusters and DT clusters.

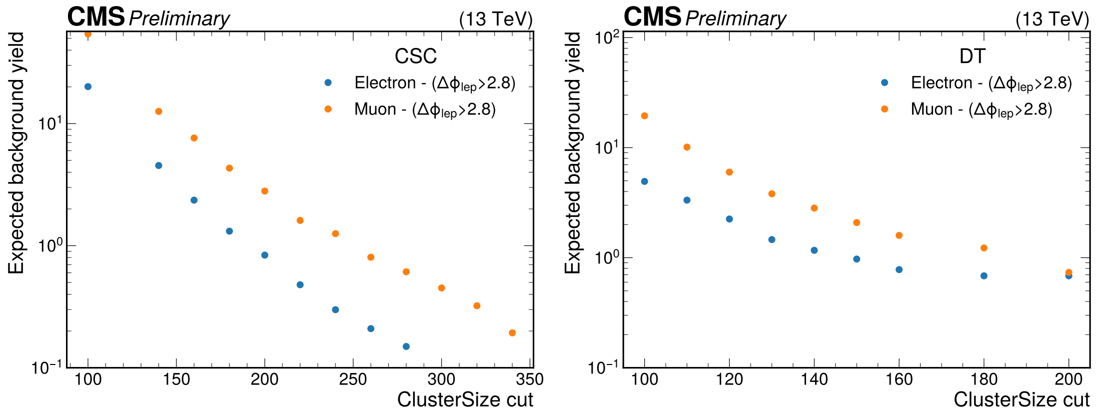

Figure 6.17: Expected background yields in bin D as a function of the cuts on N_{rechit} for CSC clusters and DT clusters.

Table 6.9: Summary of signal and background yields in the bins of the ABCD plane for the optimal ABCD thresholds,(N_{rechit},$\Delta\phi(\text{cluster}, \text{lep})$)= $(200(150), 2.8)$ for CSC(DT). The signal model consist of a HNL with the same flavor as the prompt lepton, a HNL mass of 4 GeV and $c\tau = 1\,\text{m}$. Yields correspond to luminosity of 120(122)fb^{-1} for muon(electron) channel respectively.

Channel	process	cut(N_{rechit},$\Delta\phi_{\text{lep}}$)	A	B	C	D
Muon(CSC)	bkg	(200,2.8)	21.75	6483.75	835.5	2.80
Muon(CSC)	signal	(200,2.8)	0.31	0.63	1.19	0.53
Muon(DT)	bkg	(150,2.8)	15.3	5569.6	759	2.09
Muon(DT)	signal	(150,2.8)	0.15	0.70	1.42	0.28
Electron(CSC)	bkg	(200,2.8)	7.0	2756.8	329.8	0.84
Electron(CSC)	signal	(200,2.8)	0.13	0.26	0.44	0.24
Electron(DT)	bkg	(150,2.8)	9.0	2374	256	0.97
Electron(DT)	signal	(150,2.8)	0.12	0.42	0.60	0.19

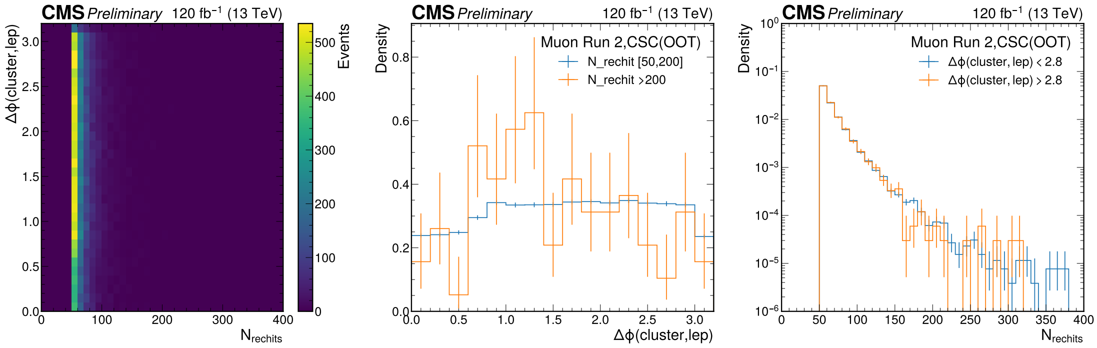

Figure 6.18: 2D distribution of N_{rechit} and $\Delta\phi(\text{cluster}, \text{lep})$ (left) of CSC clusters for the OOT control region($t_{\text{cluster}} < -12.5$ ns) in the muon channel. The middle and right panel shows 1D projections on N_{rechit} and $\Delta\phi(\text{cluster}, \text{lep})$ at the chosen thresholds.

6.5.3 Closure Tests

To validate the data-driven background estimation, two control regions are defined to test the closure of the ABCD method in these regions. Closure in this case means, that the estimated and observed number of events in bin D are compatible with the observed number of events in the same bin. Since these control regions are mostly signal free, no large difference between the predicted and observed number of events is expected, if the method works correctly. Remaining non-closures are later propagated as systematic uncertainties. The following closure tests are performed with only 120 fb^{-1} for the muon channel and 122 fb^{-1} for the electron channel of the data, since at the time of the study the data was not yet fully processed.

OOT CR

The OOT control region is defined by requiring the cluster time to be $t_{\text{cluster}} < -12.5$ ns for CSC clusters and $\text{BX}_{\text{cluster}} < 0$ for DT clusters. This region is relatively free of signal, since most of the signal is contained in the in-time region (See Fig. 6.13).

The distributions of N_{rechit} and $\Delta\phi(\text{cluster}, \text{lep})$ in the OOT control region for CSC clusters in the muon channel are shown in Fig. 6.18, for the electron channel and for DT cluster see Fig. B.1 and Fig. B.2 in the appendix. Each plot shows two distributions, being separated by the chosen threshold. Additionally, the yield in each bin of the ABCD method is measured for a scan of different thresholds close to the selected optimum chosen in Ch. 6.5.2 . The yields are shown in Tab. 6.10 for CSC clusters in the muon channel. For DT clusters and the electron channel see Tab. B.7 to Tab. B.9 in the appendix. The predicted and measured yields in bin D agree well for the thresholds chosen in Ch. 6.5.2, but for looser thresholds on N_{rechit} and $\Delta\phi(\text{cluster}, \text{lep})$ show a larger disagreement in the muon channel. This is due to the fact that the $\text{Z} \rightarrow \mu\mu$ background is impacting the signal region in a larger way at lower thresholds.

Table 6.10: Validation of the ABCD method in the OOT control region for CSC cluster selections in the muon channel.

cut(N_{rechit},$\Delta\phi_{\text{lep}}$)	A	B	C	D	Prediction($\frac{A\times C}{B}$)
(140,2.8)	390	25632	3311	40	50.38 ± 2.72
(160,2.8)	236	25786	3334	17	30.51 ± 2.06
(180,2.8)	134	25888	3337	14	17.27 ± 1.53
(200,2.8)	87	25935	3342	9	11.21 ± 1.22
(220,2.8)	50	25972	3345	6	6.44 ± 0.92
(200,2.6)	85	23952	5325	11	18.90 ± 2.07
(200,2.7)	86	24883	4394	10	15.19 ± 1.66
(200,2.8)	87	25935	3342	9	11.21 ± 1.22

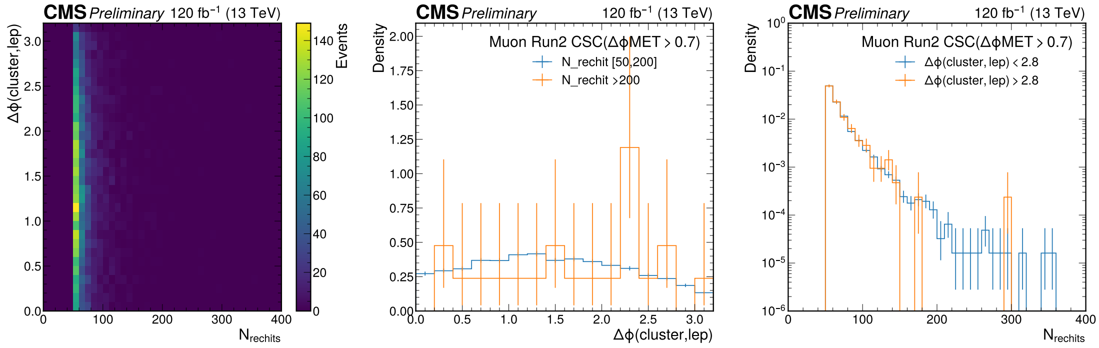

Figure 6.19: 2D distribution of N_{rechit} and $\Delta\phi_{lep}$ (left) of CSC clusters for the in-time control region($\Delta\phi_{MET} > 0.7$) in the muon channel. The middle and right panel shows the 1D projections on N_{rechit} and $\Delta\phi_{lep}$ at the chosen thresholds.

In-time CR

The in-time control region is defined by requiring $\Delta\phi(\text{cluster},p_{\text{T}}^{\text{miss}}) > 0.7$ in addition to the other signal selections. This region is expected to be signal free, since the signal clusters and the $p_{\text{T}}^{\text{miss}}$ should align.

The distributions of N_{rechit} and$\Delta\phi(\text{cluster}, \text{lep})$ in the in-time control region for CSC clusters in the muon channel are shown in Fig. 6.19, while the distributions for the electron channel and the DT clusters can be found in Fig. B.3 and Fig. B.4 in the appendix. Each plot shows two distributions, being separated by the chosen threshold. Additionally, the yield in each bin of the ABCD method is measured for a scan of different thresholds close to the selected optimum chosen in Ch. 6.5.2 . The yields are shown in Tab. 6.11 for CSC clusters in the muon channel, while the yields for the electron channel and the DT clusters are shown in Tab. B.10 to Tab. B.12. Overall a good agreement between the predicted yield in bin D and the measured bin D for the chosen thresholds in Ch. 6.5.2 can be observed. Similar to the OOT CR a disagreement at looser thresholds in the muon channelcan be observed, which can be attributed to the Z → $\mu\mu$ background.

Table 6.11: Validation of the ABCD method in the in-time control region for CSC cluster selections in the muon channel.

cut(N_{rechit},$\Delta\phi_{\mathrm{lep}}$)	A	B	C	D	Prediction($\frac{A\times C}{B}$)
(120,2.8)	212	5989	409	14	14.48 ± 1.24
(140,2.8)	112	6089	419	4	7.71 ± 0.83
(160,2.8)	64	6137	421	2	4.39 ± 0.59
(200,2.8)	20	6181	422	1	1.37 ± 0.31
(220,2.8)	14	6187	422	1	0.95 ± 0.26
(200,2.6)	18	5869	734	3	2.25 ± 0.54
(200,2.7)	18	6032	571	3	1.70 ± 0.41
(200,2.8)	20	6181	422	1	1.37 ± 0.31

6.5.4 $\mathrm{Z} \to \mu\mu$ Background Estimation

The $\mathrm{Z} \to \mu\mu$ background in the muon channel is not covered within the ABCD method, since the background is not uniformly distributed in the two ABCD variables but rather is very similar to the signal distributions. Therefore this background needs to be estimated separately. For this, a $\mathrm{Z} \to \mu\mu$ control region is defined by inverting the MB1 and ME11/12 hit selections described in Ch. 6.4.1. This region will be enhanced in clusters from muon bremsstrahlung, where $\mathrm{Z} \to \mu\mu$ is the main process contributing. To estimate the $\mathrm{Z} \to \mu\mu$ contribution the same ABCD data-driven method is applied in this CR. The observed non-closure is then taken as the background contribution from the $\mathrm{Z} \to \mu\mu$ process, labeled $N^{\mathrm{CR,D}}_{\mathrm{Z}\to\mu\mu}$, while the number of predicted events by the ABCD method in bin D of this control region is coming from $\mathrm{W} \to l\nu$ and other processes, labeled $N^{CR,D}_{ABCbkg}$. The predicted event yield from the $\mathrm{Z} \to \mu\mu$ process in this control region is then extrapolated to the signal region in bin D, labeled $N^{\mathrm{SR,D}}_{\mathrm{Z}\to\mu\mu}$, by applying a transfer factor ζ, which measures the efficiency for clusters originating from muon bremsstrahlung to fail the MB1 and ME11/ME12 vetoes:

$$N^{CR,\mathrm{D}}_{\mathrm{Z}\to\mu\mu} = N^{CR,D}_{obs} - N^{CR,D}_{ABCbkg} \tag{6.8}$$

$$N^{SR,\mathrm{D}}_{\mathrm{Z}\to\mu\mu} = \zeta \times N^{\mathrm{CR,D}}_{\mathrm{Z}\to\mu\mu} \tag{6.9}$$

Transfer Factor Measurement

The transfer factor ζ has to be measured in an orthogonal sample, which is enhanced in events with muon bremsstrahlung. This orthogonal region targets the dileptonic $\mathrm{t\bar{t}}$ process, where the muon from the top decays undergoes bremsstrahlung and produces a cluster. For the prompt lepton, an electron is selected that fires the single electron trigger. Additionally, two jets with $p_{\mathrm{T}} > 20\,\mathrm{GeV}$, $|\eta| < 2.4$ and CSV-v2 medium b-tag working point are required. The selected cluster has to be separated from the b-tagged jets by $\Delta R > 0.8$ to ensure that the cluster is not produced by the jets punching through to the muon system.

The transfer factor is then defined as:

$$\zeta = \frac{N_{\mathrm{events}}(\mathrm{t\bar{t}_{SR}})}{N_{\mathrm{events}}(\mathrm{t\bar{t}_{Inv\ MB1/ME11}})}, \tag{6.10}$$

where $N_{\text{events}}(\mathrm{t\bar{t}}_{\text{SR}})$ is the number of events for the $\mathrm{t\bar{t}}$ sample with the signal region (SR) selections and $N_{\text{events}}(\mathrm{t\bar{t}}_{\text{Inv MB1/ME11}})$ is the number of events for the $\mathrm{t\bar{t}}$ sample with the SR selections, where the MB1/ME11 selections are inverted.

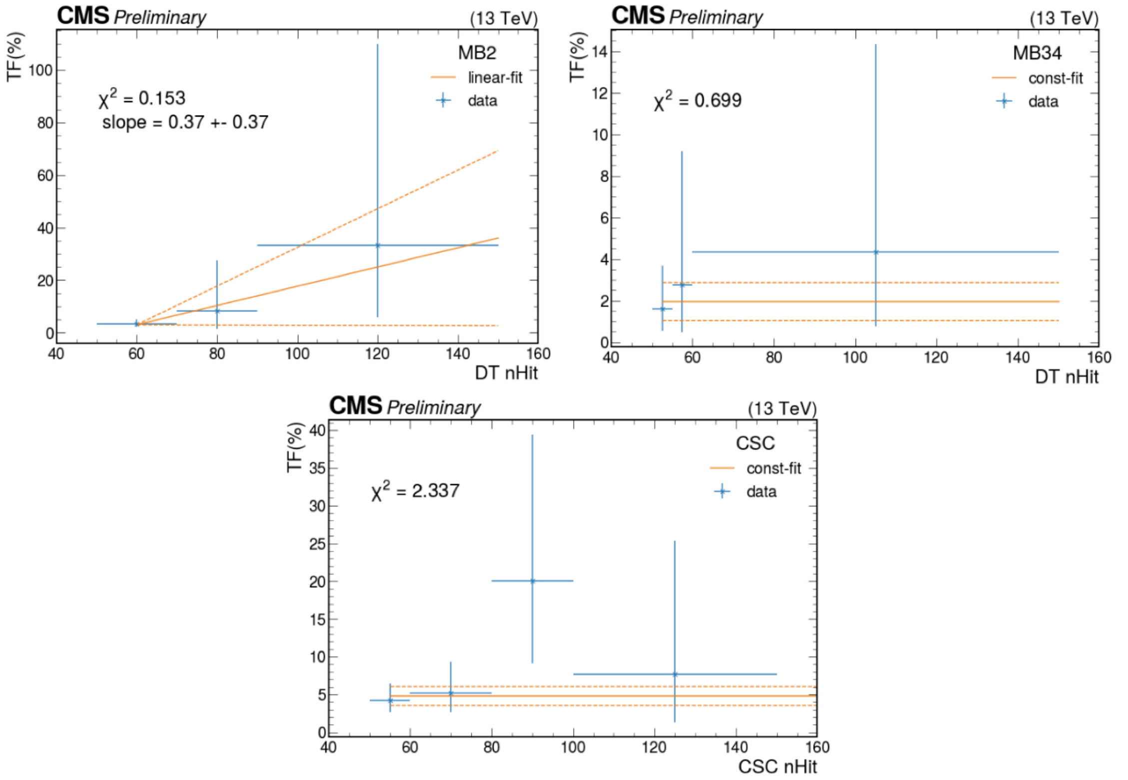

Figure 6.20: The transfer factor ζ is measured in bins of the cluster size separately for clusters in station MB2 (upper left), station MB3/4 (upper right), and in the CSC detector (bottom). The transfer factors are fitted to a linear function for clusters in station MB2, and to a constant function for clusters in the CSC and MB3/4. The uncertainty for each data point is computed with the Garwood interval [126].

The measurement of the transfer factor ζ is done in multiple bins of the cluster size separately, to check for a dependence of ζ and the cluster size. Fig. 6.20 shows the transfer factor measured in bins of the cluster size for the DT category, split into the MB2 and MB3/4 region, and CSC category. For the CSC and the MB3/4 category, a constant transfer factor is fitted to the data. For the MB2 category a linear increase in the transfer factor in regards to the cluster size can be observed, and therefore a linear fit is performed. With the linear fit, the transfer factor value at the cluster size threshold of 150 is derived, which is then used to estimate the background yields.

The choice of the fit functions used for the three categories is tested in the following. Since the number of events is rather limited, to test the choice of the fit functions the selections on the electron and on the b-jets are loosened, which results in a sufficient dataset to perform the test. The electron ID is loosened (going from tight ID to loose ID), while the b-jet CSV-v2 working point is loosened to medium and the ΔR veto is also changed to 0.4 from 0.8. The resulting sample has around 7 times more events passing the denominator selections of the transfer factor measurement. On this sample, a F-test [127] is performed to compare the fitting models: The F-statistic for two composite fit models, 1 and 2, where model 1 has fewer parameters than model 2, is constructed as:

$$F = \frac{\frac{\chi_1^2-\chi_2^2}{p_2-p_1}}{\frac{\chi_2^2}{n-p_2}}, \tag{6.11}$$

where $\chi^2_{1(2)}$ is the chi-square of model 1(2), $p_{1(2)}$ is the number of parameters of model 1(2) and n is the number of data. In this specific case, model 1 is considered a constant fit while model 2 is a linear fit. The null hypothesis is that model 2 does not provide a significantly better fit than model 1, where the F distribution has $p_2 - p_1$ and $n - p_2$ degrees of freedom. The null hypothesis is therefore rejected if the the p-value calculated for F is less than 0.05.

For the CSC and MB3/4 categories the p-value is larger than 0.05, thereby confirming the choice of model 1, a constant fit. For MB2 the p-value is 0.03, which is smaller then the 0.05 cutoff mentioned before, thereby showing that a linear fit models the data better compared to a constant fit.

Tab. 6.12 summarizes the values of ζ and the predicted $\mathrm{Z} \to \mu\mu$ background yields in the signal region. For the CSC region, the $\mathrm{Z} \to \mu\mu$ background adds 3.5 events in the signal bin, while in the DT regions the $\mathrm{Z} \to \mu\mu$ mainly affects the MB2 region with 7.2 events, while the MB3/4 region stays relatively free of the $\mathrm{Z} \to \mu\mu$ background.

Table 6.12: Summary of the $\mathrm{Z} \to \mu\mu$ background estimation.

Region	Year	$N^{CR,D}_{obs}$	$N^{CR,D}_{ABCbkg}$	$N^{CR,\mathrm{D}}_{\mathrm{Z}\to\mu\mu}$	ζ	$N^{SR,\mathrm{D}}_{\mathrm{Z}\to\mu\mu}$
CSC	Full Run2	110	35.2 ± 2.5	74.7 ± 10.7	(4.8±1.3)%	3.5 ± 1.1
DT MB2	Full Run2	30	10.1 ± 1.3	19.9 ± 5.6	(36±33)%	7.2 ± 6.9
DT MB3/4	Full Run2	5	2.7 ± 0.7	2.3 ± 2.4	(2±1)%	0.05 ± 0.05

Validation in Simulation

Even though the size of the simulated $\mathrm{Z} \to \mu\mu$ sample is very limited, a test is performed to check the amount of $\mathrm{Z} \to \mu\mu$ events in the signal region. The available sample does not have enough events to give a meaningful prediction for the signal bin D, therefore this test is performed on the whole ABCD region. The signal region selections are applied to the simulated samples and the predicted yields are summarized in Tab. 6.13. Additionally, the table contains the yields obtained by applying the transfer factor from the previous section. It can be seen that the statistical error on the predicted yields from the simulated $\mathrm{Z} \to \mu\mu$ sample is extremely large. With this in mind it can be concluded that the transfer factor and the predicted yield from the simulated sample agree within the statistical uncertainty, but this should not be taken as a strong argument for the validity of the transfer factor method.

Validation in Data

To further validate the $\mathrm{Z} \to \mu\mu$ background estimation the prediction is validated in a subset of the signal region. For this, clusters in the DT MB2 region are selected,

Table 6.13: Validation of the $Z \rightarrow \mu\mu$ background prediction performed on the $Z \rightarrow \mu\mu$ MC simulation sample. The signal region yield predictions are obtained by using transfer factors of 0.015 for DT clusters and 0.057 for CSC clusters. This study was done before updating the TF measurement to include the DT MB2 and MB3/4 split and changing the ABCD thresholds, therefore different values for the TF are used compared to Tab. 6.12

Category	MB1 or ME11/12 inverted region yield	Predicted SR yield	Simulation SR yield
DT	13406 ± 2030	202 ± 30	447 ± 419
CSC	9865 ± 1723	562 ± 98	0 ± 450

Table 6.14: Validation of the ABCD method in the inverted $p_{\mathrm{T}}^{\mathrm{miss}}$ control region for CSC and DT cluster selections in the electron channel.

Region	cut(N_{rechit},$\Delta\phi_{\mathrm{lep}}$)	A	B	C	D	Prediction($\frac{A\times C}{B}$)
DT	(150,2.8)	175	55294	9790	39	30.98 ± 2.37
CSC	(200,2.8)	10	1461	202	2	1.38 ± 0.45

which are required to have less then 120 hits. This cluster size is small enough, so that the signal contamination is rather low, in fact the S/B ratio is more then 50 times worse then the S/B ratio in the most sensitive signal region (DT-MB3/4). The proxy signal region in this validation region is then defined by requiring clusters to have between 110 and 120 hits. The full background estimation is then performed:

First the $Z \rightarrow \mu\mu$ background yield is estimated by inverting the MB1 veto in this validation region and checking the number of events, which is 37. The ABCD method then leads to a predicted background yield of 25 ± 2. The difference (12 ± 6) is then taken as the $Z \rightarrow \mu\mu$ background and multiplied with the transfer factor at a threshold of 115 hits using the fit in Fig. 6.20, yielding a $Z \rightarrow \mu\mu$ background prediction in the signal region of 2.7 ± 1.6. By performing the standard ABCD method on the validation region, a predicted yield of 9.9 ± 1.3 in bin D is expected. Therefore adding the $Z \rightarrow \mu\mu$ prediction, the total predicted yield is 12.6 ± 2.1, while the observed event yield is 12, thereby validating that the $Z \rightarrow \mu\mu$ background prediction works well.

6.5.5 Closure Test in Additional Control Region

Finally the ABCD method can also be validated in a control region, where the $p_{\mathrm{T}}^{\mathrm{miss}}$ selection is inverted ($p_{\mathrm{T}}^{\mathrm{miss}} < 30\,\mathrm{GeV}$). This control region is expected to be largely signal free, since the signal events are expected to have a large amount of $p_{\mathrm{T}}^{\mathrm{miss}}$ in alignment with the cluster. By inverting the $p_{\mathrm{T}}^{\mathrm{miss}}$ selection, the muon channel will become significantly contaminated by $Z \rightarrow \mu\mu$ events, where the cluster aligns with a low p_{T} muon which normally would be suppressed. Therefore only the results in the electron channel are checked. Tab. 6.14 shows the yields in the electron channel for DT and CSC clusters. A good agreement between the observed and predicted yields can be observed.

6.5.6 Summary of Background Estimation

A summary of the total background in each of the analysis channels is shown in Tab. 6.15. In the electron channel for the CSC region 0.8 ± 0.3 and for the DT region 2.1 ± 0.6 events are expected due to the prediction of the ABCD method. In the muon channel it can be seen that for the CSC region the $\mathrm{Z} \to \mu\mu$ contributes nearly the same amount of background (3.5 ± 1.1) as the ABCD prediction (3.7 ± 0.7). For the DT MB2 region, the $\mathrm{Z} \to \mu\mu$ contribution dominates with 7.2 ± 6.5 events, while the ABCD method predicts 1.8 ±0.6 events. In the MB3/4 the $\mathrm{Z} \to \mu\mu$ contribution is nearly zero, while the ABCD method predicts 2.1 ±0.7 events.

Table 6.15: Summary of background estimations including ABCD backgrounds and $\mathrm{Z} \to \mu\mu$ in different analysis categories.

Channel	Region	cut(N_{rechit},$\Delta\phi_{\mathrm{lep}}$)	A	B	C	Prediction($\frac{A\times C}{B}$)	$N^{SR,\mathrm{D}}_{\mathrm{Z}\to\mu\mu}$	Tot. bkg
Muon	CSC	(200,2.8)	29	7733	987	3.7 ± 0.7	3.5 ± 1.1	7.2 ±1.3
Muon	DT MB2	(150,2.8)	11	5328	888	1.8 ± 0.6	7.2 ± 6.5	9.0 ±6.5
Muon	DT MB3/4	(150,2.8)	9	818	187	2.1 ± 0.7	0.05 ± 0.05	2.1 ±0.7
Ele	CSC	(200,2.8)	6	3221	410	0.8 ± 0.3	-	0.8 ± 0.3
Ele	DT	(150,2.8)	14	2444	360	2.1 ± 0.6	-	2.1 ± 0.6

6.6 Signal Cluster Simulation

This section details the studies performed to validate the accuracy of the MDS cluster simulation in respect to the detector response, cluster reconstruction and cluster identification. This section follows the methods described in Ch. 5.6, with the main difference being the inclusion of DT clusters, a different signal model and different N_{rechit} cuts. The same tag-and-probe approach is used on the same Z $\rightarrow \mu\mu$, using muon bremsstrahlung clusters as a proxy for the signal clusters. The data samples used are the same as in Ch. 5.6, same with the selection on the tag-and-probe method. In the following only changes to the results from Ch. 5.6 will be discussed in more detail, while it will be also noted which results stay the same.

6.6.1 Cluster Efficiency

The cluster efficiency measurement is updated, since the study presented before was done for CSC clusters with $N_{\text{rechit}} > 130$. This analysis uses CSC and DT clusters, while also changing the N_{rechit} cut of CSC clusters to > 200 hits. Therefore the cluster efficiency measurement is redone.

The N_{rechit} threshold in data is varied, until the measured clustering efficiency agrees with the efficiency measured in simulation. It is found that the efficiency in data agrees with simulation at a threshold of 156 and 210 for DT and CSC clusters respectively. The systematic uncertainty is therefore evaluated by selecting these thresholds to the signal simulation and comparing the yield in the signal region bin D. For CSC clusters the yield changes between $7 - 13\%$ and $7 - 16\%$ for DT clusters. A conservative 13% on CSC and 16% for DT uncertainty is applied to the signal simulations.

6.6.2 Cluster ID Efficiency

The cluster ID is only applied to CSC clusters and is not dependent on the N_{rechit} change, therefore the 5.1 % uncertainty measured before is applied in this analysis as well.

6.6.3 Jet Veto Efficiency

The jet-veto inefficiency in simulation is a result of the accidental matching of signal clusters to pileup jets. The same procedure as described in Ch. 5.6 is applied to measure the jet-veto efficiency in simulation and data. The Z $\rightarrow \mu\mu$ control region with the tag-and-probe selections is used and the jet-veto efficiency for CSC clusters is $92.29\% \pm 0.02\%$ for data and $94.27\% \pm 0.06\%$ for simulation. The ratio between data and simulation is used as a correction factor with 2.1 $\% \pm 0.06$, where the uncertainty on the correction factor only includes statistical uncertainties.

For DT clusters the jet-veto efficiencies are measured to be $98.29\% \pm 0.01\%$ for data and $98.89\% \pm 0.02\%$ for simulation. Due to the good agreement between data and simulation, no correction is applied to the signal simulation. In Fig. 6.21 the jet-veto efficiency as a function of the number of primary vertices N_{PV} is shown. It can be observed that the jet-veto efficiency decreases with higher N_{PV} due to the higher possibility of an accidental matching.

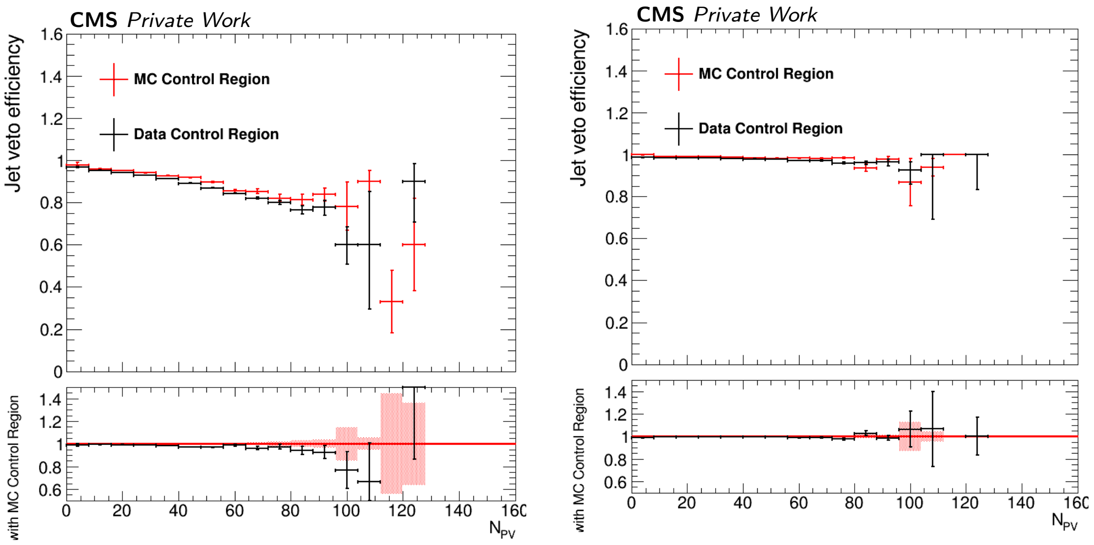

Figure 6.21: The jet-veto efficiency measured in data/MC control region for CSC(left) and DT(right) cluster selections.

6.6.4 Muon Veto Efficiency

The muon-veto inefficiency has two sources, one from accidental matching with pileup muons and one from HNL signals, that are reconstructed as muons due to the decay products of the HNL. For CSC clusters the muon-veto inefficiency measurement stays the same as described in Ch. 5.6 and a 6 % correction to the signal simulation is applied while also propagating a 4.5 % uncertainty.

For DT clusters the muon-veto inefficiency is measured to $95.71\% \pm 0.02\%$ for data and $95.88\% \pm 0.05\%$ for simulation. No correction is applied due to the good agreement between data and simulation. In Fig. 6.22 the muon-veto efficiency as a function of the number of primary vertices N_{PV} is shown.

6.6.5 RecHit and Segment Veto Efficiency

For CSC clusters the accidental matching of clusters to hits in the ME11/12, RPC hits in RE12 and RB1 and DT segments in MB1 is also checked in data and simulation. The result stays the same as in Ch. 5.6, resulting in a 3.3 % correction is applied to the signal simulation and a statistical uncertainty of 0.1 % is assigned as a systematic uncertainty.

For DT clusters the same method is used to evaluate the cluster selection uncertainties. For the RPC matching to the clusters, it is found that the efficiency in data of $98.2\% \pm 1\%$ agrees with the measured efficiency in simulation of 100%, therefore no correction is applied. The MB1 veto efficiency uncertainty is 7.4%.

6.6.6 Cluster Time Efficiency

The corrections and uncertainties for the CSC cluster time is the same as in Ch. 5.6, resulting in uncertainties of 0.9 % for the cluster time and 2.8 % for the time spread cut.

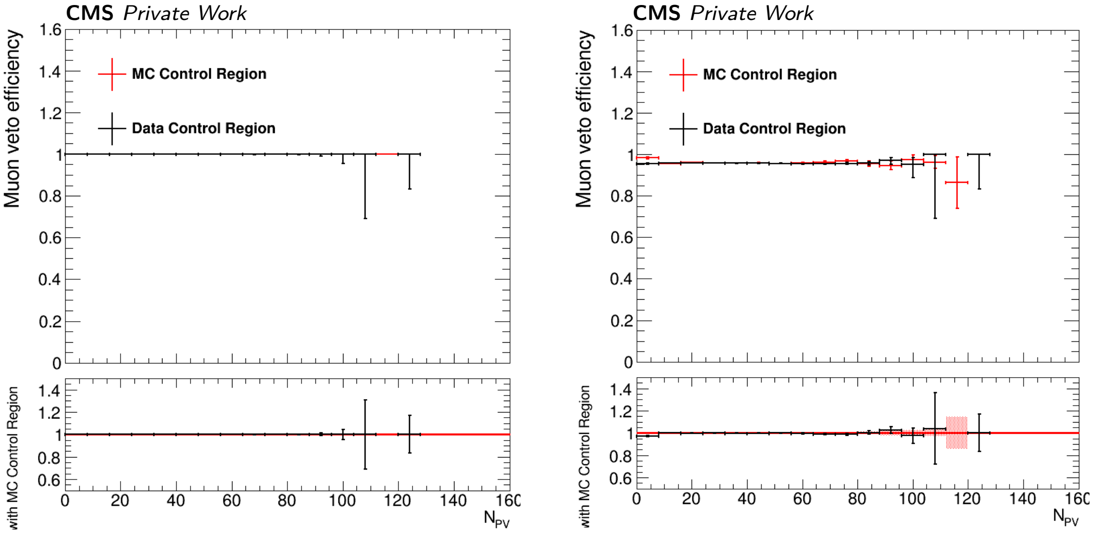

Figure 6.22: The muon-veto efficiency measured in data/MC control region for CSC(left) and DT(right) cluster selections.

For the DT time no correction or uncertainty is applied, due to the good agreement between recorded and simulated data.

Table 6.16: Summary of systematic uncertainty applied to signal simulations.

Systematic Uncertainty	Object	Size of unc.
Luminosity	-	1.6%
Pile-up	-	1%
W cross section	-	3.8%
W p_{T}	-	1.6%
Trigger	Muon	$< 0.1\%$
ID	Muon	$0.4 - 0.5\%$
ISO	Muon	$0.2 - 0.6\%$
Trigger	Electron	$0.2 - 0.3\%$
ID	Electron	$2.2 - 8.0\%$
JES	MET	2.0%
Cluster eff	CSC cluster	13%
Cut-based ID	CSC cluster	5.1%
JetVeto	CSC cluster	0.06%
MuonVeto	CSC cluster	4.5%
CSC readout	CSC cluster	1.0%
RechitVeto	CSC cluster	0.1%
Cluster time	CSC cluster	0.9%
Cluster time spread	CSC cluster	2.8%
Cluster reco	DT cluster	16%
MB1 veto	DT cluster	7.4%

6.7 Systematic Uncertainties and Simulation Corrections

The main background uncertainty reflects the statistical uncertainties in the background enriched regions of the ABCD method. These uncertainties account for between 18 and 40 % of the size of the total background, depending on the channel. Additionally, for the muon channel, the statistical uncertainty of the $\mathrm{Z} \to \mu\mu$ background estimate is propagated, consisting of the statistical uncertainty of the control region event yields and the statistical uncertainty of the transfer factor measurement. These two uncertainties account for around 30 % of the total background uncertainty.

6.7.1 Signal Uncertainties

The systematic signal uncertainties are summarized in Tab. 6.16 and will be discussed in more detail in the following sections. The signal uncertainties are dominated by the cluster modeling uncertainties.

Luminosity

The recorded data used in this analysis amounts to an integrated luminosity of 137 fb^{-1} combined for all three years of data taking and the simulated samples are normalized to this number. The measurement of the luminosity during the data taking is subject to systematic and statistical uncertainties, which are propagated as a total uncertainty of 1.6%[113–115].

Table 6.17: Summary of the uncertainty of the scale factors in the electron channel per year.

Channel	year	trigger	electron ID
DT	2018	-0.22/+0.22 %	-2.02/+3.58 %
DT	2017	-0.23/+0.23 %	-3.16/+4.80 %
DT	2016	-0.24/+0.24 %	-2.16/+3.27 %
CSC	2018	-0.23/+0.23 %	-3.56/+6.45 %
CSC	2017	-0.26/+0.26 %	-4.77/+8.07 %
CSC	2016	-0.29/+0.29 %	-3.39/+5.67 %

Pileup

As described before, the simulated distribution of the number of pileup interactions is reweighted to describe the recorded data better. The weights are derived from minimal bias samples during the data taking periods. The uncertainty on this reweighting is estimated by varying the pp inelastic cross section up and down one standard deviation and measuring the variation in the signal yield, resulting in a 1% uncertainty for all signal models [59].

W Cross Section and p_{T} Spectrum Correction

The theoretical prediction of the W boson cross section and the shape of the W boson p_{T} distribution both have a theoretical uncertainty assigned to them, which are propagated to the signal yield for the analysis. The PDF uncertainty dominates the uncertainty on the cross section which in total has a uncertainty of 3.8%.

The uncertainty on the p_{T} distribution is evaluated using the DYTURBO calculation. Using the scale variations of the NLO spectrum, the W p_{T} uncertainty is estimated, which acts as a proxy for the NNLO uncertainty. Fig. 6.23 shows the W p_{T} spectrum with six different choices of μ_F and μ_R, evaluated at NLO accuracy, where μ_F and μ_R are being varied up and down by a factor of 2 separately and coherently. The envelope of the scale variations is taken as the uncertainty of the W p_{T} spectrum correction and the impact on the yield in the signal region is evaluated to be around 1.6 %.

Lepton ID, ISO and Trigger

The uncertainties from the trigger efficiency measurements amount to > 0.1 % for the muon trigger and 0.2-0.3 % for the electron trigger. The muon ID and isolation have an 0.4-0.5 % and 0.2-0.6 % uncertainty assigned to them. The electron ID has an 2.2 - 8.0 % uncertainty assigned to it, depending on the signal region and data-taking conditions. A summary of the impact of different data taking conditions for each of the three years are given in Tab. 6.17 and Tab. 6.18 for the lepton scale factors.

Jet Energy Scale

The size of the Jet Energy Scale [86] uncertainty is 2.0 % for all signal models, since it affects the $p_{\mathrm{T}}^{\mathrm{miss}}$ cut applied in the analysis. The impact of the JES uncertainty is

Table 6.18: Summary of the uncertainty of the scale factors in the muon channel per year.

Channel	year	trigger	muon ID	muon ISO
DT	2018	-0.04/+0.04%	-0.36/+0.36%	-0.60/+0.61 %
DT	2017	-0.05/+0.05%	-0.46/+0.46%	-0.38/+0.38 %
DT	2016	-0.06/+0.06%	-0.48/+0.48%	-0.20/+0.20 %
CSC	2018	-0.05/+0.05%	-0.36/+0.36%	-0.60/+0.61 %
CSC	2017	-0.06/+0.06%	-0.46/+0.46%	-0.38/+0.38 %
CSC	2016	-0.07/+0.07%	-0.49/+0.49%	-0.20/+0.20 %

estimated by varying the p_{T} of all jets considered for the jet veto up and down by 1 σ and propagating the change to the $p_{\mathrm{T}}^{\mathrm{miss}}$ as well.

Cluster Modeling

The cluster modeling consists of the cluster efficiency, jet veto, muon veto, RecHit veto, Cluster time selection and for the CSC also the Cut-based ID. The corrections and uncertainties are described in Ch. 6.6. For CSC clusters these uncertainties

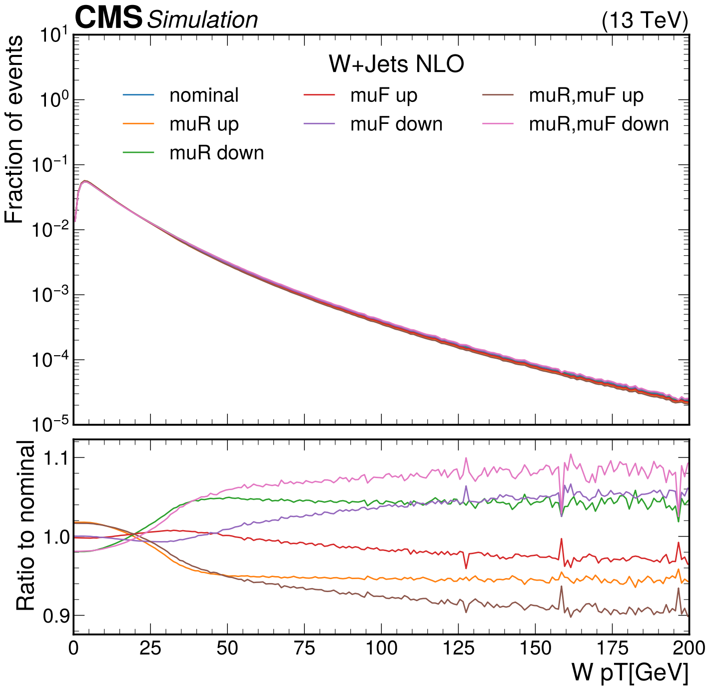

Figure 6.23: W p_T spectrum for six different choices of μ_F and μ_R, evalutated at NLO accuracy. The six different choices are μ_F and μ_R being varied up and down by a factor of 2 separately and coherently. The envelope of the scale variations is taken as the uncertainty of the W p_T spectrum correction.

amounts to 27.46 %, while for DT clusters the uncertainties sum up 23.4 %. For both CSC and DT clusters are the cluster modeling uncertainties the largest source of uncertainties.

CSC Readout

Same as in Ch. 5.7.2 the CSC readout during the data taking needs to form a pre-trigger coinciding with the L1-trigger decision. The same study is performed and a 1 % signal uncertainty is assigned.

6.7.2 Other Sources

The statistical uncertainties due to the limited number of events for the signal yield prediction is determined to be between 5 and 10%, depending on the mass and lifetime of the signal sample.

6.8 Results

The expected and observed numbers of events in the signal bin D in each of the different categories are summarized in Tab. 6.19 and are also shown in Fig. 6.24. No statistical significant excess above the background prediction is observed in any of the channels. With this absence of an excess, exclusion limits on the HNL production cross section are set using a maximum likelihood fit (See Eq. 5.4) and the background estimation method described in Ch. 6.5.1. Additionally, in the muon channel the $\mathrm{Z} \rightarrow \mu\mu$ background contribution is added in addition to the ABCD prediction. The statistical uncertainty of the $\mathrm{Z} \rightarrow \mu\mu$ background is also added as a log-normal nuisance parameter.

The DT and CSC categories are treated as separate and uncorrelated categories, that are then combined for the final results of the electron or muon channel.

The muon channel shows the larger event yields for simulated signals compared to the electron channel due to the lower p_{T} thresholds of the trigger paths and therefore the lower p_{T} cuts on the reconstructed muons. However with the additional background source of the $\mathrm{Z} \rightarrow \mu\mu$ background, the sensitivity of the muon channel becomes comparable with the electron channel.

Figure 6.25 and 6.26 show the observed asymptotic limits at 95 % CL on the cross section as a function of $c\tau$ for Majorana and Dirac type HNL of different masses in the muon and electron channels. In regions in which the observed limit is below the predicted cross section, the theory prediction is excluded. In some cases, like for the 4 GeV HNL masses, the theory prediction is below the observed limit, and therefore no cross section can be excluded. For 2 and 3 GeV masses there is a whole region being excluded, defined by the two crossing points of the theory prediction and the observed limit. Lastly for 1 GeV only 1 crossing can be seen in the tested $c\tau$ range.

Figure 6.27 shows the expected asymptotic limit at 95 % CL on the cross section as a function of $c\tau$ for Majorana type HNLs of various masses split in the CSC, DT and DT+CSC channels. It can be seen that the CSC channel dominates the sensitivity, since the channel has smaller backgrounds compared to DT clusters while having the same amount of signal.

Fig. 6.28 and 6.29 show the observed asymptotic limits at 95 % CL on the HNL coupling strength as a function of the HNL mass for Majorana and Dirac-type HNLs in the electron and muon channels. These limits feature an upper and lower branch of the asymptotic limit, corresponding to HNLs with short and long lifetimes. For short lifetimes, the acceptance starts to decrease, which is compensated by an increase in the production cross section, thereby reaching similar sensitivities as longer lifetimes. The upper branch stops at 2 GeV since the signal acceptance approaches zero. Figure 6.28 and 6.29 compare these asymptotic limits with results from other CMS analyses ([117] and [118]) and other experiments [128–132]. It can be seen that the electron improves the currently best limits from the CHARM [132] experiment in the 2.1-3.0 GeV mass region. The muon channel also shows an improvement compared to the best currently published result, improving the limits in the 1.9-3.3 GeV region compared to the Belle [129] and Delphi [131] results. For lower masses (<1.9 GeV) the analysis is not able to improve the asymptotic limits set by the BEBC[128] experiment.

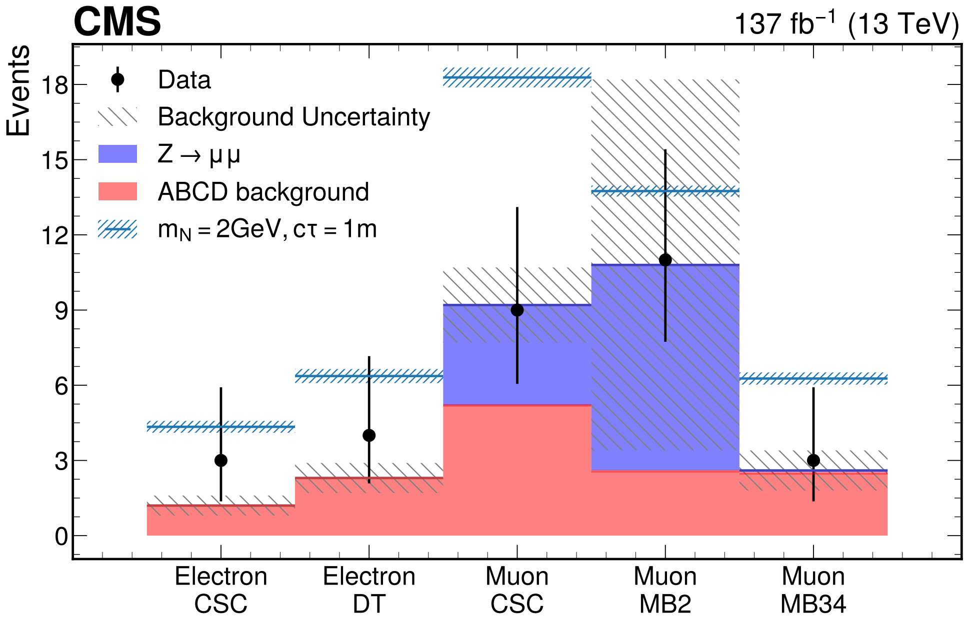

Figure 6.24: Expected and observed number of events in the different categories of the signal bin D. A 2 GeV Majoranna signal sample is also shown. Uncertainty bands include systematic and statistical uncertainties.

Table 6.19: The predicted background and the observed data are shown for the different event categories considered in the search.

Channel	Region	Non-Z → $\mu\mu$ Bkg	Z → $\mu\mu$ Bkg	Total Bkg	Data
Muon	CSC	3.7 ± 0.7	3.5 ± 1.1	7.2 ± 1.3	8
Muon	DT-MB2	1.8 ± 0.6	7.2 ± 6.5	9.0 ± 6.5	7
Muon	DT-MB3/4	2.1 ± 0.7	0.05 ± 0.05	2.1 ± 0.7	2
Electron	CSC	0.8 ± 0.3	-	0.8 ± 0.3	2
Electron	DT	2.1 ± 0.6	-	2.1 ± 0.6	3

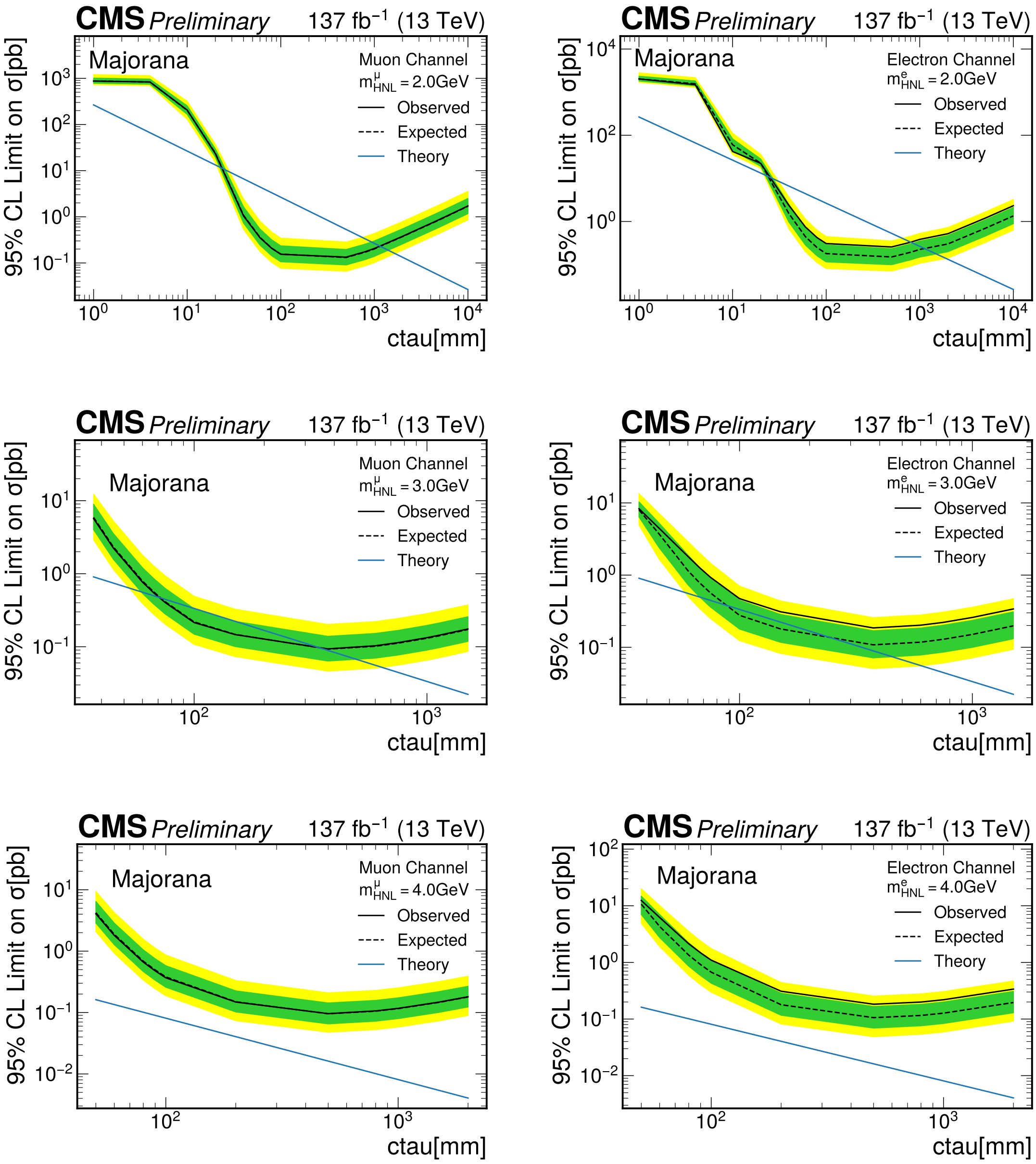

Figure 6.25: Asymptotic limit as a function of $c\tau$ for majorana HNL with various masses in muon(left) channel and electron channel(right).

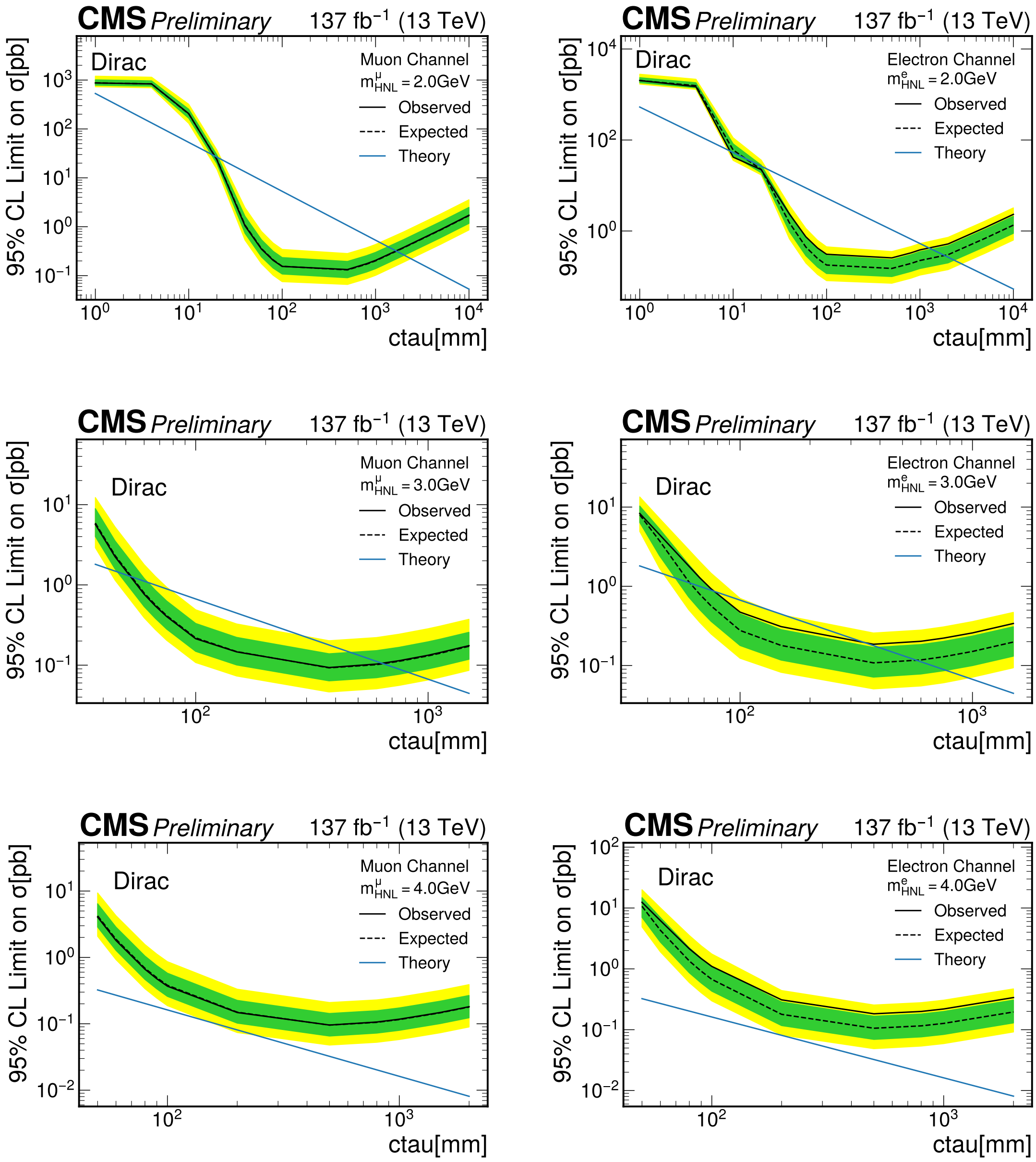

Figure 6.26: Asymptotic limit as a function of $c\tau$ for dirac HNL with various masses in muon(left) channel and electron channel(right).

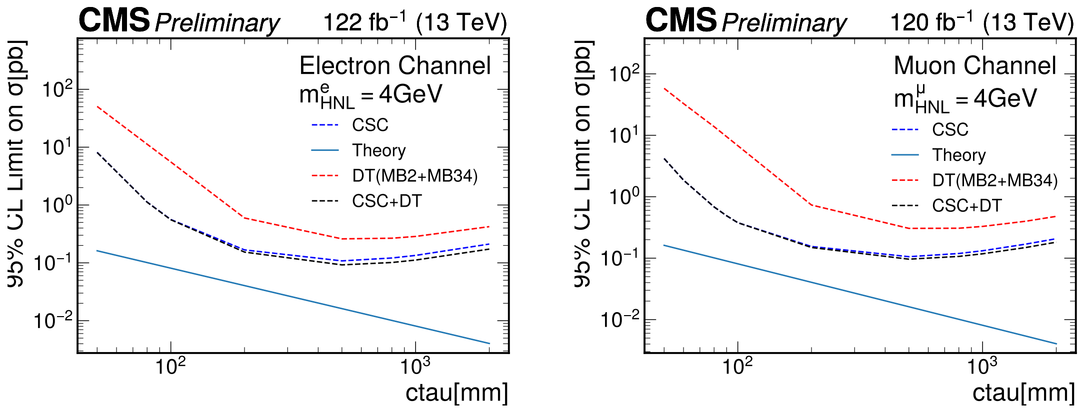

Figure 6.27: Expected asymptotic limits as a function of $c\tau$ for majorana HNL with various masses using CSC, DT and the combination of both categories. Note that these studies were performed with 120 and 122 fb^{-1}, since at the time of the study not all of the data was processed yet. No large changes are expected with the full dataset.

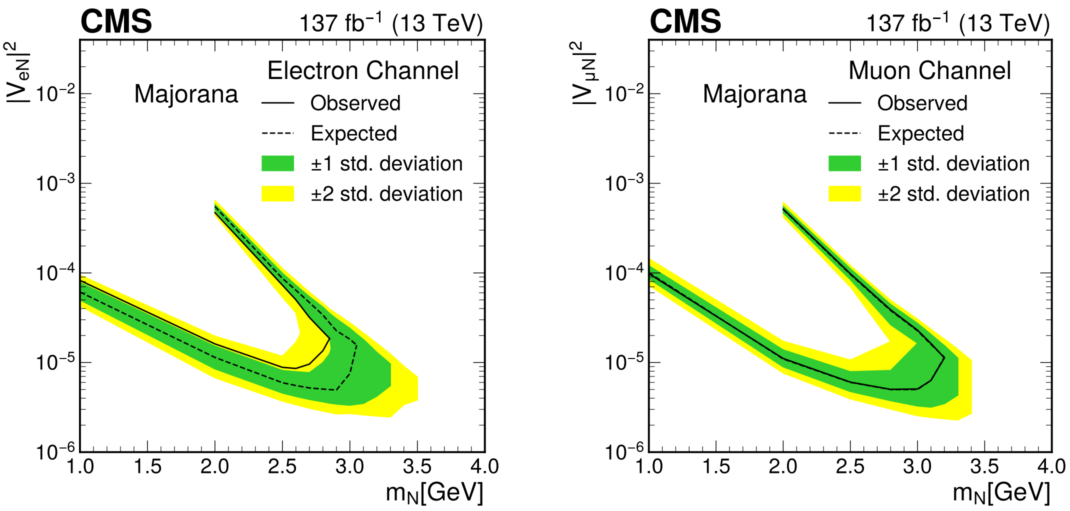

Figure 6.28: Asymptotic limit of HNL coupling strength as a function of majorana HNL mass in electron(left) channel and muon channel.

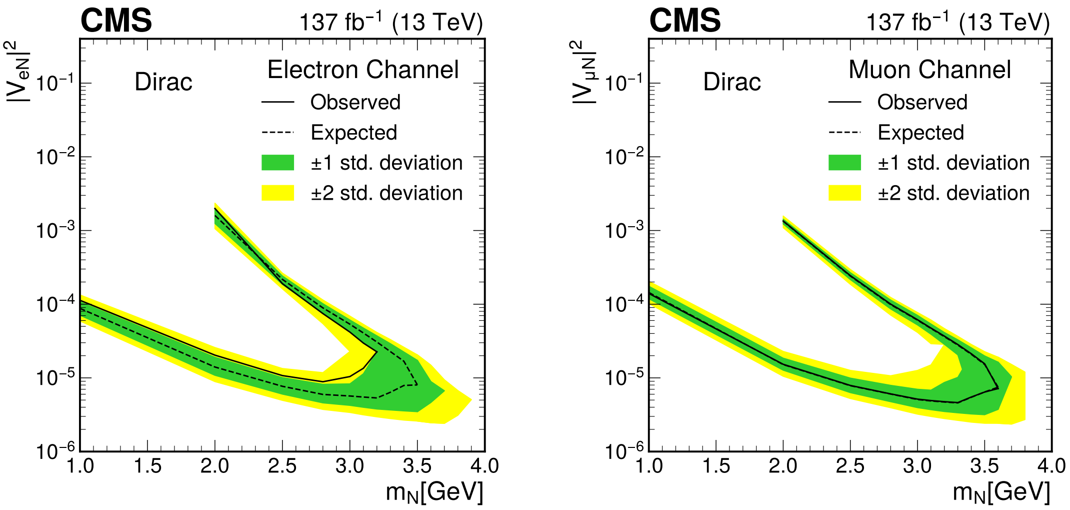

Figure 6.29: Asymptotic limit of HNL coupling strength as a function of dirac HNL mass in electron(left) channel and muon channel.

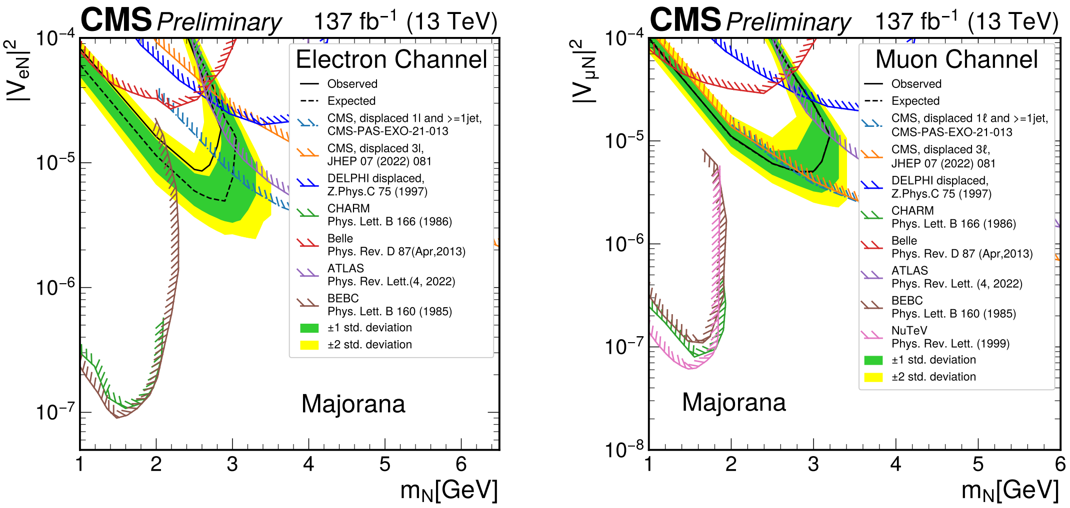

Figure 6.30: Asymptotic limit of HNL coupling strength as a function of majorana HNL mass in electron(left) channel and muon channel. Results from the DELPHI[131], Belle [129], ATLAS [130], BEBC [128], CHARM [132] and the CMS[117] collaborations are shown for reference. Result from EXO-21-013 are taken from [118].

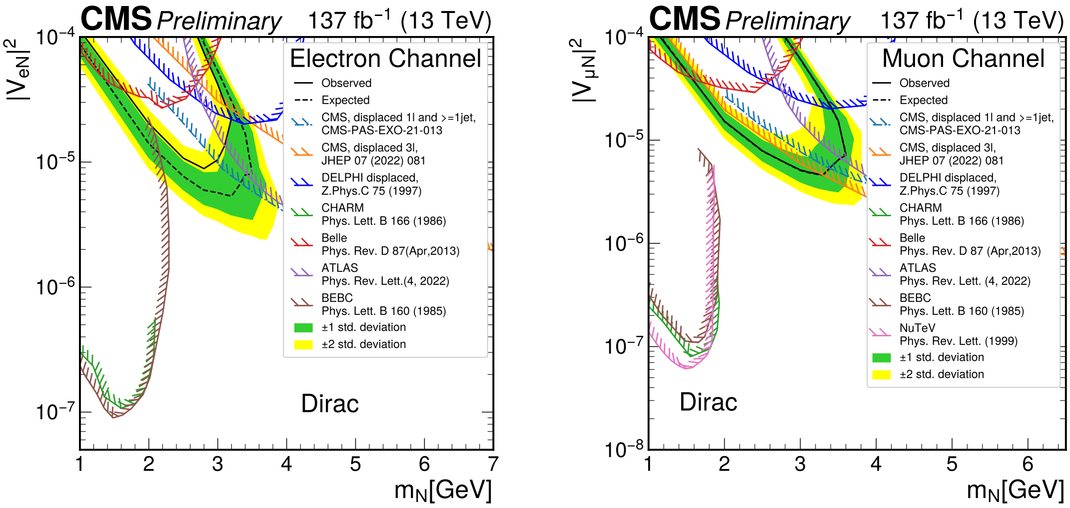

Figure 6.31: Asymptotic limit of HNL coupling strength as a function of dirac HNL mass in electron(left) channel and muon channel. Results from the DELPHI[131], Belle [129], ATLAS [130], BEBC [128] and the CMS[117] collaborations are shown for reference. Result from EXO-21-013 are taken from [118].

6.8.1 Tau HNL Limits

The search can also be interpreted as a search for tau-type HNLs, where the signal events are accepted by the triggers due to electrons and muons that are a result from the leptonic prompt tau decay. The p_{T} of the trigger leptons is smaller compared to the prompt electron and muon decays, therefore the trigger efficiency is five to ten smaller than for the muon or electron type HNLs.

Both the electron and muon channels have sensitivity towards tau-type HNLs. Fig. 6.32 shows the asymptotic limits at 95 % CL for both Majorana and Dirac τ-type HNLs in the muon, electron and combined channels. This result can also be interpreted in terms of an asymptotic limits at 95 % CL of the coupling strength as a function of the HNL mass. This interpretation is shown in Fig. 6.33, again split in the electron, muon and combined channel. The limits shown are not able to improve the results from DELPHI[131].

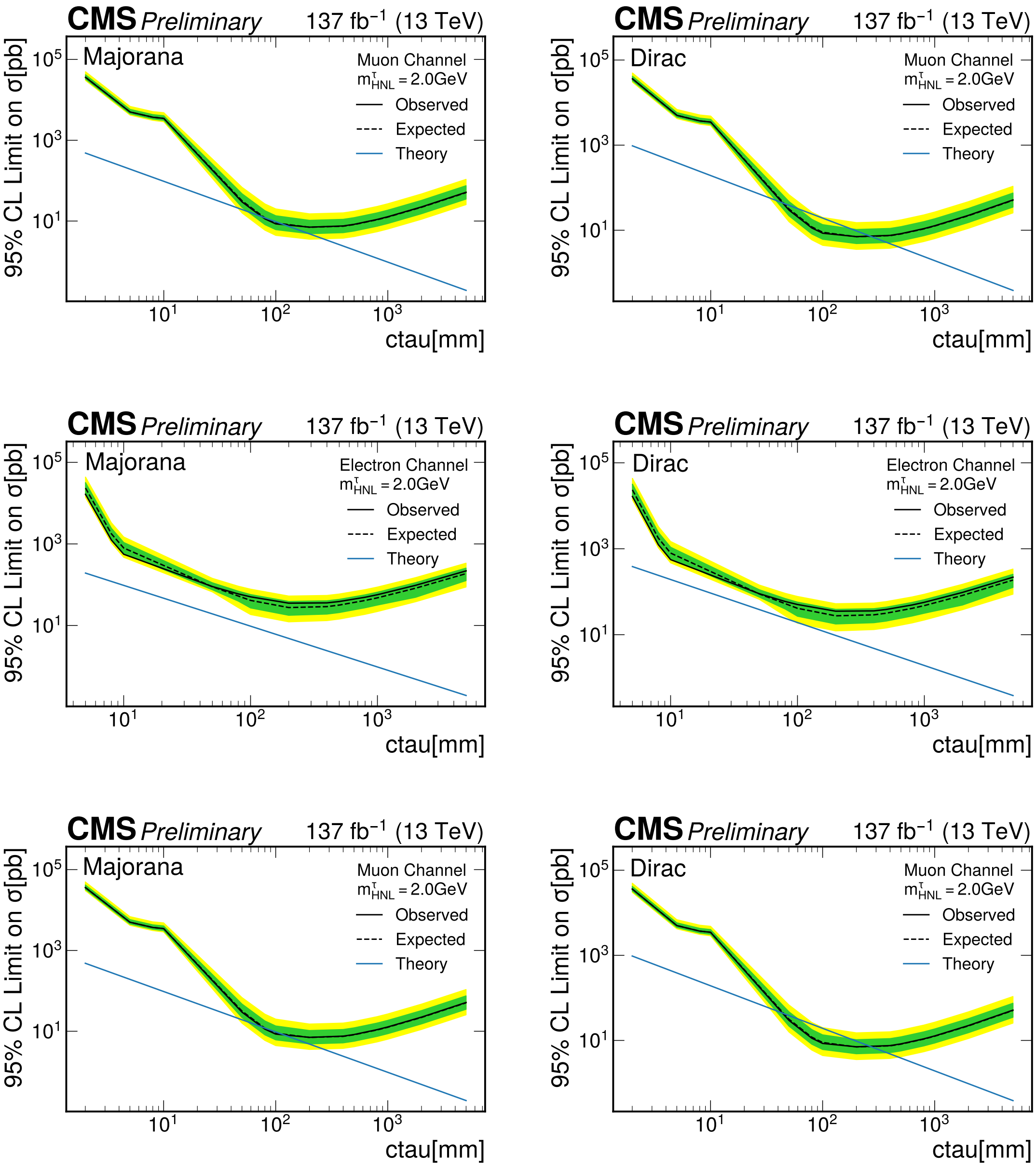

Figure 6.32: Asymptotic limit as a function of $c\tau$ for tau majorana(left) and dirac(right) HNL masses of 2 GeV in the muon channel(top), electron channel(middle) and the combination of the two channels(bottom).

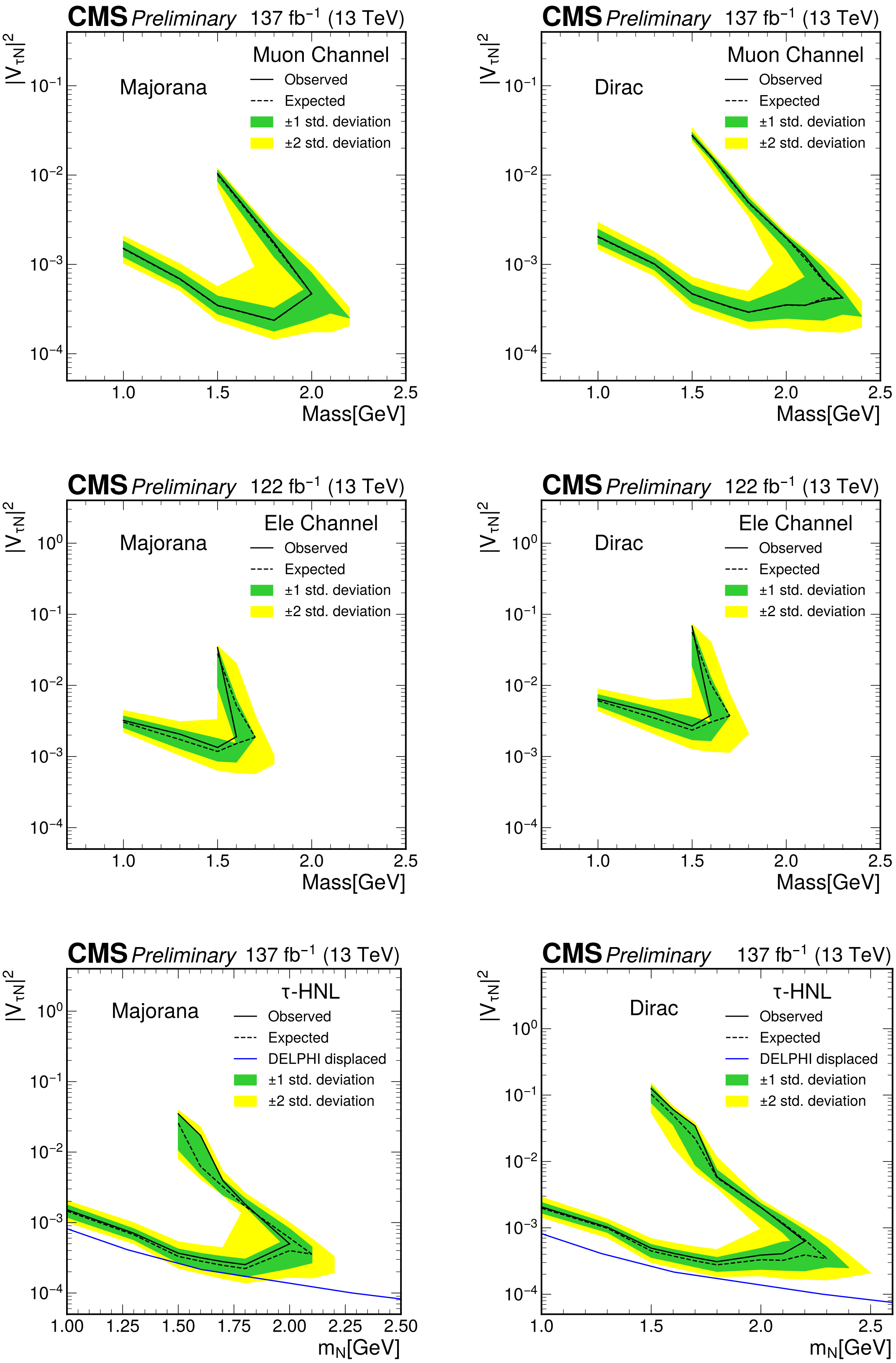

Figure 6.33: Asymptotic limit of HNL coupling strength as a function of tau-type majorana(left) and dirac(right) HNL mass in muon channel(top), electron channel(middle) and the combination of the two channels(bottom). Results from the DELPHI[131] collaboration is shown for reference in the combined result. Note that the electron plot was made with 122 fb^{-1}, since not all data was processed at that point.

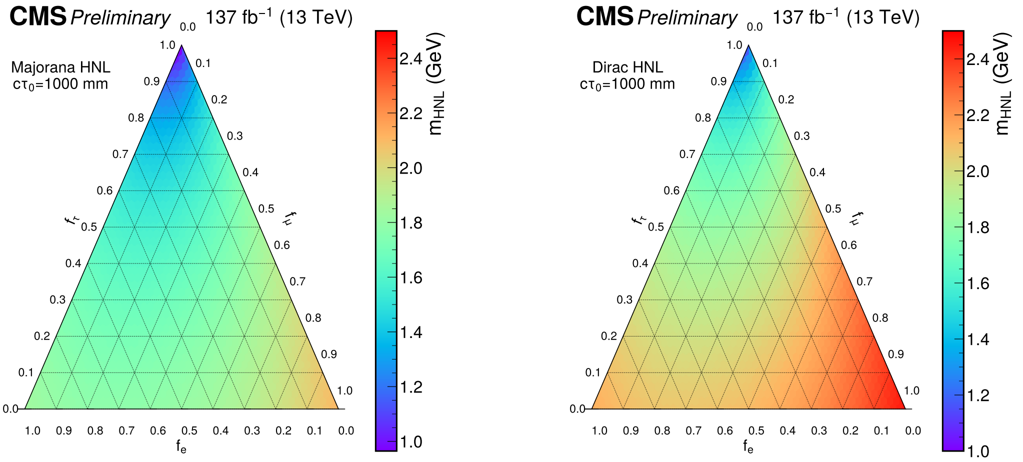

Figure 6.34: Minimum excluded mass for Majorana (left) and Dirac (right) HNLs with a fixed lifetime of 1000 mm.

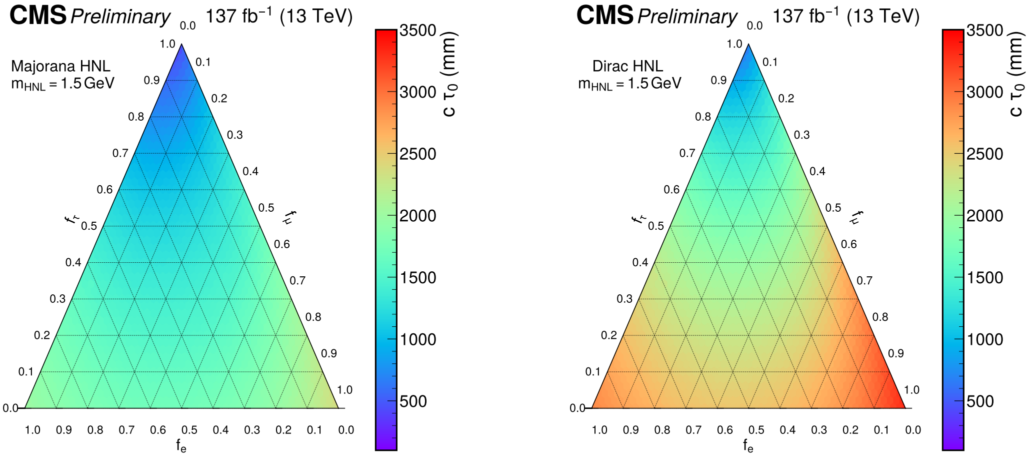

Figure 6.35: Minimum excluded lifetime for Majorana (left) and Dirac (right) HNLs with a fixed mass of 1.5 GeV.

6.8.2 HNL Limits with Mixed Flavor Couplings

The HNL cluster reconstruction efficiency is independent of the flavor and therefore the results can be interpreted for various mixed flavor coupling scenarios using the reweighting procedure described in Ch. 6.2.1. Fig. 6.34 shows the limits on the HNL mass for a fixed lifetime of 1 m and Fig. 6.35 shows the limits on the HNL lifetime for a fixed mass of 1.5 GeV. Following the general features from each of the channels it can be seen that the best sensitivity is located in the corners with large electron or muon couplings, while the limits get worse with larger tau contributions, due to the reduced sensitivity of the tau HNLs. Additionally, since both the electron and muon channels are combined for these results, the corners with pure electron or pure muon coupling show a slightly worse performance compared to the pure electron or muon results shown before. This is a result of combining the electron and muon channel, which increases the background and adds no sensitivity for the pure electron and muon coupling scenarios.

6.9 Summary

A search for long-lived Dirac or Majorana-type heavy neutral leptons (HNL) has been presented, using proton-proton collision data recorded with the CMS detector at $\sqrt{s} = 13\,\mathrm{TeV}$, corresponding to an integrated luminosity of 137 fb^{-1}. The long-lived signature of the HNL results in a displaced hadronic shower in the CMS muon system, forming a so called muon detector shower (MDS). The MDS provides a unique handle to suppress most background, along with the other selections and vetos applied to the events. This then results in a signal event exceeding the standard model background prediction by a factor of 10^7. The results are interpreted as a 95% confidence level limit on the HNL mixing parameters, setting the most stringent limits between the masses of 2.1-3.0 GeV in the electron channel and 1.9-3.3 GeV in the muon channel.

7 Summary

Most predictions from the SM have been empirically confirmed, but there is still evidence pointing towards physics beyond the SM. Long-lived particles are part of many extensions to the SM and provide unique signatures in collider experiments, which in recent years were studied closely. The standard reconstruction algorithms usually either implicitly or even explicitly assume prompt decays of the particles created in the collision, leading to well defined signatures in the detectors. This leads to reconstruction algorithms, that are often not suited for the detection of largely displaced particles, requiring the development of novel techniques.

The CMS detector is uniquely suited for hadronically decaying long-lived particles that reach the muon detectors, since the muon system and the iron return yoke together can be used as a sampling calorimeter. The resulting Muon Detector Showers (MDS) can be reconstructed using a newly developed technique and since such MDS occur relatively rarely in SM processes, a search targeting MDS is relatively background free. Since this MDS object was developed after the Run2 data taking period already concluded, no dedicated trigger paths targeting hadronic showers within the muon system existed for Run2.

This thesis presented two searches for LLPs decaying in the CMS muon system using data recorded during the years 2016 to 2018. Both searches use the newly created MDS signature to search for long-lived particles that decay hadronically inside the CMS muon system. The first search was published in 2021 [92] and targets Twin-Higgs model signatures inside the Cathode Strip Chambers (CSC). The MDS object reconstruction was originally developed in the context of this search. The MDS are reconstructed by clustering detector hits with a geometrical density based clustering algorithm. Due to the easier access to the timing information of CSC detector hits, this search was performed with only the CSC system, leaving out the Drift Tubes in the barrel region for further studies in the future. No excess for long-lived particles was observed and instead the analysis sets the most stringent limits for a Twin-Higgs model where the LLPs decay into $\mathrm{d\bar{d}}$, $\mathrm{b\bar{b}}$ and $\tau^+\tau^-$ for proper lifetimes of $c\tau > 6$, 20, and 40 m and LLP masses of 7, 15 and 40 GeV respectively. For lifetimes with $c\tau >$ 100 m this search improves the previously best limits from the ATLAS collaboration [95, 96] by a factor of 6 for a LLP mass of 7 GeV and by a factor of 2 for a LLP mass of 15, 40 and 55 GeV. This CSC cluster only search recently has been extended to also include the DT system, while the analysis strategy simultaneously has been improved the including a two cluster category. These additions improve upon the CSC only result by a factor of 2 for lifetimes above 0.2, 0.5, 2 and 18 m for LLP masses of 7, 15, 40 and 55 GeV respectively. Both analyses are limited by the low efficiency of the $p_{\mathrm{T}}^{\mathrm{miss}}$ based trigger paths. Additional models with the same signal signature are also evaluated, e.g. a dark shower model [133].

The second analysis searches for heavy neutral leptons (HNLs) that are long-lived [116]. The HNLs considered in this search are produced via charged current production and decay into a lepton and W boson, which then decays hadronically. The production mode allows the use of a single lepton based trigger path, removing one of the limiting factors of the Twin Higgs model searches. The search considers both Majorana- and Dirac-type HNLs for the search, while also allowing the mixing between different HNL flavors. The analysis sets the most stringent limits for HNL masses in the range 2.1-3.0 (1.9-3.3) GeV for electron (muon) flavor HNLs [117]. The results are also interpreted for mixed coupling scenarios.

Both analyses presented in this thesis use the novel MDS cluster object, but currently only the position of the cluster in the detector, the number of hits and the timing information of the cluster is used. One way to improve the sensitivity of both analyses, is to create cluster based variables, that also take the shape of the cluster into account. This could lead to a better identification of clusters coming from muons undergoing bremsstrahlung compared to the signal clusters that are a result of a hadronic shower. The MDS object also could be further improved by not separating between DT and CSC based cluster, especially in the η-region where a shower can travel through both systems. This more global MDS could better reconstruct showers, that currently are either not considering the hits close-by in the other detector system or clusters that are not reconstructed due to them not reaching the threshold of the required number of hits in neither the DT or the CSC system. Additionally, the $p_{\mathrm{T}}^{\mathrm{miss}}$ based Twin Higgs model searches are limited by the trigger efficiency of the trigger path. A dedicated MDS trigger was therefore developed for the Run3 data taking period, which also uses a dedicated L1 seed for CSC based clusters.

This thesis so far has mostly talked about searches at collider based multi-purpose experiments, but this is not the only way to search for long-lived particles. One possible search strategy is to develop a dedicated detector for long-lived particle searches and place it further away from the interaction point. With this experimental setup, the pp collisions of the LHC can still be used, but the amount of background events is potentially way lower due to the larger shielding. Additionally the phase space of the particles is, due to the distance to the detector, way different. Multiple such experiments have either been proposed (like the MATHUSLA detector [134] or the CODEX-b detector [135, 136]) or are already taking data (like the FASER detector [137]).

Looking ahead, with the Run3 data taking already underway, MDS based searches have a full physics program ahead. MDS are novel objects, which were first used in the context of LLPs in the searches presented in this thesis. As a new tool to interpret events they open up many exciting new possibilities for further physics analysis. One conclusion to draw from this type of analyses, is that one should think of new ways to reconstruct events with unusual signatures. Maybe with signatures like the MDS, concrete evidence for the physics beyond the SM can be found in the future.

Bibliography

[1] D. J. Griffiths, *Introduction to elementary particles; 2nd rev. version.* New York, NY: Wiley, 2008. URL: `https://cds.cern.ch/record/111880`.

[2] Particle Data Group, "Review of Particle Physics". *Progress of Theoretical and Experimental Physics* 2022.8 (Aug. 2022). 083C01. DOI: `10.1093/ptep/ptac097`.

[3] E. Fermi, "Zur Quantelung des idealen einatomigen Gases". *Zeitschrift für Physik* 36.11 (Nov. 1926), pp. 902–912. DOI: `10.1007/BF01400221`.

[4] P. A. M. Dirac and R. H. Fowler, "On the theory of quantum mechanics". *Proceedings of the Royal Society of London. Series A, Containing Papers of a Mathematical and Physical Character* 112.762 (1926), pp. 661–677. DOI: `10.1098/rspa.1926.0133`.

[5] S. Bose, "Planck's law and the light quantum hypothesis". *Journal of Astrophysics and Astronomy* 15.1 (Mar. 1994), pp. 3–7. DOI: `10.1007/BF03010400`.

[6] Y. Fukuda et al., "Measurement of the Flux and Zenith-Angle Distribution of Upward Throughgoing Muons by Super-Kamiokande". *Physical Review Letters* 82.13 (Mar. 1999), pp. 2644–2648. DOI: `10.1103/physrevlett.82.2644`.

[7] Q. R. Ahmad et al., "Direct Evidence for Neutrino Flavor Transformation from Neutral-Current Interactions in the Sudbury Neutrino Observatory". *Physical Review Letters* 89.1 (June 2002). DOI: `10.1103/physrevlett.89.011301`.

[8] K. Eguchi et al., "First Results from KamLAND: Evidence for Reactor Antineutrino Disappearance". *Physical Review Letters* 90.2 (Jan. 2003). DOI: `10.1103/physrevlett.90.021802`.

[9] M. Aker et al., *First direct neutrino-mass measurement with sub-eV sensitivity.* 2021. arXiv: `2105.08533 [hep-ex]`.

[10] ALEPH Collaboration, "An upper limit on the τ neutrino mass from three- and five-prong tau decays". *Eur. Phys. J. C* 2 (1998), pp. 395–406. DOI: `10.1007/s100520050149`.

[11] K. Assamagan et al., "Upper limit of the muon-neutrino mass and charged-pion mass from momentum analysis of a surface muon beam". *Phys. Rev. D* 53 (June 1996), pp. 6065–6077. DOI: `10.1103/PhysRevD.53.6065`.

[12] S. L. Glashow, "Partial-symmetries of weak interactions". *Nuclear Physics* 22.4 (1961), pp. 579–588. DOI: `https://doi.org/10.1016/0029-5582(61)90469-2`.

[13] A. Salam and J. C. Ward, “Electromagnetic and weak interactions”. *Selected Papers of Abdus Salam*, pp. 210–213. DOI: `10.1142/9789812795915_0029`.

[14] S. Weinberg, “A Model of Leptons”. *Phys. Rev. Lett.* 19 (Nov. 1967), pp. 1264–1266. DOI: `10.1103/PhysRevLett.19.1264`.

[15] G.'t Hooft and M. Veltman, “Regularization and renormalization of gauge fields”. *Nuclear Physics B* 44.1 (1972), pp. 189–213. DOI: `https://doi.org/10.1016/0550-3213(72)90279-9`.

[16] H. Georgi and S. L. Glashow, “Unified Weak and Electromagnetic Interactions without Neutral Currents”. *Phys. Rev. Lett.* 28 (May 1972), pp. 1494–1497. DOI: `10.1103/PhysRevLett.28.1494`.

[17] N. Cabibbo, “Unitary Symmetry and Leptonic Decays”. *Phys. Rev. Lett.* 10 (June 1963), pp. 531–533. DOI: `10.1103/PhysRevLett.10.531`.

[18] M. Kobayashi and T. Maskawa, “CP-Violation in the Renormalizable Theory of Weak Interaction”. *Progress of Theoretical Physics* 49.2 (Feb. 1973), pp. 652–657. DOI: `10.1143/PTP.49.652`.

[19] H. D. Politzer, “Reliable Perturbative Results for Strong Interactions?” *Phys. Rev. Lett.* 30 (June 1973), pp. 1346–1349. DOI: `10.1103/PhysRevLett.30.1346`.

[20] D. J. Gross and F. Wilczek, “Ultraviolet Behavior of Non-Abelian Gauge Theories”. *Phys. Rev. Lett.* 30 (June 1973), pp. 1343–1346. DOI: `10.1103/PhysRevLett.30.1343`.

[21] K. G. Wilson, “Confinement of quarks”. *Phys. Rev. D* 10 (Oct. 1974), pp. 2445–2459. DOI: `10.1103/PhysRevD.10.2445`.

[22] P. W. Higgs, “Broken Symmetries and the Masses of Gauge Bosons”. *Phys. Rev. Lett.* 13 (Oct. 1964), pp. 508–509. DOI: `10.1103/PhysRevLett.13.508`.

[23] F. Englert and R. Brout, “Broken Symmetry and the Mass of Gauge Vector Mesons”. *Phys. Rev. Lett.* 13 (Aug. 1964), pp. 321–323. DOI: `10.1103/PhysRevLett.13.321`.

[24] G. S. Guralnik, C. R. Hagen, and T. W. B. Kibble, “Global Conservation Laws and Massless Particles”. *Phys. Rev. Lett.* 13 (Nov. 1964), pp. 585–587. DOI: `10.1103/PhysRevLett.13.585`.

[25] A. G. Riess et al., “Observational Evidence from Supernovae for an Accelerating Universe and a Cosmological Constant”. *The Astronomical Journal* 116.3 (Sept. 1998), p. 1009. DOI: `10.1086/300499`.

[26] S. Perlmutter et al., “Measurements of Ω and Λ from 42 High-Redshift Supernovae”. *The Astrophysical Journal* 517.2 (June 1999), pp. 565–586. DOI: `10.1086/307221`.

[27] CDF Collaboration, “High-precision measurement of the W boson mass with the CDF II detector”. *Science* 376.6589 (2022), pp. 170–176. DOI: `10.1126/science.abk1781`.

[28] Muon $g-2$ Collaboration, “Measurement of the Positive Muon Anomalous Magnetic Moment to 0.46 ppm”. *Phys. Rev. Lett.* 126 (Apr. 2021), p. 141801. DOI: `10.1103/PhysRevLett.126.141801`.

[29] M. J. Strassler and K. M. Zurek, “Echoes of a hidden valley at hadron colliders”. *Physics Letters B* 651.5-6 (Aug. 2007), pp. 374–379. DOI: `10.1016/j.physletb.2007.06.055`.

[30] M. J. Strassler and K. M. Zurek, “Discovering the Higgs through highly-displaced vertices”. *Physics Letters B* 661.4 (Mar. 2008), pp. 263–267. DOI: `10.1016/j.physletb.2008.02.008`.

[31] T. Han et al., “Phenomenology of hidden valleys at hadron colliders”. *Journal of High Energy Physics* 2008.07 (July 2008), pp. 008–008. DOI: `10.1088/1126-6708/2008/07/008`.

[32] J. Juknevich, D. Melnikov, and M. Strassler, “A pure-glue hidden valley I. States and decays”. *Journal of High Energy Physics* 2009.07 (July 2009), pp. 055–055. DOI: `10.1088/1126-6708/2009/07/055`.

[33] M. J. Strassler, “On the Phenomenology of Hidden Valleys with Heavy Flavor” (2008). arXiv: `0806.2385 [hep-ph]`.

[34] N. Craig et al., “Naturalness in the Dark at the LHC” (2015). arXiv: `1501.05310 [hep-ph]`.

[35] C. Csáki et al., “Searching for displaced Higgs boson decays”. *Physical Review D* 92.7 (Oct. 2015). DOI: `10.1103/physrevd.92.073008`.

[36] A. Abada et al., “Inclusive displaced vertex searches for heavy neutral leptons at the LHC”. *Journal of High Energy Physics* 2019.1 (Jan. 2019). DOI: `10.1007/jhep01(2019)093`.

[37] Y. Cai et al., “Lepton Number Violation: Seesaw Models and Their Collider Tests” (2018). arXiv: `1711.02180 [hep-ph]`.

[38] T. Asaka and M. Shaposhnikov, “The νMSM, dark matter and baryon asymmetry of the universe”. *Physics Letters B* 620.1 (2005), pp. 17–26. DOI: `https://doi.org/10.1016/j.physletb.2005.06.020`.

[39] A. Boyarsky et al., “Sterile neutrino Dark Matter”. *Progress in Particle and Nuclear Physics* 104 (Jan. 2019), pp. 1–45. DOI: `10.1016/j.ppnp.2018.07.004`.

[40] M. Fukugita and T. Yanagida, “Barygenesis without grand unification”. *Physics Letters B* 174.1 (1986), pp. 45–47. DOI: `https://doi.org/10.1016/0370-2693(86)91126-3`.

[41] E. J. Chun et al., “Probing leptogenesis”. *International Journal of Modern Physics A* 33.05n06 (Feb. 2018), p. 1842005. DOI: `10.1142/s0217751x18420058`.

[42] G. Alonso-Álvarez and J. M. Cline, “Gauging lepton flavor SU(3) for the muon g - 2”. *Journal of High Energy Physics* 2022.3 (Mar. 2022). DOI: `10.1007/jhep03(2022)042`.

[43] V. Cirigliano et al., “Leptonic anomalous magnetic moments in ν SMEFT”. *Journal of High Energy Physics* 2021.8 (Aug. 2021). DOI: `10.1007/jhep08(2021)103`.

[44] K. Bondarenko et al., “Phenomenology of GeV-scale heavy neutral leptons”. *Journal of High Energy Physics* 2018.11 (Nov. 2018). DOI: `10.1007/jhep11(2018)032`.

[45] NNPDF Collaboration, "Parton distributions for the LHC Run II". *JHEP* 04 (2015), p. 040. DOI: `10.1007/JHEP04(2015)040`.

[46] NNPDF Collaboration, "Parton distributions from high-precision collider data". *The European Physical Journal C* 77.10 (Oct. 2017). DOI: `10.1140/epjc/s10052-017-5199-5`.

[47] B. Webber, "A QCD model for jet fragmentation including soft gluon interference". *Nuclear Physics B* 238.3 (1984), pp. 492–528. DOI: `https://doi.org/10.1016/0550-3213(84)90333-X`.

[48] B. Andersson et al., "Parton fragmentation and string dynamics". *Physics Reports* 97.2 (1983), pp. 31–145. DOI: `https://doi.org/10.1016/0370-1573(83)90080-7`.

[49] GEANT4 Collaboration, "Geant4—a simulation toolkit". *Nuclear Instruments and Methods in Physics Research Section A: Accelerators, Spectrometers, Detectors and Associated Equipment* 506.3 (2003), pp. 250–303. DOI: `https://doi.org/10.1016/S0168-9002(03)01368-8`.

[50] L. Evans and P. Bryant, "LHC Machine". *Journal of Instrumentation* 3.08 (Aug. 2008), S08001. DOI: `10.1088/1748-0221/3/08/S08001`.

[51] M. Benedikt et al., *LHC Design Report*. Geneva: CERN, 2004. DOI: `10.5170/CERN-2004-003-V-3`.

[52] CMS Collaboration, "The CMS experiment at the CERN LHC". *Journal of Instrumentation* 3.08 (Aug. 2008), S08004. DOI: `10.1088/1748-0221/3/08/S08004`.

[53] CMS Collaboration, *CMS Physics: Technical Design Report Volume 1: Detector Performance and Software*. Geneva: CERN, 2006. URL: `https://cds.cern.ch/record/922757`.

[54] E. Mobs, "The CERN accelerator complex - August 2018. Complexe des accélérateurs du CERN - Août 2018" (2018). General Photo. URL: `http://cds.cern.ch/record/2636343`.

[55] G. Apollinari et al., "Chapter 1: High Luminosity Large Hadron Collider HL-LHC. High Luminosity Large Hadron Collider HL-LHC". *CERN Yellow Report* 5 (2015), pp. 1–19. DOI: `10.5170/CERN-2015-005.1`.

[56] ATLAS Collaboration, "The ATLAS Experiment at the CERN Large Hadron Collider". *Journal of Instrumentation* 3.08 (Aug. 2008), S08003. DOI: `10.1088/1748-0221/3/08/S08003`.

[57] ALICE Collaboration, "The ALICE experiment at the CERN LHC". *Journal of Instrumentation* 3.08 (Aug. 2008), S08002. DOI: `10.1088/1748-0221/3/08/S08002`.

[58] LHCb Collaboration, "The LHCb Detector at the LHC". *Journal of Instrumentation* 3.08 (Aug. 2008), S08005. DOI: `10.1088/1748-0221/3/08/S08005`.

[59] CMS Collaboration, "Pileup mitigation at CMS in 13 TeV data". *Journal of Instrumentation* 15.09 (Sept. 2020), P09018. DOI: `10.1088/1748-0221/15/09/P09018`.

[60] T. Sakuma and T. McCauley, "Detector and Event Visualization with SketchUp at the CMS Experiment". *Journal of Physics: Conference Series* 513.2 (June 2014), p. 022032. DOI: `10.1088/1742-6596/513/2/022032`.

[61] CMS Collaboration, *CMS The TriDAS Project: Technical Design Report, Volume 2: Data Acquisition and High-Level Trigger. CMS trigger and data-acquisition project.* Geneva: CERN, 2002. URL: `https://cds.cern.ch/record/578006`.

[62] D. Trocino, "The CMS High Level Trigger". *Journal of Physics: Conference Series* 513.1 (June 2014), p. 012036. DOI: `10.1088/1742-6596/513/1/012036`.

[63] S. Mersi, "Phase-2 Upgrade of the CMS Tracker". *Nuclear and Particle Physics Proceedings* 273-275 (2016). 37th International Conference on High Energy Physics (ICHEP), pp. 1034–1041. DOI: `https://doi.org/10.1016/j.nuclphysbps.2015.09.162`.

[64] A. Benaglia, "The CMS ECAL performance with examples". *Journal of Instrumentation* 9.02 (Feb. 2014), p. C02008. DOI: `10.1088/1748-0221/9/02/C02008`.

[65] CMS Collaboration, *Energy Resolution of the Barrel of the CMS Electromagnetic Calorimeter.* Tech. rep. Geneva: CERN, 2007. DOI: `10.1088/1748-0221/2/04/P04004`.

[66] CMS Collaboration, "Performance of the CMS hadron calorimeter with cosmic ray muons and LHC beam data". *Journal of Instrumentation* 5.03 (Mar. 2010), T03012. DOI: `10.1088/1748-0221/5/03/T03012`.

[67] CMS Collaboration, "Performance of the CMS muon detector and muon reconstruction with proton-proton collisions at $\sqrt{s}$=13 TeV". *Journal of Instrumentation* 13.06 (June 2018), P06015. DOI: `10.1088/1748-0221/13/06/P06015`.

[68] CMS Collaboration, *The CMS muon project: Technical Design Report.* Geneva: CERN, 1997. URL: `https://cds.cern.ch/record/343814`.

[69] CMS Collaboration, *CMS Muon Drift Tubes HL-LHC Slice Test.* Tech. rep. 2021. URL: `https://cds.cern.ch/record/2790742`. arXiv: `2110.15052`.

[70] S. Park et al., "CMS endcap RPC gas gap production for upgrade". *Journal of Instrumentation* 7 (Nov. 2012), P11013. DOI: `10.1088/1748-0221/7/11/P11013`.

[71] CMS Collaboration, *CMS computing: Technical Design Report.* Submitted on 31 May 2005. Geneva: CERN, 2005. URL: `https://cds.cern.ch/record/838359`.

[72] CMS Collaboration, *Workshop lesson: CMS Data Flow.* URL: `https://cms-opendata-workshop.github.io/workshop-lesson-presel-skim/01-introduction/index.html` (visited on 08/24/2023).

[73] CMS Collaboration, "Particle-flow reconstruction and global event description with the CMS detector". *Journal of Instrumentation* 12.10 (Oct. 2017), P10003. DOI: `10.1088/1748-0221/12/10/P10003`.

[74] The CMS Collaboration, “Description and performance of track and primary-vertex reconstruction with the CMS tracker”. *Journal of Instrumentation* 9.10 (Oct. 2014), P10009. DOI: `10.1088/1748-0221/9/10/P10009`.

[75] T. Speer et al., “Track reconstruction in the CMS tracker”. *Nuclear Instruments and Methods in Physics Research Section A: Accelerators, Spectrometers, Detectors and Associated Equipment* 559.1 (2006), pp. 143–147. DOI: `https://doi.org/10.1016/j.nima.2005.11.207`.

[76] K. Rose, “Deterministic annealing for clustering, compression, classification, regression, and related optimization problems”. *Proceedings of the IEEE* 86.11 (1998), pp. 2210–2239. DOI: `10.1109/5.726788`.

[77] R. Frühwirth, W. Waltenberger, and P. Vanlaer, *Adaptive Vertex Fitting.* Tech. rep. Geneva: CERN, 2007. URL: `https://cds.cern.ch/record/1027031`.

[78] ALEPH Collaboration, “Performance of the ALEPH detector at LEP”. *Nuclear Instruments and Methods in Physics Research Section A: Accelerators, Spectrometers, Detectors and Associated Equipment* 360.3 (1995), pp. 481–506. DOI: `https://doi.org/10.1016/0168-9002(95)00138-7`.

[79] CMS Collaboration, “Performance of electron reconstruction and selection with the CMS detector in proton-proton collisions at $\sqrt{s} = 8$ TeV”. *Journal of Instrumentation* 10.06 (June 2015), P06005. DOI: `10.1088/1748-0221/10/06/P06005`.

[80] M. Cacciari, G. P. Salam, and G. Soyez, “The anti-kt jet clustering algorithm”. *Journal of High Energy Physics* 2008.04 (Apr. 2008), p. 063. DOI: `10.1088/1126-6708/2008/04/063`.

[81] Y. Dokshitzer et al., “Better jet clustering algorithms”. *Journal of High Energy Physics* 1997.08 (Sept. 1997), p. 001. DOI: `10.1088/1126-6708/1997/08/001`.

[82] CMS Collaboration, “Identification of heavy-flavour jets with the CMS detector in pp collisions at 13 TeV”. *Journal of Instrumentation* 13.05 (May 2018), P05011. DOI: `10.1088/1748-0221/13/05/P05011`.

[83] CMS Collaboration, “Identification of heavy-flavour jets with the CMS detector in pp collisions at 13 TeV”. *Journal of Instrumentation* 13.05 (May 2018), P05011. DOI: `10.1088/1748-0221/13/05/P05011`.

[84] M. Ester et al., “A Density-Based Algorithm for Discovering Clusters in Large Spatial Databases with Noise”. *Knowledge Discovery and Data Mining.* 1996.

[85] *CSC Segment Time Reconstruction.* URL: `https://github.com/cms-sw/cmssw/blob/master/DataFormats/CSCRecHit/src/CSCSegment.cc#L144-L176` (visited on 08/30/2023).

[86] CMS Collaboration, “Jet energy scale and resolution in the CMS experiment in pp collisions at 8 TeV”. *Journal of Instrumentation* 12.02 (Feb. 2017), P02014. DOI: `10.1088/1748-0221/12/02/P02014`.

[87] A. Bodek et al., “Extracting muon momentum scale corrections for hadron collider experiments”. *The European Physical Journal C* 72.10 (Oct. 2012). DOI: `10.1140/epjc/s10052-012-2194-8`.

[88] CMS Collaboration, “Electron and photon performance in CMS with the full 2016 data sample.” (2017). URL: `https://cds.cern.ch/record/2255497`.

[89] CMS Collaboration, "Electron and Photon performance in CMS with the full 2017 data sample and additional 2016 highlights for the CALOR 2018 Conference" (2018). URL: `https://cds.cern.ch/record/2320638`.

[90] CMS Collaboration, "Muon Identification and Isolation efficiency on full 2016 dataset" (2017). URL: `https://cds.cern.ch/record/2257968`.

[91] CMS Collaboration, "Muon identification and isolation efficiencies with 2017 and 2018 data" (2018). URL: `https://cds.cern.ch/record/2629364`.

[92] CMS Collaboration, "Search for Long-Lived Particles Decaying in the CMS End Cap Muon Detectors in Proton-Proton Collisions at $\sqrt{s} = 13$ TeV". *Phys. Rev. Lett.* 127 (Dec. 2021), p. 261804. DOI: `10.1103/PhysRevLett.127.261804`.

[93] CMS, *Search for Long-lived Particles Decaying in the CMS Endcap Muon System in Proton-Proton Collisions at* $\sqrt{s} = 13$ TeV. Tech. rep. Geneva: CERN, 2021. URL: `http://cds.cern.ch/record/2767484`.

[94] CMS Collaboration, "Search for long-lived particles using displaced jets in proton-proton collisions at $\sqrt{s} = 13$ TeV". *Phys. Rev. D* 104 (July 2021), p. 012015. DOI: `10.1103/PhysRevD.104.012015`.

[95] ATLAS Collaboration, "Search for long-lived particles produced in *pp* collisions at $\sqrt{s} = 13$ TeV that decay into displaced hadronic jets in the ATLAS muon spectrometer". *Phys. Rev. D* 99 (Mar. 2019), p. 052005. DOI: `10.1103/PhysRevD.99.052005`.

[96] ATLAS Collaboration, "Search for long-lived neutral particles produced in *pp* collisions at $\sqrt{s} = 13$ TeV decaying into displaced hadronic jets in the ATLAS inner detector and muon spectrometer". *Phys. Rev. D* 101 (Mar. 2020), p. 052013. DOI: `10.1103/PhysRevD.101.052013`.

[97] CMS Collaboration, *Search for long-lived particles decaying in the CMS muon detectors in proton-proton collisions at* $\sqrt{s} = 13$ TeV. Tech. rep. Geneva: CERN, 2023. URL: `http://cds.cern.ch/record/2864874`.

[98] S. Frixione, P. Nason, and C. Oleari, "Matching NLO QCD computations with parton shower simulations: the POWHEG method". *Journal of High Energy Physics* 2007.11 (Nov. 2007), p. 070. DOI: `10.1088/1126-6708/2007/11/070`.

[99] P. Nason, "A new method for combining NLO QCD with shower Monte Carlo algorithms". *Journal of High Energy Physics* 2004.11 (Dec. 2004), p. 040. DOI: `10.1088/1126-6708/2004/11/040`.

[100] S. Alioli et al., "A general framework for implementing NLO calculations in shower Monte Carlo programs: the POWHEG BOX". *Journal of High Energy Physics* 2010.6 (June 2010). DOI: `10.1007/jhep06(2010)043`.

[101] T. Sjöstrand et al., "An introduction to PYTHIA 8.2". *Comp. Phys. Comm.* 191 (2015), p. 159. DOI: `10.1016/j.cpc.2015.01.024`.

[102] CMS Collaboration, "Event generator tunes obtained from underlying event and multiparton scattering measurements". *Eur. Phys. J. C* 76 (2016), p. 155. DOI: `10.1140/epjc/s10052-016-3988-x`.

[103] CMS Collaboration, "Extraction and validation of a new set of CMS PYTHIA8 tunes from underlying-event measurements". *Eur. Phys. J. C* 80 (2020), p. 4. DOI: `10.1140/epjc/s10052-019-7499-4`.

[104] K. Hamilton et al., "NNLOPS simulation of Higgs boson production". *Journal of High Energy Physics* 2013.10 (Oct. 2013). DOI: `10.1007/jhep10(2013)222`.

[105] CMS Collaboration, *Pileup Removal Algorithms*. Tech. rep. Geneva: CERN, 2014. URL: `https://cds.cern.ch/record/1751454`.

[106] CMS Collaboration, "Performance of the CMS muon detector and muon reconstruction with proton-proton collisions at$\sqrt{s} = 13$ TeV". *Journal of Instrumentation* 13.06 (June 2018), P06015–P06015. DOI: `10.1088/1748-0221/13/06/p06015`.

[107] CMS Collaboration, *MET Analysis*. URL: `https://twiki.cern.ch/twiki/bin/view/CMSPublic/WorkBookMetAnalysis` (visited on 08/30/2023).

[108] T. Junk, "Confidence level computation for combining searches with small statistics". *Nuclear Instruments and Methods in Physics Research Section A: Accelerators, Spectrometers, Detectors and Associated Equipment* 434.2 (1999), pp. 435–443. DOI: `https://doi.org/10.1016/S0168-9002(99)00498-2`.

[109] A. L. Read, "Presentation of search results: the CLs technique". *Journal of Physics G: Nuclear and Particle Physics* 28.10 (Sept. 2002), p. 2693. DOI: `10.1088/0954-3899/28/10/313`.

[110] ATLAS Collaboration, CMS Collaboration, LHC Higgs Combination Group, *Procedure for the LHC Higgs boson search combination in Summer 2011*. Tech. rep. Geneva: CERN, 2011. URL: `https://cds.cern.ch/record/1379837`.

[111] G. Cowan et al., "Asymptotic formulae for likelihood-based tests of new physics". *The European Physical Journal C* 71.2 (Feb. 2011). DOI: `10.1140/epjc/s10052-011-1554-0`.

[112] LHC Higgs Crosssection Workinggroup, *Handbook of LHC Higgs Cross Sections: 4. Deciphering the Nature of the Higgs Sector*. Geneva: CERN, 2017. DOI: `10.23731/CYRM-2017-002`.

[113] CMS Collaboration, *CMS Luminosity Measurements for the 2016 Data Taking Period*. Tech. rep. Geneva: CERN, 2017. URL: `https://cds.cern.ch/record/2257069`.

[114] CMS Collaboration, *CMS luminosity measurement for the 2017 data-taking period at* $\sqrt{s} = 13$ Tev. CMS Physics Analysis Summary CMS-PAS-LUM-17-004. 2018. URL: `https://cds.cern.ch/record/2621960/`.

[115] CMS Collaboration, *CMS luminosity measurement for the 2018 data-taking period at* $\sqrt{s} = 13$ Tev. CMS Physics Analysis Summary CMS-PAS-LUM-18-002. 2019. URL: `https://cds.cern.ch/record/2676164/`.

[116] CMS Collaboration, *Search for long-lived heavy neutral leptons decaying in the CMS muon detectors in proton-proton collisions at* $\sqrt{s} = 13$ TeV. Tech. rep. Geneva: CERN, 2023. URL: `http://cds.cern.ch/record/2865227`.

[117] CMS Collaboration, "Search for long-lived heavy neutral leptons with displaced vertices in proton-proton collisions at $\sqrt{s}$ =13 TeV". *Journal of High Energy Physics* 2022.7 (July 2022). DOI: `10.1007/jhep07(2022)081`.

[118] CMS Collaboration, *Search for long-lived heavy neutral leptons with lepton flavour conserving or violating decays to a jet and an electron, muon, or tau lepton.* Tech. rep. Geneva: CERN, 2023. URL: `https://cds.cern.ch/record/2852843`.

[119] J. Alwall et al., “The automated computation of tree-level and next-to-leading order differential cross sections, and their matching to parton shower simulations”. *JHEP* 07 (2014), p. 079. DOI: `10.1007/JHEP07(2014)079`.

[120] D. Alva, T. Han, and R. Ruiz, “Heavy Majorana neutrinos from Wγ fusion at hadron colliders”. *Journal of High Energy Physics* 2015.2 (Feb. 2015). DOI: `10.1007/jhep02(2015)072`.

[121] C. Degrande et al., “Fully automated precision predictions for heavy neutrino production mechanisms at hadron colliders”. *Physical Review D* 94.5 (Sept. 2016). DOI: `10.1103/physrevd.94.053002`.

[122] S. Pascoli, R. Ruiz, and C. Weiland, “Heavy neutrinos with dynamic jet vetoes: multilepton searches at $\sqrt{s}$=14, 27, and 100 TeV”. *Journal of High Energy Physics* 2019.6 (June 2019). DOI: `10.1007/jhep06(2019)049`.

[123] CMS Collaboration, “Precision luminosity measurement in proton-proton collisions at $\sqrt{s} = 13\,\text{Tev}$ in 2015 and 2016 at CMS”. *Eur. Phys. J. C* 81 (2021), p. 800. DOI: `10.1140/epjc/s10052-021-09538-2`.

[124] S. Camarda et al., “DYTurbo: Fast predictions for Drell-Yan processes”. *Eur. Phys. J. C* 80.3 (2020), p. 251. DOI: `10.1140/epjc/s10052-020-7757-5`.

[125] CMS Collaboration, “Performance of electron reconstruction and selection with the CMS detector in proton-proton collisions at $\sqrt{s} = 8\,\text{Tev}$”. *Journal of Instrumentation* 10.06 (June 2015), P06005. DOI: `10.1088/1748-0221/10/06/P06005`.

[126] V. Patil and H. Kulkarni, “Comparison of confidence intervals for the Poisson mean: some new aspects”. *REVSTAT-Statistical Journal* 10.2 (2012), pp. 211–22.

[127] D. Hahs-Vaughn and R. Lomax, *Statistical Concepts: A Second Course (5th ed.)* Routledge, 2020. DOI: `https://doi.org/10.4324/9780429277825`.

[128] WA66 Collaboration, “Search for Heavy Neutrino Decays in the BEBC Beam Dump Experiment”. *Phys. Lett. B* 160 (1985), p. 207. DOI: `10.1016/0370-2693(85)91493-5`.

[129] Belle Collaboration, “Search for heavy neutrinos at Belle”. *Phys. Rev. D* 87 (2013), p. 071102. DOI: `10.1103/PhysRevD.87.071102`.

[130] ATLAS Collaboration, “Search for heavy neutral leptons in decays of W bosons using a dilepton displaced vertex in $\sqrt{s} = 13$ TeV pp collisions with the ATLAS detector”. 2022. arXiv: `2204.11988 [hep-ex]`.

[131] DELPHI collaboration, “Search for neutral heavy leptons produced in Z decays”. *Zeitschrift für Physik C Particles and Fields* 74 (1997), pp. 57–71.

[132] Charm collaboration, “A search for decays of heavy neutrinos in the mass range 0.5–2.8 GeV”. *Physics Letters B* 166.4 (1986), pp. 473–478. DOI: `https://doi.org/10.1016/0370-2693(86)91601-1`.

[133] S. Knapen, J. Shelton, and D. Xu, “Perturbative benchmark models for a dark shower search program”. *Physical Review D* 103.11 (June 2021). DOI: `10.1103/physrevd.103.115013`.

[134] D. Curtin et al., “Long-lived particles at the energy frontier: the MATHUSLA physics case”. *Reports on Progress in Physics* 82.11 (Oct. 2019), p. 116201. DOI: `10.1088/1361-6633/ab28d6`.

[135] G. Aielli et al., “Expression of interest for the CODEX-b detector”. *The European Physical Journal C* 80.12 (Dec. 2020). DOI: `10.1140/epjc/s10052-020-08711-3`.

[136] V. V. Gligorov et al., “Searching for long-lived particles: A compact detector for exotics at LHCb”. *Physical Review D* 97.1 (Jan. 2018). DOI: `10.1103/physrevd.97.015023`.

[137] FASER Collaboration, “The FASER Detector” (2022). arXiv: `2207.11427 [physics.ins-det]`.

Appendix

A Search for long-lived particles decaying in the CMS endcap muon system

This chapter contains additional material to Ch. 5.

Table A.1: Signal Efficiency(in %) of each selection for a LLP mass of 40 GeV, decaying to 2 b quarks. The cumulative efficiency is calculated with respect to the acceptance, $p_{\mathrm{T}}^{\mathrm{miss}}$ and trigger selection.

	$c\tau = 0.1$m		$c\tau = 1$m		$c\tau = 10$m		$c\tau = 100$m	
Selection	cut eff	cumulative eff	cut eff	cumulative eff	cut eff	cumulative eff	cut eff	cumulative eff
Acceptance	0.09	0.09	17.10	17.10	20.33	20.33	3.32	3.32
Trigger and MET cut	8.25	0.01	1.01	0.17	0.72	0.15	0.65	0.02
MET filters	97.75	97.75	96.86	96.86	99.23	99.23	99.46	99.46
$N_{\text{lepton}} = 0$	99.75	97.50	99.52	96.40	99.77	99.00	99.64	99.10
$N_{\text{jet}} \geq 1$	97.51	95.08	95.58	92.13	94.66	93.71	94.19	93.34
$N_{\text{CSC+DT rings}} \leq 10$	100.00	95.08	100.00	92.13	100.00	93.71	100.00	93.34
$N_{\text{cluster}} \geq 1$	91.16	86.67	73.55	67.76	61.90	58.01	57.75	53.91
muon veto	95.29	82.59	94.03	63.72	94.28	54.69	94.57	50.98
jet veto	59.23	48.92	82.75	52.73	88.17	48.23	87.86	44.79
Time cut	100.00	48.92	99.83	52.64	96.69	46.63	92.55	41.45
ME1/1 veto	46.65	22.82	81.72	43.01	87.90	40.99	85.73	35.54
ME1/2 veto	66.95	15.28	69.34	29.83	71.49	29.30	71.51	25.41
RE1/2 veto	100.00	15.28	97.16	28.98	98.20	28.78	98.96	25.15
MB1 veto	97.88	14.95	94.39	27.35	96.43	27.75	96.58	24.29
RB1 veto	100.00	14.95	96.21	26.32	97.15	26.96	96.45	23.43
η cut	41.11	6.15	83.13	21.88	89.84	24.22	90.76	21.26
time spread cut	96.32	5.92	99.00	21.66	99.11	24.00	97.29	20.69
cut-based ID	68.32	4.05	89.57	19.40	92.64	22.24	88.12	18.23
$\Delta\phi$(cluster,$p_{\mathrm{T}}^{\mathrm{miss}}$)	100.00	4.05	99.40	19.28	96.25	21.40	95.88	17.48
N_{rechit} cut	95.45	3.86	87.87	16.94	79.81	17.08	79.44	13.88

Table A.2: Signal Efficiency (in %) of each selection for a LLP mass of 55 GeV, decaying to 2 b quarks. $c\tau = 0.1$ m is not shown, because the acceptance is too small, leading to no events being left after the selections are applied. The cumulative efficiency is calculated with respect to the acceptance, $p_{\mathrm{T}}^{\mathrm{miss}}$ and trigger selection

	$c\tau = 1$m		$c\tau = 10$m		$c\tau = 100$m	
Selection	cut eff	cumulative eff	cut eff	cumulative eff	cut eff	cumulative eff
Acceptance	8.38	8.38	23.91	23.91	5.29	5.29
Trigger and MET cut	1.47	0.12	0.65	0.155	0.44	0.02
MET filters	95.46	95.46	99.35	99.35	99.61	99.61
$N_{\mathrm{lepton}} = 0$	99.46	94.94	99.71	99.06	99.82	99.44
$N_{\mathrm{jet}} \geq 1$	96.13	91.27	94.61	93.72	93.45	92.93
$N_{\mathrm{CSC+DT\ rings}} \leq 10$	100.00	91.27	100.00	93.72	100.00	92.93
$N_{\mathrm{cluster}} \geq 1$	78.23	71.40	66.64	62.45	65.26	60.64
muon veto	91.44	65.29	93.39	58.32	93.41	56.64
jet veto	67.93	44.35	87.22	50.87	89.35	50.61
Time cut	99.71	44.22	99.51	50.62	99.10	50.16
ME1/1 veto	73.19	32.37	87.74	44.41	90.29	45.29
ME1/2 veto	64.45	20.86	71.88	31.93	71.17	32.23
RE1/2 veto	98.07	20.46	98.26	31.37	98.34	31.69
MB1 veto	95.71	19.58	95.65	30.01	96.90	30.71
RB1 veto	97.63	19.12	97.31	29.20	97.81	30.04
η cut	68.27	13.05	91.24	26.64	92.02	27.64
time spread cut	98.63	12.87	98.89	26.34	98.95	27.35
cut-based ID	82.20	10.58	92.26	24.31	94.68	25.90
$\Delta\phi$(cluster,$p_{\mathrm{T}}^{\mathrm{miss}}$)	99.84	10.56	100.00	24.31	100.00	25.90
N_{rechit} cut	90.57	9.57	82.01	19.93	77.00	19.94

B Search for Long-Lived Heavy Neutral Leptons

This chapter contains additional material to Ch. 6.

Table B.3: Cut flow table for CSC cluster selections in the electron channel. The cut flow for data is compared with e-HNL with mass of 4GeV and $c\tau$ of 1m. The signal yield corresponds to a luminosity of $120fb^{-1}$ within the CSC fiducial acceptance. For each selection, the cumulative efficiency and the individual selection efficiency is computed. The last column corresponds to the ratio of individual selection efficiency between signal and data. The data sample is skimmed with at least 1 CSC or DT cluster, which has an efficiency around 10^{-4}.

	Data - Electron Channel			Signal e-HNL (4GeV,1m)			
Selection	No. of Events	cum.	eff.	Yield	cum.	eff.	eff. S/B
	7.39e+07	-	-	54.2	-	-	-
Trigger	3.23e+07	4.37e-01	0.437	16.1	2.97e-01	0.297	0.68
MET	2.11e+07	2.86e-01	0.653	11.7	2.16e-01	0.727	1.11
METfilters	2.11e+07	2.86e-01	1.000	11.7	2.16e-01	1.000	1.00
Good lepton	6.31e+06	8.54e-02	0.299	8.29	1.53e-01	0.709	2.37
$n_{\mathrm{cls}} >= 1$	5.34+06	7.23e-02	0.846	3.73	6.88e-02	0.450	0.53
$\Delta R(\mathrm{l}, \mathrm{cls}) > 0.8$	5.09+06	6.89e-02	0.953	3.72	6.86e-02	0.997	1.05
ME11/ME12 veto	3.24+05	4.38e-03	0.064	2.65	4.89e-02	0.712	11.12
JetVeto	2.96+05	4.01e-03	0.914	2.44	4.50e-02	0.921	1.01
MuonVeto	2.95+05	3.99e-03	0.997	2.37	4.37e-02	0.971	0.97
MB1 segment veto	2.93+05	3.96e-03	0.993	2.33	4.30e-02	0.983	0.99
RB1 rechit veto	2.92+05	3.95e-03	0.997	2.29	4.23e-02	0.983	0.99
RE12 veto	2.90+05	3.92e-03	0.993	2.27	4.19e-02	0.991	1.00
In-time Cut	4.93+04	6.67e-04	0.170	2.24	4.13e-02	0.987	5.81
TimeSpread Cut	3.10+04	4.19e-04	0.629	2.2	4.06e-02	0.982	1.56
ClusterID	2.38+03	3.22e-05	0.077	1.26	2.32e-02	0.573	7.44

Table B.4: Cut flow table for DT cluster selections in the electron channel. The cut flow for data is compared with e-HNL with mass of 4GeV and $c\tau$ of 1m. The signal yield corresponds to a luminosity of $120fb^{-1}$ within the DT fiducial acceptance. For each selection, the culmulative efficiency and the individual selection efficiency is computed. The last column corresponds to the ratio of individual selection efficiency between signal and data. The data sample is skimmed with at least 1 CSC or DT cluster, which has an efficiency around 10^{-4}.

	Data - Electron Channel			Signal e-HNL (4GeV,1m)			
Selection	No. of Events	cum.	eff.	Yield	cum.	eff.	eff. S/B
	7.39e+07	-	-	57.2	-	-	-
Trigger	3.23e+07	4.37e-01	0.437	21.1	3.69e-01	0.369	0.84
MET	2.11e+07	2.86e-01	0.653	14.9	2.60e-01	0.706	1.08
METfilters	2.11e+07	2.86e-01	1.000	14.9	2.60e-01	1.000	1.00
Good lepton	6.31e+06	8.54e-02	0.299	10.9	1.91e-01	0.732	2.45
$n_{\text{cls}} >= 1$	1.01e+06	1.37e-02	0.160	4.01	7.01e-02	0.368	2.30
$\Delta R(\text{l}, \text{cls}) > 0.8$	9.54e+05	1.29e-02	0.945	4.0	6.99e-02	0.998	1.06
MB1 Veto	2.32e+04	3.14e-04	0.024	2.18	3.81e-02	0.545	22.71
Jet Veto	1.67e+04	2.26e-04	0.720	2.13	3.72e-02	0.977	1.36
Muon Veto	1.66e+04	2.25e-04	0.994	1.77	3.09e-02	0.831	0.84
$RPC > 1$	1.27e+04	1.72e-04	0.765	1.74	3.04e-02	0.983	1.28
MB1 adj. wheel	1.16e+04	1.57e-04	0.913	1.69	2.95e-02	0.971	1.06
Time cut(BX=0)	2.78e+03	3.76e-05	0.240	1.67	2.92e-02	0.988	4.12
DT chimney veto	2.42e+03	3.27e-05	0.871	1.51	2.64e-02	0.904	1.04

Table B.5: Cut flow table for various signals in the muon channel. The signal yield corresponds to a luminosity of $120 fb^{-1}$.

	μ-HNL(1GeV,1m)		μ-HNL(2GeV,1m)		μ-HNL(4GeV,1m)	
Selection	Yield	eff.	Yield	eff.	Yield	eff.
NoSelection	980000.0	-	30600.0	-	934.0	-
Acceptance(CSC)	23600.0	0.024	1240.0	0.041	54.8	0.059
Acceptance(DT)	44100.0	0.030	2180.0	0.048	87.4	0.063
Trigger	10700.0	0.453	574.0	0.463	26.7	0.487
MET	10700.0	0.669	566.0	0.678	24.9	0.690
METfilters	10700.0	1.000	565.0	0.998	24.9	1.000
Good lepton	9810.0	0.917	522.0	0.924	22.9	0.920
$n_{cls} >= 1$	2630.0	0.391	157.0	0.427	8.74	0.511
$\Delta R(l, cls) > 0.8$	2470.0	0.939	148.0	0.943	8.26	0.945
ME11/ME12 veto	1770.0	0.717	102.0	0.689	5.63	0.682
JetVeto	1580.0	0.893	92.7	0.909	5.15	0.915
MuonVeto	1490.0	0.943	88.4	0.954	4.94	0.959
MB1 segment veto	1450.0	0.973	87.0	0.984	4.88	0.988
RB1 rechit veto	1430.0	0.986	85.6	0.984	4.79	0.982
RE12 veto	1410.0	0.986	83.8	0.979	4.72	0.985
In-time Cut	1400.0	0.993	82.4	0.983	4.67	0.989
TimeSpread Cut	1380.0	0.986	81.2	0.985	4.6	0.985
ClusterID	833.0	0.604	50.0	0.616	2.75	0.598
$n_{cls}(DT) >= 1$	3230.0	0.329	183.0	0.351	9.75	0.426
$\Delta R(l, cls) > 0.8$	2890.0	0.895	165.0	0.902	9.0	0.923
MB1 Veto	1680.0	0.581	94.5	0.573	4.81	0.534
Jet Veto	1630.0	0.970	91.7	0.970	4.68	0.973
Muon Veto	1050.0	0.644	61.7	0.673	3.07	0.656
$RPC > 1$	1040.0	0.990	61.0	0.989	3.02	0.984
MB1 adj. wheel	1020.0	0.981	59.6	0.977	2.94	0.974
Time cut(BX=0)	1000.0	0.980	57.9	0.971	2.9	0.986
DT chimney veto	911.0	0.911	52.7	0.910	2.62	0.903
MB2: ($N_{hit} > 150$,$\Delta\phi_{lep} > 2.8$)	55.33	0.06	3.17	0.06	0.18	0.07
MB34:($N_{hit} > 150$,$\Delta\phi_{lep} > 2.8$)	189.4	0.21	12.1	0.23	0.51	0.20

Table B.6: Cut flow table for various signals in the electron channel. The signal yield corresponds to a luminosity of $120 fb^{-1}$.

	e-HNL(1GeV,1m)		e-HNL(2GeV,1m)		e-HNL(4GeV,1m)	
Selection	Yield	eff.	Yield	eff.	Yield	eff.
NoSelection	964000.0	-	30100.0	-	919.0	-
Acceptance(CSC)	22900.0	0.024	1210.0	0.040	54.2	0.059
Acceptance(DT)	28700.0	0.030	1430.0	0.048	57.2	0.062
Trigger	9540.0	0.332	500.0	0.350	21.1	0.369
MET	6580.0	0.690	349.0	0.698	14.9	0.706
METfilters	6580.0	1.000	348.0	0.997	14.9	1.000
Good lepton	4940.0	0.751	253.0	0.727	10.9	0.732
$n_{cls} >= 1$	1160.0	0.348	67.0	0.381	3.73	0.450
$\Delta R(l, cls) > 0.8$	1160.0	1.000	66.5	0.993	3.72	0.997
ME11/ME12 veto	815.0	0.703	45.2	0.680	2.65	0.712
JetVeto	746.0	0.915	42.0	0.929	2.44	0.921
MuonVeto	721.0	0.966	40.0	0.952	2.37	0.971
MB1 segment veto	709.0	0.983	39.5	0.988	2.33	0.983
RB1 rechit veto	697.0	0.983	38.8	0.982	2.29	0.983
RE12 veto	685.0	0.983	38.5	0.992	2.27	0.991
In-time Cut	670.0	0.978	38.0	0.987	2.24	0.987
TimeSpread Cut	663.0	0.990	37.6	0.989	2.2	0.982
ClusterID	406.0	0.612	24.6	0.654	1.26	0.573
$n_{cls}(DT) >= 1$	1340.0	0.271	72.9	0.288	4.01	0.368
$\Delta R(l, cls) > 0.8$	1330.0	0.993	72.8	0.999	4.0	0.998
MB1 Veto	815.0	0.613	41.6	0.571	2.18	0.545
Jet Veto	804.0	0.987	40.8	0.981	2.13	0.977
Muon Veto	664.0	0.826	34.2	0.838	1.77	0.831
$RPC > 1$	654.0	0.985	33.7	0.985	1.74	0.983
MB1 adj. wheel	632.0	0.966	32.4	0.961	1.69	0.971
Time cut(BX=0)	617.0	0.976	32.0	0.988	1.67	0.988
DT chimney veto	554.0	0.898	29.5	0.922	1.51	0.904
$N_{hit} > 150, \Delta\phi_{lep} > 2.8$	148	0.27	6.88	0.23	0.42	0.28

B.1 OOT CR

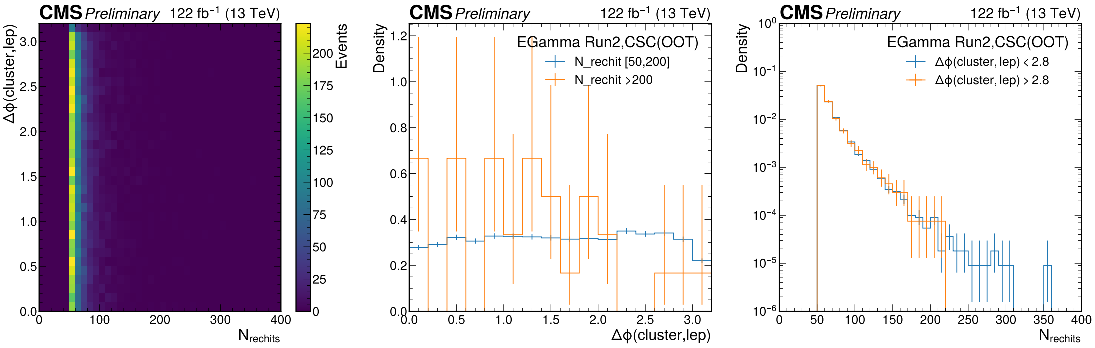

Figure B.1: 2D distribution of N_{rechit} and $\Delta\phi(\text{cluster}, \text{lep})$ (left) of CSC clusters for the OOT control region($t_{\text{cluster}} < -12.5$ ns) in the electron channel. The middle and right panel shows 1D projections on N_{rechit} and $\Delta\phi(\text{cluster}, \text{lep})$ at the chosen thresholds.

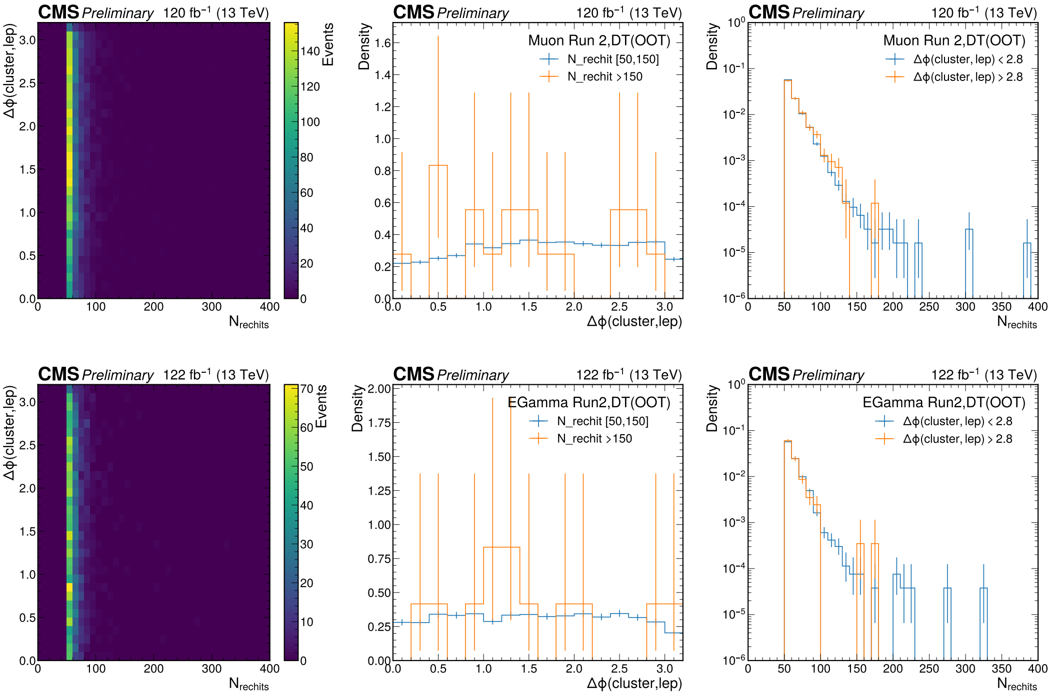

Figure B.2: 2D distribution of N_{rechit} and$\Delta\phi(\text{cluster}, \text{lep})$ (left) of DT clusters for the OOT control region($\text{BX}_{\text{cluster}} < 0$) in the muon channel (top) and electron channel(bottom). The middle and right panel shows 1D projections on N_{rechit} and $\Delta\phi(\text{cluster}, \text{lep})$ at the chosen thresholds.

Table B.7: Validation of the ABCD method in the OOT control region for CSC cluster selections in the electron channel.

cut(N_{rechit},$\Delta\phi_{\text{lep}}$)	A	B	C	D	Prediction($\frac{A\times C}{B}$)
(120,2.8)	317	10738	1281	40	37.82 ± 2.40
(140,2.8)	152	10903	1302	19	18.15 ± 1.57
(160,2.8)	79	10976	1312	9	9.44 ± 1.10
(200,2.8)	28	11027	1319	2	3.35 ± 0.64
(220,2.8)	16	11039	1321	0	1.91 ± 0.48
(200,2.6)	18	7282	1558	3	3.85 ± 0.91
(200,2.6)	27	10185	2161	3	5.73 ± 1.11
(200,2.7)	28	10611	1735	2	4.58 ± 0.87
(200,2.8)	28	11027	1319	2	3.35 ± 0.64

Table B.8: Validation of the ABCD method in the OOT control region for DT cluster selections in the muon channel.

cut(N_{rechit},$\Delta\phi_{\text{lep}}$)	A	B	C	D	Prediction($\frac{A\times C}{B}$)
(110,2.8)	83	6122	829	16	11.24 ± 1.30
(120,2.8)	49	6156	837	8	6.66 ± 0.98
(130,2.8)	31	6174	843	2	4.23 ± 0.78
(140,2.8)	23	6182	844	1	3.14 ± 0.66
(150,2.8)	17	6188	844	1	2.32 ± 0.57
(150,2.6)	15	5694	1338	3	3.52 ± 0.92
(150,2.7)	16	5941	1091	2	2.94 ± 0.74
(150,2.8)	17	6188	844	1	2.32 ± 0.57

Table B.9: Validation of the ABCD method in the OOT control region for DT cluster selections in the electron channel.

cut(N_{rechit},$\Delta\phi_{\text{lep}}$)	A	B	C	D	Prediction($\frac{A\times C}{B}$)
(90,2.8)	93	2555	278	9	10.12 ± 1.23
(110,2.8)	34	2614	285	2	3.71 ± 0.68
(120,2.8)	23	2625	285	2	2.50 ± 0.54
(130,2.8)	15	2633	285	2	1.62 ± 0.43
(150,2.8)	10	2638	285	2	1.08 ± 0.35
(150,2.6)	10	2453	470	2	1.92 ± 0.61
(150,2.7)	10	2540	383	2	1.51 ± 0.48
(150,2.8)	10	2638	285	2	1.08 ± 0.35

B.2 In-Time CR

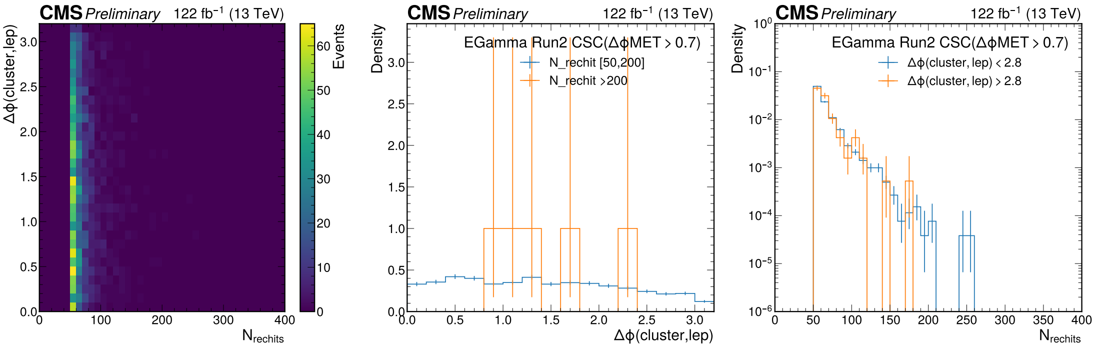

Figure B.3: 2D distribution of N_{rechit} and $\Delta\phi_{lep}$ (left) of CSC clusters for the in-time control region($\Delta\phi_{MET} > 0.7$) in the electron channel. The middle and right panel shows the 1D projections on N_{rechit} and $\Delta\phi_{lep}$ at the chosen thresholds.

Table B.10: Validation of the ABCD method in the in-time control region for CSC cluster selections in the electron channel.

cut(N_{rechit},$\Delta\phi_{\text{lep}}$)	A	B	C	D	Prediction($\frac{A\times C}{B}$)
(120,2.8)	87	2530	188	2	6.46 ± 0.85
(140,2.8)	35	2582	188	2	2.55 ± 0.47
(160,2.8)	15	2602	189	1	1.09 ± 0.29
(200,2.8)	5	2612	190	0	0.36 ± 0.16
(220,2.8)	3	2614	190	0	0.22 ± 0.13
(200,2.6)	5	2493	309	0	0.62 ± 0.28
(200,2.7)	5	2549	253	0	0.50 ± 0.22
(200,2.8)	5	2612	190	0	0.36 ± 0.16

Table B.11: Validation of the ABCD method in the in-time control region for DT cluster selections in the muon channel.

cut(N_{rechit},$\Delta\phi_{\text{lep}}$)	A	B	C	D	Prediction($\frac{A\times C}{B}$)
(100,2.8)	199	4608	463	24	20.00 ± 1.72
(120,2.8)	55	4752	479	8	5.54 ± 0.79
(130,2.8)	27	4780	484	3	2.73 ± 0.54
(140,2.8)	18	4789	484	3	1.82 ± 0.44
(150,2.8)	13	4794	485	2	1.32 ± 0.37
(150,2.6)	12	4516	763	3	2.03 ± 0.59
(150,2.7)	12	4673	606	3	1.56 ± 0.45
(150,2.8)	13	4794	485	2	1.32 ± 0.37

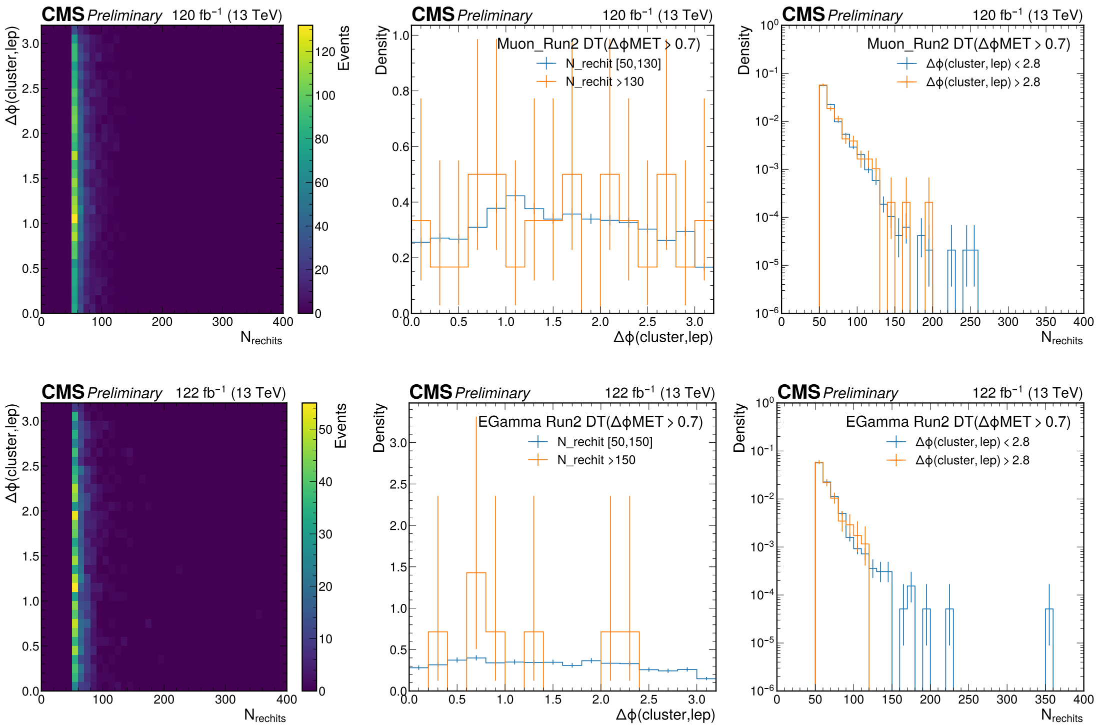

Figure B.4: 2D distribution of N_{rechit} and $\Delta\phi_{lep}$ (left) of DT clusters for the in-time control region($\Delta\phi_{MET} > 0.7$) in the muon channel (top) and electron channel(bottom). The middle and right panel shows the 1D projections on N_{rechit} and $\Delta\phi_{lep}$ at the chosen thresholds.

Table B.12: Validation of the ABCD method in the in-time control region for DT cluster selections in the electron channel.

cut(N_{rechit},$\Delta\phi_{\text{lep}}$)	A	B	C	D	Prediction($\frac{A\times C}{B}$)
(90,2.8)	89	1863	163	10	7.79 ± 1.04
(110,2.8)	40	1912	171	2	3.58 ± 0.63
(120,2.8)	26	1926	173	0	2.34 ± 0.49
(130,2.8)	19	1933	173	0	1.70 ± 0.41
(150,2.8)	7	1945	173	0	0.62 ± 0.24
(150,2.6)	7	1842	276	0	1.05 ± 0.40
(150,2.7)	7	1901	217	0	0.80 ± 0.31
(150,2.8)	7	1945	173	0	0.62 ± 0.24

Danksagung

Zu guter Letzt möchte ich mich noch bei einigen Personen bedanken, ohne deren Unterstützung und Hilfe diese Arbeit nicht möglich gewesen wäre.

Zu aller erst möchte ich mich bei Gregor Kasieczka bedanken: Danke, dass du mir vor vier Jahren die Chance gegeben hast in deiner Arbeitsgruppe zu promovieren. Auch während der schwierigen Coronazeit standest du mir immer mit Rat und Unterstützung zur Seite. Egal mit welchem Anliegen oder Plan ich zu dir kam, ich konnte mir deiner Unterstützung immer sicher sein. Besonders der drei Monate Auslandsaufenthalt am Fermilab war nur mit deiner Unterstützung möglich.

Als nächstes möchte ich meinem Zweitgutachter, Peter Schleper, bedanken. Auch wenn wir Pandemie bedingt nicht so viel Kontakt hatten, habe ich deine Fragen und Anregungen in den UHH Meetings immer gerne verfolgt und auch viel dabei gelernt.

Work wise, this thesis would have not been possible without the help and encouragement of my US based colleagues. First I want to thank Cristián Peña and Artur Apresyan. When I first meet you in 2019 during the CMS Exotica Workshop in Aachen, I could have not imagined how great this collaboration would end up. I also want to thank Martin Kwok, with whom I worked together on the HNL analysis. I will look back foundly on the countless physics and basketball discussions we had, I can not put into words how much I learned from you. Additonally, I also want to thank Christina Wang and Si Xie. The hospitality you all offered me during my stay at Fermilab was amazing, from the Barbeques at Cristiáns and Arturs house, to the Chicago Bulls game, to the times Martin took me to some of his favourite food spots around Fermilab, thank you! I can wholehearthly say, that the three months at Fermilab was my favourite part of my PhD.

Ein weiterer großer Dank geht raus an Karim El Morabit. Nachdem du schon meine Masterarbeit in Karlsruhe Korrektur lesen durftest, hast du jetzt auch wieder meine PhD Thesis lesen “dürfen”. Ohne deine Hilfe wäre die Thesis niemals in einem solchen guten Zustand. Auch deine physikalischen Verständnisfragen mit anschließenden Diskussionen haben mich sehr weitergebracht. Hoffentlich habe ich dir mit meinen ganzen Rechtschreibfehlern (“long-lived”, “punch-through”,...) nicht zu viele Nerven gekostet :D . Auch möchte ich mich bei Lisa Benato für das Korrekturlesen der Arbeit und der gemeinsamen Arbeit bedanken!

Außerdem möchte ich gerne bei Melanie Eich für sowohl die gemeinsame Zeit im Büro, als auch all die Unternehmungen und Unterstützung außerhalb der Arbeit bedanken. Die virtuellen Kaffeepausen und Kochabende werde ich immer gut in Erinnerung behalten. Natürlich möchte ich mich auch noch bei der ganzen Arbeitsgruppe Kasiezka bedanken.

Last but not least, möchte ich mich bei meiner Familie und meinen Freunden bedanken, speziell meiner Mutter Christa und meinem Bruder Mario. Egal was ist und war, kann ich mich auf eure Hilfe und Unterstützung verlassen.